Technical Report Documentation Page

1. Report No.
FHWA/TX-08/0-5506-1

2. Government Accession No.

3. Recipient's Catalog No.

4. Title and Subtitle
Design Considerations for MSE Retaining Walls Constructed in Confined Spaces

5. Report Date
October 2007

6. Performing Organization Code

7. Author(s)
Kenneth T. Kniss, Stephen G. Wright, Jorge Zornberg, Kuo-Hsin Yang

8. Performing Organization Report No.
0-5506-1

9. Performing Organization Name and Address
Center for Transportation Research
The University of Texas at Austin
3208 Red River, Suite 200
Austin, TX 78705-2650

10. Work Unit No. (TRAIS)

11. Contract or Grant No.
0-5506

12. Sponsoring Agency Name and Address
Texas Department of Transportation
Research and Technology Implementation Office
P.O. Box 5080
Austin, TX 78763-5080

13. Type of Report and Period Covered
Technical Report
9/1/2005 – 8/31/2007

14. Sponsoring Agency Code

15. Supplementary Notes
Project performed in cooperation with the Texas Department of Transportation and the Federal Highway Administration.

16. Abstract

Widening of existing highways often results in new mechanically stabilized earth (MSE) walls being placed in front of existing stable walls. The design of these walls is unique because limited right-of-way often forces the length of the reinforcing strips to be shorter than normally used. This research addressed such walls placed in a confined space.

The Plaxis finite element software was used to study the vertical and horizontal stresses in the backfill behind nondeformable walls constructed in a confined space. The vertical stresses were generally found to be less than the computed overburden pressure. A vertical stress influence factor is presented to describe the reduced vertical stresses as a function of the depth below the top of the wall and the wall aspect ratio. Horizontal earth pressures were also found to be less than those for walls that are not in a confined space. A chart was developed for estimating these reduced horizontal stresses.

Limit equilibrium analyses were also performed to evaluate the effect of walls being placed in a confined space. Factors of safety computed for noncircular slip surfaces were found to be significantly less than factors of safety computed for circular slip surfaces. Analyses employing noncircular slip surfaces are recommended for walls placed in confined spaces.

17. Key Words
Mechanically stabilized earth; retaining walls; geotechnical engineering

18. Distribution Statement
No restrictions. This document is available to the public through the National Technical Information Service, Springfield, Virginia 22161; www.ntis.gov.

19. Security Classif. (of report)	20. Security Classif. (of this page)	21. No. of pages	22. Price
Unclassified	Unclassified	176	

Form DOT F 1700.7 (8-72) Reproduction of completed page authorized

Design Considerations for MSE Retaining Walls Constructed in Confined Spaces

Kenneth T. Kniss
Stephen G. Wright
Jorge Zornberg
Kuo-Hsin Yang

CTR Technical Report:	0-5506-1
Report Date:	October 2007
Project:	0-5506
Project Title:	Design of MSE Retaining Walls Placed in Front of a Stable Face
Sponsoring Agency:	Texas Department of Transportation
Performing Agency:	Center for Transportation Research at The University of Texas at Austin

Project performed in cooperation with the Texas Department of Transportation and the Federal Highway Administration.

Center for Transportation Research
The University of Texas at Austin
3208 Red River
Austin, TX 78705

www.utexas.edu/research/ctr

Printed in the United States of America

Disclaimers

Engineering Disclaimer

Project Engineer: Stephen G. Wright
Professional Engineer License State and Number: Texas 49007
P. E. Designation: Research Supervisor

Acknowledgments

This research was sponsored by the Texas Department of Transportation with support of The University of Texas Civil Engineering Department. The Project Coordinator was Mr. Mark McClelland, P.E. His vision, helpful comments, and encouragement thought this study provided valuable guidance and were instrumental in the eventual success of this work. Ms. Rachael Ruperto was the Project Director and also provided useful guidance and encouragement as well as assured that the project remained focused and on schedule. Her contributions are greatly appreciated. We also acknowledge the contributions of the very diverse yet close group of geotechnical engineering graduate students at The University of Texas for their interest and collaboration during this work.

Products

Product 1, *Recommended Design Procedures for Placing an MSE Retaining Wall in Front of a Stable Face*, is found in Chapter 9 of this report.

Table of Contents

Chapter 1. Introduction......1
Chapter 2. Literature Review......3
2.1 Terminology......3
2.2 Field Case Study: Turner and Jensen, 2005......7
2.3 Full-Scale Field Testing: Shored Mechanically Stabilized Earth (SMSE) Wall Systems Design Guidelines, 2006 (Morrison et al., 2006)......7
2.4 Laboratory Testing......14
2.5 Limit Equilibrium Analysis......23
2.6 Data Compilation......28
2.7 Summary and Conclusion......30
Chapter 3. Modeling a Nondeformable Retaining Wall Placed In a Confined Space Using Plaxis......31
3.1 Modeling the physical space......31
3.2 Interpreting displacements output by Plaxis......38
3.3 Summary......46
Chapter 4. Soil-Wall Interaction......47
4.1 The effect of boundary conditions on vertical displacements, especially when plate elements were used to model the wall face......47
4.2 The effect of the interface reduction factor on vertical displacements......57
4.3 Conclusions on soil-wall interaction......62
Chapter 5. Comparisons of Earth Pressures Calculated by Plaxis to Measured Earth Pressures from Centrifuge Tests and to Computed Values Using Spangler and Handy's Equation......65
5.1 Experimental Test Data......65
5.2 Finite Element Modeling......67
5.3 Comparison of calculated and measured earth pressures from centrifuge tests performed by Frydman and Keissar......69
5.4 Comparison of calculated and measured earth pressures for centrifuge tests performed by Take and Valsangkar......72
5.5 The effect of soil-wall interaction on horizontal earth pressures......77
5.6 Summary and conclusions of finite element modeling of centrifuge tests......77
Chapter 6. Examination of Soil Constitutive Models in Terms of Effect on Horizontal Earth Pressures......79
6.1 Spangler and Handy's equation......79
6.2 Soil constitutive variables......79
6.3 Basis for comparisons of horizontal earth pressures calculated by Plaxis and Spangler and Handy's equation......86
6.4 Parametric analyses and comparisons for the Mohr-Coulomb model......87
6.5 Parametric analyses and comparisons for the Hardening-Soil model......89
6.6 Conclusions from parametric analyses......91
6.7 Conclusions from comparisons of values of K_{eq} calculated from results output by Plaxis and values of K_{eq} computed from Spangler and Handy's equation......91
6.8 Summary......92

Chapter 7. Effect of Wall Aspect Ratio on Vertical and Horizontal Stresses Behind a Nondeformable Wall....................93
7.1 Effect of wall aspect ratio on vertical stresses behind nondeformable walls 93
7.2 Definitions of horizontal earth pressure coefficients....................105
7.3 Effect of wall aspect ratio on horizontal earth pressures for nondeformable walls....................107
7.4 Comparison of horizontal earth pressure coefficients calculated by Plaxis to values recommended by current FHWA design guidelines....................111
7.5 Application of reduced earth pressures for the internal stability design of nondeformable walls placed in front of an existing stable face....................112
7.6 Summary and Conclusions 116
Chapter 8. Limit Equilibrium Analyses of Nondeformable MSE Walls in Front of a Stable Face....................119
8.1 Modeling a nondeformable MSE wall placed in front of a stable face using UTEXAS4.119
8.2 Searching for the critical slip surface 124
8.3 Results and discussion for critical slip surface 128
8.4 Weak interface....................137
8.5 Tension crack....................141
8.6 Factor of safety in the reinforcement....................143
8.7 Limit equilibrium analysis of a centrifuge model test 147
8.8 Conclusions and design implications....................150
Chapter 9. Summary, Conclusions, and Recommendations....................151
9.1 Modeling nondeformable walls using the finite element software known as Plaxis....................151
9.2 Studies of vertical and horizontal earth pressures 154
9.3 Limit equilibrium analyses 155
9.4 Recommendations....................156
References....................159

List of Tables

Table 2.1: Summary of backfill properties, reinforcement properties, and wall properties from literature review 29
Table 3.1: Soil constitutive parameters chosen for the linear elastic model 39
Table 3.2: Summary of displacements at the surface of a layer output by Plaxis and calculated using linear elastic theory 41
Table 3.3: Displacements at the end of construction calculated using Equation 3-14 43
Table 3.4: Results for displacements at the end of construction converted from Plaxis output and calculated using Equation 3-14 46
Table 4.1: Description of cases used to study the effect of boundary conditions on vertical displacements, especially when plate elements were used to model the wall face 48
Table 4.2: Soil properties for study of soil-wall interaction 54
Table 4.3: Assignments for cases in the study of the effect of plates on vertical displacements ..54
Table 4.4: Vertical displacements from study of boundary conditions at Point A 55
Table 4.5: Vertical displacements from study of boundary conditions at Point A arranged by boundary condition assigned to the wall face 55
Table 4.6: Vertical displacements from study of boundary conditions at Point A arranged by how the wall face was modeled 56
Table 4.7: Vertical displacements from study of boundary conditions at Point A arranged by boundary condition assigned to the wall face 56
Table 4.8: Vertical displacements from study of boundary conditions at Point A arranged by how the wall face was modeled 57
Table 4.9: Variable assignments for cases in the study of the effect of interface reduction factor on vertical displacement 58
Table 4.10: Vertical displacements calculated at point A for study of the effect of the interface reduction factor (R_{inter}) 59
Table 4.11: Vertical displacement at point A calculated for Cases 1-5 with the linear elastic and Mohr-Coulomb models 60
Table 4.12: Vertical displacement at point A for cases 6-10 with the linear elastic and Mohr-Coulomb models 61
Table 5.1: Parameters chosen to model the centrifuge tests by Frydman and Keissar and Take and Valsangkar 69
Table 6.1: Mohr-Coulomb model parameters selected for the parametric study 80
Table 6.2: Hardening-Soil model parameters selected for the parametric study 83
Table 6.3: Sets used to study the effect of Hardening-soil moduli parameters on the distribution of horizontal earth pressure coefficients 84
Table 6.4: Values of Young’s Modulus, Poisson’s ratio used to calculate Eoedref 85
Table 6.5: Equivalent total force values as determined by Plaxis and the Trapezoidal Rule 87
Table 6.6: Cases for parametric study using the Mohr-Coulomb model 87
Table 6.7: Percent change in K_{eq} relative to the baseline case for the Mohr-Coulomb model 88
Table 6.8: Percent change in Keq computed using Spangler and Handy’s (S&H) equation relative to the values calculated by Plaxis for the Mohr-Coulomb model 89
Table 6.9: Cases for parametric study using the Hardening-Soil model 90
Table 6.10: Percent change in K_{eq} relative to the baseline case for the Hardening-Soil model 90

Table 6.11: Percent change in K_{eq} calculated using Spangler and Handy's equation relative to the values calculated using the results output by Plaxis for the Hardening-Soil model......................91
Table 6.12: Parameter set for subsequent simulations using the Hardening-Soil model..............92
Table 7.1: Values of β_v plotted in Figure 7-13 104
Table 7.2: Values of β_v based on smooth curves in Figure 7-13 104
Table 8.1: X-and y-coordinates of the center of the initial circle for the four wall aspect ratios analyzed in UTEXAS4 125
Table 8.2: Factors of safety and vertical spacings corresponding to the number of points used to define the general noncircular slip surface 126
Table 8.3: Computed factors of safety for critical circular, noncircular, and bilinear slip surfaces133
Table 8.4: Values of $\phi'_{developed}$ calculated for the critical noncircular slip surfaces....................134
Table 8.5: Computed factors of safety for the case of a weak interface between the existing stable face (interface friction angle = 26.7°) and the case of no interface 138
Table 8.6: Computed factors of safety for the case of an interface with zero strength and the case of an interface with two-thirds ($\phi' = 26.7°$) the strength of the backfill between the stable face and backfill, and no interface...140
Table 8.7: Computed factors of safety when a tension crack was introduced along the interface between the stable face and backfill 142
Table 8.8: Computed factors of safety for analyses performed with general noncircular slip surfaces for walls having no interface, an interface with zero strength, and a tension crack 143
Table 8.9: Factors of safety in the reinforcement from critical circular and general noncircular slip surfaces for wall aspect ratios equal to 0.70, 0.50, and 0.30..144

List of Figures

Figure 1.1: Illustration of proposed narrow MSE wall in front of an existing stable face 1
Figure 2.1: Example of wall aspect ratio defined as L/H 4
Figure 2.2: Example of wall aspect ratio defined as W/H 4
Figure 2.3: Example of wall aspect ratio defined as b/H for a wall placed in front of an existing sloped stable face 5
Figure 2.4: Schematic showing location of total force (F) acting on the wall facing of a retaining wall...6
Figure 2.5: Snake River Canyon MSE wall, Wyoming: (a) Cross-section, (b) Construction of soil nail stabilized slope (stable face) behind new MSE retaining wall (Turner, 2005).........................7
Figure 2.6: Typical cross-section of full-scale field test with reinforcement unconnected to the existing shored wall (Morrison et al., 2006) 8
Figure 2.7: Typical cross-section of full-scale field test with reinforcement connected to the existing shored wall (Morrison et al., 2006) 9
Figure 2.8: Schematic of the instrumented wall cross-section (Morrison et al., 2006) 10
Figure 2.9: Average measured strain versus applied surcharge pressure (Morrison et al., 2006).10
Figure 2.10: Calculated horizontal earth pressure coefficients from earth pressure cell measurements (Morrison et al., 2006) 12
Figure 2.11: Measured vertical pressures for both walls (Morrison et al., 2006).........................13
Figure 2.12: Measured cumulative displacements of the MSE wall face (Morrison et al., 2006) 14
Figure 2.13: Schematic illustration of nondeformable wall used in centrifuge tests by Frydman and Keissar (1987) 16
Figure 2.14: Variation in horizontal earth pressure coefficients (k_w) with the non-dimensional depth (z/H) below the top of the backfill measured from tests performed by Frydman and Keissar with wall aspect ratios (W/H) equal to 1.10 and 0.10..17
Figure 2.15: Variation in horizontal earth pressure coefficients (k_w) with the non-dimensional depth (z/H) below the top of the backfill measured from tests performed by Frydman and Keissar and values of k_w using Spangler and Handy's equation 17
Figure 2.16: Schematic illustration of nondeformable wall used in centrifuge tests by Take and Valsangkar, 2001 18
Figure 2.17: Variation in horizontal earth pressure coefficients (k_w) with the non-dimensional depth (z/H) measured from centrifuge tests performed by Take and Valsangkar with wall aspect ratios (W/H) equal to 0.54 and 0.11...19
Figure 2.18: Schematic of model MSE wall for Woodruff centrifuge tests illustrating wrapped around facing (Woodruff, 2003)...20
Figure 2.19: Photographic images from centrifuge evaluation of the deformation of MSE walls against a rigid shoring system: (a) initial condition; (b) working stresses; (c) failure condition (Woodruff, 2003). 21
Figure 2.20: Cross-section of centrifuge model geometry showing a bilinear failure surface for L/H = W/H =0.40 (Woodruff, 2003) 22
Figure 2.21: Cross-section of centrifuge model geometry showing a linear failure surface in good agreement with the theoretical Rankine failure surface with L/H = 0.70 and W/H = 1.1 (Woodruff, 2003) 23
Figure 2.22: Wall configuration considered by Leshchinsky and Hu (2003)...............................24
Figure 2.23: Design charts developed by Leshchinsky and Hu using ReSSA for an angle of internal friction equal to 20° 25

Figure 2.24: Design charts developed by Leshchinsky and Hu using ReSSA for an angle of internal friction equal to 30° 25
Figure 2.25: Design charts developed by Leshchinsky and Hu using ReSSA for an angle of internal friction equal to 40° 26
Figure 2.26: (a) Forces acting on wall face and potential failure surfaces analyzed by Lawson and Yee (b) Horizontal earth pressure coefficients for backfill with internal friction angle (ϕ') equal to 30° (Lawson, 2005) 27
Figure 2.27: Maximum horizontal force coefficients for ϕ' = 25°, 30°, 35° and 40° (Lawson, 2005) 27
Figure 3.1: Example geometry showing finite element model of the physical space for a nondeformable retaining wall (Plaxis, 2005) 31
Figure 3.2: Example of nodes and stress points for 15-node triangular elements (Plaxis, 2005) ..32
Figure 3.3: Typical mesh generated using the default (course) setting in Plaxis for wall aspect ratios equal to (a) 0.70, and (b) 0.30 (Plaxis, 2005) 32
Figure 3.4: Locations of nodes and stress points in a 5-node interface element (Plaxis, 2005) 33
Figure 3.5: Locations of nodes and stress points when a 15-node triangular element is connected to a 5-node interface element (Plaxis, 2005) 33
Figure 3.6: Stress-strain relationship for the Linear-Elastic model (Plaxis, 2005) 34
Figure 3.7: Stress-strain relationship for the Mohr-Coulomb model (Plaxis, 2005) 35
Figure 3.8: Stress-strain relationship for the Hardening-Soil model (Plaxis, 2005) 37
Figure 3.9: Column of soil after first stage of "construction" (Plaxis, 2005) 40
Figure 3.10: Displacement at the top surface of a column of soil (D_{top}) (Plaxis, 2005) 43
Figure 3.11: Displacement at the top of layer i (D_{si}) (Plaxis, 2005) 44
Figure 3.12: Illustration of the case when the soil is at the mid-height of the column of soil (Plaxis, 2005) 45
Figure 4.1: Distribution of nodes and stress points in a 5-node plate element 47
Figure 4.2: Connection of plate element to interface element (Plaxis, 2005) 48
Figure 4.3: Example of model having no plate, no interface, and the total fixity boundary condition assigned to the nodes at the wall face (case 1) (Plaxis, 2005) 50
Figure 4.4: Example of model having no plate, no interface, and the total fixity boundary condition assigned to the nodes at the wall face (case 2) (Plaxis, 2005) 50
Figure 4.5: Example of model having no plate, an interface, and the horizontal fixity boundary condition assigned to the nodes at the wall face (case 3) (Plaxis, 2005) 51
Figure 4.6: Example of model having no plate, an interface, and the total fixity boundary condition assigned to the nodes at the wall face (case 4) (Plaxis, 2005) 51
Figure 4.7: Example of model having a plate, no interface, and the horizontal fixity boundary condition assigned to the nodes at the wall face (case 5) (Plaxis, 2005) 52
Figure 4.8: Example of model having a plate, no interface, and the total fixity boundary condition assigned to the nodes at the wall face (case 6) (Plaxis, 2005) 52
Figure 4.9: Example of model having a plate, an interface, and the horizontal fixity boundary condition assigned to the nodes at the wall face (case 7) (Plaxis, 2005) 53
Figure 4.10: Example of model having a plate, an interface, and the total fixity boundary condition assigned to the nodes at the wall face (case 8) (Plaxis, 2005) 53
Figure 4.11: Vertical displacements at point A for the linear elastic model 59
Figure 4.12: Vertical displacements at point A for the Mohr-Coulomb model 60

Figure 4.13: Deformed mesh showing movement of the soil through the boundary of the wall (Plaxis, 2005) 62
Figure 4.14: Adopted model for future finite element simulations having interface elements and the total fixity boundary condition assigned to the face of the wall (Plaxis, 2005)....................63
Figure 5.1: Schematic of cross-section of the model wall used in centrifuge tests conducted by Frydman and Keissar. 66
Figure 5.2: Schematic illustration of aluminum box and pressure cell arrangement in wall face used in centrifuge tests by Take and Valsangkar, 2001 (Take, 2001) 67
Figure 5.3: Finite element model adopted for finite element simulations of centrifuge tests having interface elements and the total fixity boundary condition assigned to the face of the wall (Plaxis, 2005) 68
Figure 5.4: Variation in horizontal earth pressure coefficients versus the nondimensional depth (z/H) measured from a centrifuge test for a wall aspect ratio equal to 1.10 performed by Frydman and Keissar, calculated by Plaxis from simulations of the centrifuge test performed by Frydman and Keissar, and computed using Spangler and Handy's equation. 70
Figure 5.5: Variation in horizontal earth pressure coefficients versus the nondimensional depth (z/H) measured from a centrifuge test for a wall aspect ratio equal to 0.30 performed by Frydman and Keissar, calculated by Plaxis from simulations of the centrifuge test performed by Frydman and Keissar, and computed using Spangler and Handy's equation. 71
Figure 5.6: Variation in horizontal earth pressure coefficients versus the nondimensional depth (z/H) measured from a centrifuge test for a wall aspect ratio equal to 0.10 performed by Frydman and Keissar, calculated by Plaxis from simulations of the centrifuge test performed by Frydman and Keissar, and computed using Spangler and Handy's equation. 72
Figure 5.7: Variation in horizontal earth pressure coefficients with the non-dimensional depth (z/H) measured from a test performed by Take and Valsangkar and calculated by Plaxis from simulations of the centrifuge test performed by Take and Valsangkar with a wall aspect ratio equal to 0.54 73
Figure 5.8: Variation in horizontal earth pressure coefficients with the non-dimensional depth (z/H) measured from a test performed by Take and Valsangkar and calculated by Plaxis from simulations of the centrifuge test performed by Take and Valsangkar with a wall aspect ratio equal to 0.11 74
Figure 5.9: Variation in horizontal earth pressure coefficients with the non-dimensional depth (z/H) calculated by Plaxis from simulations of the centrifuge tests performed by Take and Valsangkar with wall aspect ratios equal to 0.54 and 0.11. 75
Figure 5.10: Variation in horizontal earth pressure coefficients with the non-dimensional depth (z/H) computed using Spangler and Handy's equation and calculated by Plaxis from simulations of the centrifuge test performed by Take and Valsangkar with a wall aspect ratio equal to 0.54 .76
Figure 5.11: Variation in horizontal earth pressure coefficients with the non-dimensional depth (z/H) computed using Spangler and Handy's equation and calculated by Plaxis from simulations of the centrifuge test performed by Take and Valsangkar with a wall aspect ratio equal to 0.11 .77
Figure 6.1: Horizontal earth pressure coefficient distributions for unit weights equal to 14 kN/m^3 (89.1 pcf) and 20 kN/m^3 (127 pcf) 81
Figure 6.2: Horizontal earth pressure coefficient distributions for Young's Modulus equal to 10,000 kPa (≈209,000 psf) and 50,000 kPa (≈1,044,000 psf) 82
Figure 6.3: Horizontal earth pressure coefficient distributions for sets 1,2, and 3 of the three moduli 85

Figure 7.1: Plots of the vertical stress influence factor along a horizontal plane at two depths below the top of the wall for a wall aspect ratio equal to 1.00 94
Figure 7.2: Plots of the vertical stress influence factor along a horizontal plane at two depths below the top of the wall for a wall aspect ratio equal to 0.70. 95
Figure 7.3: Plots of the vertical stress influence factor along a horizontal plane at two depths below the top of the wall for a wall aspect ratio equal to 0.50 96
Figure 7.4: Plots of the vertical stress influence factor along a horizontal plane at two depths below the top of the wall for a wall aspect ratio equal to 0.30 97
Figure 7.5: Plots of the vertical stress influence factor along a horizontal plane at two depths below the top of the wall for a wall aspect ratio equal to 0.10 98
Figure 7.6: Locations of vertical planes in the center of the backfill and adjacent to the wall face for a wall aspect ratio equal to 1.00 (Plaxis, 2005)...99
Figure 7.7: Normalized vertical stress influence factor in the center of the backfill and adjacent to the wall face for a wall aspect ratio equal to 1.00..100
Figure 7.8: "Best fit" line for the vertical stress influence factors for a wall aspect ratio equal to 1.00...101
Figure 7.9: "Best fit" line for the vertical stress influence factors for a wall aspect ratio equal to 0.70...101
Figure 7.10: "Best fit" line for the vertical stress influence factors for a wall aspect ratio equal to 0.50...102
Figure 7.11: "Best fit" line for the vertical stress influence factors for a wall aspect ratio equal to 0.30...102
Figure 7.12: "Best fit" line for the vertical stress influence factors for a wall aspect ratio equal to 0.10...103
Figure 7.13: Values of the vertical stress influence factors at the top and bottom of the wall plotted as a function of the wall aspect ratio...104
Figure 7.14: Values of β_v determined from sensitivity study 105
Figure 7.15: Variation in the horizontal earth pressure coefficients expressed by k_{ob} and k_{sr} at the center of the backfill with the nondimensional depth (z/H). 106
Figure 7.16: Variation in the horizontal earth pressure coefficients expressed by k_{ob} and k_{sr} adjacent to the wall face with the nondimensional depth (z/H)...106
Figure 7.17: Distribution of horizontal earth pressure coefficients adjacent to the wall face and in the center of the backfill for a wall aspect ratio equal to 0.70 108
Figure 7.18: Variation in the normalized horizontal earth pressure coefficients at the wall face (k_w/K_a) with the nondimensional depth (z/H) for wall aspect ratios equal to 0.70, 0.50, 0.30, and 0.10...109
Figure 7.19: Variation in the normalized horizontal earth pressure coefficients at the center of the backfill (k_c/K_a) with the nondimensional depth (z/H) for wall aspect ratios equal to 0.70, 0.50, 0.30, and 0.10..109
Figure 7.20: Normalized equivalent horizontal earth pressure coefficients along the wall and in the center of the backfill versus wall aspect ratios 111
Figure 7.21: Variation of the normalized horizontal earth pressure coefficients with depth in the center of the wall versus the current FHWA MSE wall design guideline recommended values (Elias et al., 2001) 112
Figure 7.22: Design chart used to calculate the value of $T_{max,i}$ in the FHWA design guidelines (Elias et al., 2001) 113

Figure 7.23: Proposed design chart produced from Plaxis simulations of nondeformable walls placed in front of an existing stable face for wall aspect ratios equal to 0.70, 0.50, 0.30, and 0.10.114
Figure 7.24: Values of the vertical stress influence factor, β_v at the top and bottom of the wall plotted as a function of the wall aspect ratio..116
Figure 8.1: Geometry of a nondeformable MSE wall placed in front of a stable face in UTEXAS4 (Wright, 1999)..120
Figure 8.2: Schematic of assumed distribution of tensile stresses in the reinforcement 122
Figure 8.3: Distribution of tensile strength in the reinforcement for a wall with an aspect ratio equal to 0.70 (Wright, 1999)..123
Figure 8.4: Location of points at which the tensile strength of the reinforcement begins to decrease from the maximum value to zero at the free end of the reinforcement (Wright, 1999)124
Figure 8.5: Example of an inverted circle (Wright, 1999)...125
Figure 8.6: Initial noncircular slip surface defined by seven points for a wall with an aspect ratio equal to 0.70 (Wright, 1999)..126
Figure 8.7: Initial noncircular slip surface defined by three points for a wall with an aspect ratio equal to 0.70 (Wright, 1999)..127
Figure 8.8: Critical circular slip surface for a wall aspect ratio equal to 0.70 (Wright, 1999)....128
Figure 8.9: Critical circular slip surface for a wall aspect ratio equal to 0.50 (Wright, 1999)....129
Figure 8.10: Critical circular slip surface for a wall aspect ratio equal to 0.30 (Wright, 1999)..129
Figure 8.11: Critical noncircular slip surface for a wall aspect ratio equal to 0.70 (Wright, 1999)130
Figure 8.12: Critical noncircular slip surface for a wall aspect ratio equal to 0.50 (Wright, 1999)130
Figure 8.13: Critical noncircular slip surface for a wall aspect ratio equal to 0.30 (Wright, 1999)131
Figure 8.14: Critical bilinear slip surface for an aspect ratio equal to 0.70 (Wright, 1999)........132
Figure 8.15: Critical bilinear slip surface for a wall aspect ratio equal to 0.50 (Wright, 1999)..132
Figure 8.16: Critical bilinear slip surface for a wall aspect ratio equal to 0.30 (Wright, 1999)..133
Figure 8.17: Shapes for the critical noncircular slip surface, theoretical Rankine failure surface for the fully mobilized shear strength (ϕ'), and theoretical Rankine failure surface for the developed shear strength ($\phi'_{developed}$) and a wall aspect ratio of 0.70...135
Figure 8.18: Shapes for the critical noncircular slip surface, theoretical Rankine failure surface for the fully mobilized shear strength (ϕ'), and theoretical Rankine failure surface for the developed shear strength ($\phi'_{developed}$) and a wall aspect ratio of 0.50...136
Figure 8.19: Shapes for the critical noncircular slip surface, theoretical Rankine failure surface for the fully mobilized shear strength (ϕ'), and theoretical Rankine failure surface for the developed shear strength ($\phi'_{developed}$) and a wall aspect ratio of 0.30...137
Figure 8.20: Example geometry for a MSE wall using a zone of material weaker than the backfill along the interface between the stable face and backfill (Wright, 1999)...................................138
Figure 8.21: Critical slip surface from the general noncircular search for a wall aspect ratio equal to 0.70 with no interface (Wright, 1999) 139
Figure 8.22: Critical slip surface from the general noncircular search for a wall aspect ratio equal to 0.70 with a weak interface (Wright, 1999) 139
Figure 8.23: Critical slip surface from the general noncircular search for wall aspect ratio equal to 0.70 with no interface (Wright, 1999) 140
Figure 8.24: Critical slip surface from the general noncircular search for a wall aspect ratio equal to 0.70 with an interface with zero strength (Wright, 1999)..141
Figure 8.25: Location of the bottom of a tension crack for a UTEXAS simulation having wall aspect ratio equal to 0.70 (Wright, 1999) 142

Figure 8.26: Critical slip surfaces when the soil shear strength is fully developed for a wall aspect ratio equal to 0.70 144
Figure 8.27: Critical slip surfaces when the soil shear strength is fully developed for a wall aspect ratio equal to 0.50 145
Figure 8.28: Critical slip surfaces when the soil shear strength is fully developed for a wall aspect ratio equal to 0.30 145
Figure 8.29: Critical noncircular slip surfaces found for the factor of safety in the soil shear strength and the factor of safety in the reinforcement for a wall aspect ratio of 0.70 146
Figure 8.30: Critical noncircular slip surfaces found for the factor of safety in the soil shear strength and the factor of safety in the reinforcement for a wall aspect ratio of 0.50 146
Figure 8.31: Critical noncircular slip surfaces found for the factor of safety in the soil shear strength and the factor of safety in the reinforcement for a wall aspect ratio of 0.30 147
Figure 8.32: Critical noncircular slip surface for limit equilibrium analysis of centrifuge model test 149
Figure 8.33: Cross-section of centrifuge model geometry showing a bilinear failure surface for L/H = W/H =0.40 (Woodruff, 2005) 149
Figure 9.1: Example geometry showing finite element model of the physical space for an nondeformable retaining wall (Plaxis, 2005)...152
Figure 9.2: Adopted model for finite element simulations having interface elements and the total fixity boundary condition assigned to the face of the wall (Plaxis, 2005).................................153

Chapter 1. Introduction

As the population has increased, transportation demand has increased so that development of urban areas has become a priority, which has led to widening of existing highways to improve traffic flow. Widening has often resulted in new mechanically stabilized earth (MSE) walls being placed in front of existing stable walls. Figure 1-1 is an illustration of a new MSE wall placed in front of a stable face. The design of an MSE wall such as the one shown in Figure 1-1 is unique because the limited right-of-way forces the length of the reinforcing strips to be less than current design guidelines (Elias et al., 2001) suggest. In other words, the new MSE wall must be narrow in comparison to typical MSE walls. As MSE wall becomes narrower, the stiffness of the wall increases and in the limiting case, the wall experiences very little deformation.

In anticipation of the need for constructing narrower than normal retaining walls in confined spaces, the Texas Department of Transportation (TxDOT) sponsored the investigation of the design of narrow retaining walls in front of stable faces, which is discussed in this report. The construction of narrow retaining walls is not addressed in the current Federal Highway Administration (FHWA) guidelines (Elias et al., 2001). The existing state-of-practice suggests a minimum wall width and MSE reinforcement length equal to 70 percent of the wall height. Presently, very little field data exist on the topic; however several centrifuge model laboratory tests and numerical analyses have been performed. These studies suggest the mechanics of narrow retaining walls are different from traditional walls, and earth pressures are different from conventional earth pressures due to the wall geometry.

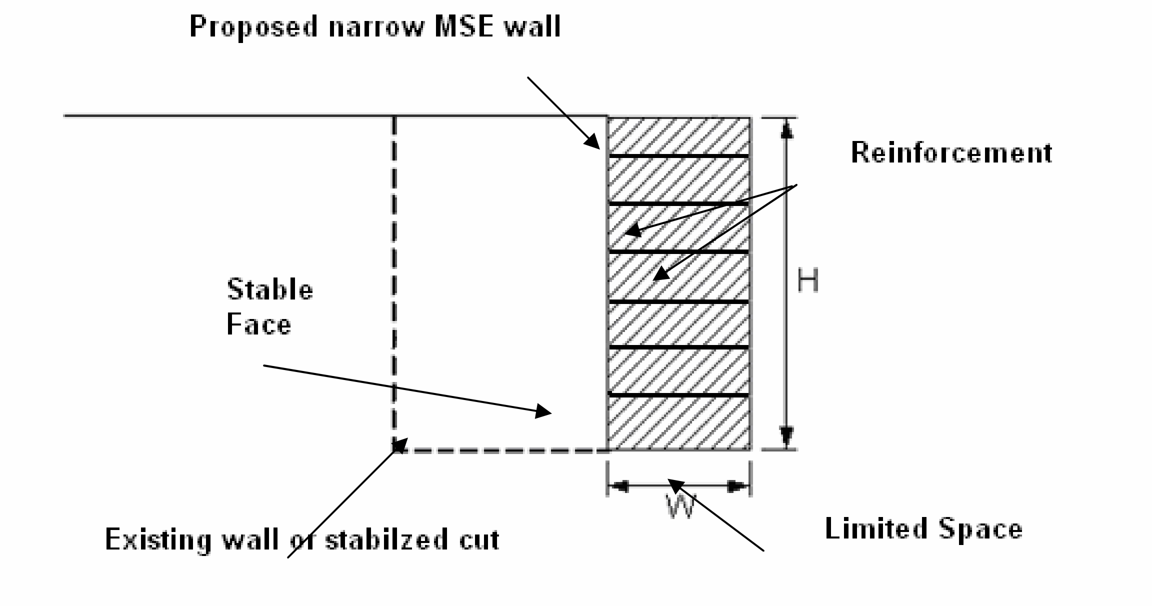

Figure 1.1: Illustration of proposed narrow MSE wall in front of an existing stable face

In the following chapters, the design of MSE walls in front of a stable face is investigated using the finite element method in the computer software known as Plaxis. In Chapter 2, a review of the literature is presented. The studies available in the literature include a field case study, full-scale field testing, laboratory testing, and numerical analyses. Modeling a nondeformable MSE wall using the Plaxis software (Plaxis, 2005) is addressed in Chapter 3. In Chapter 4, studies are performed to gain understanding about soil-wall interaction using Plaxis. Chapter 5 presents the verification of the software for this study based on experimental measurements and an arching theory. An investigation of the sensitivity of horizontal earth pressure coefficients calculated by the Plaxis software for two soil constitutive models and parameters is presented in Chapter 6. The effects of wall aspect ratio on horizontal and vertical stresses and their application to current design guidelines for internal stability of MSE walls are discussed in Chapter 7. In Chapter 8, limit equilibrium analyses are performed using the slope stability program, UTEXAS4 (Wright, 1999). The purpose of the limit equilibrium analyses was to evaluate global stability for varying wall geometries. Finally, Chapter 9 presents the summary and conclusions of the work discussed in the previous chapters, as well as recommendations for finite element modeling of MSE walls, design of MSE walls, and future research.

Chapter 2. Literature Review

A literature review was conducted to review information related to MSE walls placed in a confined space, i.e., MSE walls having a wall aspect ratio (width-to-height ratio) less than 0.70 and placed in front of an existing stable face. The literature review yielded information from a case study, a full-scale field test, laboratory tests, and numerical analyses. A field case study was found that illustrated the practical application of a MSE wall placed in front of a stable face. A full-scale field testing program designed to study the stresses, strains, and displacements in MSE walls placed in a confined space was also reviewed. Laboratory tests provided additional information. Most of the laboratory experimental results have focused on horizontal earth pressures against nondeformable walls and provide insight into the effect of wall aspect ratio on horizontal earth pressure coefficients. One centrifuge model test examined displacements and locations of the failure surfaces for model MSE walls placed in a confined space. Studies employing limit equilibrium analyses were also reviewed. Limit equilibrium analyses have been used to calculate earth pressure coefficients and produce design charts to calculate the horizontal earth pressures, particularly for wall aspect ratios less than 70 percent.

2.1 Terminology

Although the literature discussed in this chapter has focused on horizontal earth pressure coefficients, authors have used different terminology to describe the geometry of retaining walls and to define horizontal earth pressure coefficients. To avoid confusion, a unified set of notation has been adopted and is described below.

2.1.1 Geometry

For the purposes of this study, the wall aspect ratio for walls with reinforcement is described as the ratio of the length of the reinforcement (L) to the height of the wall (H). In contrast, the wall aspect ratio for walls without reinforcement is described as the ratio of the width of the wall (W) to the height of the wall (H). Examples of these two conditions are shown in Figures 2-1 and 2-2.

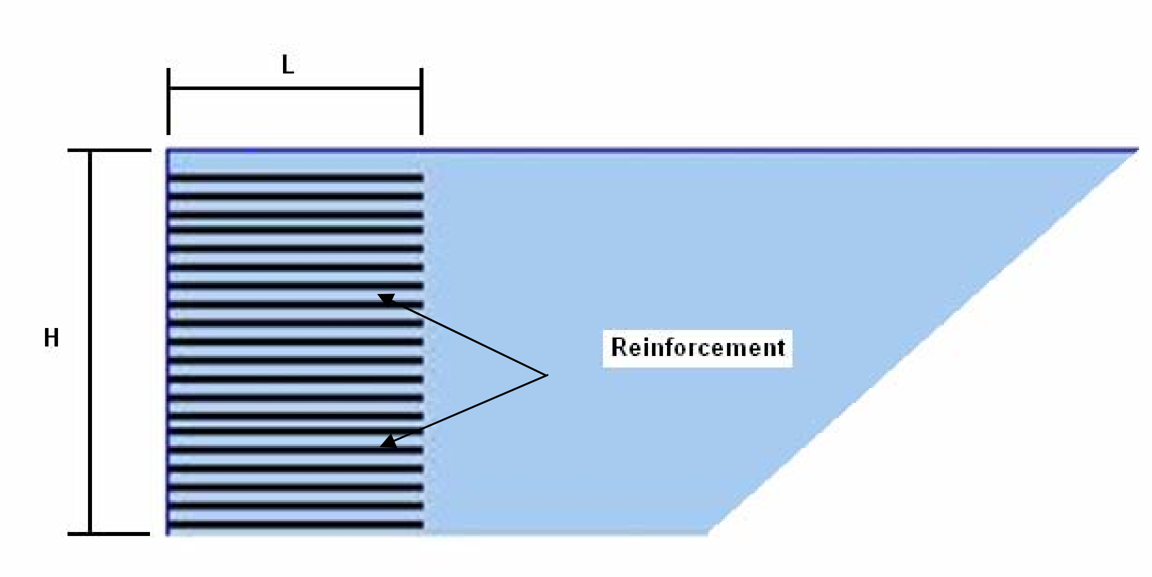

Figure 2.1: Example of wall aspect ratio defined as L/H

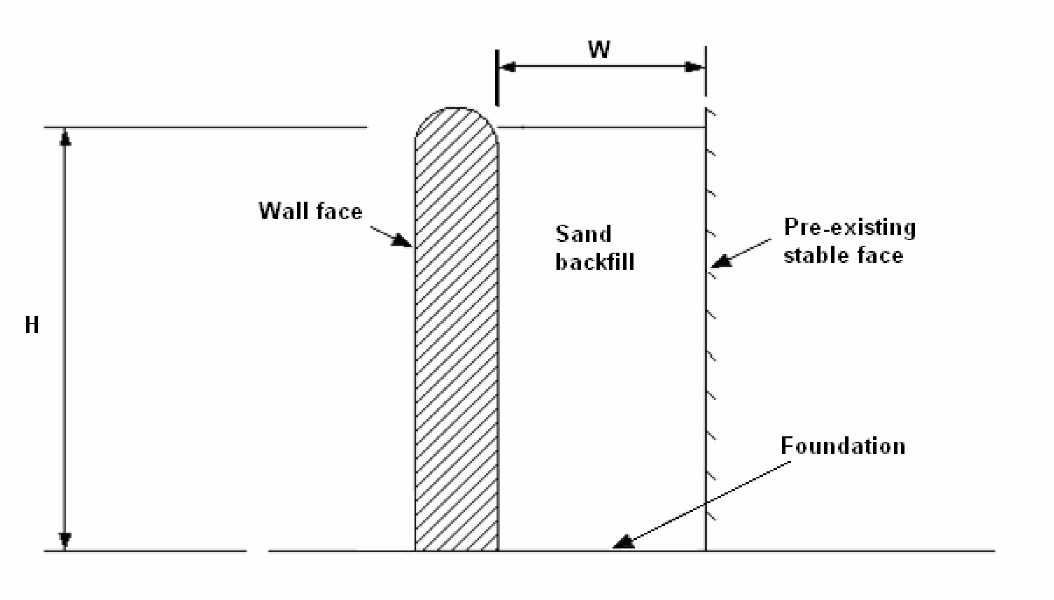

Figure 2.2: Example of wall aspect ratio defined as W/H

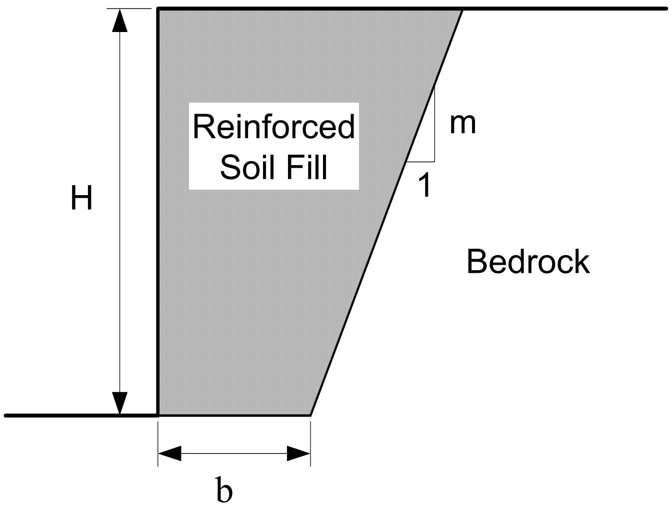

Figure 2.3: Example of wall aspect ratio defined as b/H for a wall placed in front of an existing sloped stable face

In some cases, the existing stable face for walls studied was not vertical as shown in Figure 2-2, but was sloped as illustrated in Figure 2-3. In these cases, the wall aspect ratio was described as the ratio of the width of the base of the wall (b), to the height of the wall (H). Various variables pertaining to the geometry of the wall are as follows:

- b = width of the base of the wall.
- H = height of the wall
- L = length of the reinforcement
- m = slope of the existing stable slope if it is not vertical
- W = width of the wall. "W" is used when the existing stable slope is vertical
- Z = depth below the top surface of the retaining wall

2.1.2 Earth Pressures

The way in which horizontal (lateral) earth pressure coefficients have been expressed in the literature has varied greatly among different publications. The letter "K" or "k" will be used to describe horizontal earth pressure coefficients in this report. The capitalized letter "K" is used to indicate the value of horizontal earth pressure coefficients when the coefficients are independent of the depth below the top of the wall. For example, "K" is used when the horizontal earth pressure coefficient was calculated using the total force acting on the side wall, such as the wall facing as shown in Figure 2-4. In this case, "K" is defined as follows:

$$K = \frac{F}{\frac{1}{2}\gamma H^2} \qquad \text{Eq. 2-1}$$

where F is the total force acting on the side wall, γ is the unit weight of the backfill, and H is the height of the wall. The capitalized letter "K" is also used to represent the theoretical active and at-rest theoretical horizontal earth pressure coefficients designated as K_a and K_0, respectively. For the purposes of this report, the active and at-rest earth pressure coefficients are defined by the angle of internal friction (ϕ') of the soil and expressed by Equations 2-2 and 2-3.

$$K_a = \tan^2\left(45 - \frac{\phi'}{2}\right) \qquad \text{Eq. 2-2}$$

$$K_0 = 1 - \sin(\phi') \qquad \text{Eq. 2-3}$$

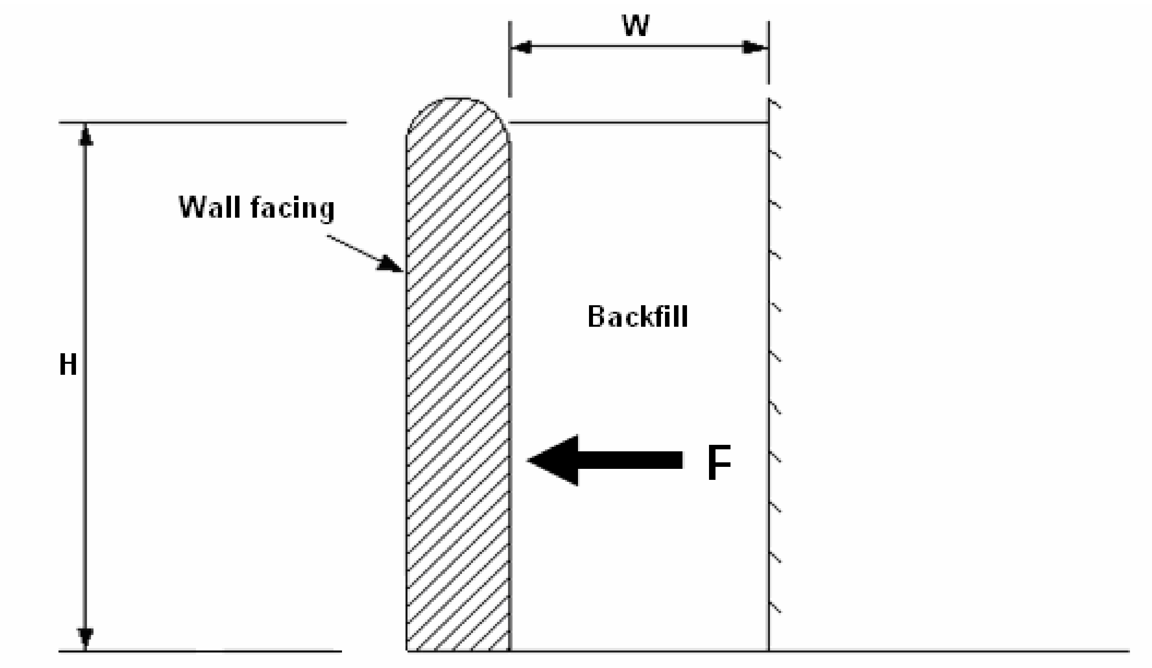

Figure 2.4: Schematic showing location of total force (F) acting on the wall facing of a retaining wall.

In this report the lowercase letter "k" is used to indicate the value of the horizontal earth pressure coefficient when the value varies with depth. For example, the value of the horizontal earth pressure coefficient calculated from the results output by Plaxis for a given depth is represented by k. The backfill material used in the studies reported in the literature and in the finite element simulations is assumed to be dry, free-draining. Therefore, the horizontal earth pressure coefficients reported represent both total and effective stresses. The values of k determined from measurements of stress and stresses calculated by numerical analyses or closed form solutions are computed using one of the following equations,

$$k = \frac{\sigma_h}{\gamma z} \qquad \text{Eq. 2-4}$$

where σ_h is the value of the horizontal stress and z is the depth below the top surface of the wall, or

$$k = \frac{\sigma_h}{\sigma_v} \qquad \text{Eq. 2-5}$$

where σ_v is the value of the vertical stress. For clarity, a distinction between Equations 2-4 and 2-5 will be made prior to presenting either of these coefficients.

2.2 Field Case Study: Turner and Jensen, 2005

Turner and Jensen documented the expansion of a section of a 50-year old highway in Snake River Canyon, Wyoming. The existing slope was stabilized using two soil nail walls, and a new part of the roadway was supported by a MSE wall placed in front of the existing upper soil nail wall (Figure 2-5). The 12,000 square foot MSE wall was 25 feet high and involved select backfill reinforced with galvanized metal strips and modular block facing. In this case, the MSE wall had a wall aspect ratio approximately equal to 1.00, so the example does not fit the criteria of a wall placed in a confined space. However, the case study by Turner and Jensen provides an example of a MSE wall placed in front of an existing stable face.

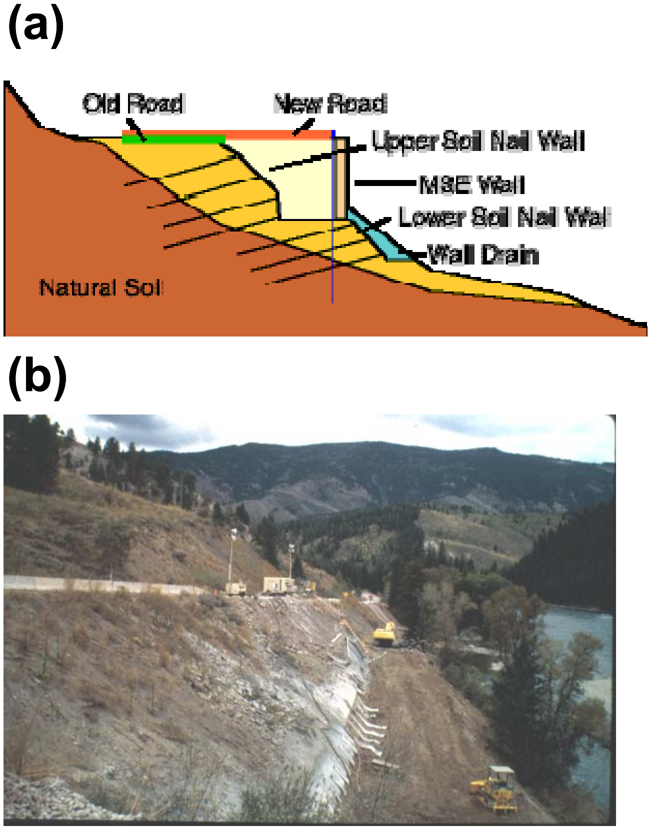

Figure 2.5: Snake River Canyon MSE wall, Wyoming: (a) Cross-section, (b) Construction of soil nail stabilized slope (stable face) behind new MSE retaining wall (Turner, 2005)

2.3 Full-Scale Field Testing: Shored Mechanically Stabilized Earth (SMSE) Wall Systems Design Guidelines, 2006 (Morrison et al., 2006)

The need for consistent design procedures for the widening of existing roads or construction of new roadways in rugged terrain inspired the FHWA to conduct full-scale field tests as part of a larger effort to develop design guidelines for the Federal Lands Highway. The goal of the field testing program was to measure stresses, strains, and displacements in a MSE wall with a wall aspect ratio less than 70 and placed in front of a steep stabilized backslope or “shored wall.”

To replicate this case, a steep wall was constructed in a test pit by placing reinforced concrete beams fixed laterally across the back of the test pit. The “shored wall” acts as an existing stable face. In front of the existing “shored wall,” two MSE walls were built using uniaxial structural geogrid reinforcement from Tensar. Figures 2-6 and 2-7 show cross-sections of the two walls. The reinforcement extended for the full width of the wall. The width of the wall was equal to 25 percent of the height of the wall (W/H = 0.25) at the bottom of the wall and 39 percent of the height of the wall (W/H = 0.39) at the top of the wall. In one wall (Figure 2-6), the reinforcement terminated at the “shored” wall. The reinforcement in this wall was termed “unconnected” because it was not connected to the existing stable face. In the other wall (Figure 2-7), the reinforcement was extended a minimum of 1 meter (3.28 feet) behind the existing stable face and embedded in the existing shored wall. The reinforcement in this wall was termed “connected.” The purpose of building two walls was to determine if there was any benefit to connecting the reinforcement to the existing stable face.

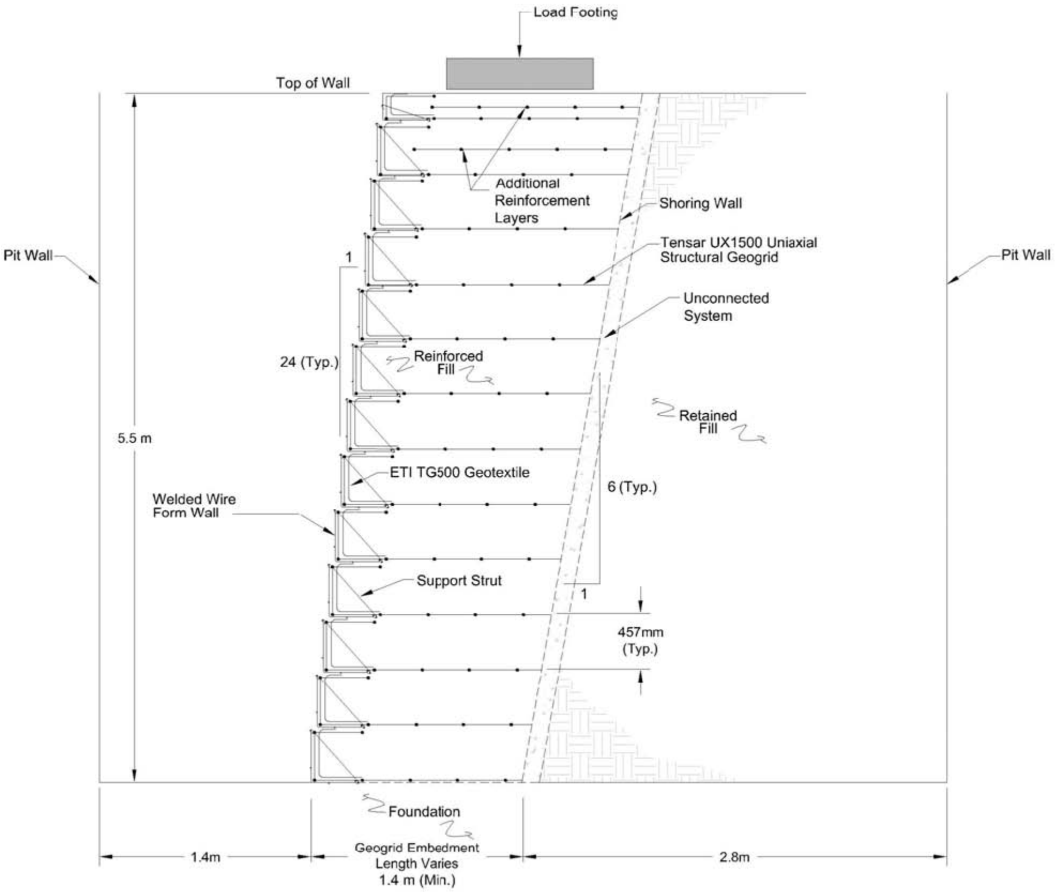

Figure 2.6: Typical cross-section of full-scale field test with reinforcement unconnected to the existing shored wall (Morrison et al., 2006)

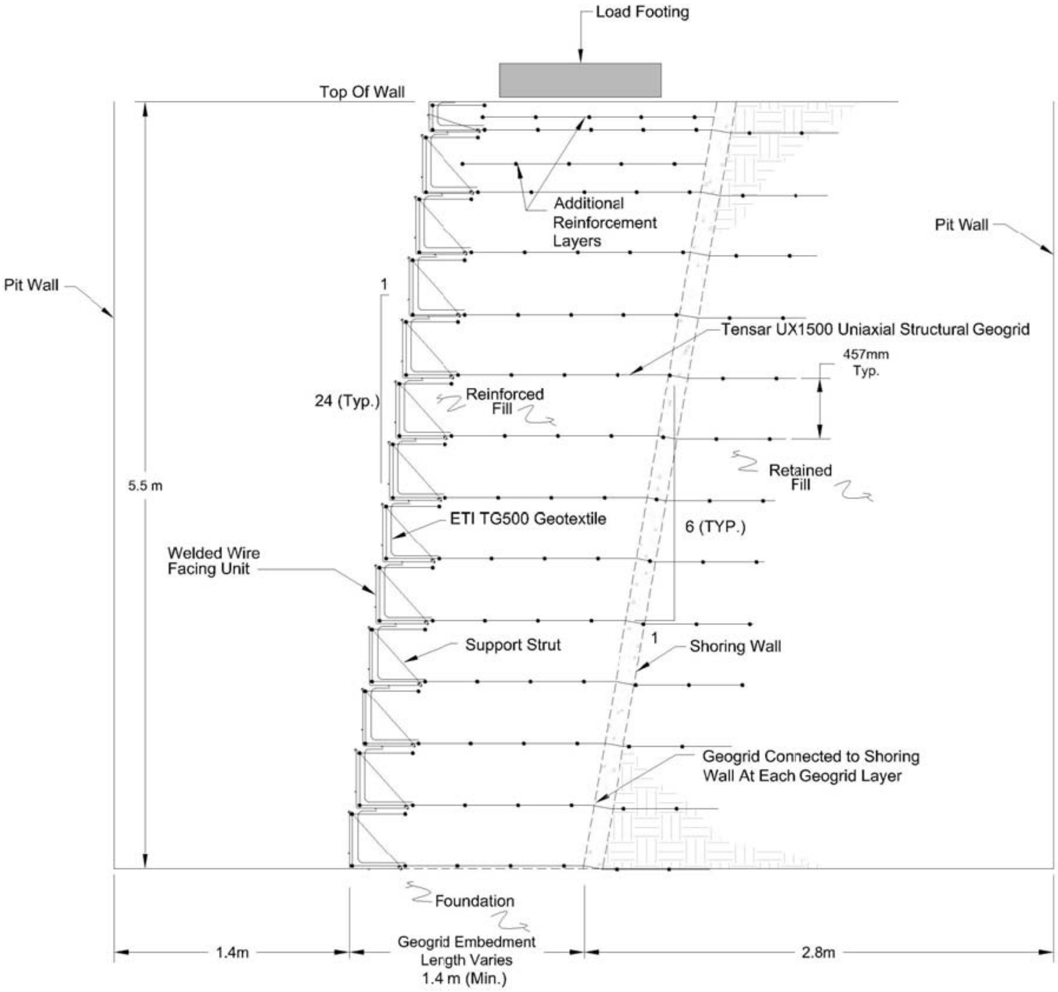

Figure 2.7: Typical cross-section of full-scale field test with reinforcement connected to the existing shored wall (Morrison et al., 2006)

A rectangular footing measuring 2.5 m (8.2 feet) long and 1.0 m (3.28 feet) wide was placed at the top of each wall for the purpose of loading the wall. The wall was loaded incrementally to a maximum surcharge of 356 kPa. Strain gauges, pressure cells, and inclinometers were installed to measure loads and deformations. The strain gauges were placed on four layers of geogrid reinforcement. The layers are identified as lifts 2, 5, 8, and 11 in Figure 2-8. The average measured strain in the geogrid reinforcement was less than 1 percent which is well within the serviceability limits of the reinforcement (Figure 2-9). The results suggest the reinforcement was not approaching a state of failure even when a very high surcharge was applied. Also, the average strain was approximately equal for both walls, which implies there was no benefit to connecting the reinforcement to the existing shored wall.

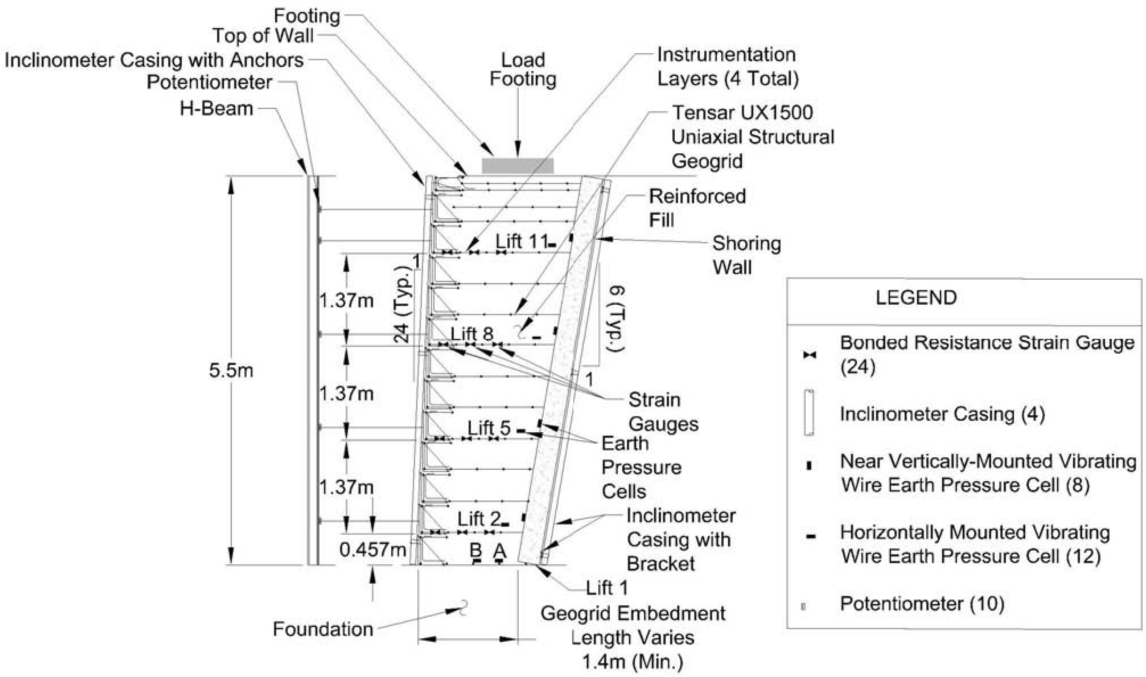

Figure 2.8: Schematic of the instrumented wall cross-section (Morrison et al., 2006)

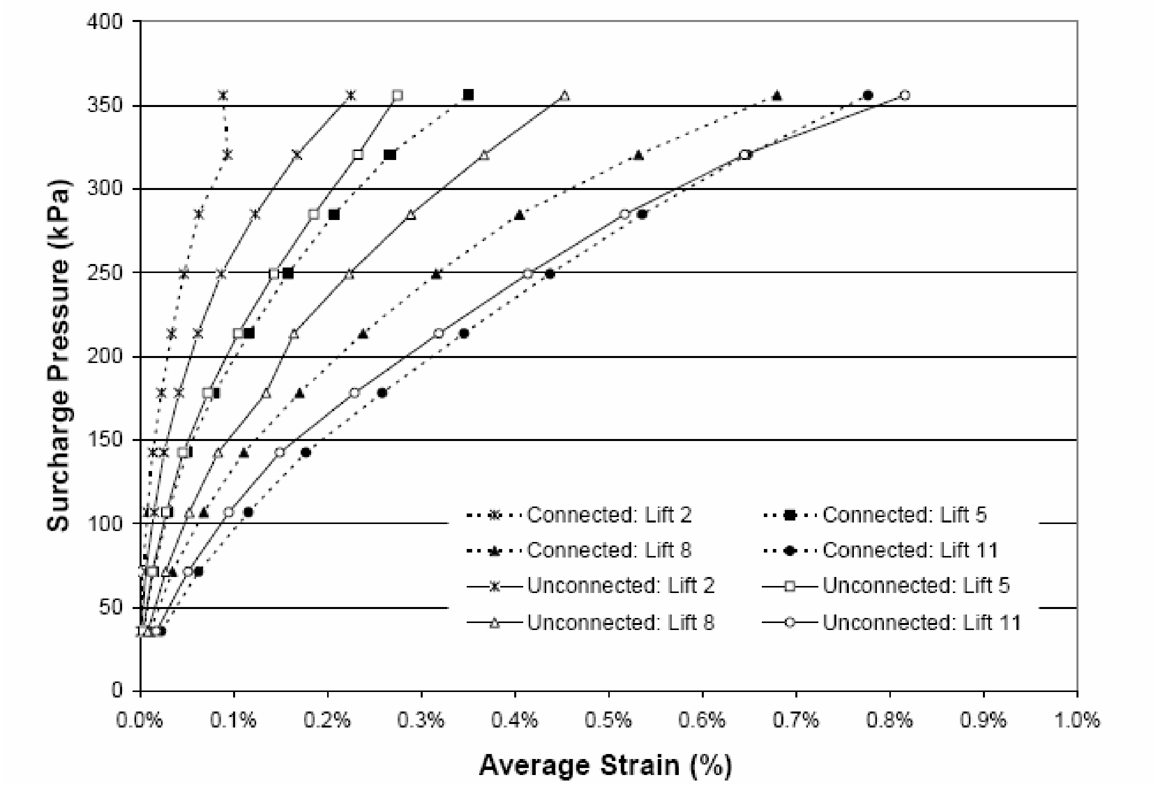

Figure 2.9: Average measured strain versus applied surcharge pressure (Morrison et al., 2006)

Earth pressure cells were mounted on the “shored wall” to measure horizontal and vertical earth pressures on the stable face at heights (h) above the bottom of the wall approximately equal to 0.5, 1.8, 3.2, and 4.6 m (15.1 feet). The “shored wall” was slightly inclined so the measured earth pressures had both horizontal and vertical components. Earth pressure cells were also placed in the backfill adjacent to the stable face to measure the vertical stresses, as shown in Figure 2-8. Also, at the bottom of the wall, two earth pressure cells were installed. One cell was located adjacent to the existing stable face and the other cell was located halfway between the existing stable face and the MSE wall facing. The values of calculated horizontal earth pressure coefficients (k), based on measurements from the horizontal earth pressure cells over the height of the wall for both walls, are shown in Figure 2-10. The horizontal earth pressure coefficient (k) was found by dividing the measured horizontal earth pressure (σ_h) by the measured vertical earth pressure (σ_v) as expressed by Equation 2-5. The backfill used in the full-scale field tests had an angle of internal friction (ϕ’) of approximately 40° and the corresponding theoretical active earth pressure coefficient (K_a) was 0.22. The values of the horizontal earth pressure coefficients calculated from measurements taken near the top of the wall, 4.6 m (15.1 feet) above the bottom of the wall, were higher than at the other elevations where earth pressures were measured, primarily because the pressure cells located near the top of the wall were greatly influenced by the loads applied through the footing. As the depth below the top surface of the wall increased, the applied load was supported in part by the “shored wall” and wall facing, thus the applied load had less effect on the measured earth pressures as the depth below the top surface of the wall increased. The calculated earth pressure coefficients were also less than the theoretical active earth pressure coefficient for horizontal earth pressures measured at wall heights of approximately 3.2 m, 1.8 m, and 0.5 m (32., 1.8 and 0.5 feet) in Figure 2-10. For the wall with unconnected reinforcement, the data for a height of approximately 1.8 m (5.9 feet) is incorrect because one of the pressure cells failed during loading of the wall.

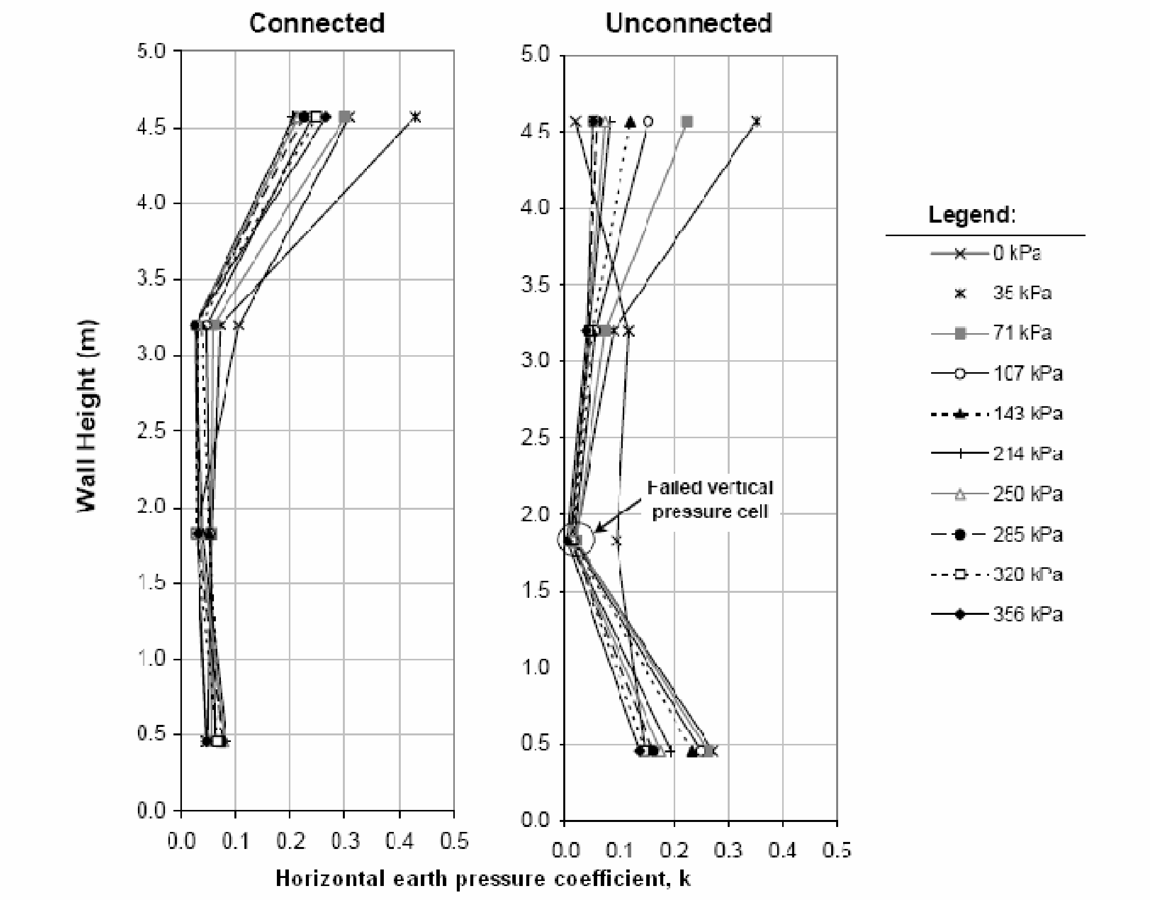

Figure 2.10: Calculated horizontal earth pressure coefficients from earth pressure cell measurements (Morrison et al., 2006)

Measured vertical pressures are plotted for both walls in Figure 2-11. The authors calculated the vertical overburden pressure using a crude approximation commonly referred to as the "2:1 method" for surcharge values equal to 0, 35, and 356 kPa. The calculations for approximating the vertical overburden pressure using the "2:1 method" are described in most soil mechanics text books, such as Holtz and Kovacs (1981). The measured vertical pressures and the approximate vertical overburden pressures for zero surcharges are in good agreement. However, the measured vertical earth pressures are greater than the calculated vertical overburden pressures for surcharges of 35 and 356 kPa.

The measured vertical pressures at the base of the wall were approximately 20 percent less at the earth pressure cell located near the stable face than at the earth pressure cell located halfway between the existing stable face and MSE wall facing. The difference in vertical earth pressure suggests the "shored" wall is supporting some of the vertical stress.

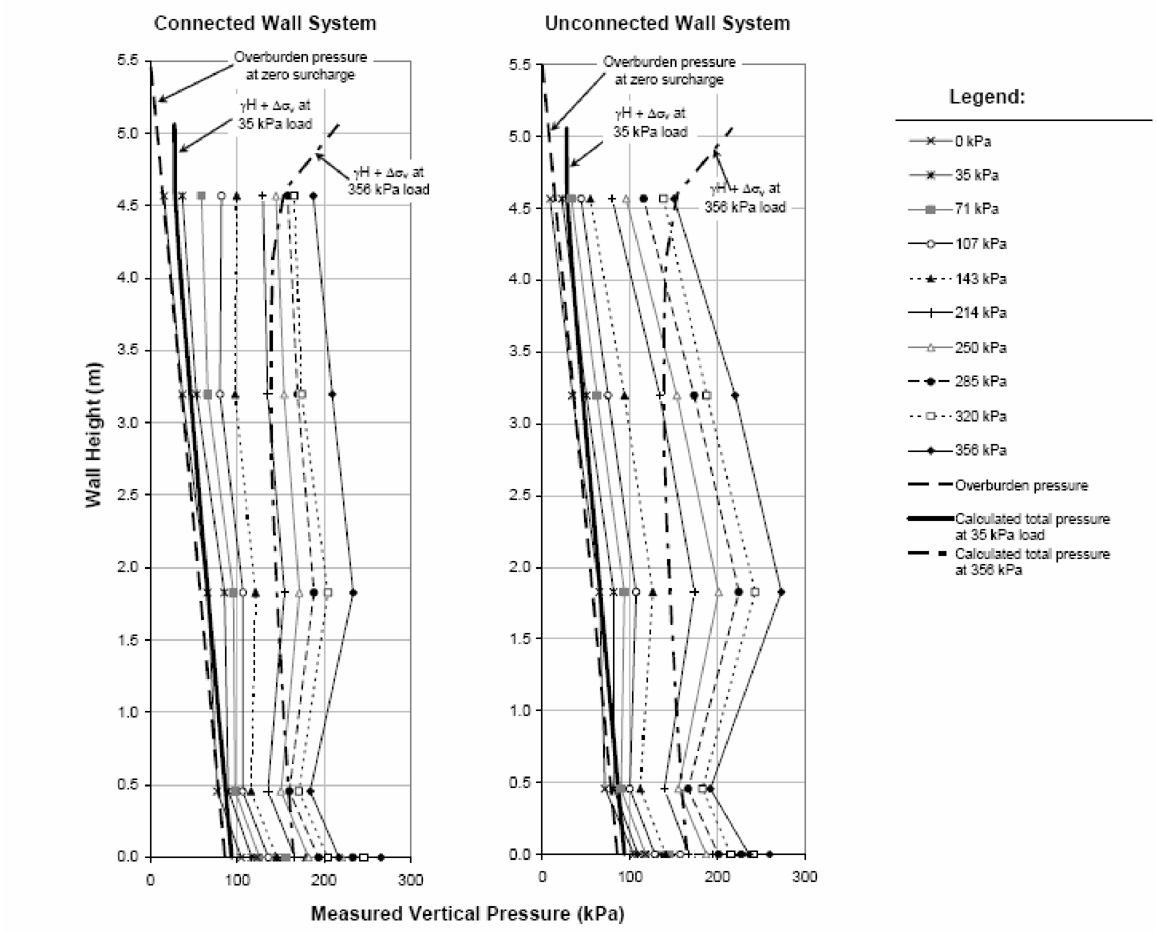

Figure 2.11: Measured vertical pressures for both walls (Morrison et al., 2006)

Four inclinometers were installed for the test walls. In each MSE wall, one inclinometer was installed adjacent to the face of the wall to measure the horizontal deflection of the wall face, and one inclinometer was installed adjacent to the existing stable face to measure the horizontal deflection of the "shored wall." The displacements were measured assuming the top of the inclinometer casing at the top of the MSE wall was a fixed point, i.e., displacements were measured relative to the top of the wall. The "shored" wall exhibited negligible deflection. The cumulative displacements measured from the inclinometers for the MSE wall facing are shown in Figure 2-12. The maximum horizontal cumulative displacement was approximately 8 mm (0.31 feet) in both walls. There was little difference in the inclinometer readings for the connected and unconnected reinforcement designs.

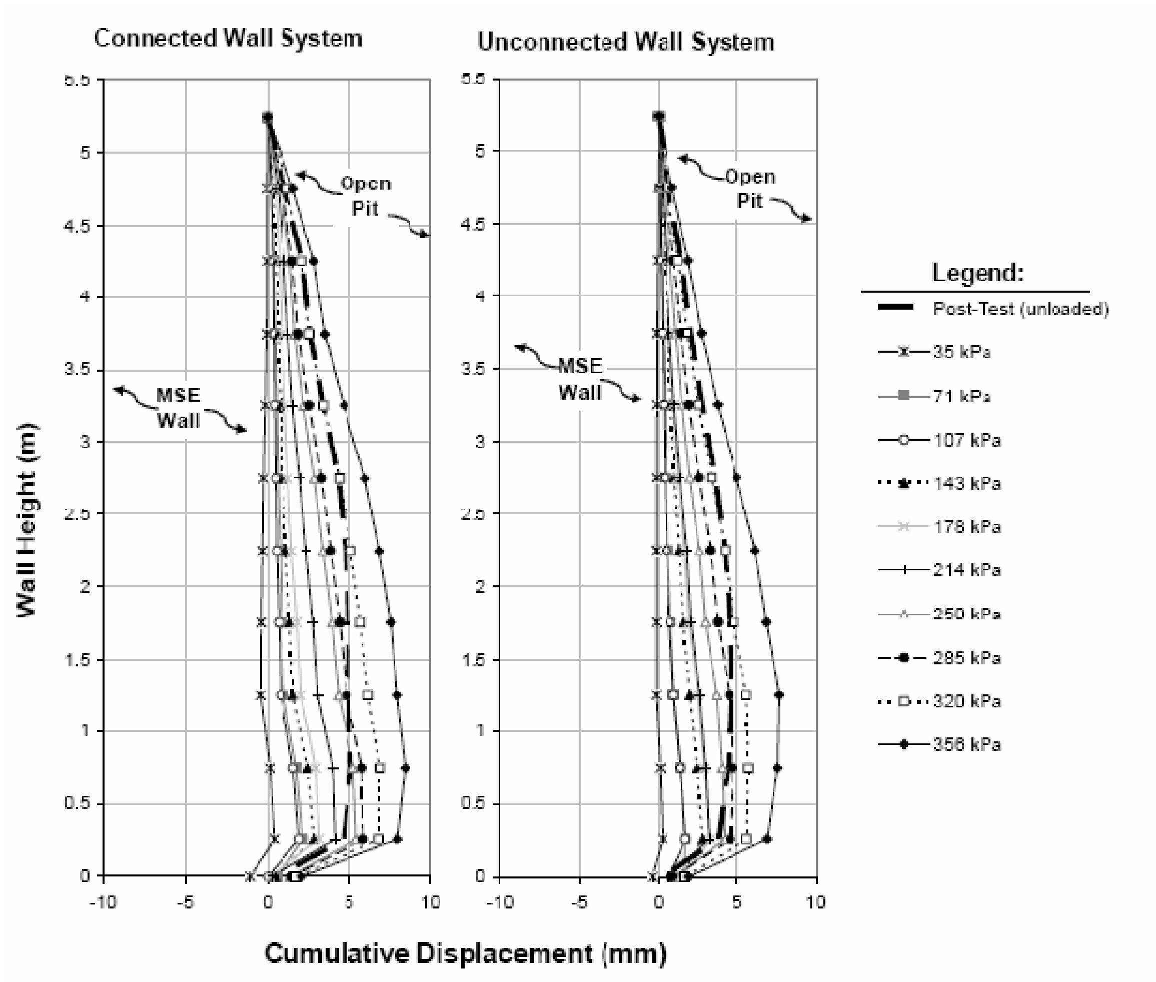

Figure 2.12: Measured cumulative displacements of the MSE wall face (Morrison et al., 2006)

2.4 Laboratory Testing

Several series of laboratory tests were described in the literature and are described below. Centrifuge model tests in particular were helpful in understanding how earth pressures are affected by the aspect ratio of the wall.

2.4.1 H.A. Janssen, 1895 (translated by Sperl, 2006)

Janssen (Sperl, 2006) was one of the first engineers to describe the behavior of granular material in a confined space. He was interested in the pressures exerted on a silo by granular materials such as grain or corn. Janssen built a model silo and measured the weight of the corn at the bottom of the silo. The results showed that the weight at the bottom of the silo was less than the weight of the corn in the silo. Janssen hypothesized that the weight of the corn was transmitted to the side walls and he developed an equation to predict the horizontal pressure on the sidewall. Because his experiments were performed with granular materials, his findings were also applicable to granular soils such as sand and gravel. Janssen's hypothesis that the weight of granular materials is transmitted to the side walls of a container became widely accepted and is often referred to as "Janssen's arching theory" or simply "arching theory" today. Although his original equation has been modified over the years, Janssen is still given credit for discovering the reduction of horizontal and vertical earth pressures caused by the interaction between a granular material and a wall.

2.4.2 Spangler and Handy, 1984

Horizontal earth pressures in soil resulting from arching effects are addressed by Spangler and Handy (1982). They suggest the horizontal earth pressure (σ_h) is given by the following equation based in part on Janssen's original arching theory.

$$\sigma_h = \frac{\gamma\,\mathrm{W}}{2\tan(\delta)} * \left[1 - \exp\left(-2\mathrm{K}\left(\frac{\mathrm{z}}{\mathrm{W}}\right)\tan(\delta)\right)\right] \qquad \text{Eq. 2-6}$$

where W is the width of the constrained space, z is the depth of the point of interest below the top of the wall, δ is the interface friction angle between the soil and wall, K is the horizontal earth pressure coefficient, and γ is the unit weight of the backfill. The value of the horizontal earth pressure coefficient, K, was not specified by Spangler and Handy, however, in subsequent analyses it was assumed that K was equal to the theoretical at-rest earth pressure coefficient (K_0) as defined using Jaky's empirical formula ($K_0 = 1\text{-}\sin(\phi')$).

Spangler and Handy developed Equation 2-6 by first assuming the weight of granular backfill placed between a retaining wall and existing stable face was supported in part by friction between the backfill and retaining wall and between the backfill and existing stable face. They then assumed that the weight of the backfill supported by the retaining wall and existing stable face was a function of the friction between the backfill and respective surfaces.

2.4.3 Frydman and Keissar, 1987

Frydman and Keissar (1987) present an early centrifuge model study of earth pressures in a confined space. They examined the horizontal earth pressures transferred to a rigid retaining wall by granular fill confined between a wall and an existing stable face. They performed a series of centrifuge tests on model retaining walls with no reinforcement. A schematic of the model retaining wall is shown in Figure 2-13. Tests were performed for wall aspect ratios (W/H) ranging from 0.10 to 1.1, and horizontal earth pressures against the wall facing were measured. Tests were performed on a rigid wall that was prevented from moving during the experiment.

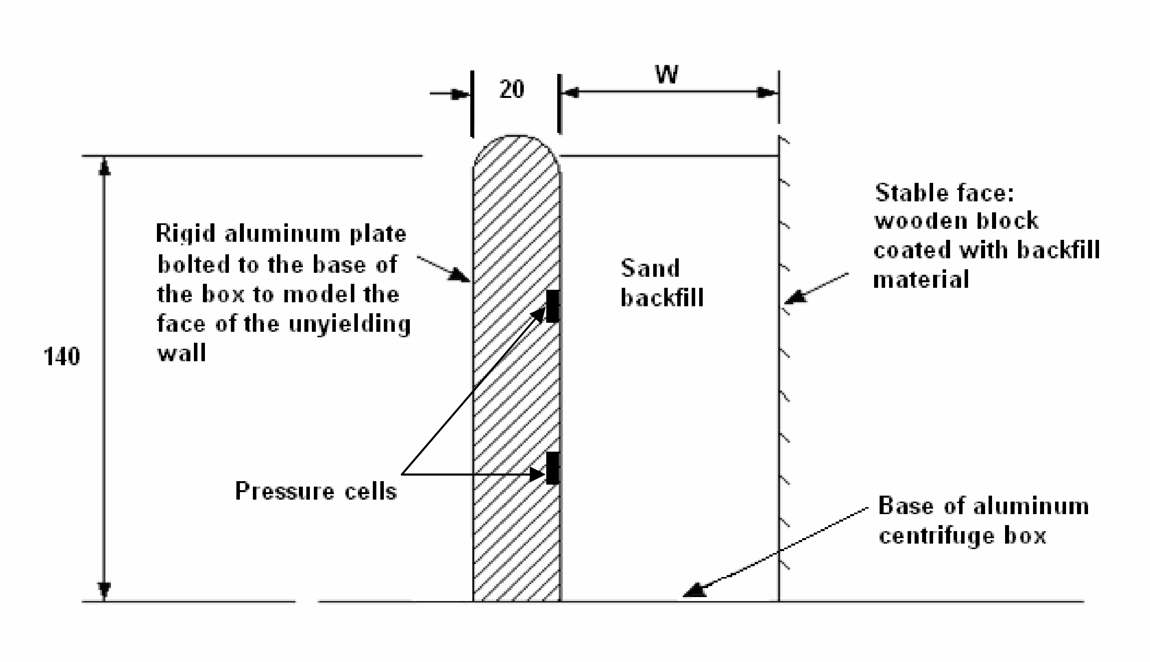

Figure 2.13: Schematic illustration of nondeformable wall used in centrifuge tests by Frydman and Keissar (1987)

The variation in horizontal earth pressure coefficients at two locations below the top surface of the wall measured from tests performed by Frydman and Keissar for wall aspect ratios equal to 1.10 and 0.10 is shown in Figure 2-14. The results are presented as normalized values. The depth is expressed as a nondimensional depth z/H where z is the depth below the top of wall and H is the height of the wall. Similarly, the horizontal earth pressures acting on the wall are represented by a non-dimensional horizontal earth pressure coefficient k_w. The values of k_w were calculated by dividing the measured horizontal stresses (σ_h) by the overburden pressure (γz). Frydman and Keissar found that the earth pressure coefficients decreased with depth and as the wall aspect ratio decreased. The variation in horizontal earth pressure coefficients at two locations below the top surface of the wall measured from tests performed by Frydman and Keissar for wall aspect ratios equal to 1.10 and 0.10 and the values of k_w calculated using Spangler and Handy's equation (Eq. 2-6) are shown in Figure 2-15. The values of the horizontal earth pressure coefficients calculated by Spangler and Handy's equation (Eq. 2-6) agree well with the values measured by Frydman and Keissar. However, Frydman and Keissar also concluded that significant variations from the theoretical value may occur next to the wall, due to small variations in placement conditions (e.g., localized compaction effects, slight variation in density, etc).

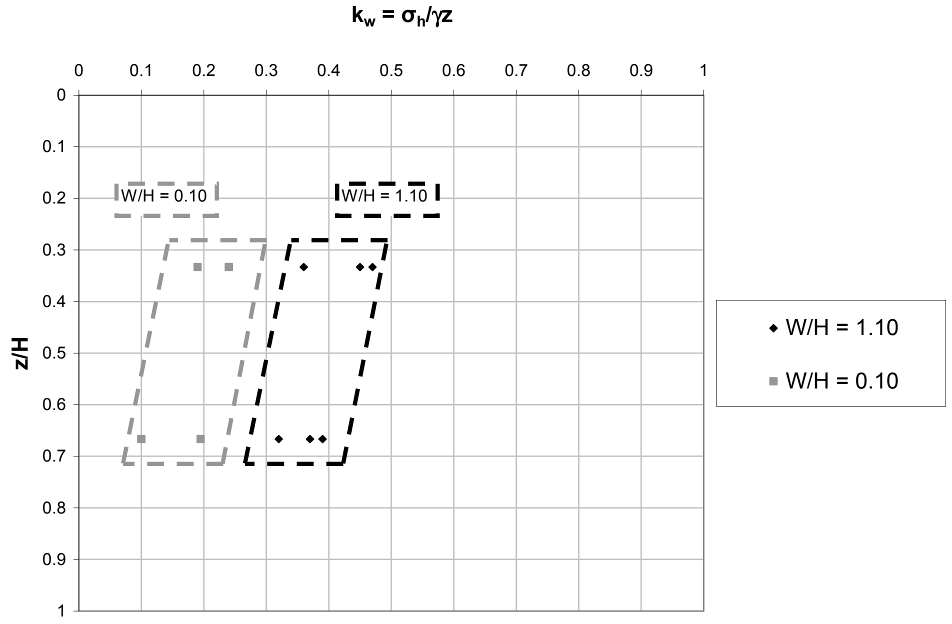

Figure 2.14: Variation in horizontal earth pressure coefficients (k_w) with the non-dimensional depth (z/H) below the top of the backfill measured from tests performed by Frydman and Keissar with wall aspect ratios (W/H) equal to 1.10 and 0.10

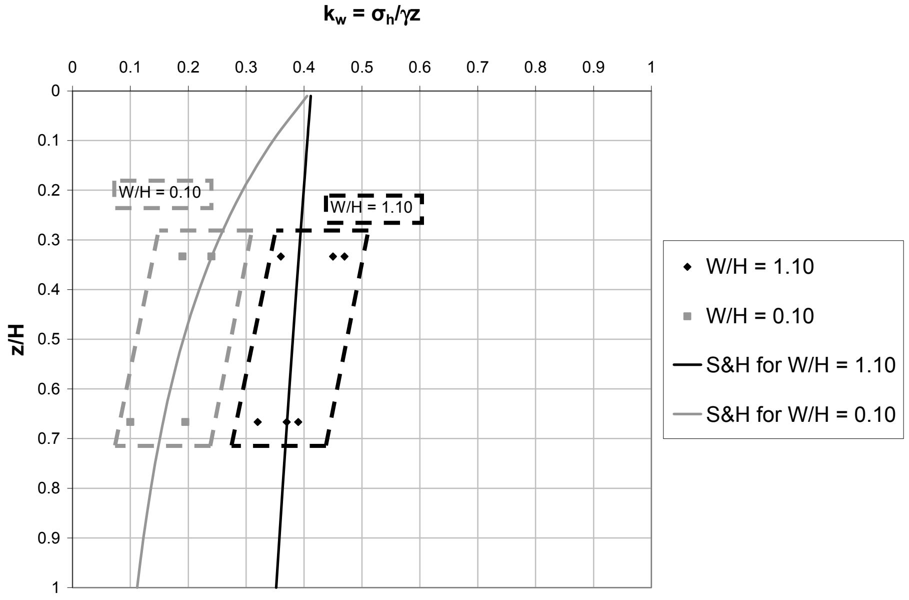

Figure 2.15: Variation in horizontal earth pressure coefficients (k_w) with the non-dimensional depth (z/H) below the top of the backfill measured from tests performed by Frydman and Keissar and values of k_w using Spangler and Handy's equation

2.4.4 Take and Valsangkar, 2001

Take and Valsangkar also studied the earth pressures in a confined space using centrifuge tests. A schematic of their centrifuge testing apparatus is shown in Figure 2-16. They conducted an extensive series of experiments to evaluate the use of flexible subminiature pressure cells in centrifuge tests. The pressure cells were used to measure horizontal earth pressures behind nondeformable retaining walls in a confined space. Take and Valsangkar investigated the influence of three primary variables: relative density of the backfill, the angle of internal friction of the interface between the backfill and existing stable face, and the wall aspect ratio (W/H). Relative densities of the backfill equal to 34 and 79 percent were used in the experiments. To vary the angle of internal friction of the interface between the backfill and existing stable face, they used both an aluminum surface and an aluminum surface with 120A-grit sandpaper bonded to it. The earth pressure cells were connected to the opposite wall, which was also made of aluminum and represented the (nondeformable) retaining wall. Centrifuge tests were performed for wall aspect ratios ranging from 0.10 to 1.3.

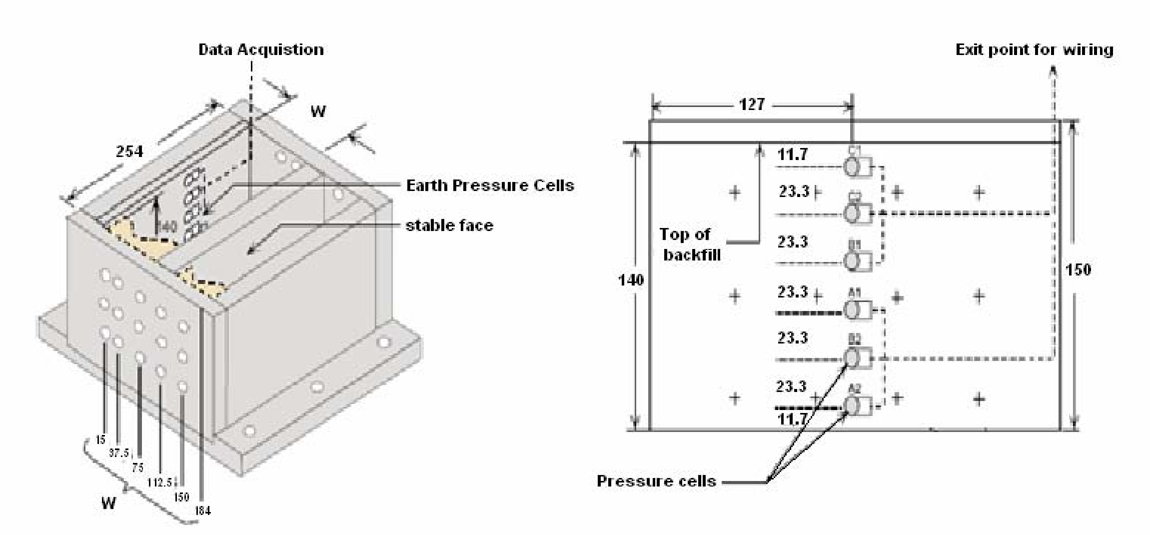

Figure 2.16: Schematic illustration of nondeformable wall used in centrifuge tests by Take and Valsangkar, 2001

Take and Valsangkar's tests showed that the horizontal earth pressures decreased as the relative density increased, apparently as a result of the angle of internal friction increasing from 30° to 36°. They also showed that the earth pressure decreased as the angle of interface friction between the backfill and existing stable face increased. Finally, the results indicated that the horizontal earth pressures generally decreased as the wall aspect ratio decreased.

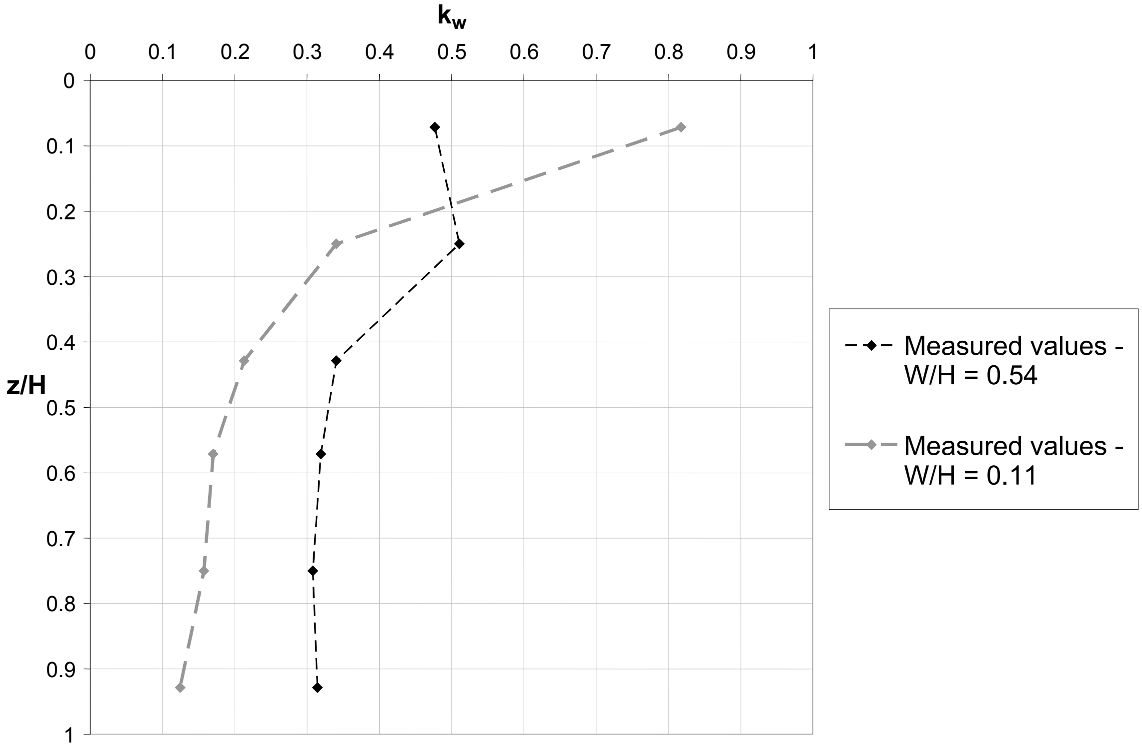

Figure 2.17: Variation in horizontal earth pressure coefficients (k_w) with the non-dimensional depth (z/H) measured from centrifuge tests performed by Take and Valsangkar with wall aspect ratios (W/H) equal to 0.54 and 0.11

The variation in horizontal earth pressure coefficients (k_w) with nondimensional depth (z/H) measured in Take and Valsangkar's centrifuge tests for wall aspect ratios (W/H) of 0.54 and 0.11 is shown in Figure 2-17. The depth is expressed as a non-dimensional depth z/H where z is the depth below the top of wall and H is the height of the wall. Similarly, the horizontal earth pressures along the wall are represented by a non-dimensional horizontal earth pressure coefficient k_w. The values of k_w were calculated by dividing the horizontal stress (σ_h) by the overburden pressure (γz). The earth pressure coefficients measured in the test with a wall aspect ratio equal to 0.11 are generally less than those measured in the test with a wall aspect ratio equal to 0.54. Also, the values of k_w decreased with depth below the top of the wall. Take and Valsangkar also concluded that the measured horizontal earth pressures acting on the nondeformable model walls showed good agreement with values computed using Spangler and Handy's equation (Eq. 2-6).

2.4.5 Woodruff, 2003

Woodruff (2003) performed a comprehensive series of centrifuge model tests on reinforced soil walls adjacent to a stable face ("shoring"). Woodruff tested 24 different walls with reinforcement lengths (L) ranging from 0.17 to 0.9 times the wall height (H). The reinforcement extended from the face of the wall to the stable face and the length, L, was defined as the length from the face of the wall to the stable face. Tests were performed with reinforcement of three different tensile strengths, and layouts involving five different vertical spacing arrangements. To form the facing for the model MSE wall, the reinforcement was “wrapped around” the fill, as shown in Figure 2-18. The reinforcement was extended to meet the stable face in all tests but was not connected to it.

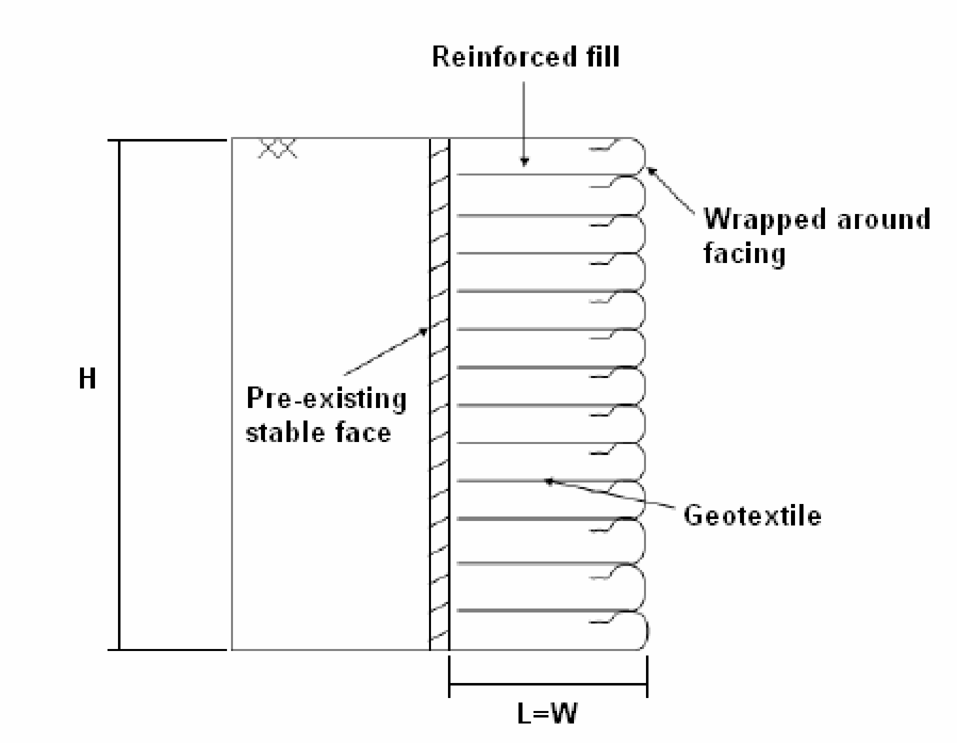

Figure 2.18: Schematic of model MSE wall for Woodruff centrifuge tests illustrating wrapped around facing (Woodruff, 2003)

Woodruff loaded each wall to failure and recorded the acceleration ("g" force) required to fail the wall. High-speed video cameras were used to capture deformations of the wall. Figure 2-19 shows the cross-sections of a typical model as it was subjected to increased gravitational forces in the centrifuge. The horizontal lines shown in the figure indicate the location of geosynthetic reinforcement. In Figure 2-19a, the model is shown in its initial condition at an acceleration of 1-g. Figure 2-19b shows the condition corresponding to working stress levels, and Figure 2-19c shows the wall at failure.

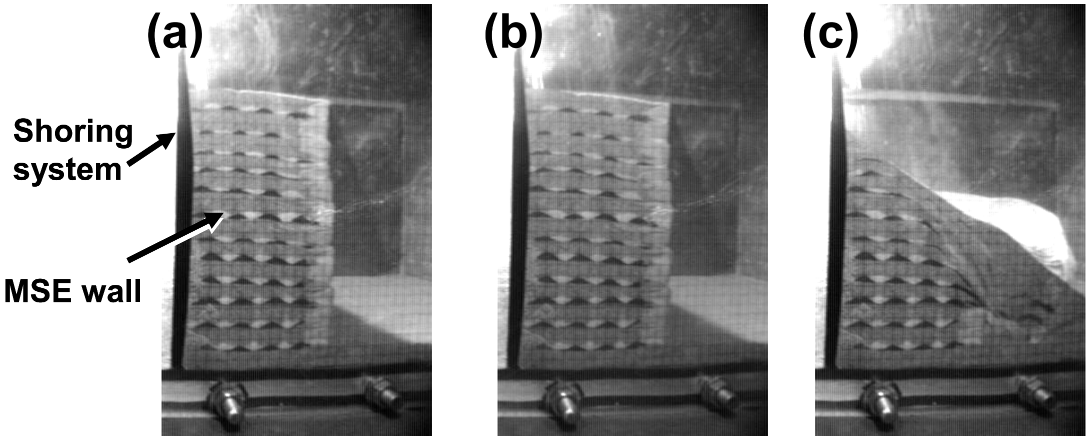

Figure 2.19: Photographic images from centrifuge evaluation of the deformation of MSE walls against a rigid shoring system: (a) initial condition; (b) working stresses; (c) failure condition (Woodruff, 2003).

The location of the failure surface was determined from observed tears in each layer of reinforcement. The observed tears suggested that failure surfaces were either linear or bilinear. For walls with aspect ratios ranging from 0.26 to 0.70, the failure surface was bilinear, i.e., the failure surface was composed of two straight line segments. An example of such a bilinear failure surface is shown by the triangles in Figure 2-20 for a wall with an aspect ratio of 0.40. The inclination of the failure surfaces from the toe of the wall to the “shoring” ranged from 48° to 57° measured from horizontal. When the failure surface reached the “shoring” it abruptly changed direction and followed the soil-wall interface to the top of the wall.

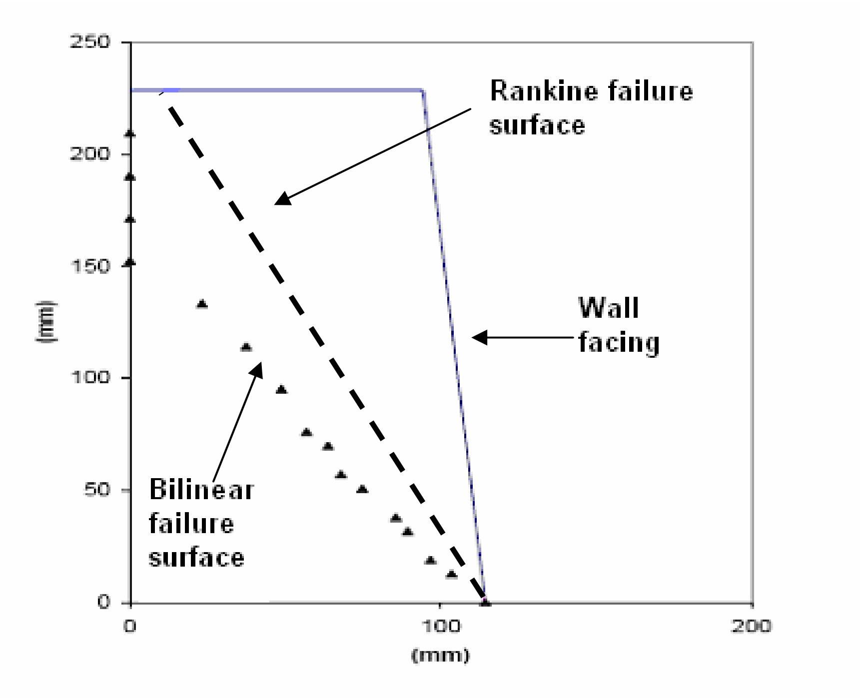

Figure 2.20: Cross-section of centrifuge model geometry showing a bilinear failure surface for L/H = W/H =0.40 (Woodruff, 2003)

For tests performed on walls with an aspect ratio of at least 0.70, the failure surface was linear, but the angle of inclination was less than the inclination of the theoretical Rankine failure surface. The theoretical Rankine failure surface should start at the toe and extend to the top of the wall at an angle (β) equal to 45 + ϕ'/2 measured from the horizontal. For the soil used in the centrifuge tests, the angle of internal friction (ϕ') was equal to 42.2° and, thus β is equal to 66.1°.

In one and only one test, Woodruff constructed a model with the reinforcement length equal to 70 percent of the height of the wall while the total width of the wall was 110 percent of the wall height. A diagram of the wall geometry and failure surface for this case is shown in Figure 2-21. The theoretical Rankine failure surface is represented by a dashed line in Figure 2-21, and the triangles indicate the locations of tears observed in the reinforcements. In this case only, the failure surface agreed well with the theoretical Rankine failure surface. Woodruff implied the reason that the observed failure surface agreed well with the theoretical Rankine failure surface was that there was retained fill behind the MSE structure.

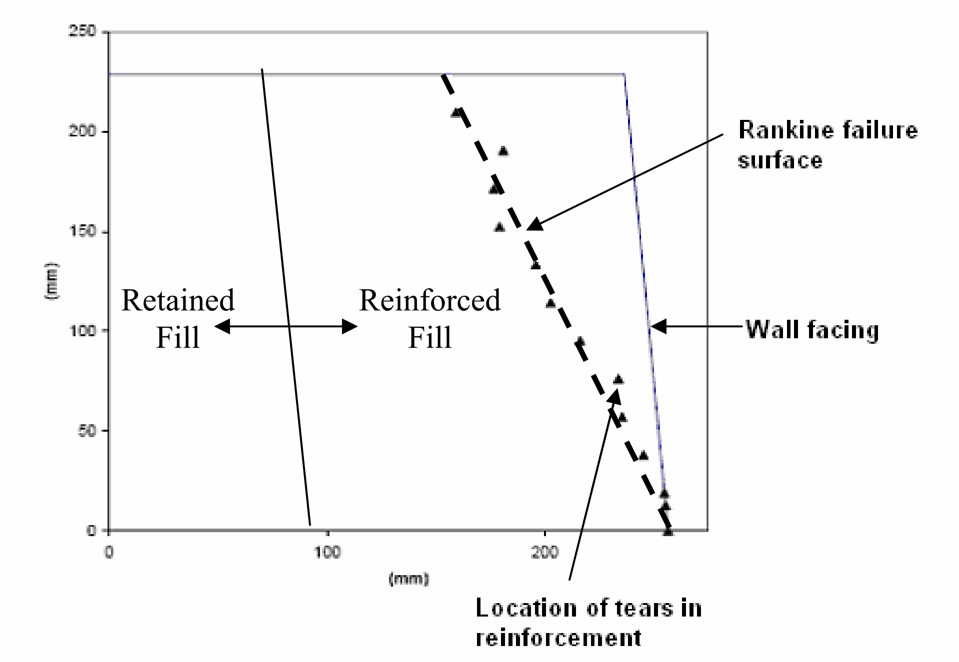

Figure 2.21: Cross-section of centrifuge model geometry showing a linear failure surface in good agreement with the theoretical Rankine failure surface with L/H = 0.70 and W/H = 1.1 (Woodruff, 2003)

Woodruff's experimental work provides a valuable source of performance data for walls like those of interest in this study and was used to compare the shape of the failure surface from limit equilibrium analyses with experimental results.

2.5 Limit Equilibrium Analysis

Leshchinsky, Hu, and Han (2003) and Lawson and Yee (2005) performed limit equilibrium analyses to study the effects of wall aspect ratio on the horizontal earth pressure coefficients. Results of both studies are presented below.

2.5.1 Leshchinsky, Hu, and Han, 2003

Leshchinsky, Hu, and Han performed a series of limit equilibrium analyses of MSE walls placed in a confined space using the program ReSSA 2.0. The authors considered the geometry shown in Figure 2-22. They varied the wall aspect ratio at the bottom of the wall (b/H) and the inclination of the backslope (m).

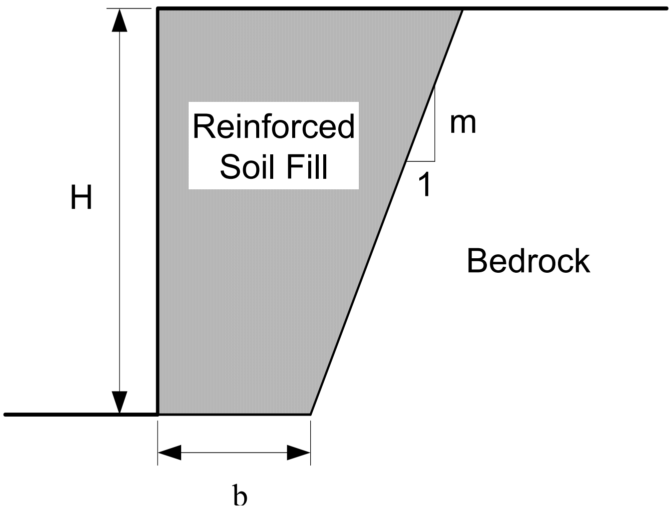

Figure 2.22: Wall configuration considered by Leshchinsky and Hu (2003).

The purpose of the limit equilibrium analyses was to calculate the force required for equilibrium with the shear strength of the soil fully developed. Thus, the required force corresponds to the conditions normally assumed for Rankine active earth pressures. They assumed circular slip surfaces and used the Simplified Bishop method of slices. The resultant earth pressure force was assumed to act at the lower third point of the wall.

Based on their limit equilibrium analyses Leshchinsky, Hu, and Han presented a series of design charts in Figures 2-23 through 2-25 for the earth pressure coefficient expressed as a ratio of the calculated horizontal earth pressure coefficient, K, to the Rankine active earth pressure coefficient, K_a defined in Equation 2-2. The calculated earth pressure coefficient was determined from Equation 2-7,

$$K = \frac{P_a^{'}}{\frac{1}{2}\gamma H^2} \qquad \text{Eq. 2-7}$$

where P’a is the value of the resultant force found from limit equilibrium analyses with the Simplified Bishop procedure, γ is the total unit weight of the fill, and H is the height of the wall. The ratio of the calculated horizontal earth pressure coefficient (K) to the Rankine active earth pressure coefficient (K_a) was designated as R ($R = K/K_a$).

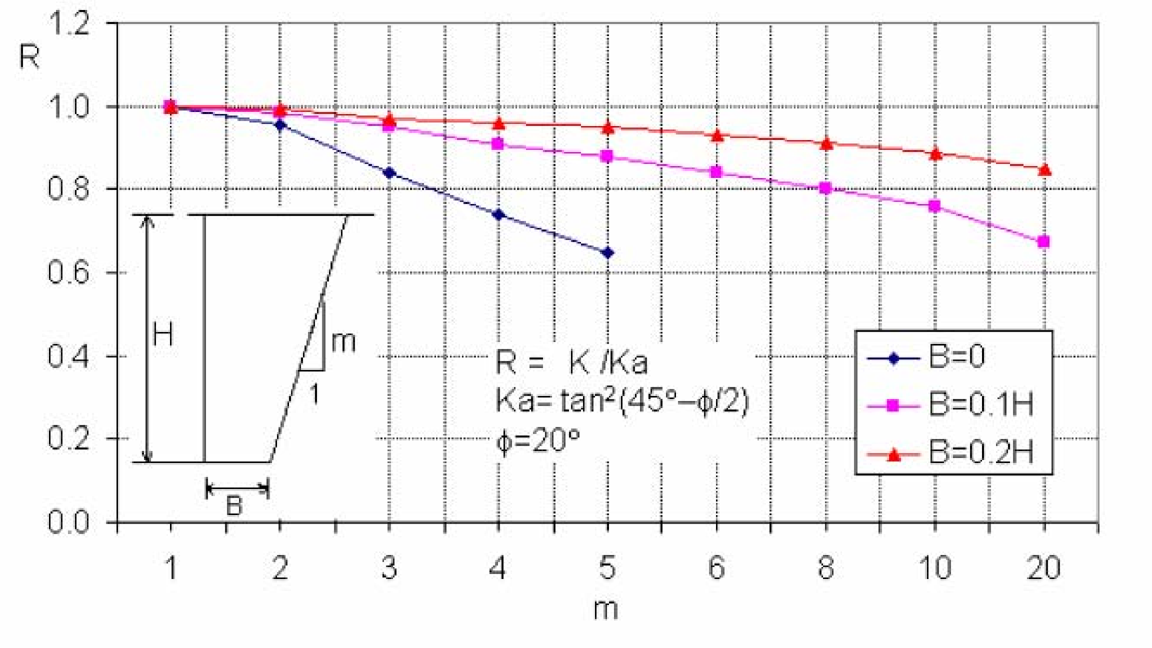

Figure 2.23: Design charts developed by Leshchinsky and Hu using ReSSA for an angle of internal friction equal to 20°

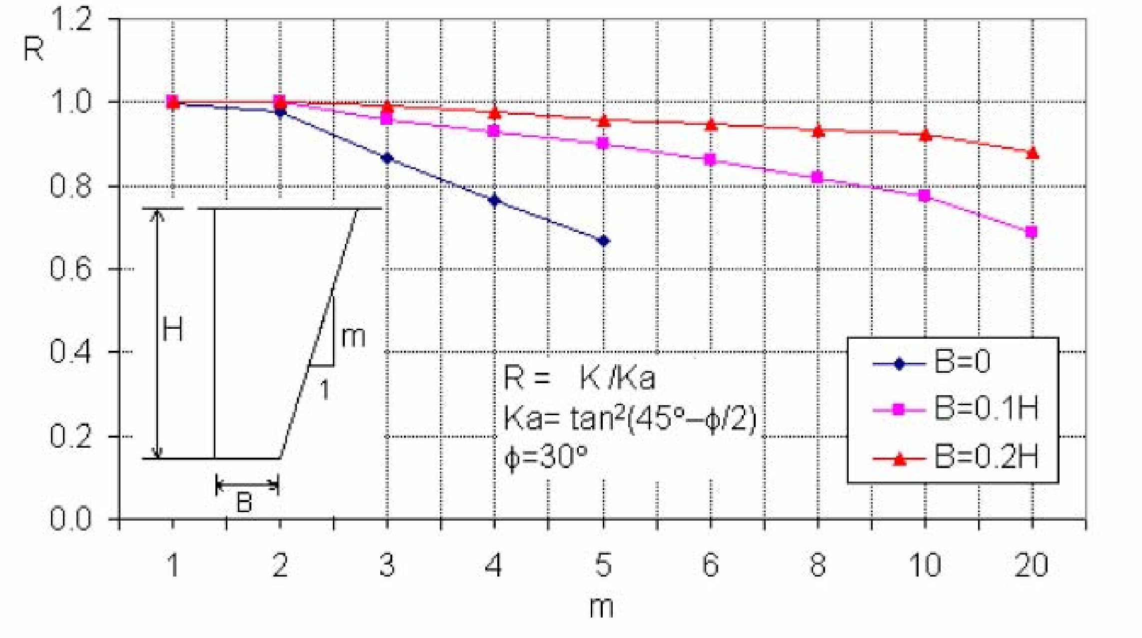

Figure 2.24: Design charts developed by Leshchinsky and Hu using ReSSA for an angle of internal friction equal to 30°

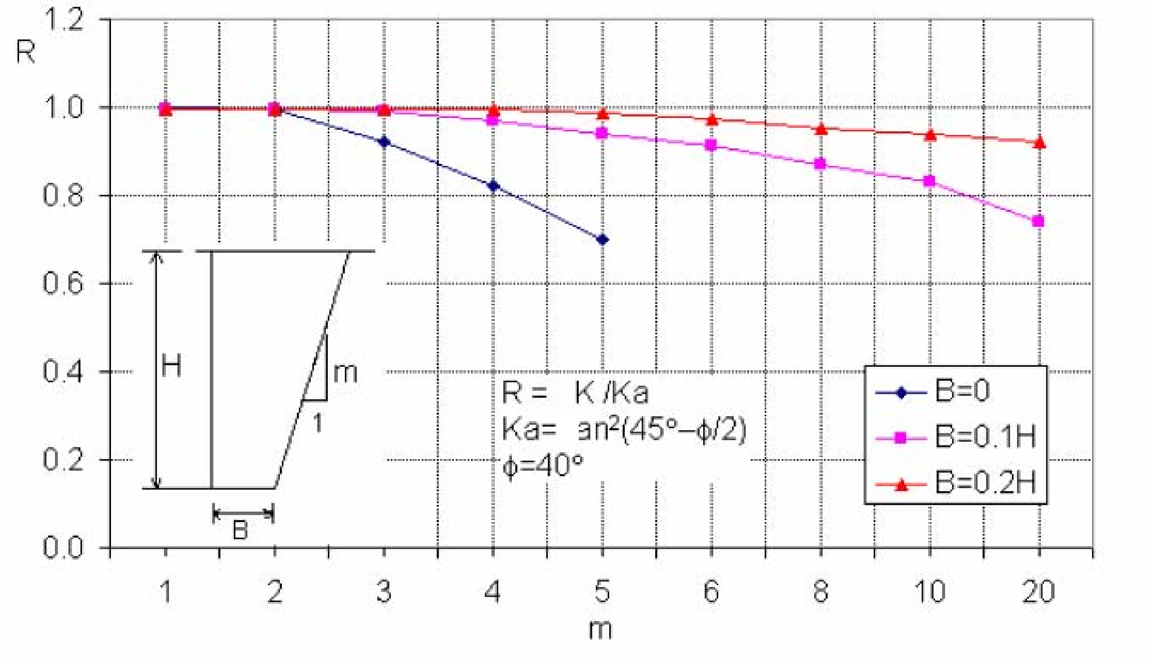

Figure 2.25: Design charts developed by Leshchinsky and Hu using ReSSA for an angle of internal friction equal to 40°

Leshchinsky, Hu and Han showed that as the wall aspect ratio (b/H) decreased, the value of R also decreased. They also showed that as the inclination of the backslope increased, i.e., the backslope became more vertical, the value of R decreased. They concluded weaker reinforcements may be used when the space is confined because the driving force is reduced; however, the driving force is only reduced significantly when the wall aspect ratio is less than or about 20 percent of the wall height, i.e. $b/H \leq 0.20$.

2.5.2 Lawson and Yee, 2005

Lawson and Yee (2005) also developed charts for earth pressure coefficients using limit equilibrium procedures. Lawson and Yee used the same geometry as Leshchinsky, Hu and Han (Figure 2-22). They considered both planar and bilinear slip surfaces, as shown in Figure 2-26a. Lawson and Yee showed that the horizontal earth pressures were less than or equal to the Rankine active earth pressures when the wall aspect ratio was less than or equal to 70 percent of the wall height, i.e., $b/H \leq 0.70$. They also showed that the horizontal earth pressure coefficients decreased as the wall aspect ratio decreased (Figure 2-26b).

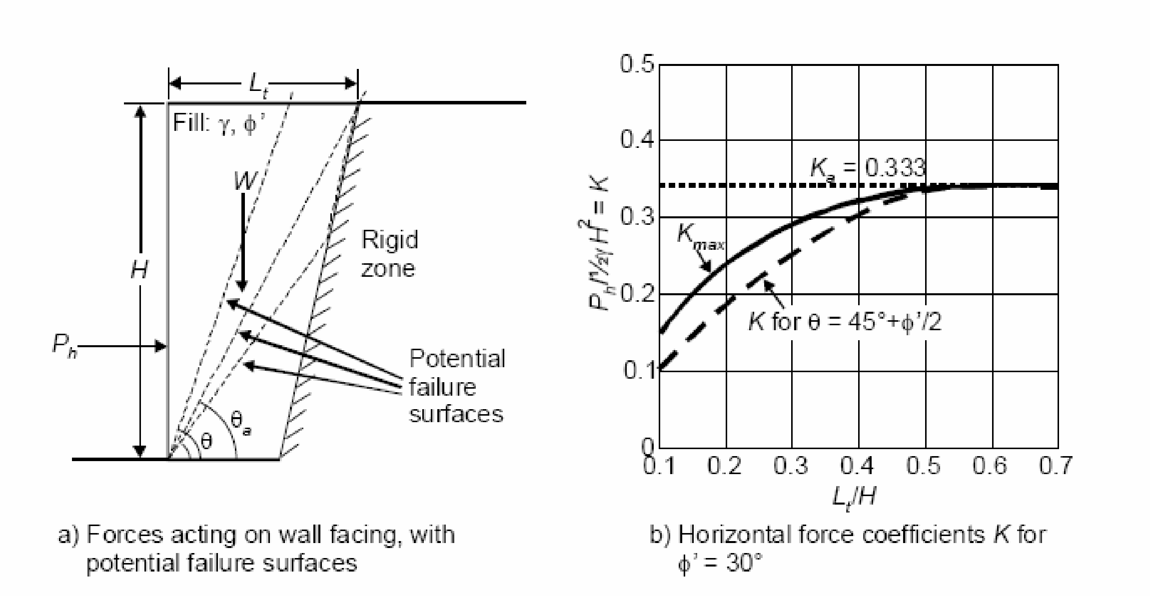

Figure 2.26: (a) Forces acting on wall face and potential failure surfaces analyzed by Lawson and Yee (b) Horizontal earth pressure coefficients for backfill with internal friction angle (ϕ') equal to 30° (Lawson, 2005)

The variation of the horizontal earth pressure coefficients as a function of the wall aspect ratio (b/H) and angle of internal friction (ϕ') is shown in Figure 2-27. Lawson and Yee showed that both the friction angle of the backfill and the wall aspect ratio govern the magnitude of the horizontal earth pressure coefficient acting on the face of the wall. Figure 2-27 illustrates this point for several angles of internal friction.

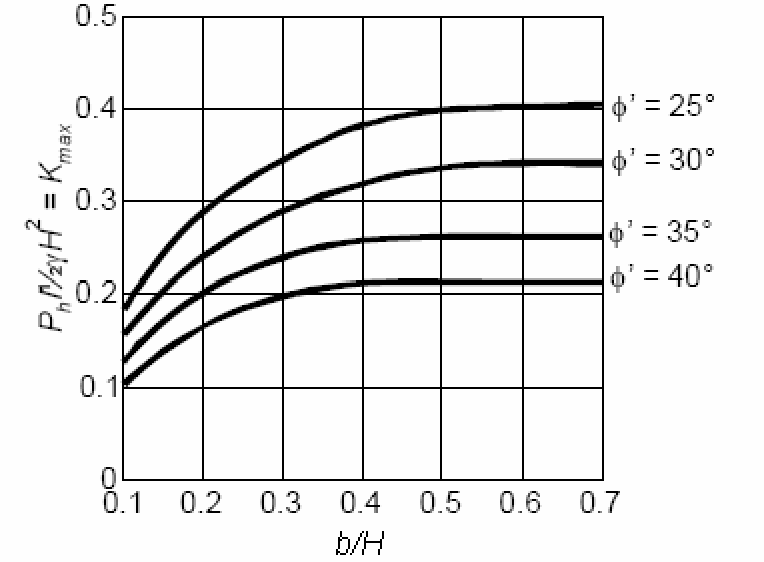

Figure 2.27: Maximum horizontal force coefficients for ϕ' = 25°, 30°, 35° and 40° (Lawson, 2005)

Lawson and Yee also studied the effects of wall aspect ratio for aspect ratios less than 70 percent of the wall height, i.e., L/H < 0.70, on the development of forces in the reinforcement. They concluded that the force developed in the reinforcements may not be fully dissipated when the reinforcement reaches the back of the wall (existing stable face). To achieve stability, Lawson and Yee recommend the forces be dissipated either by: 1) connecting the reinforcements to anchors or nails inserted into the rigid zone, or 2) extending the reinforcement in the form of a wraparound at the rear of the reinforced fill zone.

2.6 Data Compilation

One goal of the literature review was to compile data relating to properties of typical soil backfill, properties of reinforcement, and typical geometries used to construct MSE walls. The literature discussed in Sections 2.2 through 2.5 was the most relevant to the topic of MSE walls placed in a confined space, however, other sources were found that provided useful information about MSE walls. The properties of the soil backfill, the properties of the reinforcement, and the geometry used to construct the MSE walls or model MSE walls from the literature review presented in Sections 2.2 through 2.5 and the additional information are summarized in Table 2-1.

Table 2.1: Summary of backfill properties, reinforcement properties, and wall properties from literature review

		Backfill Properties					Reinforcement	Dimension				Wall		
Data Category	Author(s)	Angle of internal friction, ϕ' (Degree)	Unit weight, γ (kN/m^3)	Relative Density, D_r (%)	Young's Modulus, E (kPa)	Poisson's ratio, n	Type	Height (m)	Width (m)	Vertical Spacing (m)	Aspect Ratio	Material	Friction tan(δ)	G-Level
Guildlines	FHWA (Elias et al., 2001)	34-40 (30 uniform)	95% AASHTO T-99	--	--	--	Steel Strips and Mats	Varies	Varies	32 (inch) max	0.5-0.7	Formed Concrete	0.2 - 0.6	1
	NCMA (Simac et al., 1997)	26-36	95% Standard Proctor	--	--	--	Geotextiles	Varies	Varies	Varies	> 0.6	Concrete Block	0.31 - 0.45	1
Laboratory Tests	Frydman and Keissar(1987)	36	14 - 16.4	70	--	--	None	195 (mm)	Varies	--	1.1, 0.3, 0.22, 0.19, 0.1	Aluminum and Glass	0.36-0.47 and 0.21-0.27	10 to 15
	Take and Valsangkar (2001)	30/36	13.1 - 15.9	34 and 79	--	--	None	140 (mm)	Varies	--	1.31, 0.536, 0.271, 0.107	Aluminum and Sand Paper	0.42-0.47 and 0.62-0.73	35.7
	Woodruff (2003)	36.7	14.76 - 16.70	70	--	--	Pellon Sew-in and Pellon True-grid	230 - 250 (mm)	Varies	10 to 50 (mm)	0.17, 0.2, 0.25, 0.3, 0.4, 0.5, 0.6, 0.7, 0.9	Aluminum	0.75	1 to 50
Full-scale Tests	Allen and Bathurst (2003, 2005)	37-40	16.8 - 20.4	--	--	--	Steel Strip, Bar Mat, and WW Mat	6.1-16.8	Varies	0.15	--	--	--	1
	Morrison et al., (2006)	40	14.8	--	--	--	Tensar UX1500 Uniaxial Structural Geogrid	5.5	1.4 - 2.2	0.457	0.25-0.39	Concrete	--	1
	Filz and Duncan (1997)	30-40	18.1 - 21.2	--	--	--	None	1.4 - 24.4	Varies	--	0 to 0.4 cantilever wall	Concrete	0.45-0.62	1
Field Case Studies	Turner and Jensen (2005)	36~32	--	--	--	--		7.6	7	--	1.1	--	--	1
Numerical Analyses	Hatami and Bathurst (2005)	44	16.8	--	57500	0.49	Geogrid	3.6	5.95	0.6	1.65	Modular Block	44	1
	Lawson and Yee (2005)	25,30,35,40	20	--	--	--	Geogrid	5.6	3	0.2	0.62	Quartzite	--	1
	Leschinsky, Hu and Han (2003)	20~45	20	--	--	--	--	--	--	--	0 - 0.2	--	--	1
	Ling et al. (2000)	45 (5)	16	--	10360	0.42	Uniaxial HDPE Geogrids (Tensar SR55)	6	5	0.5	0.83	Modular Block	16.5	1
	Zornberg & Mitchell (1994)	46.1 (5.3)	21.1	--	45650	--	Geotextile	12.6	10	0.38	0.7	--	--	1

2.7 Summary and Conclusion

Based on the work described in this chapter, the following conclusions can be drawn about the earth pressures in the backfill behind retaining walls placed in front of a stable face and constructed within a confined space:

1. Earth pressures decrease as the aspect ratio (W/H) of the wall decreases, and the roughness of the interface between the backfill and wall increases.
2. For relatively stiff wall systems with small wall aspect ratios (W/H), the horizontal earth pressure coefficient will approach the at-rest value near the top of the wall and decrease with depth due to arching effects.
3. For relatively stiff wall systems, the horizontal earth pressure coefficients can become less than the Rankine active earth pressure coefficient (K_a) when the wall aspect ratio is very small.

Chapter 3. Modeling a Nondeformable Retaining Wall Placed in a Confined Space Using Plaxis

The finite element software known as Plaxis (Version 8.2) (Plaxis, 2005) was used to perform the finite element studies presented in this report. As the wall aspect ratio of MSE walls becomes smaller, the walls may become stiffer. In the extreme limiting case the walls become nondeformable. Thus, there is interest in understanding this limiting case of nondeformable walls. The features of Plaxis, the manner in which nondeformable retaining walls were modeled using Plaxis, and the procedure to calculate the displacements at the end of construction from the displacements output by Plaxis are presented in this chapter.

3.1 Modeling the physical space

Plaxis Version 8.2 is designed for two-dimensional modeling and analyses of physical space. A graphical interface allows the user to draw a cross-section of the physical space. In the study of nondeformable walls, the physical space has five main components: the backfill, the backfill-wall face and backfill-stable face interface, the wall face, the existing stable face, and the foundation. An example cross-section of the region modeled with Plaxis is shown in Figure 3-1.

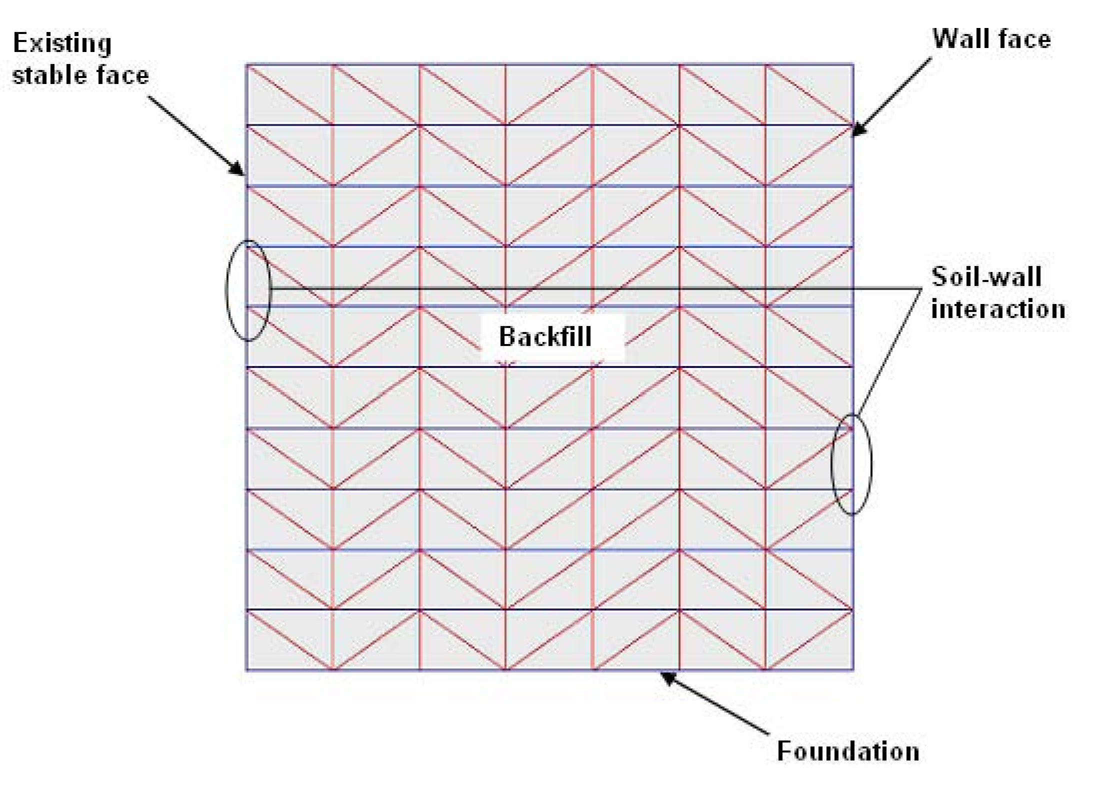

Figure 3.1: Example geometry showing finite element model of the physical space for a nondeformable retaining wall (Plaxis, 2005)

3.1.1 Backfill

The backfill was modeled using a finite element mesh created by Plaxis. The mesh consisted of 15-node triangular elements. The backfill is divided into several horizontal layers, as shown in Figure 3-1, so that elements were confined into discrete horizontal layers that were later used to simulate "stages" of construction in the analyses with Plaxis. The locations of nodes and stress points in a 15-node triangular element are shown in Figure 3-2. The size of the elements in the mesh may be selected prior to generating the mesh. In Plaxis, the default element size used for generating the mesh is referred to as "coarse." A typical mesh generated using the "coarse" mesh option in Plaxis is illustrated in Figure 3-3 for wall aspect ratios equal to 0.70 (a), and 0.30 (b).

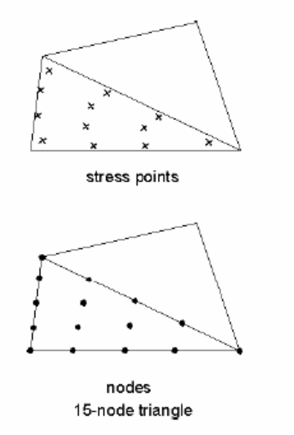

Figure 3.2: Example of nodes and stress points for 15-node triangular elements (Plaxis, 2005)

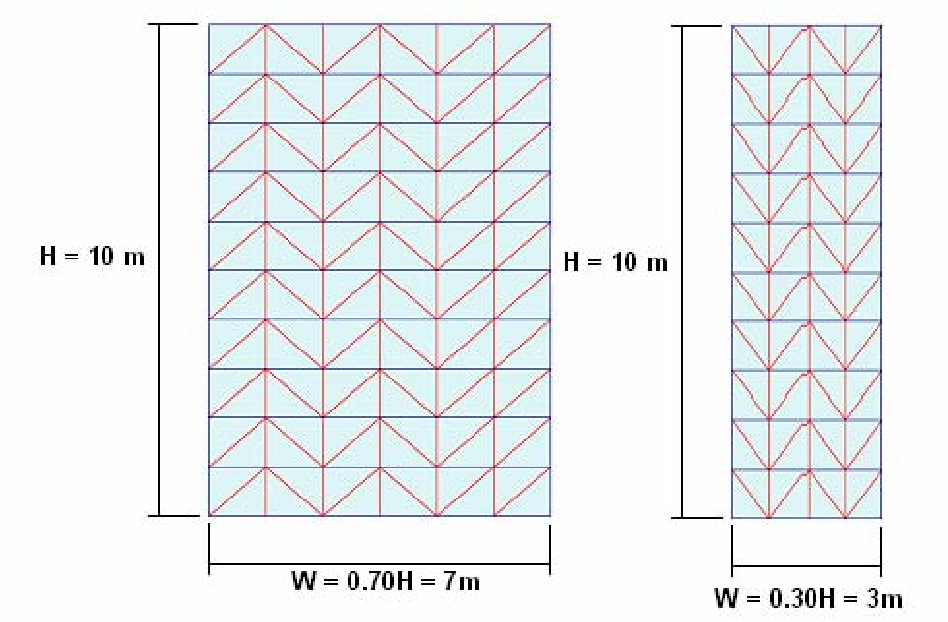

Figure 3.3: Typical mesh generated using the default (course) setting in Plaxis for wall aspect ratios equal to (a) 0.70, and (b) 0.30 (Plaxis, 2005)

3.1.2 Soil-wall interaction

The soil-wall interaction was modeled using thin rectangular elements called interface elements. The locations of nodes and stress points in a 5-node interface element are shown in Figure 3-4. The interface element shown in Figure 3-4 is given a small, finite thickness in Plaxis, but in reality the interface has zero thickness. In Plaxis, interface elements are assigned an imaginary *virtual thickness,* which is a dimension used to define the material properties of the interface in Plaxis. The virtual thickness is the product of a *virtual thickness factor* and the size of triangular elements. By default, Plaxis uses a virtual thickness factor equal to 0.10. The default value of the virtual thickness factor was used in all simulations.

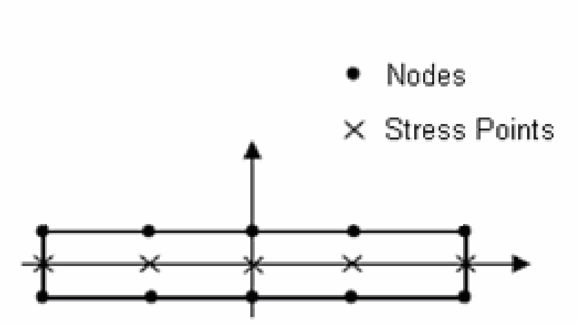

Figure 3.4: Locations of nodes and stress points in a 5-node interface element (Plaxis, 2005)

Each element is connected to other elements or to a boundary. Triangular elements will share the nodes along each side of the triangle. When a triangle is connected to an interface element, they also share nodes, as shown in Figure 3-5.

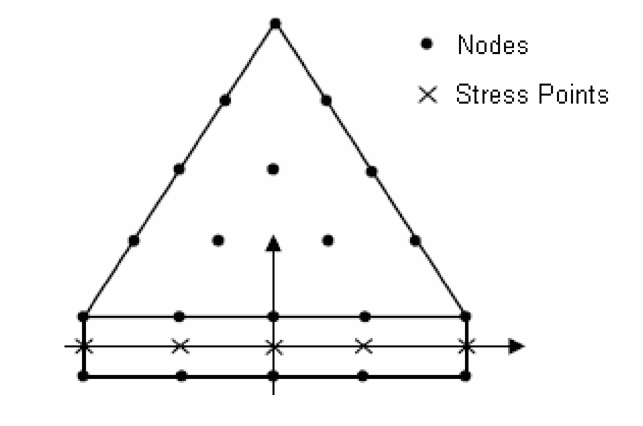

Figure 3.5: Locations of nodes and stress points when a 15-node triangular element is connected to a 5-node interface element (Plaxis, 2005)

The degree of interaction between the soil and wall is modeled by choosing an appropriate value of the interface reduction factor, R_{inter}, which relates the interface strength to the shear strength of the soil. The interface strength is characterized by a bilinear Mohr-Coulomb model (see Section 3.1.4.2).

3.1.3 Boundary Conditions - wall face, existing stable face, and foundation

A total fixity boundary condition was imposed at the foundation for all simulations. The nodes along a boundary having a total fixity boundary condition were fixed against horizontal and vertical movement. Both the horizontal fixity with the freedom to move vertically and the total fixity condition were imposed at the wall face and existing stable face to study the effects of the boundary conditions on displacements in Chapter 4. The total fixity condition was applied to simulate a rough wall, i.e., a wall with a surface that produces friction between the soil and wall. The nodes along a boundary having a horizontal fixity boundary condition with the freedom to move vertically were fixed against horizontal movement and free to move in the vertical direction. The horizontal fixity condition was applied to simulate a smooth wall, i.e., a wall with a surface that has no interaction with the soil.

3.1.4 Soil Constitutive Models

Three constitutive models were investigated to model the soil in Plaxis: linear elastic, Mohr-Coulomb, and Hardening-Soil. The models are described below.

Linear Elastic model

The linear elastic model is the least complicated model in Plaxis. A graphical representation of the linear elastic model is shown in Figure 3-6. The constitutive parameters are Young's Modulus (E) and Poisson's ratio (ν). The linear elastic model was used primarily to understand how Plaxis computed certain quantities, such as settlement, because the results are easily reproducible by hand.

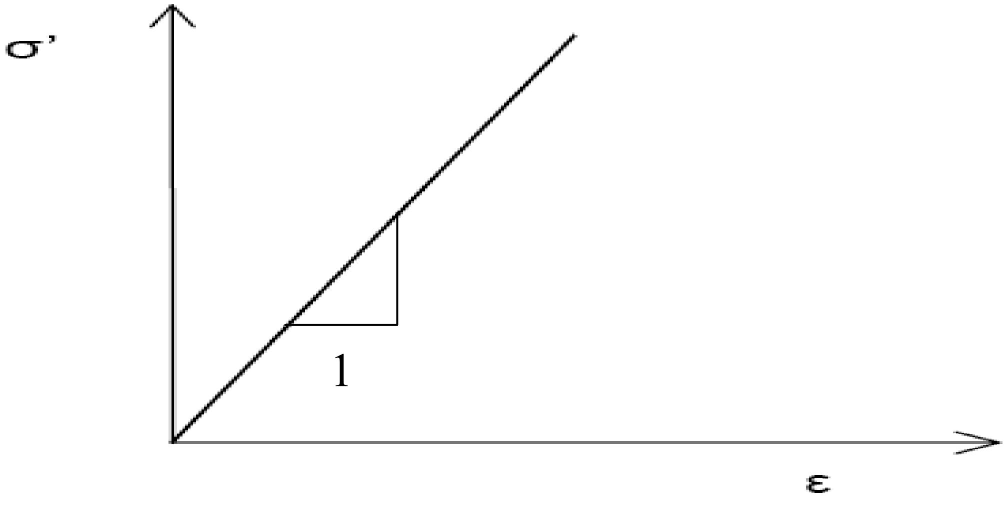

Figure 3.6: Stress-strain relationship for the Linear-Elastic model (Plaxis, 2005)

Mohr-Coulomb model

The Mohr-Coulomb model is an elastic-plastic model (Figure 3-7). In this model a yield surface is defined such that when the soil reaches or surpasses a predefined stress state, deformation is no longer completely recoverable. Five soil constitutive parameters are required for the Mohr-Coulomb model: Young's Modulus (E), Poisson's ratio (ν), angle of internal friction (ϕ'), cohesion (c'), and dilatancy angle (ψ). In all simulations, the goal was to model the backfill as a cohesionless material. Because the Mohr-Coulomb model is simple and requires relatively few parameters, it was used to simulate laboratory tests found in the literature for which a complete characterization of the soil used in tests was not reported.

Figure 3.7: Stress-strain relationship for the Mohr-Coulomb model (Plaxis, 2005)

Poisson's ratio (ν). Poisson's ratio significantly impacts the horizontal stresses and needs to be chosen carefully. The documentation on Plaxis (Plaxis, 2005) suggests that Poisson's ratio should be chosen such that:

$$\frac{\nu}{1-\nu} \geq \frac{1-\sin(\phi)}{1+\sin(\phi)} \quad . \qquad \text{Eq. 3-1}$$

The inequality represented by Equation 3-1 states that the at-rest horizontal earth pressure coefficient based on the theory of elasticity and Poisson's ratio should be greater than the earth pressure coefficient for active earth pressures, i.e., failure of the soil. This is necessary to ensure that the stresses do not exceed the shear strength of the soil. If the stresses exceed the strength of the soil, the calculations in Plaxis are terminated before the final stage of construction is completed. Finding a range of values for Poisson's ratio that satisfies Equation 3-1 was accomplished as follows:

A value for the angle of internal friction, ϕ' was assumed.

The developed friction angle, $\phi_{\text{developed,}}$ was calculated from Equation 3-2.

$$\phi_{\text{developed}} = \arctan(\tan(\phi')/\mathrm{F}) \qquad \text{Eq. 3-2}$$

where F is a factor of safety. A factor of safety of 1.5 was used.

The "developed" horizontal earth pressure coefficient for the active condition was calculated using $\phi_{\text{developed}}$ and the equation,

$$K_{developed} = \frac{1-\sin(\phi_{developed})}{1+\sin(\phi_{developed})} \qquad \text{Eq. 3-3}$$

Poisson's ratio corresponding to the "developed" horizontal earth pressure coefficient was calculated based on Equation 3-1 as

$$\nu = \frac{K_{developed}}{1+K_{developed}} \qquad \text{Eq. 3-4}$$

<u>Angle of Internal Friction (ϕ').</u> The values selected for the angles of internal friction (ϕ') varied depending on what was being studied. The values of ϕ' are given at the appropriate places in Chapters 4, 5, 6 and 7.

<u>Cohesion (c').</u> In all the simulations performed for this study, the soil was modeled as cohesionless soil. However, in Plaxis, when the value of the cohesion is equal to zero, a warning message cautions, "Use small cohesion to improve calculation performance". The Plaxis documentation suggested using a value equal to 0.20 kPa (4 psf) (Plaxis, 2005). This value of cohesion was used in all simulations.

<u>Dilatancy (ψ).</u> The dilatancy angle (ψ) describes the behavior of soil during expansion and will depend on the angle of internal friction. The Plaxis documentation recommends that the dilatancy angle be chosen such that it is 30 degrees less than the angle of internal friction (ϕ') (Plaxis, 2005). Thus,

$$\psi = \phi - 30 \qquad \text{Eq. 3-5}$$

Equation 3-5 was used to determine the value of the dilatancy angle for all simulations in the study.

Hardening-Soil model

The most rigorous and complex soil constitutive model used in this study was what Plaxis refers to as the "Hardening-Soil model." The model is based on an adaptation of the well known Duncan Hyperbolic model. The Hardening-Soil model employs a non-linear stress-strain curve like the one shown in Figure 3-8. The Hardening-Soil model uses some of the same parameters as the Mohr-Coulomb model, specifically, the angle of internal friction (ϕ'), cohesion (c'), and the dilatancy angle (ψ). These parameters are the same as those described earlier for the Mohr-Coulomb model. The additional parameters unique to the Hardening-Soil model are described below. The Hardening-Soil model was used in the parametric analyses presented in Chapter 6 and to study the effect of wall aspect ratios on earth pressures presented in Chapter 7.

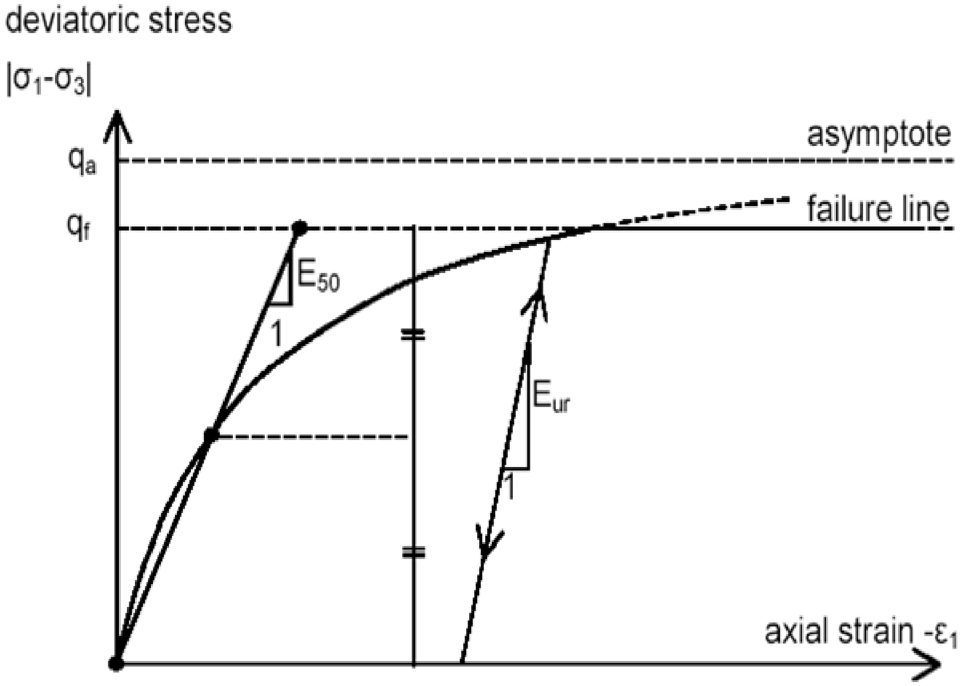

Figure 3.8: Stress-strain relationship for the Hardening-Soil model (Plaxis, 2005)

Modulus of Elasticity. Three moduli are used to describe the stress-strain characteristics in the Hardening-Soil model. The values of the moduli input into Plaxis represent reference values corresponding to a "reference pressure." In all simulations, the "reference pressure" was assumed to be equal to atmospheric pressure (101.3 kPa or 2116 psf). Plaxis uses the reference values of the moduli to calculate new moduli based on the state of stress, i.e., the value of the minor principal stress. The moduli change in accordance with the state of the minor principal stress, and thus, the stress-strain curve is nonlinear, as shown in Figure 3-8.

Modulus parameter, E_{50}^{ref}. The modulus parameter, E_{50}^{ref}, characterizes plastic straining due to primary deviatoric loading (Plaxis, 2005). The parameter E_{50}^{ref} also represents a secant stiffness in a drained triaxial test. A modulus, E_{50}, is calculated from E_{50}^{ref} based on the minor principal stress. The units for E_{50}^{ref} are force per unit area (stress).

Modulus parameter, E_{oed}^{ref}. The modulus parameter, E_{oed}^{ref}, characterizes plastic straining due to primary compression (Plaxis, 2005). The parameter E_{oed}^{ref} also represents a tangent stiffness for primary oedometer loading. A modulus, E_{oed} is calculated from E_{oed}^{ref} based on the minor principal stress. The units for E_{oed}^{ref} are force per unit area (stress).

Modulus parameter, E_{ur}^{ref}. The modulus parameter, E_{ur}^{ref}, measures the elastic unloading and reloading. The Plaxis documentation recommends using a value of E_{ur}^{ref} equal to three times E_{50}^{ref} (Plaxis, 2005). A modulus, $E_{ur,}$ is calculated from E_{ur}^{ref} based on the minor principal stress. The units for E_{ur}^{ref} are force per unit area (stress).

Unload-Reload Poisson's Ratio (ν_{ur}). The unload-reload Poisson's Ratio is a parameter used to capture the soil response for the unload-reload curve. A value of 0.20 is suggested in the Plaxis documentation. No relationship between the unload-reload Poisson's ratio and Poisson's ratio corresponding to the Mohr-Coulomb model is indicated in the Plaxis documentation. The unload-reload Poisson's ratio is dimensionless.

Failure Ratio (R_f). The failure ratio is the ratio between the asymptotic value of shear stress for the hyperbolic stress-strain curve and the actual peak deviatoric stress at failure. The failure ratio has no units.

Power Variable (m). The parameter, m, measures the degree that the stiffness of the soil depends on the minor principal stress. The power variable is dimensionless.

3.1.5 Interface Strength Parameters

The interface reduction factor (R_{inter}) relates the strength of the interface between the soil and a structure to the shear strength of the soil. It affects all the strength parameters of the interface, including the angle of internal friction and cohesion. Only cohesionless soils were considered in the simulations, thus the interface reduction factor (R_{inter}) can be expressed in terms of the angle of internal friction and the interface friction angle by Equation 3-6.

$$R_{\text{inter}} = \frac{\tan(\delta)}{\tan(\phi'_{\text{soil}})} \qquad \text{Eq. 3-6}$$

where δ is the interface friction angle, and ϕ'_{soil} is the angle of internal friction of the soil. The interface reduction factor is dimensionless.

3.1.6 Staged Construction

Plaxis has the ability to simulate construction using *staged construction* where the soil layers are added to the geometry in stages. Staged construction was used in all the finite element analyses presented herein. The soil layers are added, beginning with the bottom of the wall and ending with the top of the wall, to simulate the construction of a retaining wall in the field.

3.2 Interpreting displacements output by Plaxis

The displacements reported by Plaxis for the end of construction represent displacements due to all changes in stress. These include displacements resulting from the surcharge placed above each layer and compression resulting from the weight of the soil in each layer. The displacements output by Plaxis for any level represent the displacements due to the cumulative effects of compression of all soil layers beneath the point of interest. Thus, the displacements are largest at the top of the wall because they represent the cumulative compression of all soil layers. In contrast, the displacement of interest at the end of construction should be zero at the top of the wall because the top of the backfill only exists at the end of construction and thus, does not displace any during construction. To convert the displacements computed by Plaxis into more meaningful "construction displacements", first a procedure was developed to illustrate the computational scheme used in Plaxis for calculating the displacements at the surface of a layer. Based on this procedure, another procedure was developed to convert the displacements at the surface of a layer calculated by Plaxis to displacements at the end of construction.

3.2.1 Computational scheme used by Plaxis

To illustrate the computational scheme used in Plaxis for calculating the displacements at the surface of a layer, a simulation was performed in which a column of soil was “built” in layers using staged construction. For simplicity, one-dimensional compression was assumed. The column of soil was constructed in six layers and each layer was 5 feet thick. The total height of the column was 30 feet. At the bottom of the column of soil a total fixity boundary condition was assigned. Along the sides of the column horizontal fixity was assumed and the nodes were allowed to move freely in the vertical direction. The boundary condition along the vertical side walls is analogous to placing rollers along the boundary. The linear elastic soil constitutive model was chosen for the simulation because the results could easily be duplicated by hand calculations using linear elastic theory. The values chosen for the unit weight and soil constitutive parameters are listed in Table 3-1.

Table 3.1: Soil constitutive parameters chosen for the linear elastic model

Total Unit Weight, γ (pcf)	130
Poisson's Ratio, ν	0.333
At-Rest Earth Pressure Coefficient, K_0	0.500
Young's Modulus, E (psf)	15000

For the first stage of “construction,” one layer of soil 5 feet thick was placed as shown in Figure 3-9. The vertical displacement at the top of the layer reported by Plaxis was 0.0724 ft (0.87 inches).

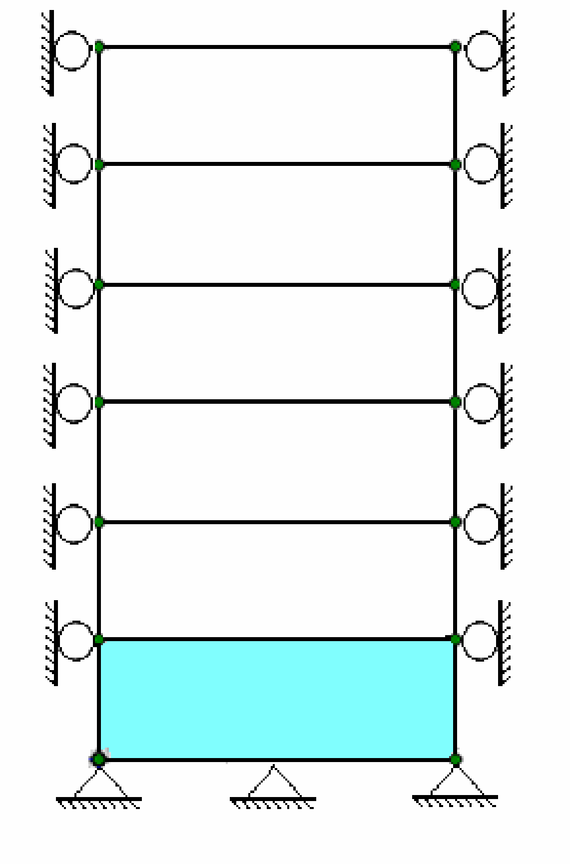

Figure 3.9: Column of soil after first stage of "construction" (Plaxis, 2005)

Using linear elastic theory, the compression of a given layer, S, can be calculated by integrating the strain caused by the weight of the soil layer over the height of the layer, i.e.,

$$S = \int_0^h \varepsilon_v * dh \qquad \text{Eq. 3-7}$$

where: h is the height of the layer, and ε_v is the strain in the vertical direction computed using linear elastic theory

$$\varepsilon_v = \frac{\sigma_y}{E} - \frac{v\sigma_x}{E} - \frac{v\sigma_z}{E} \qquad \text{Eq. 3-8}$$

where: $\sigma_y=\gamma h$ and $\sigma_x=\sigma_z=\gamma h K_0$.

Using the values from Table 3-1, choosing the height of the layer to be 5 feet and solving for "S" yields the value 0.0723 feet (0.87 inches) for the compression of the layer. The value for the compression of the soil layer output by Plaxis and the value for the compression of the soil layer calculated from linear elastic theory are the same.

For the second stage of construction, a second layer of soil 5 feet thick was placed on top of the first layer. The magnitude of the displacement output by Plaxis for the top of the second layer was 0.2894 feet (3.47 inches). The compression of the first layer of soil resulting from the surcharge of the second layer can be calculated by determining the strain due to the surcharge and multiplying that value by the height of the layer being compressed. Designating the compression of a layer resulting from a surcharge applied to the top of the layer as Q, one can write

$$Q = \varepsilon_v * \Delta h \qquad \text{Eq. 3-9}$$

where: Δh is the height of the layer and ε_v is the same as shown in Equations 3-7 and 3-8. Using the values from Table 3-1, choosing the height of the layer to be 5 feet and computing a value for "Q" yields the value 0.1445 feet (1.734 inches). The first layer, originally placed in the first stage, has now experienced compression from the weight of the soil in the first layer and from the surcharge caused by the weight of the second layer. Therefore the total compression of the first layer is equal to the summation of "S" and "Q." The value of the summation is equal to 0.2168 feet (2.602 inches). Also, the second layer experienced compression (S) caused by the self-weight of the soil in the second layer. Thus, the total compression is the summation of compression from the first two layers and is equal to 0.2890 feet (3.47 inches). This value (0.2890 ft) is essentially the same as the value (0.2894 feet) output by Plaxis.

Based on the example just described, it was found that the following general equation could be used to calculate the displacements at the top surface of the column of soil after "n" stages of construction:

$$C = \frac{n * (n-1) * Q}{2} + n * S \qquad \text{Eq. 3-10}$$

where C is the total compression of all n layers, n is the number of stages (layers), Q ($\varepsilon_v * \Delta h$) is the compression of one single layer resulting from the surcharge applied to the top of the layer by another single layer, and S ($\int_0^h \varepsilon_v * dh$) is the compression of one layer resulting from the weight of the soil in the layer. The compression of the layers calculated using linear elastic theory and the displacements at the top of each layer output by Plaxis at the end of each stage are shown in Table 3-2. The percent difference between the displacements output by Plaxis and the values calculated using Equation 3-10 was on the order of one-tenth of one percent, thus confirming the procedure used by Plaxis to calculate and report displacements.

Table 3.2: Summary of displacements at the surface of a layer output by Plaxis and calculated using linear elastic theory

	Displacement (ft)	Compression (ft)	
Layer	Plaxis	Equation 3-10	% difference
1	0.0724	0.0723	0.127
2	0.2894	0.2890	0.109
3	0.6510	0.6503	0.110
4	1.1570	1.1561	0.075
5	1.8080	1.8065	0.085
6	2.6040	2.6013	0.104

3.2.2 Adjusting displacements output by Plaxis

The displacements that are of interest are the displacements at the end of construction where the displacement of the top of the backfill is equal to zero. As seen in Table 3-2, the displacement actually calculated by Plaxis at the top of the backfill (layer 6) is 2.6040 feet.

Because the value output by Plaxis was different from the displacement at the end of construction, a procedure was developed to adjust the displacements output by Plaxis such that they correspond to displacements for the end of construction. This process is described in the following section.

Finding the displacements at the end of construction

The displacements at the end of construction can be calculated using the constrained modulus. The constrained modulus (M) is the ratio of vertical stress to vertical strain under one-dimensional compression and expressed by Equation 3-11.

$$M = \frac{\Delta\sigma_v}{\varepsilon_v} \qquad \text{Eq. 3-11}$$

In the case of an elastic soil the constrained modulus can be expressed in terms of Young's modulus and Poisson's ratio as follows:

$$\frac{\Delta\sigma_v}{\varepsilon_v} = M = \frac{E}{1 - 2\left(\frac{\nu^2}{1-\nu}\right)} \qquad \text{Eq. 3-12}$$

The strain at a point b in the backfill behind a wall of height (H) may be found by rearranging Equation 3-12 and solving for ε_v, i.e.,

$$\varepsilon_v = \frac{\Delta\sigma_v}{\frac{E}{1 - 2\left(\frac{\nu^2}{1-\nu}\right)}} \qquad \text{Eq. 3-13}$$

Multiplying the strain by the height, H_b, of point b above the bottom of the wall, the displacement of the layer due to the change in stress produced by soil placed above the height, H_b, is given by

$$D_b = \left(\frac{\gamma(H - H_b)}{M}\right)H_b \qquad \text{Eq. 3-14}$$

where D_b is the displacement at point b.

The displacements computed from Equation 3-14 are the displacements at the end of construction. The displacements calculated at the bottom and top of the wall ($H_b = 0$ and $H_b = H$, respectively) will be zero. Using Equation 3-14, the displacements at the end of construction for the top of each layer is shown in Table 3-3.

Table 3.3: Displacements at the end of construction calculated using Equation 3-14

Layer	Displacement at the end of construction (ft)
0	0
1	0.723
2	1.157
3	1.302
4	1.157
5	0.723
6	0

Procedure to adjust displacements output by Plaxis

A procedure was developed to convert the displacements output by Plaxis into the displacements at the end of construction. The displacements reported by Plaxis include the displacements due to the self-weight of the soil and the change in the vertical stress produced by overlying fill. Thus to find the calculated displacements at the end of construction from the displacements reported by Plaxis, the displacements resulting from the self-weight of the soil (e.g., S) in each layer must be subtracted from the displacements reported by Plaxis.

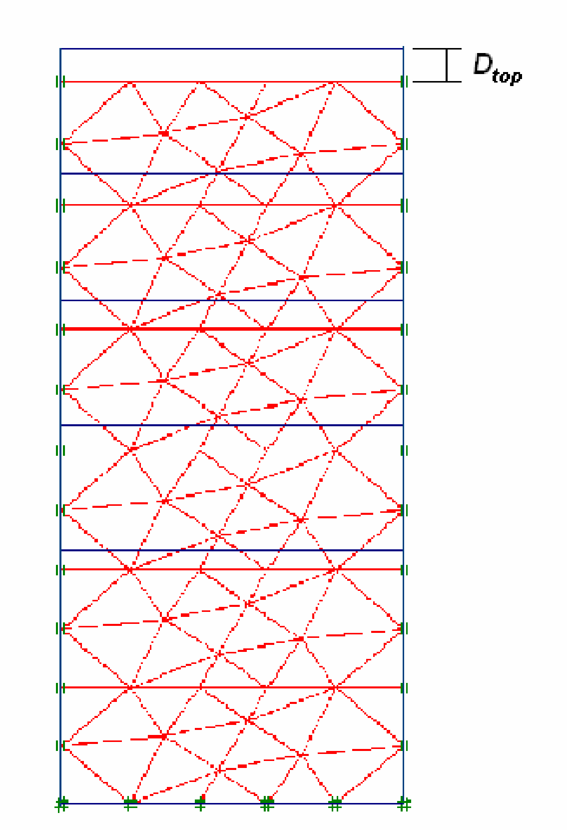

Figure 3.10: Displacement at the top surface of a column of soil (D_{top}) (Plaxis, 2005)

In Plaxis, the displacement at the top surface of the column of soil at the end of construction is given in the output phase and will be labeled D_{top} (Figure 3-10). Also, the displacement at the top surface of a layer after "i" stages can be recorded and will be labeled D_{si} (Figure 3-11). The difference between these two values(D_{top}-D_{si}) is the summation of four displacements: The displacement in the layers above the top of layer i are the result of the self-weight of the soil in each layer above layer i (1), and the surcharge on the layers above layer i (2). The displacements in layer i (3) are caused by the surcharge of all the layers on top of layer i. Finally, the displacement in the layers below the top of layer i (4) is caused by the surcharge of all the layers on top of layer i and can be expressed as (D_{top}-D_{si}). The compression of the layers above layer i (C_{top-i}) is found using Equation 3-10 where n is the number of layers above layer i, i.e., the total number of layers minus i. The quantity C_{top-i} represents the displacements in the layers above the top of layer i resulting from the self-weight of the soil in each layer and any other surcharge. When this quantity (C_{top-i}) is subtracted from the value of (D_{top}-D_{si}), the remainder (D_{top}-D_{si}-C_{top-i}) is the displacement at the top of layer i resulting only from the surcharge of all the layers on top of layer i.

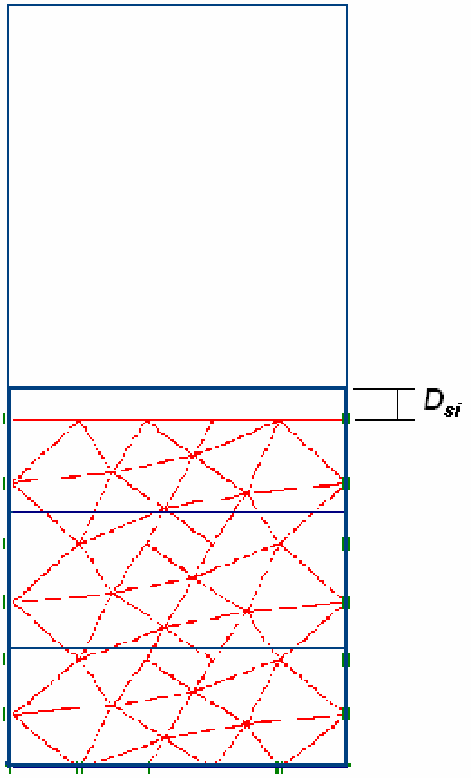

Figure 3.11: Displacement at the top of layer i (D_{si}) (Plaxis, 2005)

For example, consider the previous case where the fill was constructed in six layers, each 5 feet thick. The displacement at the end of construction at the mid-height of the column of soil (15 feet above the base of the wall) can be calculated as follows: The displacement at the top surface of the column of soil from Plaxis for the end of construction (D_{top}) was 2.6040 feet. The mid-height of the column of soil was reached after stage 3, as shown in Figure 3-12.

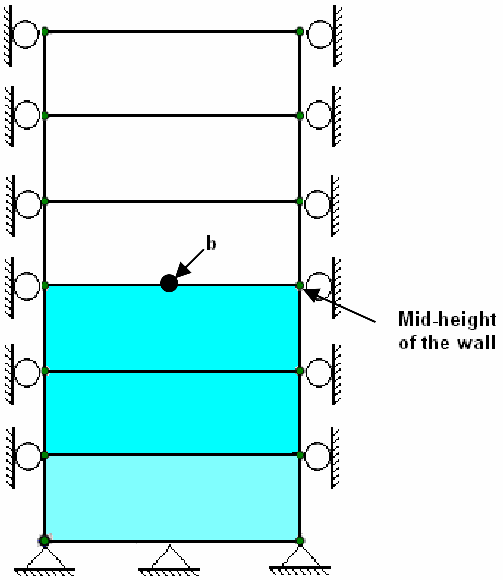

Figure 3.12: Illustration of the case when the soil is at the mid-height of the column of soil (Plaxis, 2005)

The displacement, D_{si}, reported by Plaxis at the end of stage 3 for the top of layer 3 (point b) was equal to 0.6510 feet. Values of "S" and "Q" were calculated using Equations 3-7 and 3-8, respectively, for a 5-foot thick layer having the soil properties listed in Table 3-1. The compression (S) of one layer caused by its self-weight was calculated from Equation 3-7 to be 0.0723 feet (0.87 inches). The compression of one layer caused by the surcharge applied to the top of the one layer (Q) was computed from Equation 3-8 to be 0.145 feet (1.73 inches). Then, the compression of the soil layers above the soil layer at the end of stage "i" was calculated using Equation 3-14. Three layers (labeled 4, 5, and 6 in Figure 3-12) of soil are between the top surface of the column of soil and the top surface of the layer placed at the end of stage 3. Thus, the value of C_{top-i} at the top of layer 3 is equal to the compression of layers 4, 5, and 6, calculated using Equation 3-14, i.e. C_{top-i} = 0.650 feet. Finally, the value of C_{top-i} is subtracted from the quantity D_{top} (2.6040 feet) - D_{si} (0.6510 feet) and the adjusted displacement is equal to 1.303 feet. This value agrees well with the displacement at the end of construction found using the constrained modulus at the mid-height of the wall (1.302 feet). The adjusted displacements are compared to the values calculated using the constrained modulus in Table 3-4. The maximum percent difference was less than three-tenths of one-percent, which indicates excellent agreement between the displacements calculated from the Plaxis output and the values calculated using Equation 3-14.

Table 3.4: Results for displacements at the end of construction converted from Plaxis output and calculated using Equation 3-14

	Adjusted Plaxis Displacements				Equation 3-14			
Layer	D_{top} (ft)	D_{si} (ft)	$C_{top\text{-}i}$ (ft)	Displacement at the end of construction (ft)	$\Delta\sigma_v$ (psf)	ε_{yy}	Displacement at the end of construction (ft)	**% difference**
0	2.604	0.0000	2.601	0.003	3900	0.174	0	N/A
1	2.604	0.0724	1.806	0.725	3250	0.145	0.723	0.286
2	2.604	0.2894	1.156	1.159	2600	0.116	1.157	0.131
3	2.604	0.6510	0.650	1.303	1950	0.087	1.302	0.078
4	2.604	1.1570	0.289	1.158	1300	0.058	1.157	0.084
5	2.604	1.8080	0.072	0.724	650	0.029	0.723	0.085
6	2.604	2.6040	0.000	0.000	0	0.000	0	N/A

3.3 Summary

For the simulations performed to model nondeformable retaining wall in Plaxis, the backfill was modeled using 15-node triangular elements with the mesh coarseness left at the default setting. The backfill-wall face and backfill-stable face interface interaction was modeled using 5-node interface elements. Staged construction was used to simulate the chronological construction of the nondeformable retaining walls. Finally, the computational scheme used in Plaxis to calculate the displacements at the top of a column of soil was illustrated and a procedure to adjust the displacements reported by Plaxis such that they correspond to displacements at the end of construction were presented.

Chapter 4. Soil-Wall Interaction

Two series of studies were performed with Plaxis to investigate soil-wall interaction. The goal of these studies was to determine the appropriate boundary conditions to use in Plaxis when modeling a nondeformable wall. Specifically, the studies were designed to understand how vertical displacements are affected by the boundary conditions, including the use of plate elements to model the wall face and the influence of the interface reduction factor, R_{inter}, which was described in Chapter 3. The studies were conducted using the linear elastic and Mohr-Coulomb constitutive models. The constitutive model for the behavior of interface elements is the same for the Mohr-Coulomb and Hardening-Soil models, additional simulations were not run using the Hardening-Soil constitutive model.

4.1 The effect of boundary conditions on vertical displacements, especially when plate elements were used to model the wall face

To model the wall face, two options were considered. One option was to assign a boundary condition such as the fixed horizontal-free vertical or total fixity boundary conditions discussed in Chapter 3 to the nodes at the wall face. The other option was to use plate elements to model the wall face and assign a boundary condition to the exposed (outside) surface of the plate elements. The following study was performed to determine which of the two options was more appropriate for modeling the face of a nondeformable wall.

In Plaxis, plates are structural elements used to model slender structures with flexural rigidity (or bending stiffness) and axial stiffness. The plate element in Plaxis is also referred to as a beam element. The element has both length and width and can react to both tensile and compressive stresses. The behavior of a plate is defined by the bending stiffness, EI, and the axial stiffness, EA. The 5-node plate elements used in this study are illustrated in Figure 4-1 When the plate is used in conjunction with interface elements, the interface and plate elements share common nodes as shown in Figure 4-2. The plate is represented by the dashed line in Figure 4-2. Plate elements are given an equivalent thickness based on the values of EA and EI.

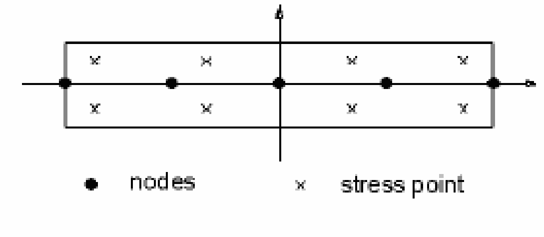

Figure 4.1: Distribution of nodes and stress points in a 5-node plate element

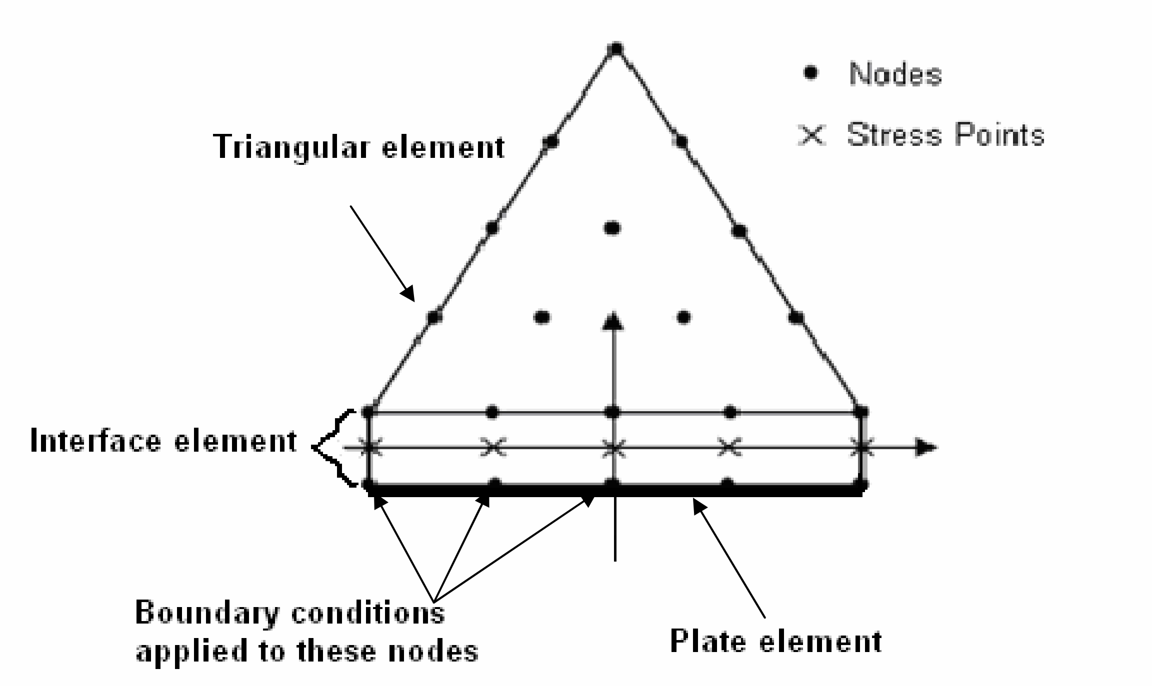

Figure 4.2: Connection of plate element to interface element (Plaxis, 2005)

For the purpose of this study, the properties of the plate were held constant for all simulations. The properties of the plate were selected to make the plate essentially rigid. The axial stiffness (EA) was 5 x 10^{10} kN/m and the bending stiffness (EI) was 1.67 x 10^{8} kN/m^{2}/m. Further information about properties of the plate will be presented in a separate report for this project.

Eight cases were analyzed to study the effect of boundary conditions on vertical displacements, particularly when plate elements were used to model the wall face. Each set of conditions for the plate, interface elements, and boundary conditions is referred to as a "Case." For example, Case 1 in Table 4-1 is the condition where there is no plate, no interface elements, and the fixed horizontal-free vertical fixity boundary condition applied to the wall face. All eight cases are described in Table 4-1.

Table 4.1: Description of cases used to study the effect of boundary conditions on vertical displacements, especially when plate elements were used to model the wall face.

Case No.	Plate Elements	Interface elements	Boundary condition at the wall face
1	No	No	Fixed Horizontal - Free Vertical
2	No	No	Total Fixity
3	No	Yes	Fixed Horizontal - Free Vertical
4	No	Yes	Total Fixity
5	Yes	No	Fixed Horizontal - Free Vertical
6	Yes	No	Total Fixity
7	Yes	Yes	Fixed Horizontal - Free Vertical
8	Yes	Yes	Total Fixity

The purpose of including plate elements in some simulations, but not others was to determine the effect of the plate on the vertical displacements. The purpose of including interface elements was to determine the influence of interface elements on displacements. The boundary conditions assigned to the wall face were systematically varied between fixed horizontal-free vertical and total fixity. The purpose of changing the boundary conditions was to determine the influence of boundary conditions on displacements.

The eight cases are illustrated schematically in Figures 4-3 through 4-10. An example of the model having no plate or interface elements and the fixed horizontal-free vertical boundary condition assigned to the wall face (Case 1) is shown in Figure 4-3. Two-dimensional triangular elements were used to model the backfill. Because soil-wall interaction was expected to be greatest for small aspect ratios, the width of the wall for these parametric studies was chosen to be narrow such that the wall aspect ratio was equal to 0.20, i.e., the wall is 10 m (32.8 feet) tall and 2 m (6.56 feet) wide. The full width of the wall is represented by a broken line in Figure 4-3. Taking advantage of symmetry, the width of the wall modeled in the actual finite element analyses was only one-half the full width, i.e., the finite element model was 1 m (3.28 feet) wide. The vertical axis of symmetry was modeled by assigning fixed horizontal-free vertical boundary conditions to the left side of the geometry in all the simulations. By assuming a vertical axis of symmetry exists at the centerline of the model wall, the displacements calculated by Plaxis on one side of the axis are assumed to be equivalent on the other side of the axis. Also, the soil-wall interaction between the wall face and backfill is assumed to be the same as the soil-wall interaction between the existing stable face and the backfill.

The face of the wall is located on the exposed right side of the wall in Figure 4-3 and the foundation is located at the bottom of the model wall. The total fixity boundary condition was assigned to the foundation in every case. The total fixity boundary condition in Figure 4-3 is indicated by a pin and the fixed horizontal-free vertical boundary condition is indicated by a roller. Point A was used as a reference point for calculations of vertical displacements. Point A is always located on the top of the backfill at the node nearest the wall face.

When no interface elements were included in the model, two-dimensional triangular elements were distributed evenly and uniformly throughout the backfill as exhibited in Figure 4-3. However, when interface elements are included, the two-dimensional triangular elements are skewed toward the face of the wall because additional rectangular elements were created, e.g., Figure 4-5. The distribution of the triangular and rectangular interface elements was not affected further when plate elements were introduced to model the wall face.

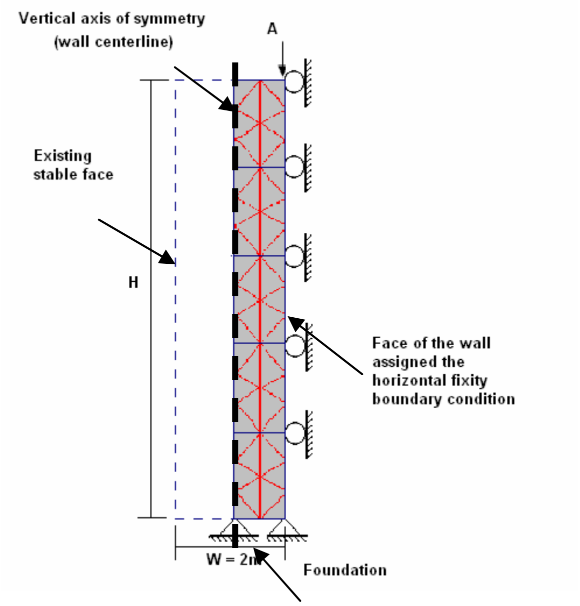

Figure 4.3: Example of model having no plate, no interface, and the total fixity boundary condition assigned to the nodes at the wall face (case 1) (Plaxis, 2005)

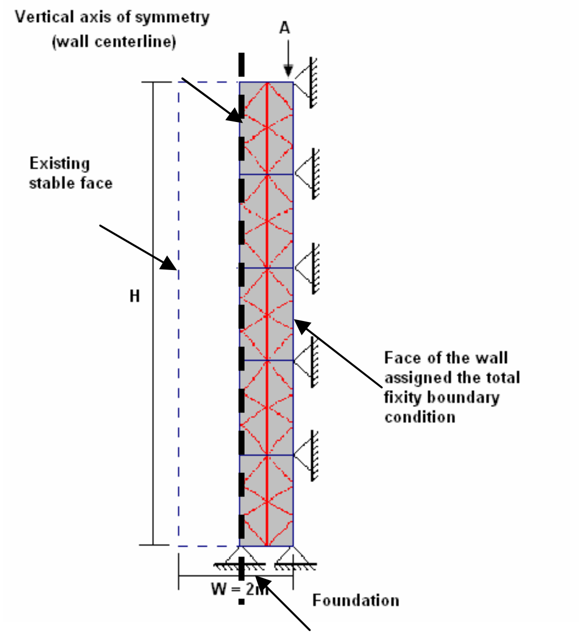

Figure 4.4: Example of model having no plate, no interface, and the total fixity boundary condition assigned to the nodes at the wall face (case 2) (Plaxis, 2005)

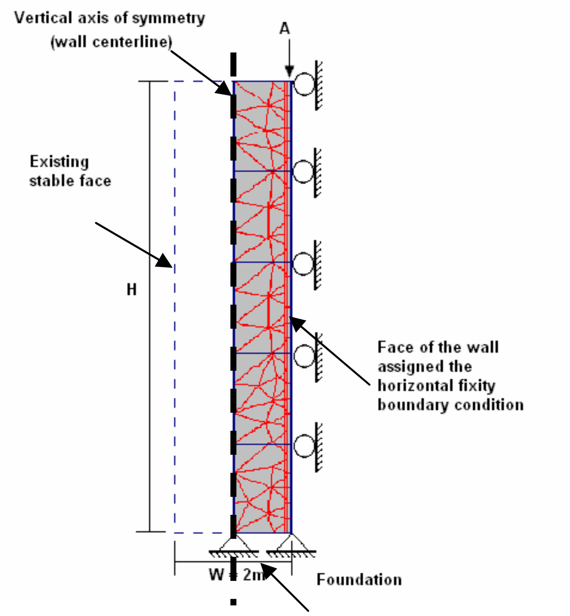

Figure 4.5: Example of model having no plate, an interface, and the horizontal fixity boundary condition assigned to the nodes at the wall face (case 3) (Plaxis, 2005)

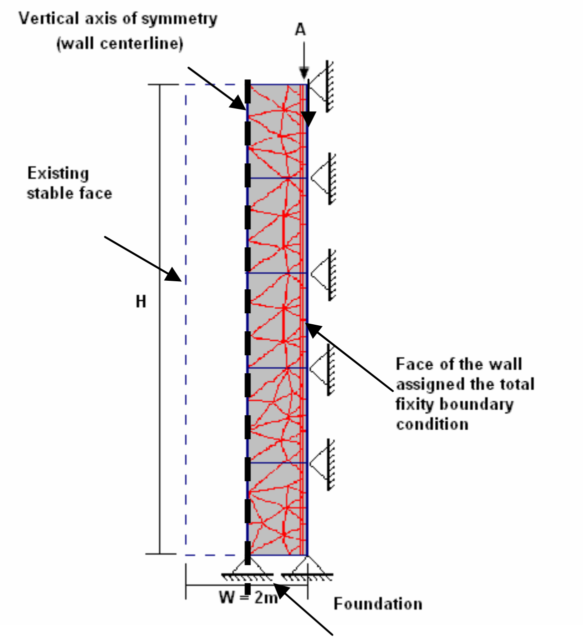

Figure 4.6: Example of model having no plate, an interface, and the total fixity boundary condition assigned to the nodes at the wall face (case 4) (Plaxis, 2005)

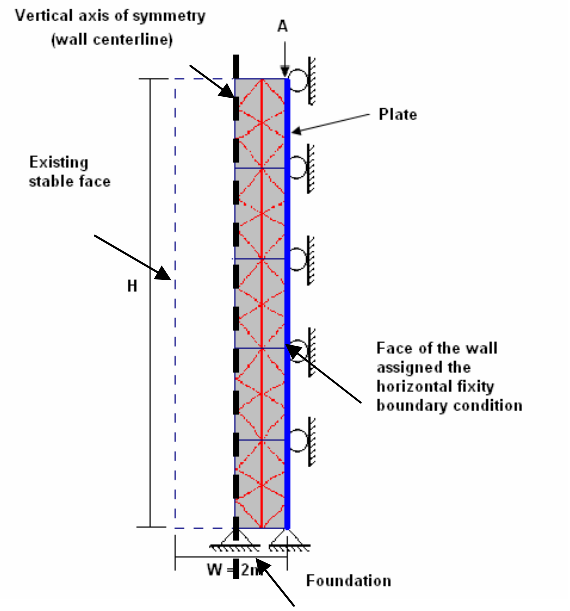

Figure 4.7: Example of model having a plate, no interface, and the horizontal fixity boundary condition assigned to the nodes at the wall face (case 5) (Plaxis, 2005)

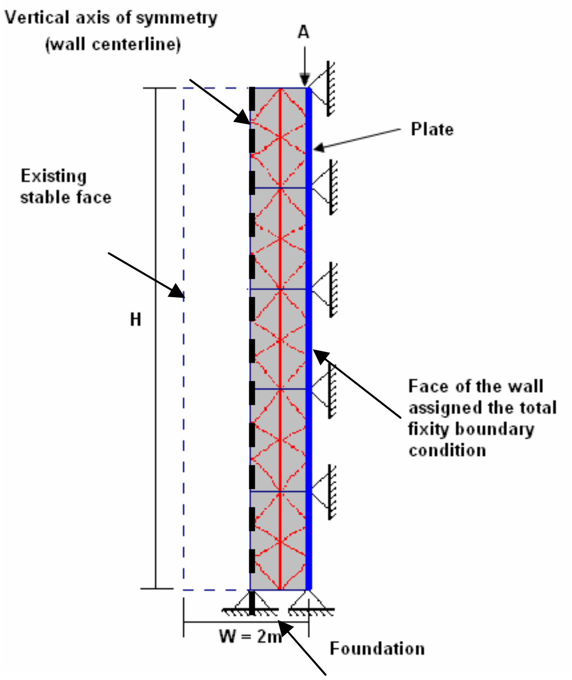

Figure 4.8: Example of model having a plate, no interface, and the total fixity boundary condition assigned to the nodes at the wall face (case 6) (Plaxis, 2005)

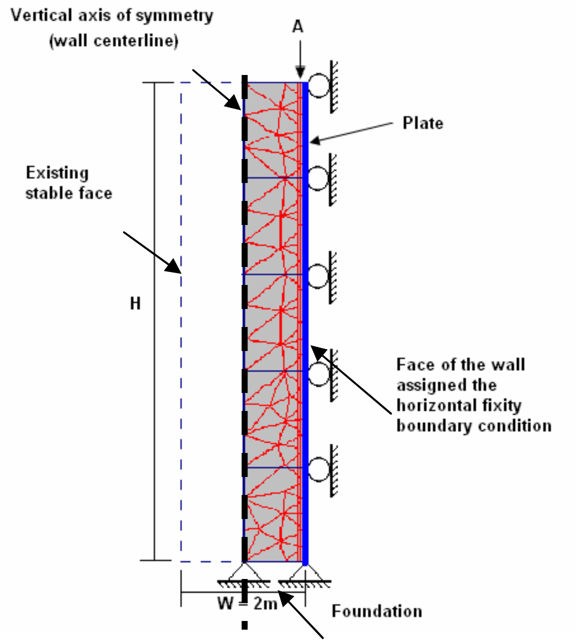

Figure 4.9: Example of model having a plate, an interface, and the horizontal fixity boundary condition assigned to the nodes at the wall face (case 7) (Plaxis, 2005)

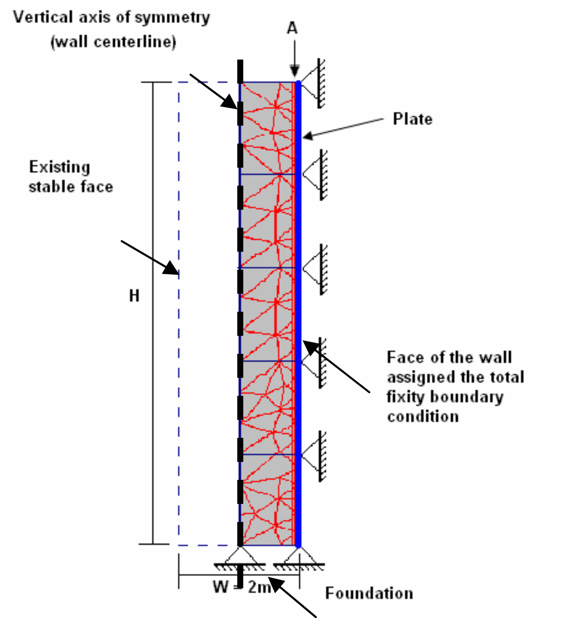

Figure 4.10: Example of model having a plate, an interface, and the total fixity boundary condition assigned to the nodes at the wall face (case 8) (Plaxis, 2005)

Displacements were calculated for each of the eight cases described in Table 4-1 using both the linear elastic and Mohr-Coulomb soil constitutive models. The properties of the backfill selected for each model are summarized in Table 4-2. The interface reduction factor (R_{inter}) was assigned a value of 1.00 in the study implying that the soil in the interface elements had the same shear strength as the rest of the soil. Sixteen analyses were performed (eight linear elastic and eight Mohr-Coulomb). The cases assigned for each model are displayed in Table 4-3.

Table 4.2: Soil properties for study of soil-wall interaction

Linear Elastic Model	
Property	Value
E (kPa)	10000
ν	0.25
γ (kN/m^3)	14
R_{inter}	1

Mohr-Coulomb Model	
Property	Value
E (kPa)	10000
ν	0.25
γ (kN/m^3)	14
ϕ (deg)	30
c (kPa)	0.2
R_{inter}	1

Table 4.3: Assignments for cases in the study of the effect of plates on vertical displacements

Linear Elastic Model				
Case No.	**Plate Elements**	**Interface elements**	**Model**	**Boundary condition at the wall face**
1	No	No	Figure 4-3	Fixed Horizontal - Free Vertical
2	No	No	Figure 4-4	Total Fixity
3	No	Yes	Figure 4-5	Fixed Horizontal - Free Vertical
4	No	Yes	Figure 4-6	Total Fixity
5	Yes	No	Figure 4-7	Fixed Horizontal - Free Vertical
6	Yes	No	Figure 4-8	Total Fixity
7	Yes	Yes	Figure 4-9	Fixed Horizontal - Free Vertical
8	Yes	Yes	Figure 4-10	Total Fixity

Mohr-Coulomb Model				
Case No.	**Plate Elements**	**Interface elements**	**Model**	**Boundary condition at the wall face**
1	No	No	Figure 4-3	Fixed Horizontal - Free Vertical
2	No	No	Figure 4-4	Total Fixity
3	No	Yes	Figure 4-5	Fixed Horizontal - Free Vertical
4	No	Yes	Figure 4-6	Total Fixity
5	Yes	No	Figure 4-7	Fixed Horizontal - Free Vertical
6	Yes	No	Figure 4-8	Total Fixity
7	Yes	Yes	Figure 4-9	Fixed Horizontal - Free Vertical
8	Yes	Yes	Figure 4-10	Total Fixity

4.1.2 Results and discussion from study of boundary conditions, especially when the plate was used to model the wall face

Vertical displacements at point A are summarized in Table 4-4 for both the linear elastic and Mohr-Coulomb models. The results presented in Table 4-4 are discussed separately for the linear elastic and Mohr-Coulomb models in the next sections. The effects of interface elements, plate elements, and boundary conditions on displacements are all addressed.

Table 4.4: Vertical displacements from study of boundary conditions at Point A

Linear Elastic Model					
Case No.	**Plate Elements**	**Interface elements**	**Model**	**Boundary condition at the wall face**	**Displacement at A (m)**
1	No	No	Figure 4-3	Fixed Horizontal - Free Vertical	0.058
2	No	No	Figure 4-4	Total Fixity	0.002
3	No	Yes	Figure 4-5	Fixed Horizontal - Free Vertical	0.058
4	No	Yes	Figure 4-6	Total Fixity	0.002
5	Yes	No	Figure 4-7	Fixed Horizontal - Free Vertical	0.003
6	Yes	No	Figure 4-8	Total Fixity	0.002
7	Yes	Yes	Figure 4-9	Fixed Horizontal - Free Vertical	0.003
8	Yes	Yes	Figure 4-10	Total Fixity	0.002

Mohr-Coulomb Model					
Case No.	**Plate Elements**	**Interface elements**	**Model**	**Boundary condition at the wall face**	**Displacement at A (m)**
1	No	No	Figure 4-3	Fixed Horizontal - Free Vertical	0.058
2	No	No	Figure 4-4	Total Fixity	0.000
3	No	Yes	Figure 4-5	Fixed Horizontal - Free Vertical	0.059
4	No	Yes	Figure 4-6	Total Fixity	0.001
5	Yes	No	Figure 4-7	Fixed Horizontal - Free Vertical	0.000
6	Yes	No	Figure 4-8	Total Fixity	--
7	Yes	Yes	Figure 4-9	Fixed Horizontal - Free Vertical	0.003
8	Yes	Yes	Figure 4-10	Total Fixity	0.003

4.1.3 Linear elastic model

The results shown in Table 4-4 for the linear elastic model demonstrate that the interface elements had no effect on the vertical displacements for Cases 1 through 8. The lack of effect of interface elements on the vertical displacements in the linear elastic model can be seen more clearly in Table 4-5, where the cases are grouped by similar pairs with and without interface elements. The reason the interface elements had no effect in the linear elastic model is because the linear elastic model does not allow for plastic deformations. Because the stress applied to the elements, both triangular and interface, was the same for every case, all the elements experienced the same deformations.

Table 4.5: Vertical displacements from study of boundary conditions at Point A arranged by boundary condition assigned to the wall face

Linear Elastic Model					
Case No.	**Plate Elements**	**Interface elements**	**Model**	**Boundary condition at the wall face**	**Displacement at A (m)**
1	No	No	Figure 4-3	Fixed Horizontal - Free Vertical	0.058
3	No	Yes	Figure 4-5	Fixed Horizontal - Free Vertical	0.058
5	Yes	No	Figure 4-7	Fixed Horizontal - Free Vertical	0.003
7	Yes	Yes	Figure 4-9	Fixed Horizontal - Free Vertical	0.003
2	No	No	Figure 4-4	Total Fixity	0.002
4	No	Yes	Figure 4-6	Total Fixity	0.002
6	Yes	No	Figure 4-8	Total Fixity	0.002
8	Yes	Yes	Figure 4-10	Total Fixity	0.002

When the assigned boundary condition at the wall face is total fixity (Cases 2, 4, 6 and 8), the vertical displacements are identical. However, when the fixed horizontal-free vertical boundary condition is assigned (Cases 1, 3, 5 and 7), the plate elements have a large impact on the vertical displacements. The presence of the plate severely restricts vertical displacements.

The results for the eight cases are rearranged in Table 4-6 according to whether or not a plate element was used to model the wall face. When the wall face is modeled as an exposed surface with no plate (Cases 1-4), the magnitudes of the vertical displacements are very different and depend on the boundary condition assigned to the nodes at the exposed wall face. However, when a plate is introduced to model the wall face (Cases 5-8), the magnitudes of the vertical displacements are similar because the displacements are controlled largely by the stiffness of the plate. The displacements for the cases with a plate in which fixed horizontal-free vertical was assigned at the wall face (Cases 5 and 7) are probably higher than the cases with a plate in which total fixity was assigned at the wall face (Cases 6 and 8) because of the weight of the soil pulling downward on the shared common nodes between the soil (triangular or interface) and the plate elements.

Table 4.6: Vertical displacements from study of boundary conditions at Point A arranged by how the wall face was modeled

Linear Elastic Model					
Case No.	**Plate Elements**	**Interface elements**	**Model**	**Boundary condition at the wall face**	**Displacement at A (m)**
1	No	No	Figure 4-3	Fixed Horizontal - Free Vertical	0.058
3	No	Yes	Figure 4-5	Fixed Horizontal - Free Vertical	0.058
2	No	No	Figure 4-4	Total Fixity	0.002
4	No	Yes	Figure 4-6	Total Fixity	0.002
5	Yes	No	Figure 4-7	Fixed Horizontal - Free Vertical	0.003
7	Yes	Yes	Figure 4-9	Fixed Horizontal - Free Vertical	0.003
6	Yes	No	Figure 4-8	Total Fixity	0.002
8	Yes	Yes	Figure 4-10	Total Fixity	0.002

4.1.4 Mohr-Coulomb model

For the analyses with the Mohr-Coulomb model (Table 4-4), the interface elements had very little effect on the vertical displacements, particularly when the displacements were significant (Cases 1 and 3). The effect of interface elements on the vertical displacements in the Mohr-Coulomb model can be seen more clearly in Table 4-7. In one case, Case 6, Plaxis failed to run successfully, and the reason could not be determined. Repeated attempts to discover the problem and successfully run the simulation failed

Table 4.7: Vertical displacements from study of boundary conditions at Point A arranged by boundary condition assigned to the wall face

Mohr-Coulomb Model					
Case No.	**Plate Elements**	**Interface elements**	**Model**	**Boundary condition at the wall face**	**Displacement at A (m)**
1	No	No	Figure 4-3	Fixed Horizontal - Free Vertical	0.058
3	No	Yes	Figure 4-5	Fixed Horizontal - Free Vertical	0.059
5	No	No	Figure 4-4	Total Fixity	0.000
7	No	Yes	Figure 4-6	Total Fixity	0.001
2	Yes	No	Figure 4-7	Fixed Horizontal - Free Vertical	0.000
4	Yes	Yes	Figure 4-9	Fixed Horizontal - Free Vertical	0.003
6	Yes	No	Figure 4-8	Total Fixity	--
8	Yes	Yes	Figure 4-10	Total Fixity	0.003

In three pairs of Cases (1 and 3), (2 and 4), and (5 and 7), the vertical displacements compare favorably. The use of plate elements to model the wall face and the boundary conditions assigned to the wall face are also in agreement in each pair of cases. Apparently, the reason the interface elements had very little effect in the analyses with the Mohr-Coulomb model is that the interface reduction factor (R_{inter}) was 1.00, which gave the interface elements the maximum possible strength, i.e., the same strength as the backfill. As a result, the increase in displacements when interface elements are included is relatively small.

When the assigned boundary condition at the exposed wall face was total fixity (Cases 2, 4 and 8), the vertical displacements agreed favorably. However, when fixed horizontal-free vertical is the assigned boundary condition at the wall face (Cases 1, 3, 5, and 7), the plate elements had a large impact on the displacements.

The cases are arranged in Table 4-8 according to whether a plate element was introduced to model the wall face. When a plate was not used to model the wall facing (Cases 1-4), the magnitudes of the vertical displacements depend on the boundary condition assigned at the wall face. However, when a plate was used to model the wall face, the magnitudes of the vertical displacements are nearly identical or very small.

Table 4.8: Vertical displacements from study of boundary conditions at Point A arranged by how the wall face was modeled

Mohr-Coulomb Model					
Case No.	**Plate Elements**	**Interface elements**	**Model**	**Boundary condition at the wall face**	**Displacement at A (m)**
1	No	No	Figure 4-3	Fixed Horizontal - Free Vertical	0.058
3	No	Yes	Figure 4-5	Fixed Horizontal - Free Vertical	0.059
2	No	No	Figure 4-4	Total Fixity	0.000
4	No	Yes	Figure 4-6	Total Fixity	0.001
5	Yes	No	Figure 4-7	Fixed Horizontal - Free Vertical	0.000
7	Yes	Yes	Figure 4-9	Fixed Horizontal - Free Vertical	0.003
6	Yes	No	Figure 4-8	Total Fixity	--
8	Yes	Yes	Figure 4-10	Total Fixity	0.003

4.1.5 Conclusions from study of boundary conditions especially when the plate was used to model the wall face

Modeling a nondeformable wall using plate elements had a similar effect as using a total fixity boundary condition along the wall face because both the plate and the total fixity boundary condition constrain the movement of the nodes at the wall face. Thus, to model a nondeformable wall, a total fixity boundary condition can be selected instead of including additional plate elements to simulate the wall facing.

4.2 The effect of the interface reduction factor on vertical displacements

To determine the effect of the interface reduction factor (R_{inter}) on vertical displacements, a second study was conducted. Interface elements were used to model the interaction between the soil and wall face in all cases. The geometry and soil properties used in the second study were the same as those used for the study described in the previous section. The boundary conditions on the wall face were systematically varied between fixed horizontal-free vertical and total fixity. Table 4-9 shows how the interface reduction factors and boundary conditions were assigned for each simulation. Each combination of interface reduction factors and boundary conditions is referred to as a “Case.” For example, Case 1 in Table 4-9 corresponds to an interface reduction factor equal to 0.010 and a total fixity boundary condition

The maximum value of the interface reduction factor selected was 1.00 because that represents the maximum strength that an interface can have. The minimum value chosen for R_{inter} was 0.010 which is the minimum value Plaxis would accept for the interface reduction factor. Other values selected for the study were 0.100, 0.400, and 0.700.

Table 4.9: Variable assignments for cases in the study of the effect of interface reduction factor on vertical displacement

Linear Elastic Model		
Case No.	**Interface Reduction Factor**	**Boundary condition at the wall face**
1	0.010	Total Fixity
2	0.100	Total Fixity
3	0.400	Total Fixity
4	0.700	Total Fixity
5	1.000	Total Fixity
6	0.010	Fixed Horizontal - Free Vertical
7	0.100	Fixed Horizontal - Free Vertical
8	0.400	Fixed Horizontal - Free Vertical
9	0.700	Fixed Horizontal - Free Vertical
10	1.000	Fixed Horizontal - Free Vertical

Mohr-Coulomb Model		
Case No.	**Interface Reduction Factor**	**Boundary condition at the wall face**
1	0.010	Total Fixity
2	0.100	Total Fixity
3	0.400	Total Fixity
4	0.700	Total Fixity
5	1.000	Total Fixity
6	0.010	Fixed Horizontal - Free Vertical
7	0.100	Fixed Horizontal - Free Vertical
8	0.400	Fixed Horizontal - Free Vertical
9	0.700	Fixed Horizontal - Free Vertical
10	1.000	Fixed Horizontal - Free Vertical

4.2.2 Results from study of interface reduction factors

The vertical displacements calculated at point A, the values of the interface reduction factors, and the boundary conditions for each case are summarized in Table 4-10. The variation in vertical displacements calculated at point A with interface reduction factor, R_{inter}, are shown in Figures 4-11 and 4-12 for the linear elastic and Mohr-Coulomb models, respectively.

Table 4.10: Vertical displacements calculated at point A for study of the effect of the interface reduction factor (R_{inter})

Linear Elastic Model			
Case No.	**Interface Reduction Factor**	**Boundary condition at the wall face**	**Displacement at A (m)**
1	0.010	Total Fixity	0.063
2	0.100	Total Fixity	0.016
3	0.400	Total Fixity	0.001
4	0.700	Total Fixity	0.000
5	1.000	Total Fixity	0.000
6	0.010	Fixed Horizontal - Free Vertical	0.065
7	0.100	Fixed Horizontal - Free Vertical	0.062
8	0.400	Fixed Horizontal - Free Vertical	0.059
9	0.700	Fixed Horizontal - Free Vertical	0.058
10	1.000	Fixed Horizontal - Free Vertical	0.058

Mohr-Coulomb Model			
Case No.	**Interface Reduction Factor**	**Boundary condition at the wall face**	**Displacement at A (m)**
1	0.010	Total Fixity	--
2	0.100	Total Fixity	0.072
3	0.400	Total Fixity	0.014
4	0.700	Total Fixity	0.005
5	1.000	Total Fixity	0.001
6	0.010	Fixed Horizontal - Free Vertical	--
7	0.100	Fixed Horizontal - Free Vertical	0.092
8	0.400	Fixed Horizontal - Free Vertical	0.060
9	0.700	Fixed Horizontal - Free Vertical	0.059
10	1.000	Fixed Horizontal - Free Vertical	0.059

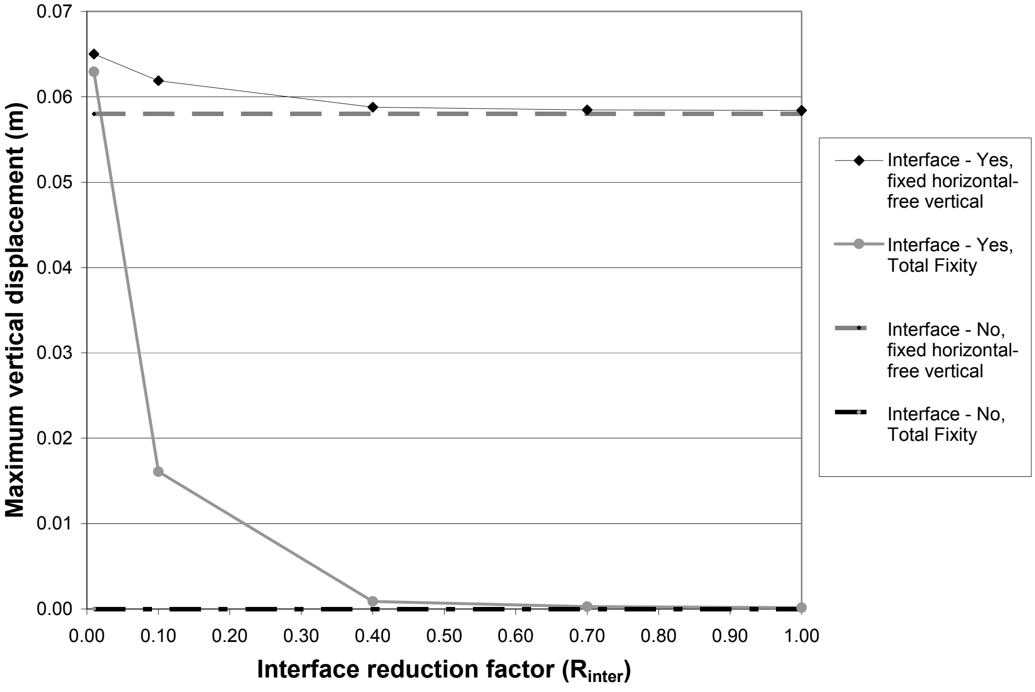

Figure 4.11: Vertical displacements at point A for the linear elastic model

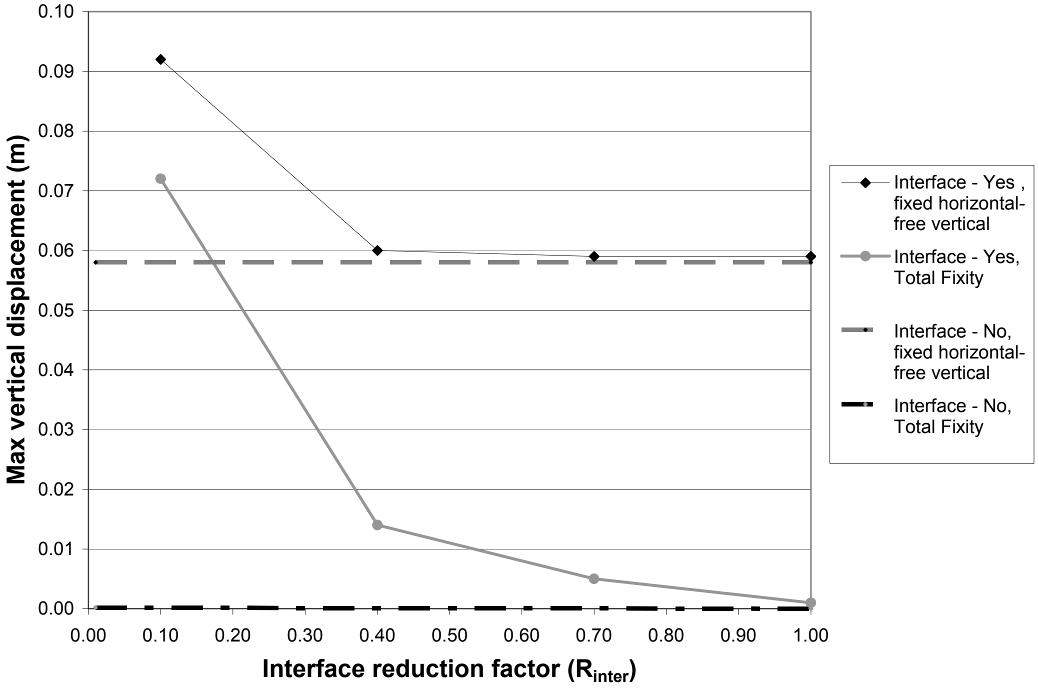

Figure 4.12: Vertical displacements at point A for the Mohr-Coulomb model

4.2.3 Discussion of results from study of interface reduction factor

The vertical displacements calculated at point A with the linear elastic model for cases with the total fixity of nodes at the wall face (Cases 1 through 5) increase as the interface reduction factor decreased. As the interface reduction factor decreased, the strength and stiffness of the interface also decreased. Thus the displacements increased as shown in Table 4-11. The same behavior was observed for Cases 1 through 5 with the Mohr-Coulomb model. In case 1, the interface reduction factor was equal to 0.010 and the simulation failed to run successfully because the interface was too weak.

Table 4.11: Vertical displacement at point A calculated for Cases 1-5 with the linear elastic and Mohr-Coulomb models

Case No.	Interface Reduction Factor	Constitutive model	Boundary condition at the wall face	Displacement at A (m)
1	0.010	linear elastic	Total Fixity	0.063
2	0.100	linear elastic	Total Fixity	0.016
3	0.400	linear elastic	Total Fixity	0.001
4	0.700	linear elastic	Total Fixity	0.000
5	1.000	linear elastic	Total Fixity	0.000
1	0.010	Mohr-Coulomb	Total Fixity	--
2	0.100	Mohr-Coulomb	Total Fixity	0.072
3	0.400	Mohr-Coulomb	Total Fixity	0.014
4	0.700	Mohr-Coulomb	Total Fixity	0.005
5	1.000	Mohr-Coulomb	Total Fixity	0.001

The interface reduction factor (R_{inter}) had a negligible effect on the vertical displacement calculated at point A by both constitutive models for the cases with the fixed horizontal-free vertical boundary condition assigned at the wall face (cases 6 through 10) except when the value of R_{inter} became less than 0.100 (Table 4-12). In case 6 with the Mohr-Coulomb model and R_{inter}

= 0.010, the simulation failed to run successfully apparently because the interface strength was too low.

Table 4.12: Vertical displacement at point A for cases 6-10 with the linear elastic and Mohr-Coulomb models

Case No.	Interface Reduction Factor	Constitutive model	Boundary condition at the wall face	Displacement at A (m)
6	0.010	linear elastic	Fixed Horizontal - Free Vertical	0.065
7	0.100	linear elastic	Fixed Horizontal - Free Vertical	0.062
8	0.400	linear elastic	Fixed Horizontal - Free Vertical	0.059
9	0.700	linear elastic	Fixed Horizontal - Free Vertical	0.058
10	1.000	linear elastic	Fixed Horizontal - Free Vertical	0.058
6	0.010	Mohr-Coulomb	Fixed Horizontal - Free Vertical	--
7	0.100	Mohr-Coulomb	Fixed Horizontal - Free Vertical	0.092
8	0.400	Mohr-Coulomb	Fixed Horizontal - Free Vertical	0.060
9	0.700	Mohr-Coulomb	Fixed Horizontal - Free Vertical	0.059
10	1.000	Mohr-Coulomb	Fixed Horizontal - Free Vertical	0.059

With the Mohr-Coulomb model, as the strength of the interface was reduced, the stresses in more of the interface elements exceed the yield stress and plastic deformations increased. According to Tables 4-11 and 4-12, when the value of R_{inter} is less than 0.100 (case 6 with the Mohr-Coulomb model) the plastic deformations increase quickly. As explained in Section 4.1.1.1, the linear elastic model does not allow for plastic deformations, however, the resistance of the interface is still controlled in part by the value of the interface reduction factor as described in the following section.

4.2.4 Linear elastic soil-wall interaction

In the linear elastic model the vertical and horizontal stiffness of the interface elements are decreased as a function of the interface reduction factor, R_{inter}. When the interface reduction factor is reduced, the soil can actually move into the wall, thus yielding an unrealistic pattern of displacements as shown in Figure 4-13.

For elastic interface elements, the displacements are calculated using values for the one-dimensional compression modulus and shear modulus as follows:

$$E_{oed,i} = 2 * G_i \left(\frac{1-\nu_i}{1-2\nu_i} \right) \qquad \text{Eq. 4-1}$$

$$G_i = R^2_{\text{inter}} G_{soil} \le G_{soil} \qquad \text{Eq. 4-2}$$

where: $E_{oed,I}$ is the one-dimensional compression modulus, G_i is the shear modulus of the interface, and ν_i is Poisson's ratio of the interface ($\nu_i = 0.45$), and the displacements are calculated both perpendicular (gap displacement) and parallel (slip displacement) to the interface. Accordingly,

$$\text{elastic gap displacement} = \frac{\sigma * t_i}{E_{oed,i}} \qquad \text{Eq. 4-3}$$

and,

$$\text{elastic slip displacement} = \frac{\tau * t_i}{G_i} \qquad \text{Eq. 4-4}$$

where t_i is the virtual thickness of the interface. These equations also apply for other soil constitutive models when the interface element is elastic. As seen in Equations 4-3 and 4-4, Plaxis calculates the elastic interface displacements based on the stress in the element. For low values of the interface reduction factor (R_{inter}), both shear and normal stiffness become small. In Figure 4-13, the thin grey lines represent the initial position of the elements, the solid black lines represent the final position of the elements, and the thick dashed black lines represent the wall face and existing stable face. Because the horizontal fixity is only applied to the nodal points at the wall face, only those points are fixed. As a result, when the interface reduction factor is very low, the other nodes are free to move beyond the boundary.

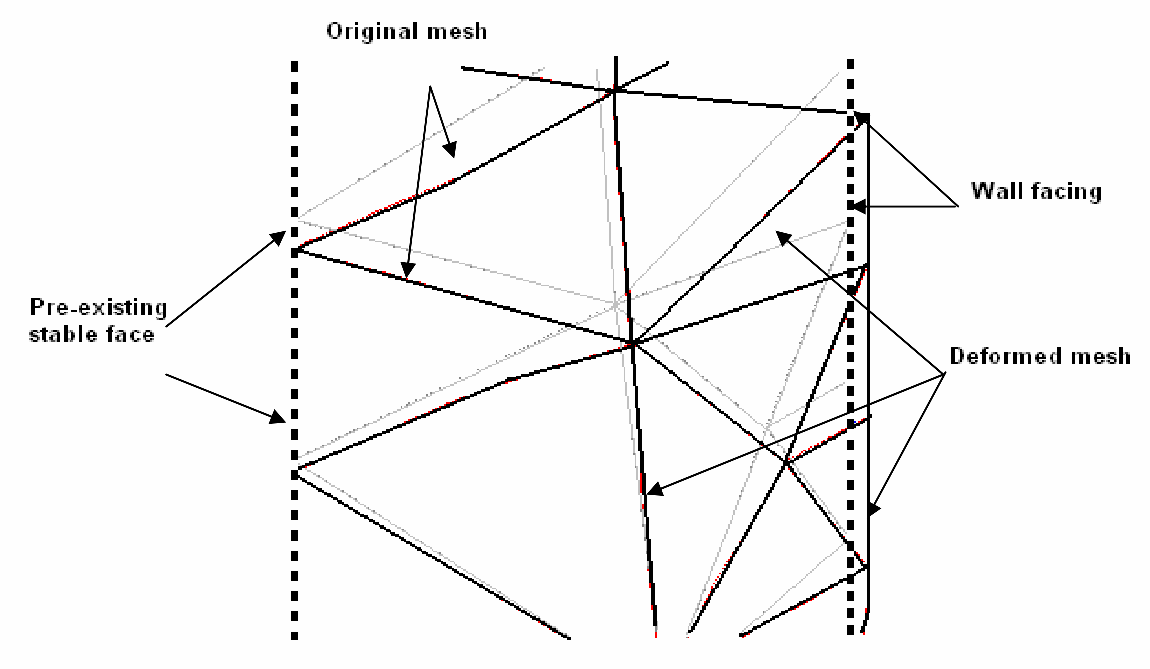

Figure 4.13: Deformed mesh showing movement of the soil through the boundary of the wall (Plaxis, 2005)

4.2.5 Conclusions from study of interface reduction factor

The interface reduction factor should be chosen carefully due to the dramatic effect on displacements from small changes in its value. Furthermore, if the values of R_{inter} are less than or equal to 0.100 the displacements can increase severely and may become unrealistic because the strength or stiffness of the interface elements is unreasonably low.

4.3 Conclusions on soil-wall interaction

Based on the studies performed in this chapter, an appropriate way to model the soil wall interaction is to place interface elements at the wall face and assign a total fixity boundary condition to the nodes at the wall face. This model was adopted for further study and is shown in Figure 4-14. Also, values of the interface reduction factor (R_{inter}) less than 0.100 will not be used because they may cause an unrealistic pattern of displacements.

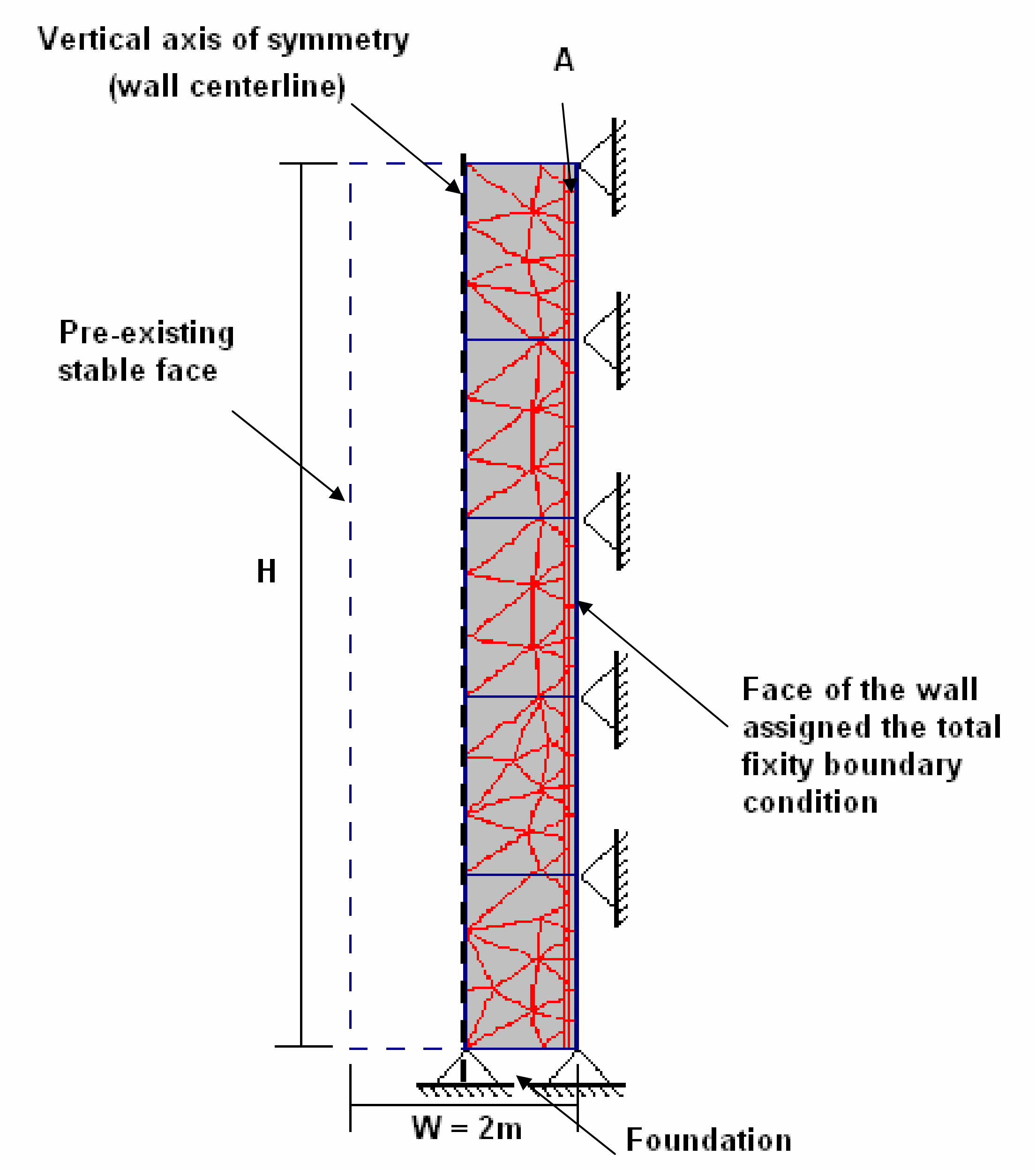

Figure 4.14: Adopted model for future finite element simulations having interface elements and the total fixity boundary condition assigned to the face of the wall (Plaxis, 2005)

Chapter 5. Comparisons of Earth Pressures Calculated by Plaxis to Measured Earth Pressures from Centrifuge Tests and to Computed Values Using Spangler and Handy's Equation

Centrifuge tests were performed by Frydman and Keissar (1987) and Take and Valsangkar (2001) to measure the horizontal earth pressures behind nondeformable retaining walls. To verify that the Plaxis finite element software could reliably predict the horizontal earth pressures behind nondeformable retaining walls, finite element simulations were performed to model these centrifuge tests. Results of the finite element analyses were then compared to values based on measurements from the centrifuge tests. Horizontal earth pressure coefficients calculated by Plaxis were also compared to values calculated using Spangler and Handy's equation described in Section 2.4.2.

5.1 Experimental Test Data

The first set of test data used for comparison was from centrifuge tests performed by Frydman and Keissar (1987). They conducted a series of centrifuge tests to investigate the earth pressures on retaining walls near stable faces. The models were built in an aluminum box in a space 210 mm high x 100 mm wide x 327 mm long. Each model included a rigid aluminum plate (195 mm high x 100 mm wide x 20 mm thick) fixed to the base of the box. The stable face was modeled by a wooden block coated with the backfill material, so that the friction between the stable face and backfill was essentially equal to the angle of internal friction of the backfill. A schematic of the cross-section of the model is shown in Figure 5-1. The height of the sand backfill was equal to the height of the aluminum plate or 195 mm. The width of the sand backfill was varied to determine the effect of wall aspect ratio on the measured horizontal earth pressures. Load cells were inset flush with the wall at one-third and two-thirds the height of the wall below the top of the backfill, i.e. z = 0.33H and 0.67H.

The granular fill was described as Haifa Bay uniform fine sand with particle sizes ranging from 0.10 to 0.30 mm and a minimum and maximum dry unit weight of approximately 14.0 and 16.4 kN/m^3, respectively. The sand was placed at a relative density of approximately 70 percent which corresponds to a dry density of approximately 15.6 kN/m^3. Direct shear tests were performed on the sand at this relative density gave an angle of internal friction (ϕ') of approximately 36°. Also, direct shear tests were performed on the interface between the sand and aluminum to determine the angle of interface friction (δ). The angle of interface friction (δ) ranged from approximately 20° to 25°.

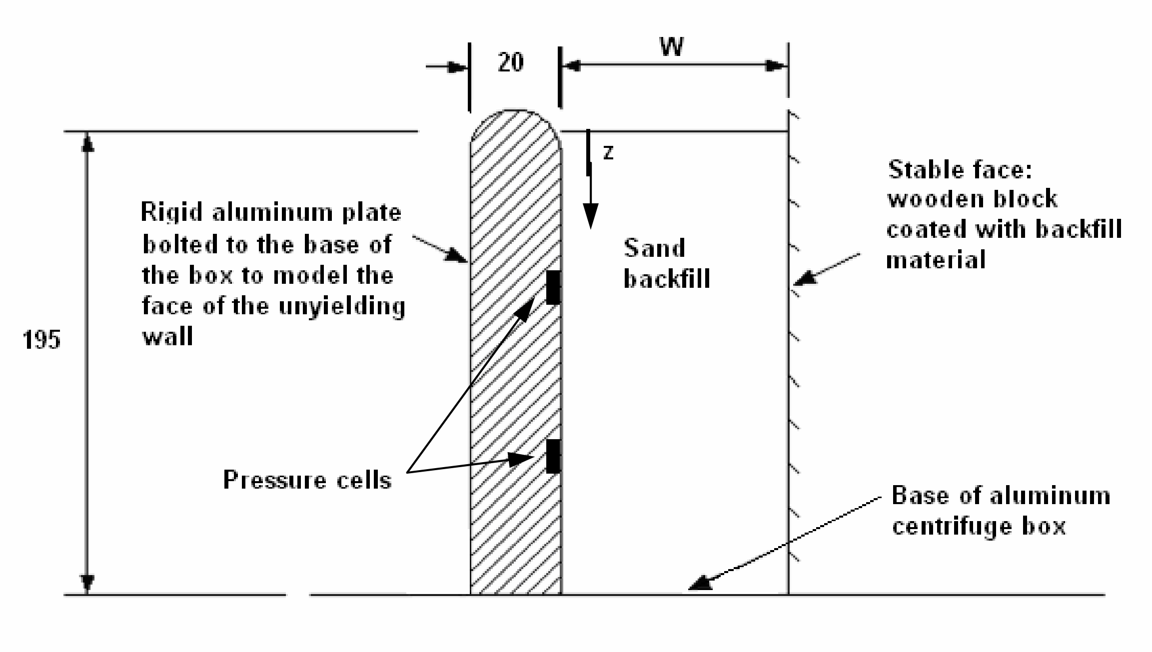

Figure 5.1: Schematic of cross-section of the model wall used in centrifuge tests conducted by Frydman and Keissar.

The second set of data was from centrifuge tests performed by Take and Valsangkar in 2001. The models were built in an aluminum box in a space 150 mm high x 200 mm wide x 254 mm long. To model the stable face a rigid aluminum plate (150 mm high x 254 mm long x 16 mm thick) was bolted (fixed) to the base of the box. The height of the backfill in these tests was 140 mm high, and the backfill had various widths corresponding to wall aspect ratios (W/H) ranging from 0.10 to 1.31. A schematic of the aluminum box is shown in Figure 5-2. Six pressure cells were distributed evenly over the height of the model retaining wall as illustrated in Figure 5-2.

The backfill material was classified as poorly graded sand with little or no fines. The mean particle size of the backfill was 0.4 mm. The backfill was compacted to dry unit weights of 13.4 and 16.2 kN/m^3, corresponding to relative densities of approximately 34 and 79 percent, respectively. A series of direct shear tests was performed to determine the peak angle of internal friction (ϕ'_p) and the peak interface friction angle (δ_p) with aluminum. For a relative density of 34 percent, the peak angle of internal friction was 30°. The peak friction angle for the soil-aluminum interface was approximately 23°. For a relative density of 79 percent, the peak angle of internal friction was 36°, and the peak interface friction angle was approximately 25°.

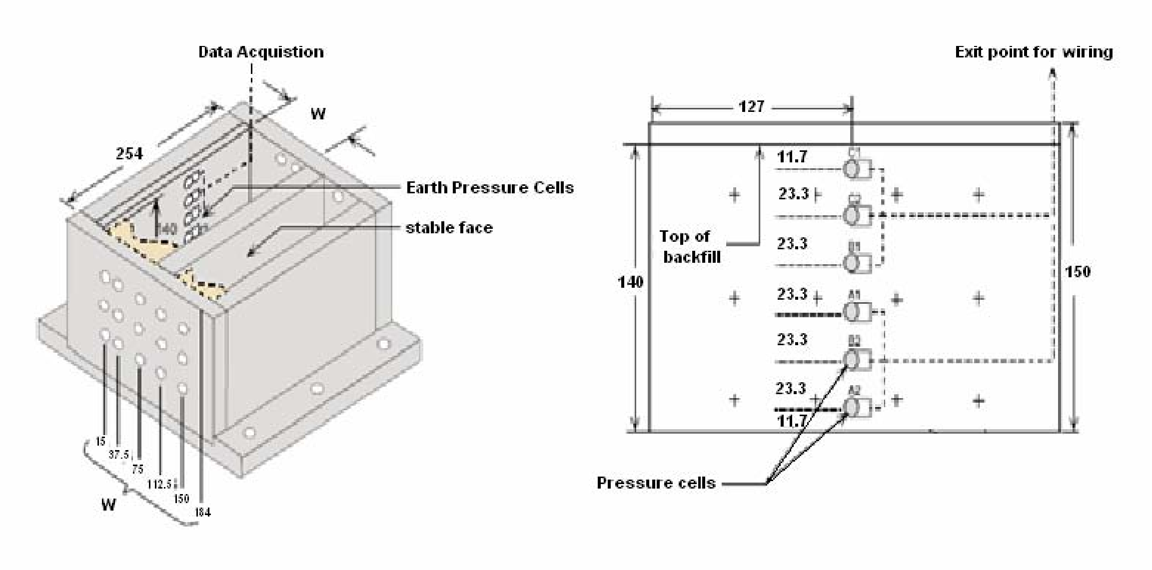

Figure 5.2: Schematic illustration of aluminum box and pressure cell arrangement in wall face used in centrifuge tests by Take and Valsangkar, 2001 (Take, 2001)

5.2 Finite Element Modeling

A finite element model was developed based on the studies conducted in Chapters 3 and 4. The model is illustrated in Figure 5-3. The Mohr-Coulomb soil constitutive model was chosen because of its simplicity, availability of sufficient data to define the soil constitutive parameters, and the belief that the Mohr-Coulomb model adequately captured the soil-wall interaction. The properties selected for the simulations are summarized in Table 5-1. Young's modulus was assumed to be 30,000 kPa which was the average of values of Young's Modulus found in the literature. The value of Poisson's ratio was calculated using the procedure outlined in Chapter 3 for a friction angle (ϕ') of 36°and is equal to 0.30. The value of the dilatancy angle was calculated using Equation 3-5 for a friction angle of 36° and is equal to 6°. Unit weights were selected such that the relative densities matched as closely as possible. In the centrifuge tests performed by Frydman and Keissar, the relative density was approximately 70 percent corresponding to a unit weight of 15.6 kN/m^3. A similar relative density (79 percent) was used by Take and Valsangkar for some tests. Thus, the material properties for the centrifuge tests performed by Take and Valsangkar were based on the backfill having a relative density of approximately 79 percent.

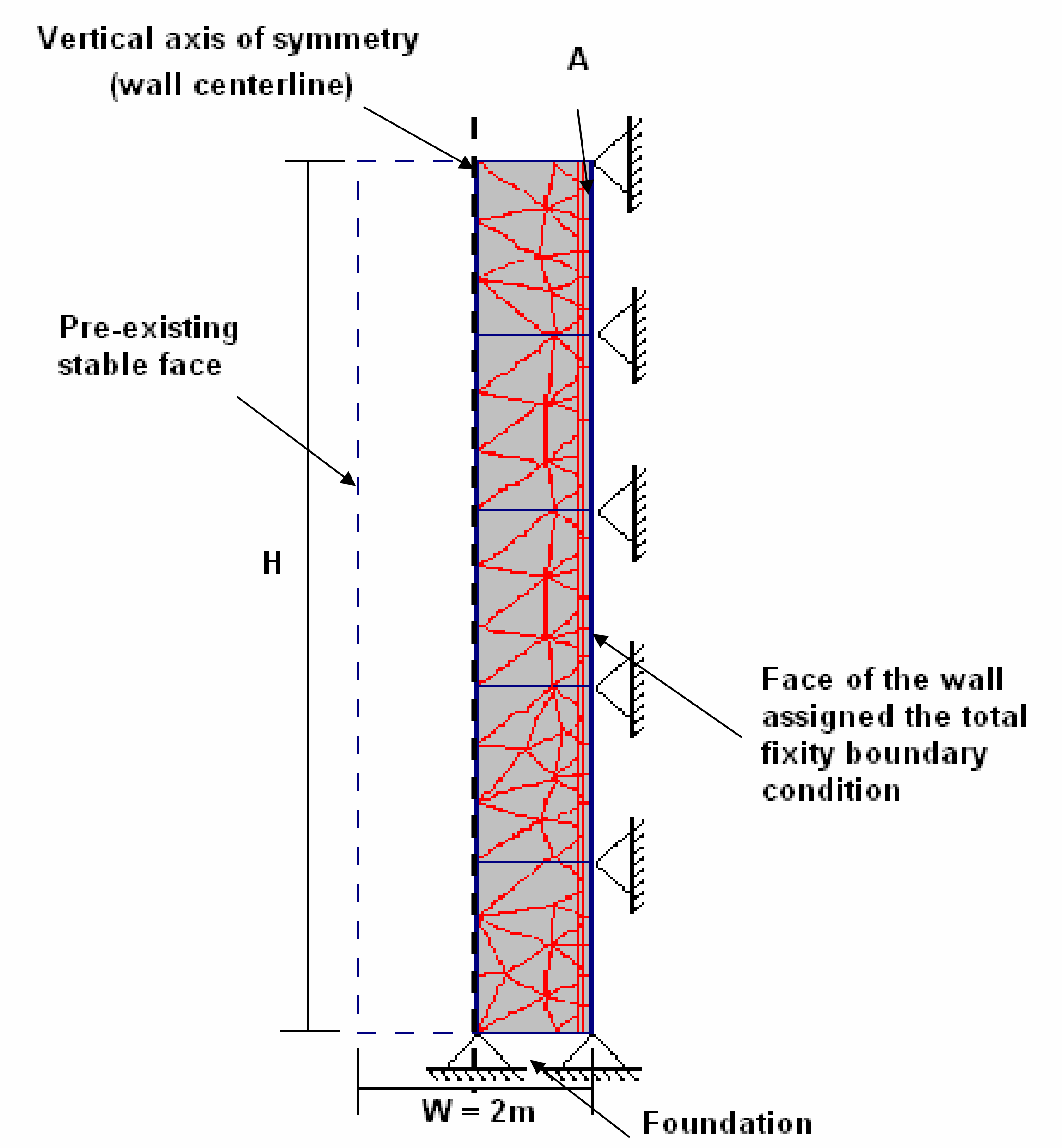

Figure 5.3: Finite element model adopted for finite element simulations of centrifuge tests having interface elements and the total fixity boundary condition assigned to the face of the wall (Plaxis, 2005)

Table 5.1: Parameters chosen to model the centrifuge tests by Frydman and Keissar and Take and Valsangkar

Variable	Frydman and Keissar	Take and Valsangkar
Angle of internal friction, ϕ' (˚)	36	36
Unit weight, γ (kN/m^3)	15.6	16.2
Young's Modulus, E (kPa)	30,000	30,000
Poisson's Ratio, ν	0.3	0.3
Interface Reduction Factor, R_{inter}	0.667	0.667
Dilatancy Angle, ψ (˚)	6	6
Cohesion (kPa)	0.2	0.2

5.3 Comparison of calculated and measured earth pressures from centrifuge tests performed by Frydman and Keissar

The earth pressures measured by Frydman and Keissar and calculated by Plaxis simulations of the centrifuge tests were expressed as normalized values. The horizontal earth pressures adjacent to the wall face are represented by a nondimensional horizontal earth pressure coefficient, k_w. The values of k_w were calculated by dividing the horizontal stress (σ_h) by the overburden pressure (γz). The horizontal stresses used to calculate k_w were either measured in the centrifuge tests or calculated by Plaxis in the simulations of the centrifuge tests. Similarly, the depth is expressed as a nondimensional depth z/H where z is the depth below the top of wall and H is the height of the wall. The variation in horizontal earth pressure coefficients (k_w) with nondimensional depth (z/H) from Frydman and Keissar are shown in Figures 5-4 through 5-6 for wall aspect ratios of 1.10, 0.30, and 0.10, respectively. The horizontal earth pressure coefficients adjacent to the wall calculated by Plaxis from simulations of the centrifuge tests and computed using Spangler and Handy’s equation are also shown in these figures. The horizontal earth pressure coefficients from all three sources agree favorably for all three wall aspect ratios.

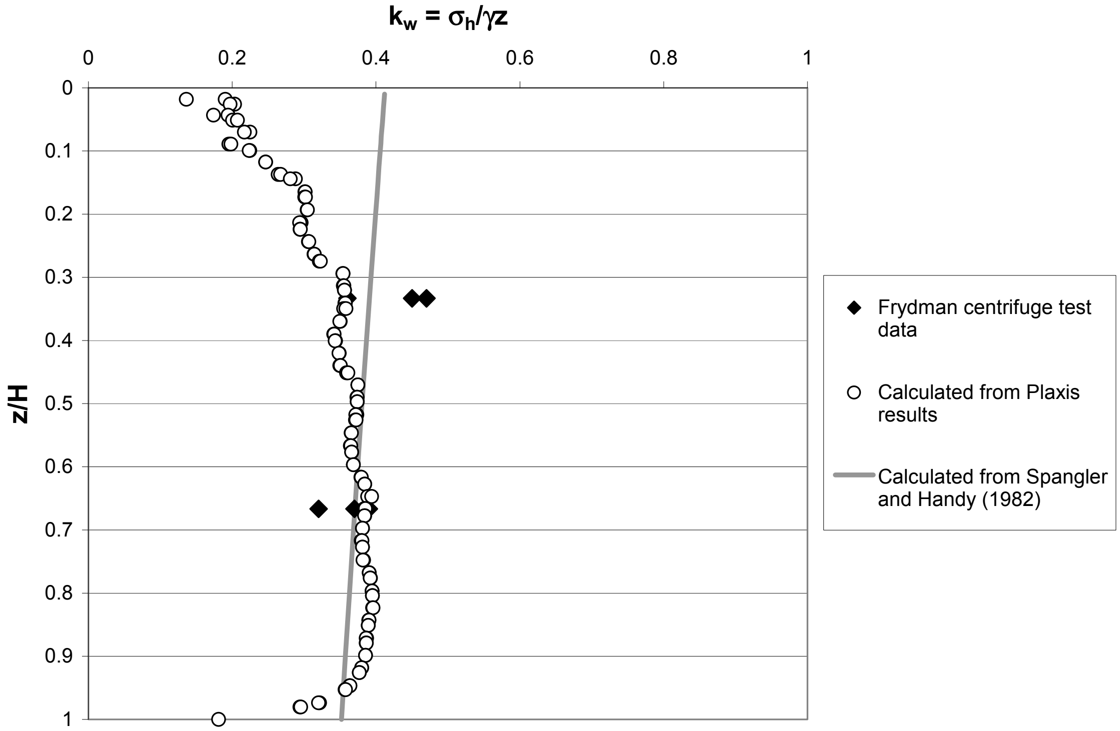

Figure 5.4: Variation in horizontal earth pressure coefficients versus the nondimensional depth (z/H) measured from a centrifuge test for a wall aspect ratio equal to 1.10 performed by Frydman and Keissar, calculated by Plaxis from simulations of the centrifuge test performed by Frydman and Keissar, and computed using Spangler and Handy's equation.

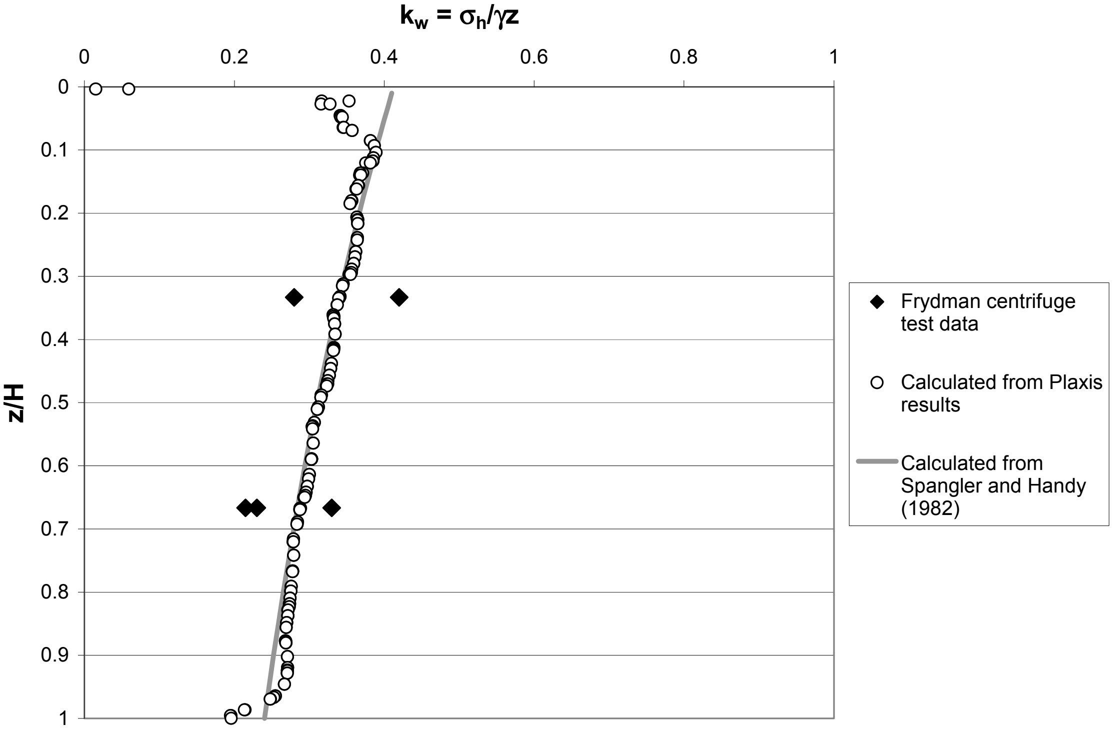

Figure 5.5: Variation in horizontal earth pressure coefficients versus the nondimensional depth (z/H) measured from a centrifuge test for a wall aspect ratio equal to 0.30 performed by Frydman and Keissar, calculated by Plaxis from simulations of the centrifuge test performed by Frydman and Keissar, and computed using Spangler and Handy's equation.

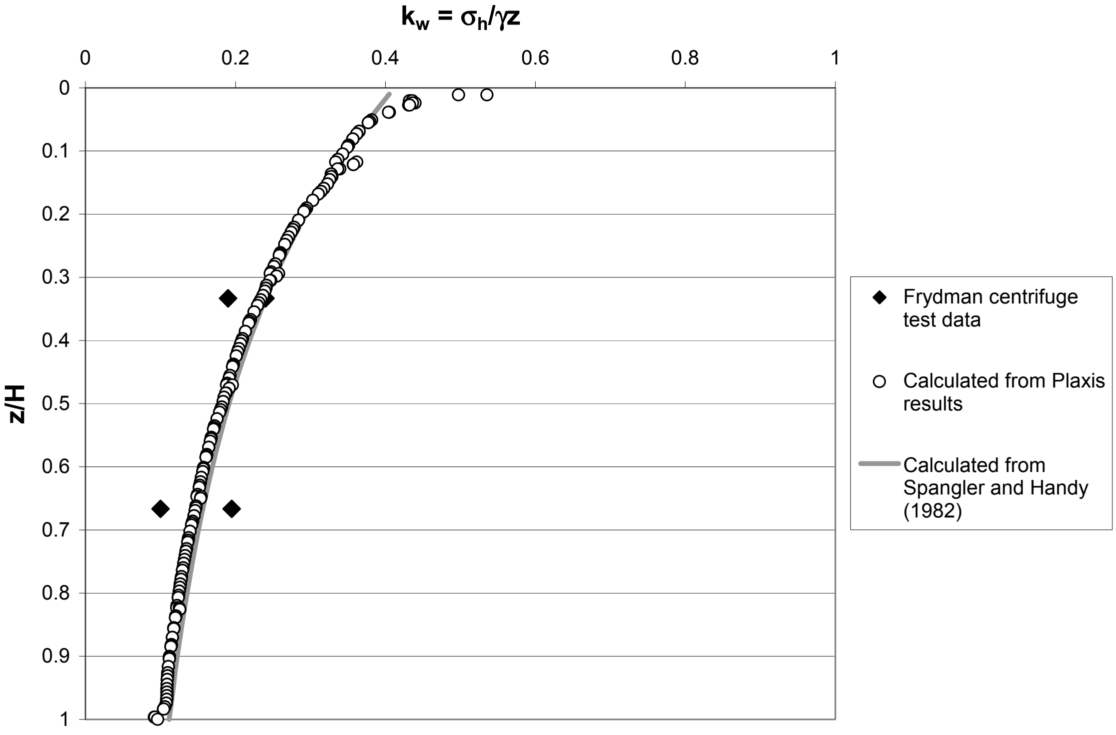

Figure 5.6: Variation in horizontal earth pressure coefficients versus the nondimensional depth (z/H) measured from a centrifuge test for a wall aspect ratio equal to 0.10 performed by Frydman and Keissar, calculated by Plaxis from simulations of the centrifuge test performed by Frydman and Keissar, and computed using Spangler and Handy's equation.

5.4 Comparison of calculated and measured earth pressures for centrifuge tests performed by Take and Valsangkar

The centrifuge tests performed by Take and Valsangkar (2001) for wall aspect ratios equal to 0.54 and 0.11 were simulated in Plaxis analyses. The horizontal earth pressures from these centrifuge tests are presented in Figures 5-7 and 5-8 using the same normalized representation described for the data presented in Section 5.3. The variations in horizontal earth pressure coefficients (k_w) with nondimensional depth (z/H) based on the measurements performed by Take and Valsangkar are presented in Figures 5-7 and 5-8 for wall aspect ratios of 0.54 and 0.11, respectively. The horizontal earth pressure coefficients adjacent to the wall calculated by Plaxis are also shown in Figures 5-7 and 5-8.

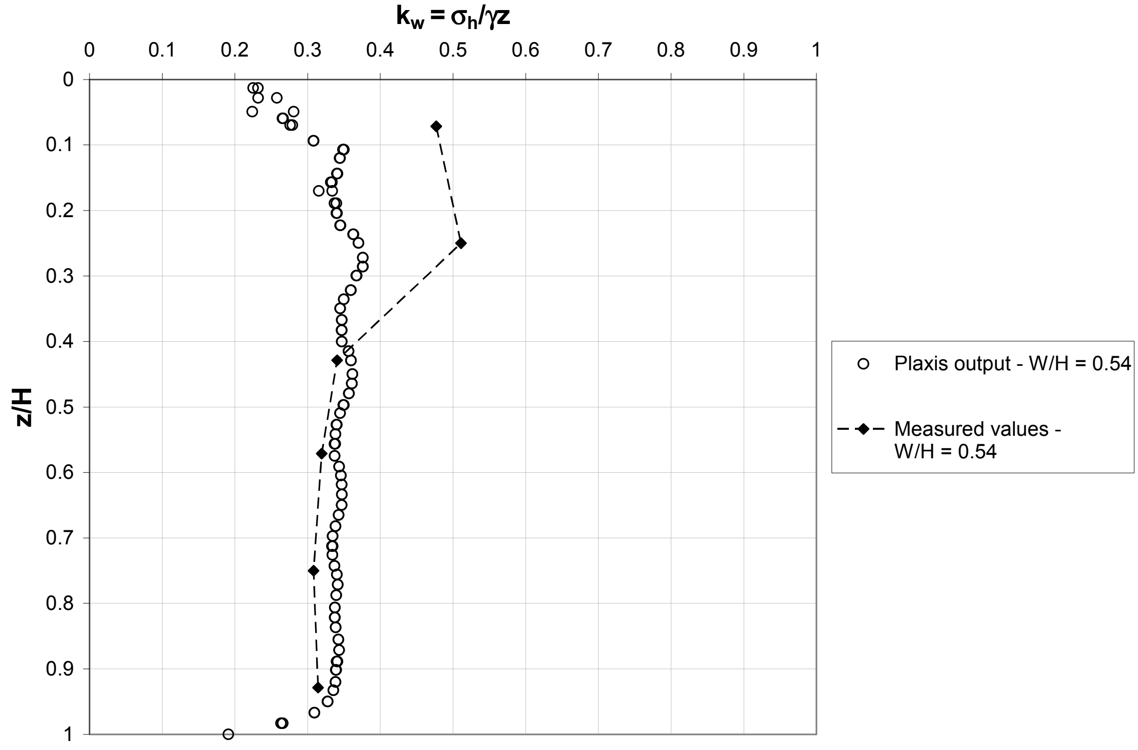

Figure 5.7: Variation in horizontal earth pressure coefficients with the non-dimensional depth (z/H) measured from a test performed by Take and Valsangkar and calculated by Plaxis from simulations of the centrifuge test performed by Take and Valsangkar with a wall aspect ratio equal to 0.54

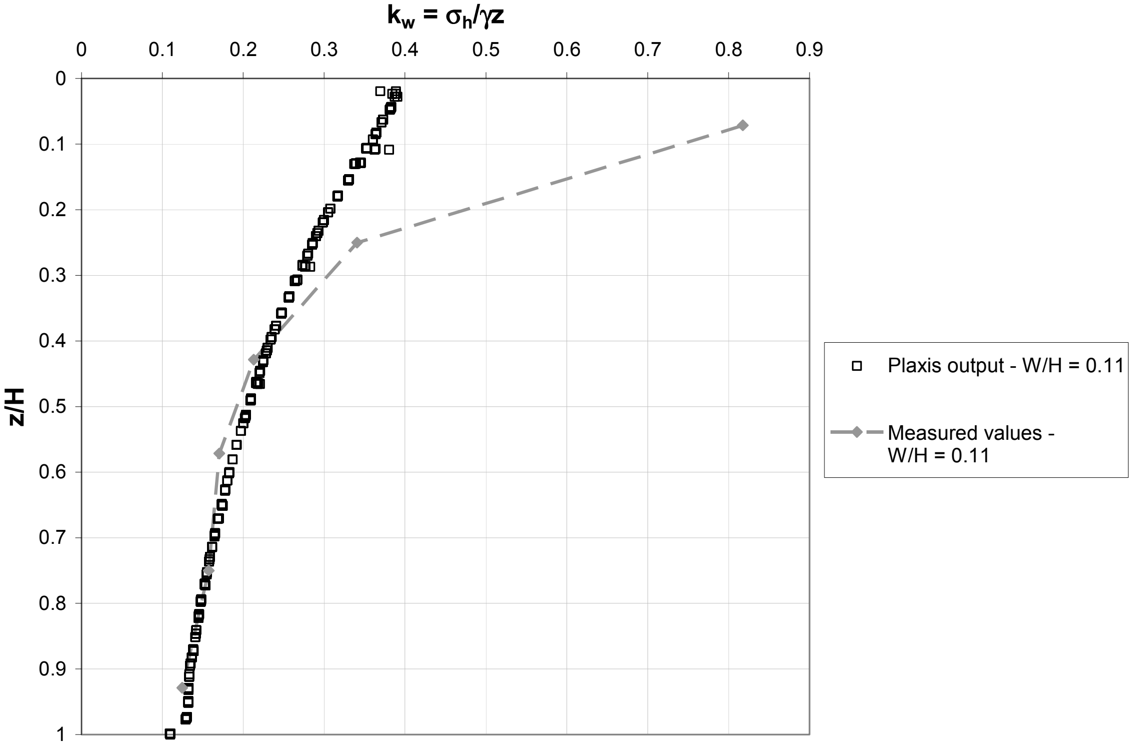

Figure 5.8: Variation in horizontal earth pressure coefficients with the non-dimensional depth (z/H) measured from a test performed by Take and Valsangkar and calculated by Plaxis from simulations of the centrifuge test performed by Take and Valsangkar with a wall aspect ratio equal to 0.11

The values calculated by Plaxis and the values measured by Take and compare favorably for depths greater than about one-third the wall height, i.e. z/H > 0.33. However, at shallower depths (z/H < 0.33), the calculated horizontal earth pressures do not match the measured values well. The reason for the poor agreement between the measured and calculated values of the horizontal earth pressure coefficients at shallower depths is not known, however, the pressures for which the pressure cells were calibrated in Take's and Valsangkar's tests may have had some impact. In the conclusion of their paper, Take and Valsangkar state,

> "…this research also indicates that, where flexible boundary pressure cells are used, the calibration might need to be undertaken at a stiffness representative of the boundary zone next to the pressure cells rather than at the bulk stiffness of the entire model".

Thus the earth pressures measured by the pressure cells near the top surface of the backfill may have been different from the earth pressures for which the earth pressure cells were calibrated.

The variations in horizontal earth pressure coefficients with nondimensional depth calculated by Plaxis for wall aspect ratios equal to 0.54 and 0.11 are shown in Figure 5-9. The horizontal earth pressure coefficients for the wall with an aspect ratio equal to 0.11 are generally less than the horizontal earth pressure coefficients for the wall with an aspect ratio equal to 0.54.

Also, for a wall aspect ratio of 0.11 the horizontal earth pressure coefficients decreased with depth at a much greater rate than when the wall aspect ratio was equal to 0.54.

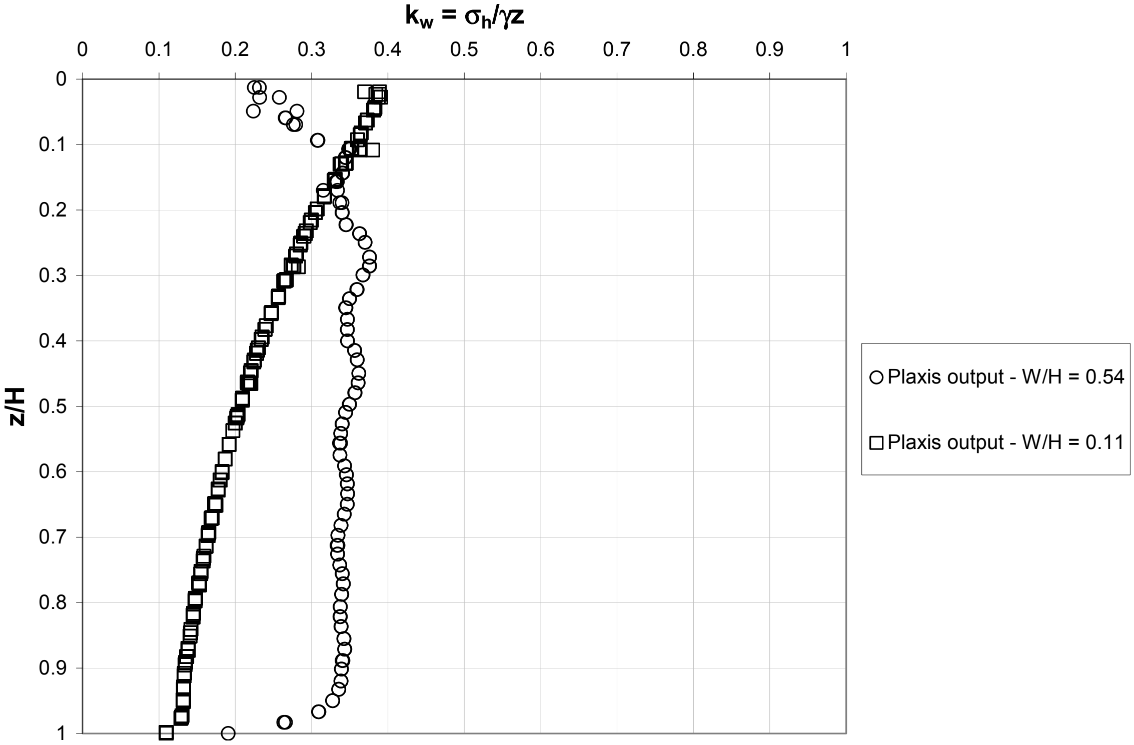

Figure 5.9: Variation in horizontal earth pressure coefficients with the non-dimensional depth (z/H) calculated by Plaxis from simulations of the centrifuge tests performed by Take and Valsangkar with wall aspect ratios equal to 0.54 and 0.11.

The variations in horizontal earth pressure coefficients with the nondimensional depth computed using Spangler and Handy's equation and calculated by Plaxis from simulations of the centrifuge test performed by Take and Valsangkar are shown in Figures 5-10 and 5-11 for wall aspect ratios of 0.54 and 0.11, respectively. The values computed using Spangler and Handy's equation and calculated by Plaxis from simulations of the centrifuge tests performed by Take and Valsangkar matched well.

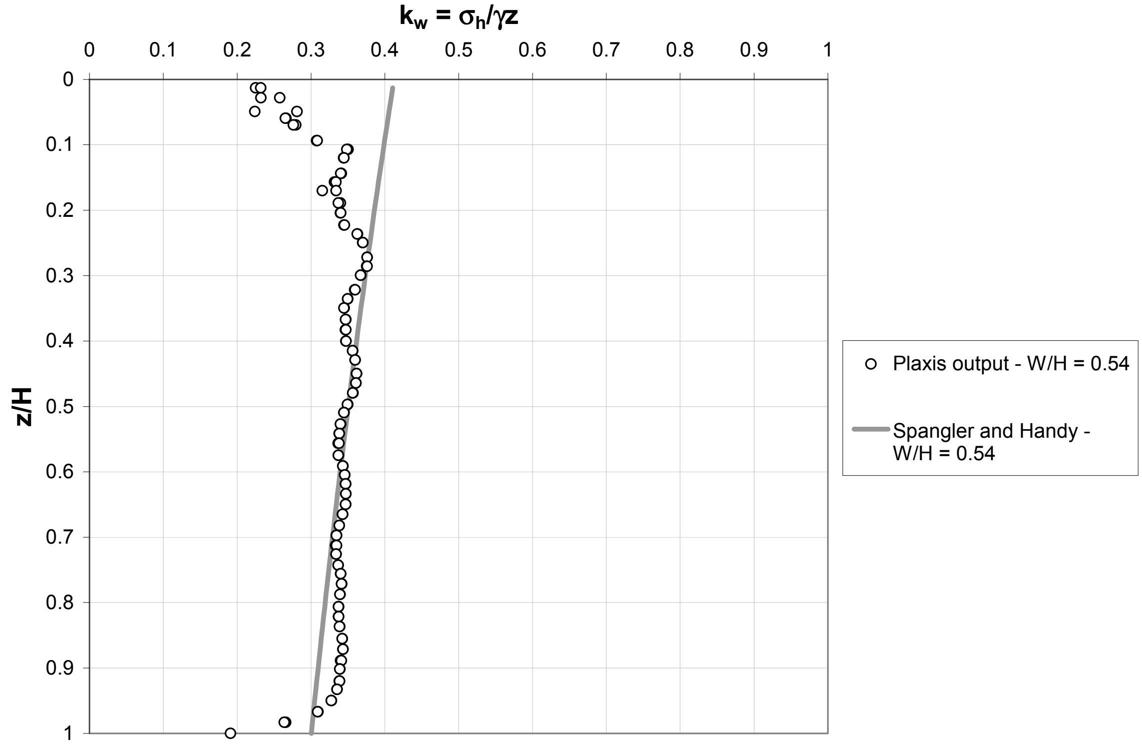

Figure 5.10: Variation in horizontal earth pressure coefficients with the non-dimensional depth (z/H) computed using Spangler and Handy's equation and calculated by Plaxis from simulations of the centrifuge test performed by Take and Valsangkar with a wall aspect ratio equal to 0.54

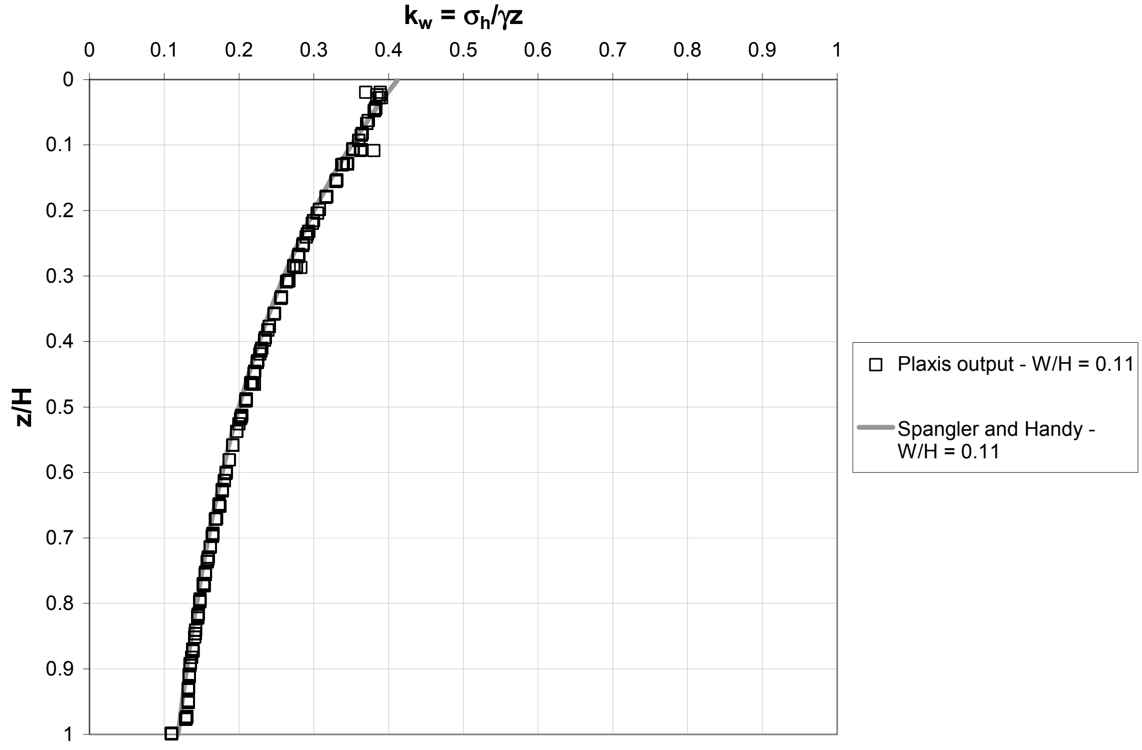

Figure 5.11: Variation in horizontal earth pressure coefficients with the non-dimensional depth (z/H) computed using Spangler and Handy's equation and calculated by Plaxis from simulations of the centrifuge test performed by Take and Valsangkar with a wall aspect ratio equal to 0.11

5.5 The effect of soil-wall interaction on horizontal earth pressures

For nondeformable walls, the soil-wall interaction causes the horizontal earth pressure coefficients to decrease with depth and decreasing wall aspect ratio. As the depth below the top of the backfill increases, the soil-wall interaction increases. As a result, the horizontal earth pressures are lower near the bottom of the wall. As the wall aspect ratio decreases, the soil-wall interaction caused the horizontal earth pressure coefficients to decrease.

5.6 Summary and conclusions of finite element modeling of centrifuge tests

Centrifuge tests performed by Frydman and Keissar (1987) and Take and Valsangkar (2001) were modeled using Plaxis. The horizontal earth pressure coefficients (k_w) calculated from the measured earth pressures in the centrifuge tests and the values of k_w calculated from the Plaxis simulations agree favorably. Similarly, the values of k_w computed using Spangler and Handy's equation matched well the horizontal earth pressure coefficients calculated from measured values and from Plaxis simulations. Because the results of Plaxis simulations agreed well with the horizontal earth pressure coefficients based on measured data, Plaxis is believed to have the ability to capture the effects of soil-wall interaction and wall aspect ratio on horizontal earth pressures. The comparisons presented in this chapter, thus validate use of Plaxis for further analyses to calculate horizontal earth pressure coefficients.

Chapter 6. Examination of Soil Constitutive Models in Terms of Effect on Horizontal Earth Pressures

As a wall moves away from the backfill, the horizontal earth pressure coefficients decrease. However, when inextensible reinforcement is used to construct a MSE wall, the movement of the wall will be relatively small. Also, as the wall aspect ratio decreases, particularly for walls with inextensible reinforcement, the wall is likely to be stiffer and undergo less movement. Thus, the limiting condition of a wall that does not move, i.e. the wall is nondeformable, may be approached. This chapter focuses on the horizontal earth pressures for walls that do not move.

As part of the evaluation of nondeformable walls, a parametric study was performed to better understand how the soil properties input into a finite element analysis affected the horizontal earth pressure coefficients at the wall face. First, the procedure is explained and a theory for calculating horizontal earth pressure coefficients is discussed. Next, the basis for selecting soil constitutive parameters for finite element analyses is discussed. Based on the results of the parametric study, several comparisons are made. Comparisons were made based on the equivalent horizontal earth pressure coefficient which was calculated from the results of finite element analyses. The sensitivity of the equivalent horizontal earth pressure coefficient is discussed in relation to the Mohr-Coulomb and Hardening-Soil constitutive models. Also, the horizontal earth pressure coefficients calculated from Spangler and Handy's equation (Eq. 6-1) are compared to the horizontal earth pressure coefficients calculated from the results of the Plaxis simulations using both the Mohr-Coulomb and Hardening-Soil models. Finally, a decision is made regarding which soil constitutive model will be used to conduct further simulations on nondeformable walls.

6.1 Spangler and Handy's equation

The principal of an arching theory and an equation to calculate horizontal earth pressure coefficients for granular material next to an nondeformable wall were introduced in Chapter 2. According to Spangler and Handy, the horizontal earth pressure (σ_h) is given by the following equation:

$$\sigma_h = \frac{\gamma \, \mathrm{W}}{2\tan(\delta)} * \left[1 - \exp\left(-2\mathrm{K}\left(\frac{\mathrm{z}}{\mathrm{W}} \right) \tan(\delta) \right) \right] \qquad \text{Eq. 6-1}$$

where W is the width of the constrained space, z is the depth of the point of interest below the top of the wall, δ is the interface friction angle between the soil and wall, K is the horizontal earth pressure coefficient based on Jaky's empirical formula for at-rest earth pressures (K_0 = 1-sin(ϕ')), and γ is the unit weight of the backfill.

6.2 Soil constitutive variables

The variables chosen for the sensitivity study are based in part on data compiled in Table 2-1 of the literature review presented in Chapter 2. Some judgment was used to select the values for the parametric study. The Mohr-Coulomb and Hardening soil models were used to study the effect of soil constitutive variables on the horizontal earth pressure coefficients along a vertical plane adjacent to the wall face.

6.2.1 Soil constitutive variables for the Mohr-Coulomb model

The soil parameters for the Mohr-Coulomb constitutive model are summarized in Table 6-1. The parameters have been organized into Sets A, B and C. Set A corresponds to the lower bound for the values of the parameters, Set C corresponds to the upper bound for the values and Set B is encompassed by the boundaries defined by Sets A and C. The bases for selecting each parameter are discussed in the following sections.

Table 6.1: Mohr-Coulomb model parameters selected for the parametric study

Mohr-Coulomb Model			
Variable	Values		
Set	A	B	C
Angle of internal friction, ϕ' (˚)	30	37	44
Unit weight, γ (kN/m^3)	17	17	17
Young's Modulus, E (kPa)	30000	30000	30000
Poisson's Ratio, ν	0.28	0.31	0.34
Dilatancy Angle, ψ (˚)	0	7	14
Interface Reduction Factor, R_{inter}	0.20	0.60	1.00

Angle of Internal Friction (ϕ')

A reasonable minimum value for the friction angle for the MSE wall backfill was judged to be about 30°. Similarly, a maximum value for the angle of internal friction was judged to be about 44°. The average of these two values (37°) was also chosen for the study. Thus, for the parametric study, friction angles of 30, 37, and 44 degrees were assumed.

Unit Weight (γ)

The unit weight was chosen to be equal to 17 kN/m^3 (108 pcf) for all analyses. Only one value was selected because the horizontal earth pressure coefficients were relatively insensitive to the value of the unit weight. The horizontal earth pressures are a function of the unit weight and the horizontal earth pressure coefficients are calculated by dividing the horizontal earth pressures by the overburden pressures (γz), therefore the value of the unit weight should not affect the magnitude of the horizontal earth pressure coefficient. To test this hypothesis, two simulations were performed in which the parameters were held constant except for the unit weight (Note: the unit weight is not a soil constitutive parameter but was still required for the finite element simulations).

The minimum and maximum values reported in the literature for unit weight of the backfill material were 14 kN/m^3 (89.1 pcf) and 21 kN/m^3 (134 pcf) respectively. However, a more reasonable maximum value was judged to be 20 kN/m^3 (127 pcf). As a result, unit weights of 14 kN/m^3 (89.1 pcf) and 20 kN/m^3 (127 pcf) were used in the simulations. The variations in the horizontal earth pressure coefficients along a vertical plane adjacent to the wall face calculated from the results of Plaxis analyses are plotted in Figure 6-1. The horizontal earth pressures calculated by Plaxis were obtained by drawing a user-selected cross section at the wall face. The horizontal earth pressure coefficients at the wall face (k_w) were then computed by dividing the calculated horizontal stress (σ_h) by the overburden stress ($\sigma_{ov} = \gamma z$). The distributions of horizontal earth pressure coefficients for both unit weights are very similar. Thus, the effect of unit weight was judged to be small and a single value of 17 kN/m^3 (108 pcf) was used for the balance of the analyses.

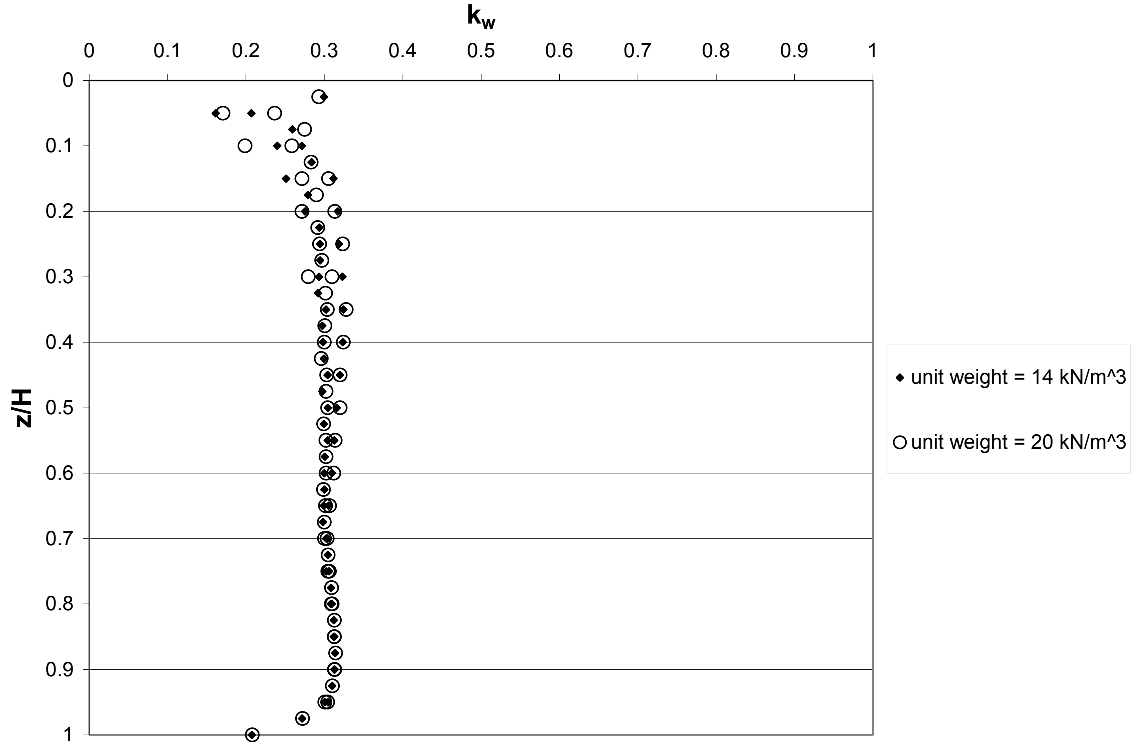

Figure 6.1: Horizontal earth pressure coefficient distributions for unit weights equal to 14 kN/m^3 (89.1 pcf) and 20 kN/m^3 (127 pcf)

Modulus of elasticity or Young's modulus (E)

Young's modulus was chosen to be equal to 30,000 kPa (≈627,000 psf). A single value of Young's Modulus was used because the horizontal earth pressure coefficients are relatively insensitive to the value used. To demonstrate that Young's Modulus has little effect on the horizontal earth pressure coefficients, two simulations were performed in which the variables were held constant with the exception of Young's modulus.

Based on the literature review conducted in Chapter 2, the minimum and maximum values of Young's Modulus were judged to be 10,000 kPa (≈209,000 psf) and 50,000 kPa (≈1,044,000 psf), respectively. Thus, Young's Moduli of 10,000 kPa (≈209,000 psf) and 50,000 kPa (≈1,044,000 psf) were selected. The variations in horizontal earth pressure coefficients along a vertical plane adjacent to the wall face calculated from Plaxis are plotted in Figure 6-2. Refer to Section 6.3.1.2 for a description of how values of k_w were calculated. The distributions of horizontal earth pressure coefficients are very similar. Hence, the value of Young's Modulus has negligible effect and a single value of 30,000 kPa (≈627,000 psf) was selected for the balance of the analyses.

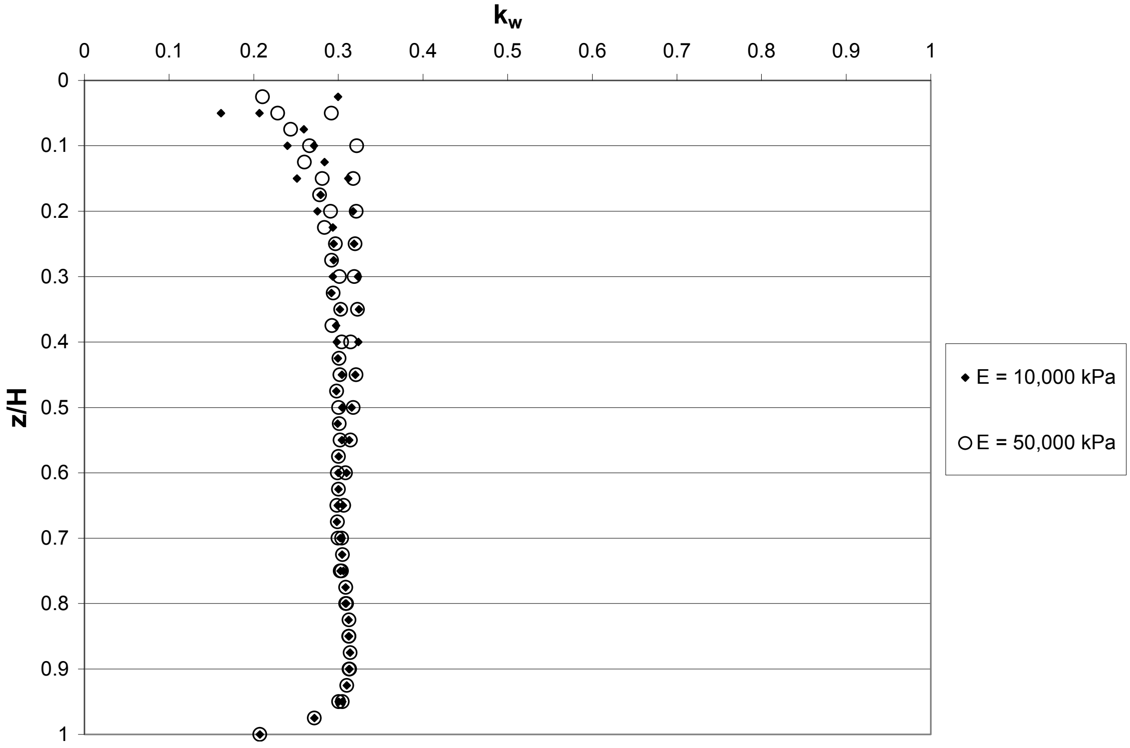

Figure 6.2: Horizontal earth pressure coefficient distributions for Young's Modulus equal to 10,000 kPa (≈209,000 psf) and 50,000 kPa (≈1,044,000 psf)

Poisson's ratio (ν)

Using the procedure to estimate Poisson's ratio based on values of ϕ' and $\phi'_{developed}$ described in Chapter 3, the values of 0.28, 0.31, and 0.34 were calculated corresponding to friction angles of 30°, 37°, and 44° respectively.

Interface Reduction Factor (R_{inter})

The interface reduction factor, R_{inter}, can be expressed as

$$R_{inter} = \frac{\tan(\delta)}{\tan(\phi)} \qquad \text{Eq. 6-2}$$

where δ is the interface friction angle and ϕ' is the angle of internal friction of the cohesionless backfill.

The Federal Highway Administration suggests the maximum value of the interface friction angle (δ) for design is two-thirds the angle of internal friction of the backfill (ϕ') (Elias et al., 2001), i.e. $\delta = (2/3)\phi'$. Although the relationships suggested by the FHWA are presumably for walls experiencing active earth pressures, and the nondeformable wall may not develop active earth pressures, the relationship suggested by the FHWA was judged to be satisfactory for this study. Substituting $\delta = (2/3)\phi'$ into Equation 6-2 and solving for R_{inter} yields a value of R_{inter} of approximately 0.600 when ϕ' equals 37°. Consequently, the interface reduction factor was set equal to 0.600. To test the sensitivity of the horizontal earth pressure coefficients to the value of R_{inter} the maximum value of the interface friction angle (δ) was assumed to be equal to the internal angle of friction which corresponds to an interface reduction factor of 1.00. The minimum value for the interface reduction factor was chosen such that the stiffness of the interface would not be reduced to the point that displacements became unrealistic as described in Chapter 4. The minimum value was judged to be 0.200.

Dilatancy angle (ψ)

The dilatancy angle (ψ) describes the behavior of soil during expansion and the Plaxis documentation suggests it is related to the friction angle. The Plaxis documentation recommends that the dilatancy angle be chosen such that it is 30° less than the angle of internal friction (ϕ') (Plaxis, 2005). Thus,

$$\psi = \phi' - 30 \qquad \text{Eq. 6-3}$$

Based on this recommendation and the angles of internal friction chosen for the parametric study (30°, 37°, and 44°), the values for the dilatancy angle were 0°, 7°, and 14° respectively.

6.2.2 Soil constitutive variables for the Hardening-Soil model

The angle of internal friction (ϕ'), unit weight (γ), interface reduction factor (R_{inter}), and dilatancy angle (ψ) were assigned the same values for the Hardening-Soil model and the Mohr-Coulomb model. A complete list of the variables used in the analyses with the Hardening-Soil model and their values is presented in Table 6-2. Similar to Table 6-1, the variables used for the Hardening-Soil model have been organized into Sets A, B and C. The upper and lower bounds for the values of the variables are represented in Sets A and B, respectively. Set B is encompassed by the boundaries defined by Sets A and C. The logic for selecting the values of each parameter is discussed in the following section.

Table 6.2: Hardening-Soil model parameters selected for the parametric study

Hardening-Soil Model			
Variable	Values		
Set	A	B	C
Angle of internal friction, ϕ' (˚)	30	37	44
Unit weight, γ (kN/m^3)	17	17	17
E_{50}^{ref} (kPa)	30,000	30,000	30,000
E_{oed}^{ref} (kPa)	27,000	27,000	27,000
E_{ur}^{ref} (kPa)	90,000	90,000	90,000
Unload-Reload Poisson's ratio, ν_{ur}	0.10	0.20	0.30
Failure Ratio, R_f	0.50	0.70	0.90
Power Variable, m	0.30	0.50	0.70
Dilatancy angle, ψ (˚)	0	7	14
Interface Reduction Factor, R_{inter}	0.200	0.600	1.00

Modulus of Elasticity

Three variables, E_{50}^{ref}, E_{oed}^{ref}, and E_{ur}^{ref}, are used to describe the modulus of elasticity in the Hardening-Soil model. The values selected for these variables were 30,000 kPa, 27,000 kPa, and 90,000 kPa, respectively, as shown in Table 6-2. Only a single value was used for each of the three moduli because they do not affect the distribution of horizontal earth pressure coefficients when chosen using the definitions discussed in the following section. To illustrate the small effect that the values of the three moduli have no effect on the horizontal earth pressure coefficients, three simulations were performed in which the variables were held constant with the exception of the three moduli. The values chosen for the three moduli were organized into three Sets as shown in Table 6-3 and are designated as Set 1, Set 2, and Set 3. The bases for selecting the values of the moduli in each Set are discussed next.

Table 6.3: Sets used to study the effect of Hardening-soil moduli parameters on the distribution of horizontal earth pressure coefficients

Set #	1	2	3
E_{50}^{ref} (kPa)	10,000	30,000	50,000
E_{oed}^{ref} (kPa)	9,000	27,000	45,000
E_{ur}^{ref} (kPa)	30,000	90,000	150,000

Modulus parameter, E_{50}^{ref}. The values selected for E_{50}^{ref} were the same as those selected for Young's Modulus in the parametric study with the Mohr-Coulomb model. The values selected were 10,000 kPa (≈209,000 psf), 30,000 kPa (≈627,000 psf), and 50,000 kPa (≈1,044,000 psf).

Modulus parameter, E_{oed}^{ref}. The values of E_{oed}^{ref} selected were 9,000 kPa (≈188,000 psf), 27,000 kPa (≈564,000 psf), and 45,000 kPa (≈940,000 psf). These values were determined as follows: Initially, values were selected to be equal to the constrained modulus (M) based on values for Young's Modulus and Poisson's ratio used with the Mohr-Coulomb model, i.e. $E_{oed}^{ref} = M$. The constrained modulus (M) was expressed as

$$M = \frac{E}{1 - 2\left(\frac{\nu^2}{1-\nu}\right)} \qquad \text{Eq. 6-4}$$

The values of E_{oed}^{ref} corresponding to the values of Young's Modulus and Poisson's ratio are shown in Table 6-4. However, when these values for E_{oed}^{ref} were input into Plaxis, an error message was given that the value of E_{oed}^{ref} was too high. To compensate for this problem, a new set of values for E_{oed}^{ref} was chosen such that E_{oed}^{ref} was equal to E_{50}^{ref}. However, again Plaxis indicated the value of E_{oed}^{ref} was too high for the case where the angle of internal friction was 44°. Rather than only adjust the value for $\phi' = 44°$, the value of E_{oed}^{ref} was chosen to be equal to $0.90 * E_{50}^{ref}$. Using this as a guideline the values of E_{oed}^{ref} shown in Table 6-3 were finally adopted.

Table 6.4: Values of Young's Modulus, Poisson's ratio used to calculate Eoedref

Young's Modulus, E (kPa)	Poisson's Ratio, ν	E_{oed}^{ref} (kPa)
10,000	0.28	12,784
30,000	0.31	49,030
50,000	0.34	104,467

Modulus parameter, E_{ur}^{ref}. The Plaxis documentation recommends using a value of E_{ur}^{ref} equal to three times E_{50}^{ref}. Accordingly, values of 30,000 kPa (≈627,000 psf), 90,000 kPa (≈1,880,000 psf), and 150,000 kPa (≈3,130,000 psf) were selected for E_{ur}^{ref}.

Set 1 had the smallest values of each modulus and set 3 had the largest values of each modulus. The variations in the horizontal earth pressure coefficient (k_w) versus the nondimensional depth (z/H) for each set are shown in Figure 6-3. The values of the horizontal earth pressure coefficients are very similar for all three Sets of moduli. Therefore, only a single set of values was used for the remaining analyses presented in this chapter. The second set (Set 2) of moduli was chosen for the parametric study (E_{ur}^{ref} =30,000 kPa (≈627,000 psf), E_{ur}^{ref} = 27,000 kPa (≈564,000 psf), E_{ur}^{ref} = 90,000 kPa (≈1,880,000 psf)).

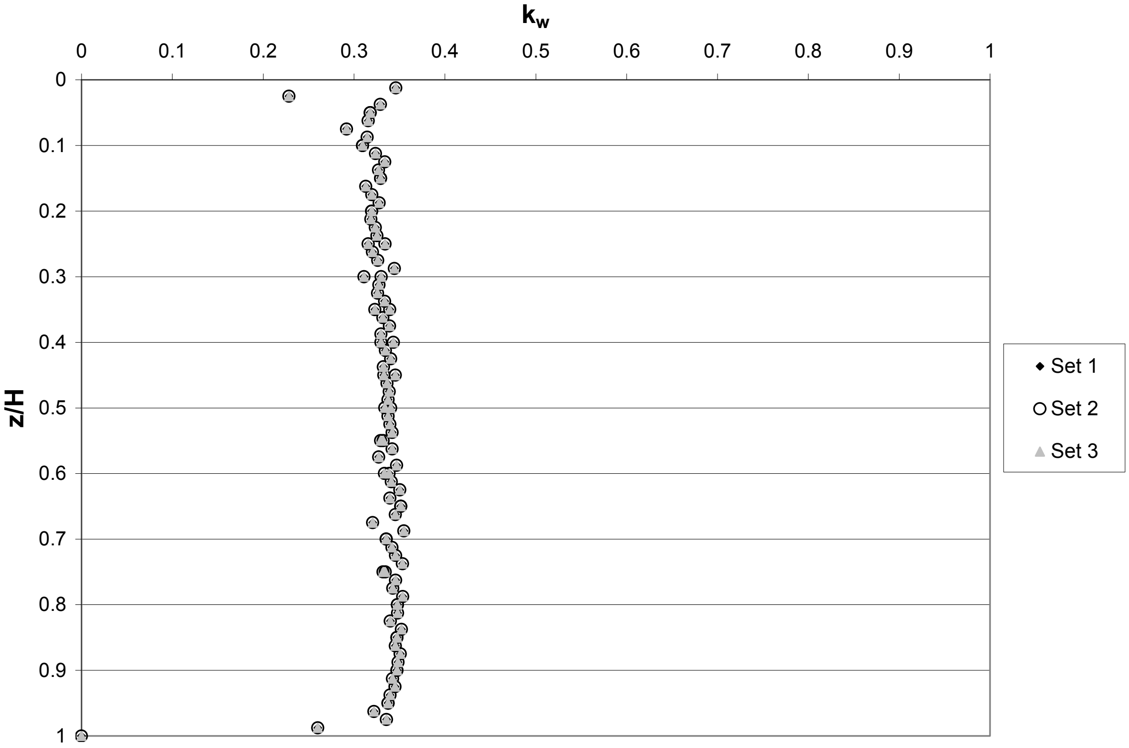

Figure 6.3: Horizontal earth pressure coefficient distributions for sets 1,2, and 3 of the three moduli

Unload-Reload Poisson's ratio (ν_{ur})

The Plaxis documentation (Plaxis, 2005) suggests using an unload-reload Poisson's ratio (ν_{ur}) of 0.20. For the parametric study, a minimum value of 0.10 and a maximum value of 0.30 were used in addition to a value of 0.20.

Failure Ratio (R_f)

The failure ratio (R_f) is the ratio of the deviatoric stress at failure to the ultimate deviatoric stress. Duncan (Duncan et al., 1980), suggests the values of R_f are between 0.50 and 0.90 for most soils. To include these values, values of 0.50, 0.70, and 0.90 were assumed for the parametric study.

Power Variable (m)

The parameter, m, is a measure of how the stiffness of the soil depends on the minor principal stress. Based on the literature review the values corresponding to pure sand (0.3), sand and silt (0.5), and clayey sand/sandy clay (0.7) were selected.

6.3 Basis for comparisons of horizontal earth pressures calculated by Plaxis and Spangler and Handy's equation

To compare the horizontal earth pressures calculated by various methods, a procedure was developed to calculate equivalent horizontal earth pressure coefficient by which all the cases could be compared. The equivalent horizontal earth pressure coefficient, K_{eq}, was calculated from the equivalent total horizontal force acting on the wall face. The equivalent total horizontal force, $F_{eq,}$ was obtained by integrating the horizontal stresses over the height of the wall. The relationship between the equivalent total force and the equivalent horizontal earth pressure (K_{eq}) is expressed as

$$F_{eq} = \frac{1}{2}\gamma K_{eq} H^2 \qquad \text{Eq. 6-5}$$

Thus,

$$K_{eq} = \frac{F_{eq}}{\frac{1}{2}\gamma H^2} \qquad \text{Eq. 6-6}$$

It was relatively easy to calculate K_{eq} from the Plaxis simulations because Plaxis can calculate and output the equivalent total force on a vertical cross-section drawn adjacent to the wall face. Finding K_{eq} was more difficult for earth pressures computed using Spangler and Handy's equation (Eq. 6-1). First the horizontal earth pressures were computed using their equation at each point for which Plaxis calculated the horizontal stresses or approximately every 0.25 m. Next, the Trapezoidal Rule (Apostol, 1962) was used to integrate the horizontal stresses from the top of the backfill to the foundation, i.e. z = 0 m to z = 10 m and thus find the equivalent total force, F_{eq}. The Trapezoidal Rule was also used to integrate the horizontal stresses calculated by Plaxis to verify that the force output directly by Plaxis was the same as the force calculated from the horizontal stresses output by Plaxis.

Table 6-5 is a comparison of the equivalent total force calculated directly by Plaxis, and the equivalent total force calculated by applying the Trapezoidal Rule to the horizontal stresses calculated by Plaxis at the wall face using the parameters in Set B of the Hardening-Soil model (Table 6-2). The values of the equivalent total force calculated by both methods are very similar.

Table 6.5: Equivalent total force values as determined by Plaxis and the Trapezoidal Rule

Method of Calculating F_{eq}	Equivalent Total Force, F_{eq} (kN/m)
Plaxis Output	284.15
Trapezoidal Rule	284.46

6.4 Parametric analyses and comparisons for the Mohr-Coulomb model

To determine which Mohr-Coulomb soil constitutive parameters had the largest impact on the horizontal earth pressure coefficients, a parametric study was conducted. The finite element model used for this parametric study was the same as the finite element model described at the conclusion of Chapter 4 and illustrated in Figure 4-14. First, Set B from Table 6-1 for the Mohr-Coulomb model was chosen as the baseline case. After establishing a baseline case, several of the variables in Set B were changed, one-by-one, while the other variables were held constant. The variables that were changed were the angle of internal friction (ϕ'), Poisson's ratio (ν), the interface reduction factor (R_{inter}), and the dilatancy angle (ψ). Eight cases in addition to the baseline case were analyzed. The nine cases are summarized in Table 6-6. The variable that was changed from the baseline case is highlighted.

Table 6.6: Cases for parametric study using the Mohr-Coulomb model

MOHR-COULOMB MODEL						
Case No.	γ (kN/m^3)	E (kPa)	ϕ' (˚)	ν	ψ (°)	Rinter (˚)
Baseline	17	30000	37	0.31	7	0.6
1	17	30000	30	0.31	7	0.6
2	17	30000	44	0.31	7	0.6
3	17	30000	37	0.28	7	0.6
4	17	30000	37	0.34	7	0.6
5	17	30000	37	0.31	0	0.6
6	17	30000	37	0.31	14	0.6
7	17	30000	37	0.31	7	1.0
8	17	30000	37	0.31	7	0.2

6.4.2 Parametric Analysis – Mohr-Coulomb model

The values of the equivalent horizontal earth pressure coefficients (K_{eq}) are summarized in Table 6-7. The percent difference from the baseline case is also shown for each case where a parameter was changed.

Table 6.7: Percent change in K_{eq} relative to the baseline case for the Mohr-Coulomb model

Plaxis Output		
Case No.	Keq	% difference from baseline
Baseline	0.361	--
1	0.374	3.54
2	0.349	-3.29
3	0.320	-11.52
4	0.405	12.10
5	0.361	0.00
6	0.361	0.01
7	0.326	-9.62
8	0.349	-3.45

In Table 6-7 the differences in K_{eq} relative to the baseline case for Cases 3, 4, and 7 exceeded five percent. These cases are considered to be more important than cases where the difference was less than five percent. In cases 3 and 4 the value of Poisson's ratio was varied. The value of Poisson's ratio is difficult to determine for a soil but is generally assumed to be between 0.3 and 0.4. However, varying Poisson's ratio by just 0.03 caused a change in K_{eq} of more than 10 percent. Thus, the impact of Poisson's ratio is significant given the uncertainty in its value. In case 7 the interface reduction factor (R_{inter}) was increased from 0.600 to 1.00. When the value of R_{inter} was increased to 1.00, the horizontal earth pressure coefficient decreased by about 10 percent. As shown in Chapter 4, the interface reduction factor has a large impact on the soil displacements. Apparently, the horizontal earth pressures are also strongly affected by the interface reduction factor. It was anticipated that the angle of internal friction (cases 1 and 2) would also have a significant impact on the values of K_{eq} however the angle of internal friction (ϕ') caused the value of K_{eq} to change by less than four percent for the Mohr-Coulomb model.

6.4.3 Comparisons between values of K_{eq} calculated from the results output by Plaxis for the Mohr-Coulomb model and values of K_{eq} computed from Spangler and Handy's equation

Values of K_{eq} were also computed based on Spangler and Handy's equation (Eq. 6-1). The values of K_{eq} computed using Spangler and Handy's equation for each case are compared to the values calculated using Plaxis for the same case in Table 6-8. For example, the parameters used to calculate K_{eq} for case 1 by Plaxis were also used to compute K_{eq} for case 1 using Spangler and Handy's equation. The column labeled Plaxis (%+Δ) contains the percent difference between the value of K_{eq} computed using Spangler and Handy's equation and the value of K_{eq} calculated using Plaxis. In most cases, the values of K_{eq} computed using Spangler and Handy's equation and the values of K_{eq} calculated by Plaxis were different by at least 6-1/2 percent. The differences were largest for cases 1 and 2 in which the angle of internal friction (ϕ') was changed from the baseline case and case 4 in which Poisson's ratio (ν) was increased. The value of K_{eq} was significantly decreased from the value calculated by Plaxis when Poisson's ratio was increased from 0.31 to 0.34 (case 4) because Spangler and Handy's equation is not a function of Poisson's ratio. Thus the horizontal stresses computed by their equation were not increased relative to the baseline case, but the value calculated by Plaxis increased significantly. However, when Poisson's ratio was decreased (case 3) the value of K_{eq} was not significantly different than the value calculated by Plaxis. The dilatancy angle,ψ, (cases 5 and 6) had no effect on the value of K_{eq} computed from Spangler and Handy's equation because their equation is not a function of the dilatancy angle. The interface reduction factor (R_{inter}) was used to change the value of the interface friction angle, δ, input into Spangler and Handy's equation. The difference between values computed by Spangler and Handy's equation and calculated by Plaxis were not greater than eight percent. However, the value of K_{eq} computed using Spangler and Handy's equation increased when R_{inter} decreased, but the value calculated by Plaxis decreased when R_{inter} decreased.

Table 6.8: Percent change in Keq computed using Spangler and Handy's (S&H) equation relative to the values calculated by Plaxis for the Mohr-Coulomb model

Spangler and Handy's equation			
Case No.	K_{eq} (Plaxis)	K_{eq} (S&H)	Plaxis %+?
baseline	0.361	0.338	-6.52
1	0.374	0.426	14.05
2	0.349	0.260	-25.67
3	0.320	0.338	5.66
4	0.405	0.338	-16.61
5	0.361	0.338	-6.52
6	0.361	0.338	-6.52
7	0.326	0.305	-6.60
8	0.349	0.376	7.87

6.5 Parametric analyses and comparisons for the Hardening-Soil model

The same finite element model was used for the parametric study with the Hardening-Soil model as was used with the Mohr-Coulomb model. Set B in Table 6-2 was chosen as the baseline case for the Hardening-Soil model. After establishing a baseline case, several of the variables in Set B were changed, one-by-one, while the other variables were held constant. The variables that were changed were the angle of internal friction (ϕ'), unload-reload Poisson's ratio (ν_{ur}), failure ratio (R_f), power variable (m), dilatancy angle (ψ), and the interface reduction factor (R_{inter}). A total of 12 cases in addition to the baseline case were analyzed with Plaxis. The 13 cases are summarized in Table 6-9 with the variable that was changed from the baseline case highlighted.

Table 6.9: Cases for parametric study using the Hardening-Soil model

HARDENING-SOIL MODEL											
Case No.	γ (kN/m^3)	E_{50} (kPa)	E-oed (kPa)	E-ur (kPa)	ϕ' (?)	ν_{ur}	R_f	m	ψ (?)	R_{inter}	W/H
Baseline	17	30000	27000	90000	37	0.2	0.70	0.5	7	0.6	0.7
1	17	30000	27000	90000	30	0.2	0.70	0.5	7	0.6	0.7
2	17	30000	27000	90000	44	0.2	0.70	0.5	7	0.6	0.7
3	17	30000	27000	90000	37	0.1	0.70	0.5	7	0.6	0.7
4	17	30000	27000	90000	37	0.3	0.70	0.5	7	0.6	0.7
5	17	30000	27000	90000	37	0.2	0.50	0.5	7	0.6	0.7
6	17	30000	27000	90000	37	0.2	0.90	0.5	7	0.6	0.7
7	17	30000	27000	90000	37	0.2	0.70	0.3	7	0.6	0.7
8	17	30000	27000	90000	37	0.2	0.70	0.7	7	0.6	0.7
9	17	30000	27000	90000	37	0.2	0.70	0.5	0	0.6	0.7
10	17	30000	27000	90000	37	0.2	0.70	0.5	14	0.6	0.7
11	17	30000	27000	90000	37	0.2	0.70	0.5	7	1.0	0.7
12	17	30000	27000	90000	37	0.2	0.70	0.5	7	0.2	0.7

6.5.2 Parametric Analysis – Hardening-Soil model

The values of the equivalent horizontal earth pressure coefficients (K_{eq}) are displayed in Table 6-10. The percent difference from the baseline case is also shown for each case where a parameter was changed.

Table 6.10: Percent change in K_{eq} relative to the baseline case for the Hardening-Soil model

Calculated by Plaxis		
Case No.	K_{eq}	% difference from baseline
Baseline	0.334	0.00
1	0.423	26.43
2	0.266	-20.55
3	0.337	0.67
4	0.335	0.29
5	0.333	-0.38
6	0.341	1.87
7	0.334	0.01
8	0.341	2.12
9	0.339	1.42
10	0.337	0.83
11	0.328	-1.78
12	0.346	3.43

In Table 6-10 the only cases showing a percent change greater than five percent relative to the baseline case are cases 1 and 2. In cases 1 and 2 the angle of internal friction (ϕ') was changed.

6.5.3 Comparisons between values of K_{eq} calculated from the results output by Plaxis for the Hardening-Soil model and values of K_{eq} computed from Spangler and Handy's equation

The values of K_{eq} computed using Spangler and Handy's equation are compared to the values of K_{eq} calculated by Plaxis in Table 6-11. The column labeled Plaxis (%$\underline{+}\Delta$) contains the percent difference between the values of K_{eq} computed using Spangler and Handy's equation and the values of K_{eq} calculated by Plaxis. The only cases in which Spangler and Handy's equation failed to match the Plaxis output within five percent were cases 11 and 12 in which the interface reduction factor (R_{inter}) was changed. In cases 11 and 12, the directions of change (increase or decrease) were the same for both calculations of K_{eq}.

Table 6.11: Percent change in K_{eq} calculated using Spangler and Handy's equation relative to the values calculated using the results output by Plaxis for the Hardening-Soil model

Spangler and Handy's equation			
Case No.	K_{eq} (Plaxis)	K_{eq} (S&H)	%+?
Baseline	0.334	0.338	1.11
1	0.423	0.426	0.80
2	0.266	0.26	-2.10
3	0.337	0.338	0.43
4	0.335	0.338	0.81
5	0.333	0.338	1.49
6	0.341	0.338	-0.75
7	0.334	0.338	1.10
8	0.341	0.338	-0.99
9	0.339	0.338	-0.31
10	0.337	0.338	0.27
11	0.328	0.305	-7.11
12	0.346	0.376	8.75

6.6 Conclusions from parametric analyses

Based on the parametric analysis, the most influential parameters on the value of K_{eq} for conducted using the Mohr-Coulomb model are Poisson's ratio (ν) and the interface reduction factor (R_{inter}). Unfortunately, the value of Poisson's ratio is very difficult to determine precisely. Thus, the Mohr-Coulomb model may not be the best choice to model the behavior of the backfill behind a nondeformable retaining wall. Based on the parametric analysis conducted using the Hardening-Soil model, the most influential parameter on K_{eq} for a nondeformable wall was the angle of internal friction (ϕ'). The angle of internal friction was expected to be very influential and compared to other parameters, values can be determined relatively easily and accurately from laboratory tests. Although the Hardening-Soil model has more parameters than the Mohr-Coulomb model, the sensitivity of the horizontal earth pressures to most of those parameters is less. Therefore, the Hardening-Soil model was selected to model the behavior of the backfill in studies of vertical and horizontal stresses behind nondeformable retaining walls (Chapter 7).

6.7 Conclusions from comparisons of values of K_{eq} calculated from results output by Plaxis and values of K_{eq} computed from Spangler and Handy's equation

The values of K_{eq} computed using Spangler and Handy's equation agreed favorably with the values of K_{eq} calculated by Plaxis for the case of a nondeformable wall, particularly when the Hardening-Soil model was used in Plaxis. Consequently, Spangler and Handy's equation appears to be reasonable for calculating the horizontal earth pressures for nondeformable walls.

6.8 Summary

A parametric study was conducted to determine the relative importance of soil properties for calculating the horizontal earth pressures when using both the Mohr-Coulomb and Hardening-Soil constitutive models. An equivalent horizontal earth pressure coefficient, K_{eq}, was introduced as a means by which earth pressures based on different sets of parameters and/or different approaches to calculating the earth pressures could be compared easily. Comparisons were made between the values of K_{eq} computed from Spangler and Handy's equation and the values of K_{eq} calculated by Plaxis for a nondeformable wall.

The parametric analysis showed the Hardening-Soil model was the best choice to model the behavior of the backfill for a nondeformable retaining wall. The comparisons between the values of K_{eq} computed using Spangler and Handy's equation and the values of K_{eq} calculated by Plaxis using the Hardening-Soil model indicate that Spangler and Handy's equation provides reasonable values for horizontal earth pressures.

Based on the results of the parametric analysis, parameters in the Hardening-Soil model were selected for use in subsequent simulations presented in Chapter 7. For the analyses in Chapter 7, it seemed more logical to use an interface reduction factor, R_{inter}, of 0.667 or two-thirds based on the Plaxis documentation (Plaxis, 2005) and current design guidelines (Elias et al., 2001). The difference between using this value and the baseline value chosen for the parametric study (0.600) was expected to be minor, thus the analyses performed in this chapter were not redone. The parameters and their corresponding values are shown in Table 6-12.

Table 6.12: Parameter set for subsequent simulations using the Hardening-Soil model.

Hardening-Soil Model	
Variable	Value
ϕ' (?)	37
γ (kN/m^3)	17
E_{50}^{ref} (kPa)	30000
E_{oed}^{ref} (kPa)	27000
E_{ur}^{ref} (kPa)	90000
ν_{ur}	0.20
R_f	0.70
m	0.50
ψ (?)	7
R_{inter}	0.667

Chapter 7. Effect of Wall Aspect Ratio on Vertical and Horizontal Stresses Behind a Nondeformable Wall

A series of parametric finite element analyses was performed with Plaxis to study how the vertical and horizontal stresses behind a nondeformable wall vary as the wall aspect ratio decreases. The results of these analyses are presented in this chapter. The manner in which the appropriate stresses can be incorporated into current design guidelines is also presented.

7.1 Effect of wall aspect ratio on vertical stresses behind nondeformable walls

Finite element analyses were performed for walls with aspect ratios (W/H) of 1.00, 0.70, 0.50, 0.30, and 0.10. The finite element model used to study the effect of wall aspect ratio on vertical stresses was basically the same as the finite element model proposed at the conclusion of Chapter 4 in Figure 4-14. The soil constitutive model selected for the simulations was the Hardening-Soil model based on the study conducted in Chapter 6. At the conclusion of Chapter 6, a set of parameters was selected for use in the studies of vertical and horizontal stresses presented in the following sections. These parameters were used in the studies presented in this chapter.

The variations in vertical stresses were examined along both horizontal and vertical planes. For presentation purposes, the vertical stresses (σ_v) were expressed as normalized values by dividing the vertical stresses by the vertical overburden pressure (γz). The ratio of σ_v to γz is expressed by the symbol, β_v which is termed the "vertical stress influence factor." The following sections discuss the investigation of the vertical stresses. Horizontal stresses are then discussed in later sections.

7.1.1 Variation in vertical stress with lateral distance

To determine how the vertical stress varied across the width of the backfill, simulations were performed with wall aspect ratios equal to 1.00, 0.70, 0.50, 0.30, and 0.10. The variation in vertical stress influence factors (□v) with horizontal position are plotted in Figures 7-1 through 7-5. The variations in □v at depths of one-fourth and three-fourths the wall height below the top of the wall, i.e. z/H = 0.25 and 0.75, respectively with horizontal position are displayed in Figures 7-1(a) and 7-1(b) for a wall aspect ratio of 1.00. In these figures the horizontal (x) coordinates are expressed as normalized values, x/W, by dividing the x-coordinates by the width of the wall (W). The same format was used to plot the variations in vertical stresses for wall aspect ratios of 0.70, 0.50, 0.30, and 0.10 in Figures 7-2 through 7-5, respectively. Three important observations can be made from the plots of vertical stress influence factors with horizontal position. First, the values of the vertical stress influence factors are highest near the center of the backfill and lowest near the boundaries. Second, the values of the vertical stress influence factors along the horizontal plane at a height of three-fourths the wall height below the top of the wall are less than the values at a height of one-fourth the wall height below the top of the wall. In other words as the depth below the top of the wall increases, the vertical stress influence factor decreases. Third, as the wall aspect ratio decreases, the magnitudes of the vertical stress influence factors decrease. Thus, the values of the vertical stress influence factors decrease horizontally from the center of the backfill to the wall face, with depth below the top of the wall and with decreasing wall aspect ratio.

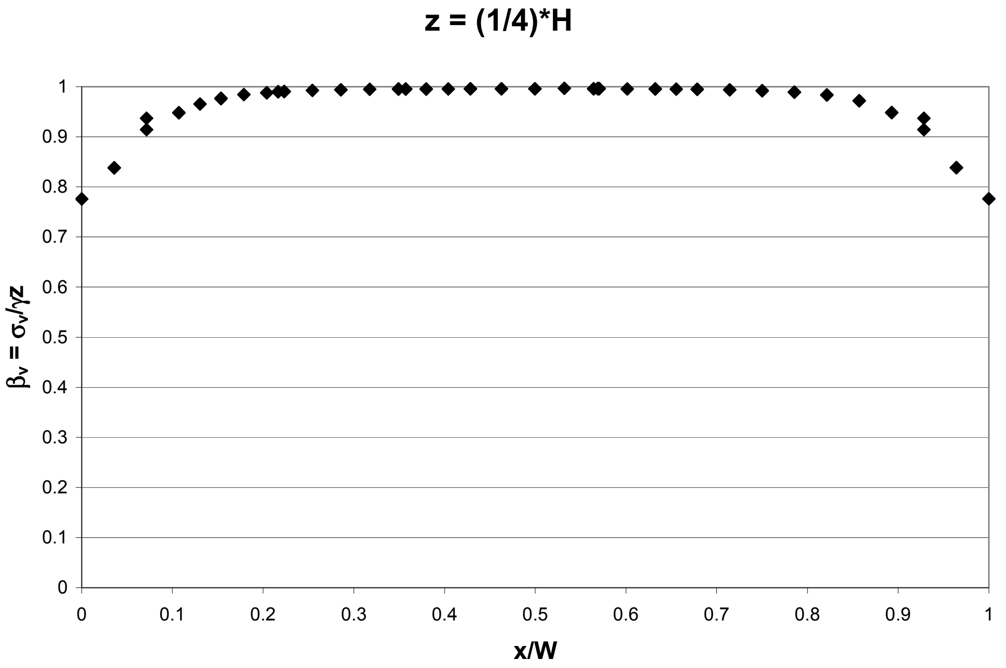

(a) Variation of vertical stress factor along a horizontal plane at one-fourth the wall height below the top of the wall

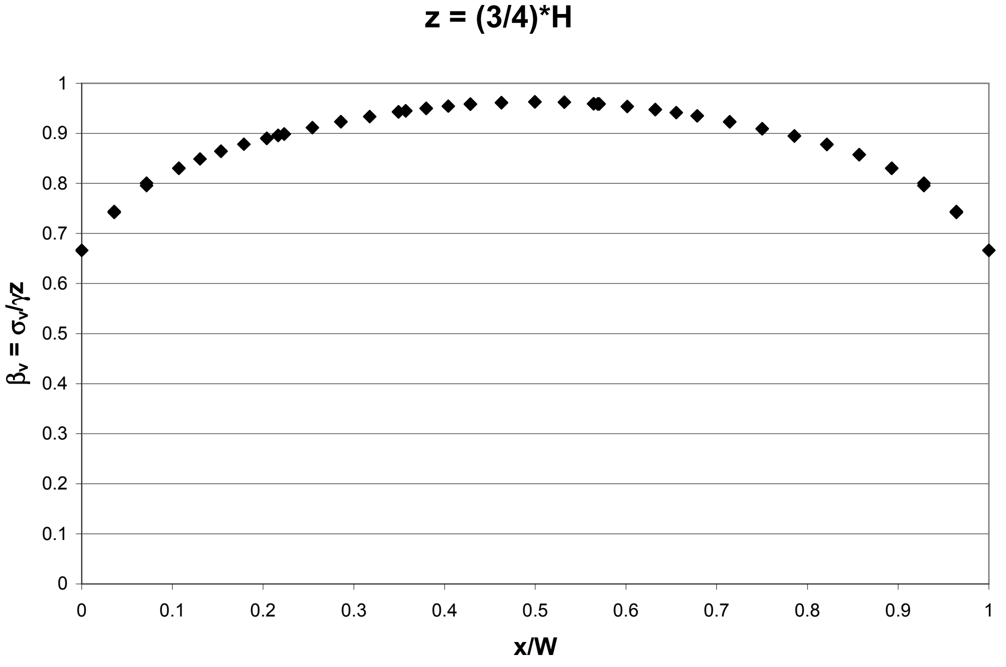

(b) Variation of vertical stress factor along a horizontal plane at three-fourths the wall height below the top of the wall

Figure 7.1: Plots of the vertical stress influence factor along a horizontal plane at two depths below the top of the wall for a wall aspect ratio equal to 1.00

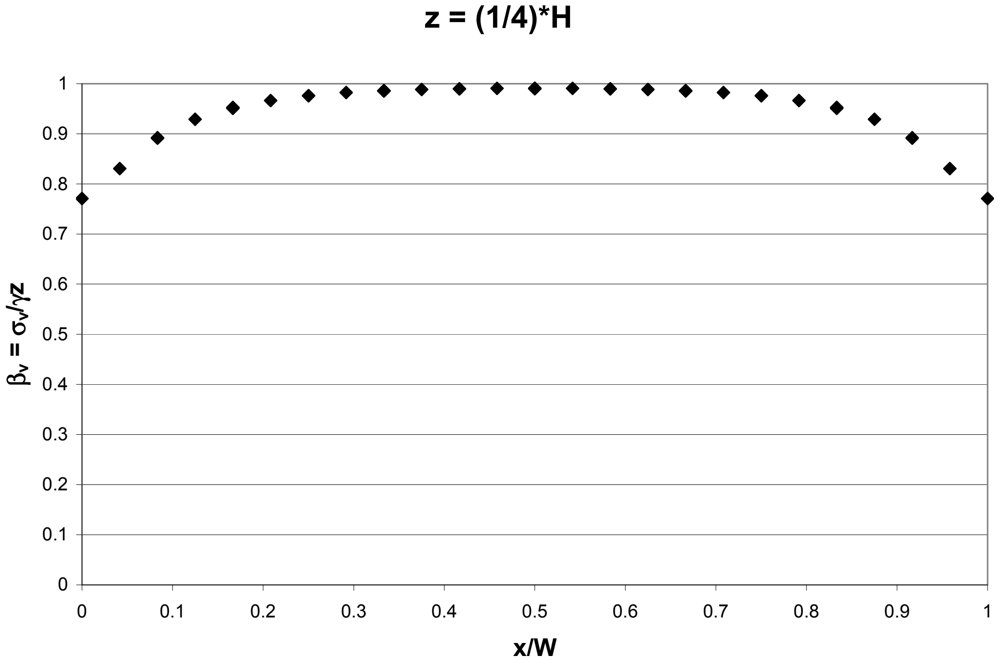

(a) Variation of vertical stress factor along a horizontal plane at one-fourth the wall height below the top of the wall

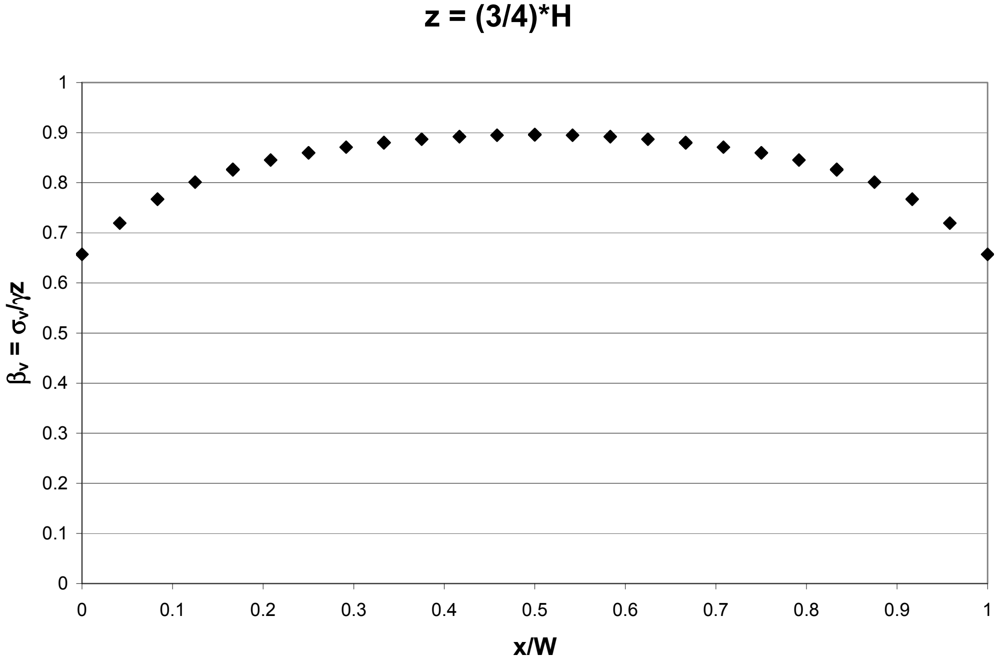

(b) Variation of vertical stress factor along a horizontal plane at three-fourths the wall height below the top of the wall

Figure 7.2: Plots of the vertical stress influence factor along a horizontal plane at two depths below the top of the wall for a wall aspect ratio equal to 0.70.

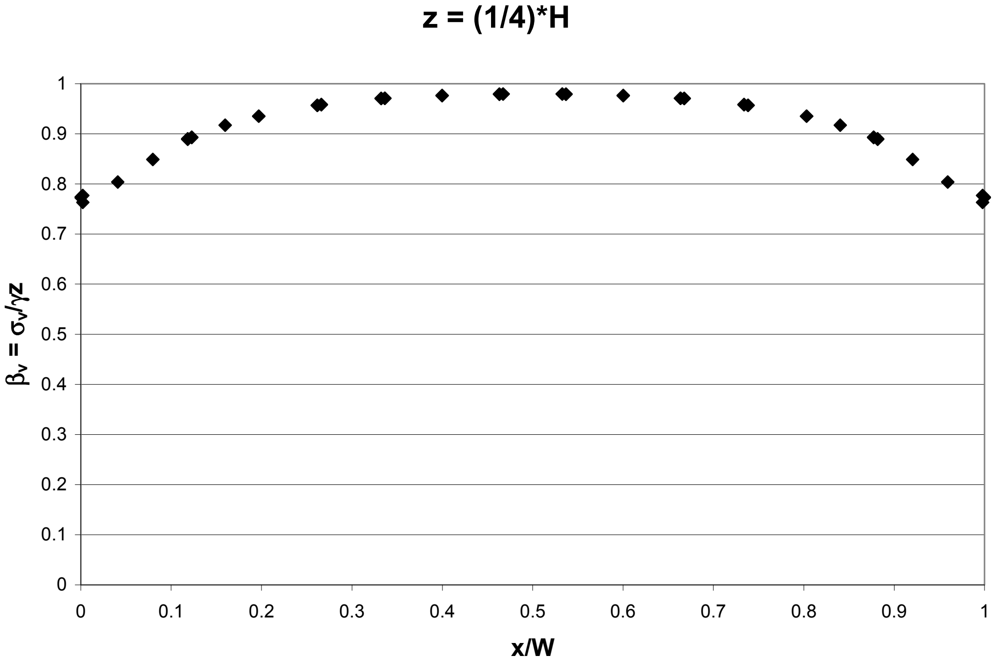

(a) Variation of vertical stress factor along a horizontal plane at one-fourth the wall height below the top of the wall

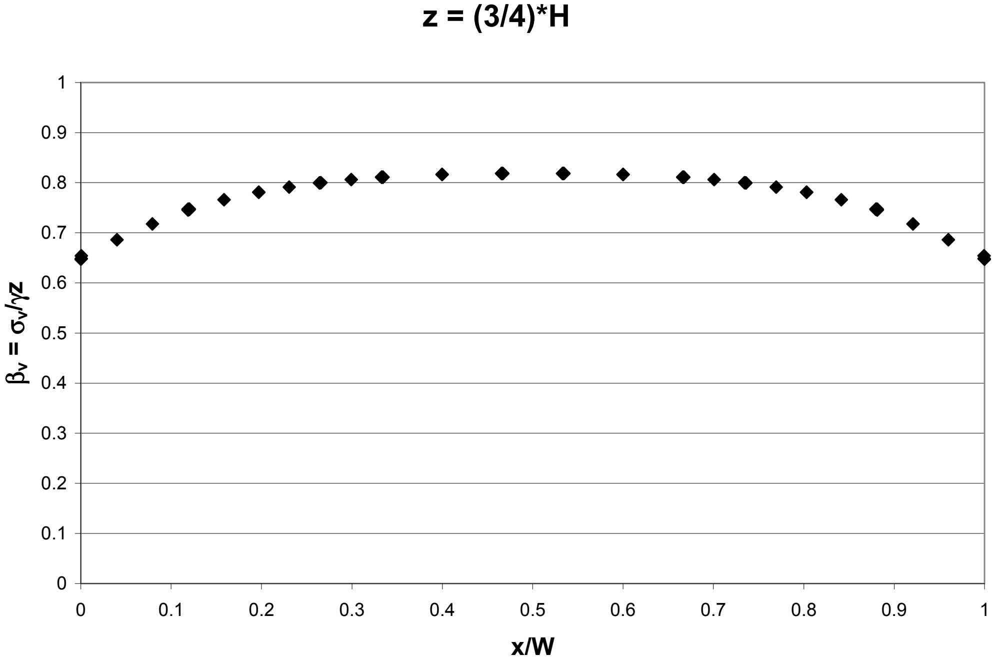

(b) Variation of vertical stress factor along a horizontal plane at three-fourths the wall height below the top of the wall

Figure 7.3: Plots of the vertical stress influence factor along a horizontal plane at two depths below the top of the wall for a wall aspect ratio equal to 0.50

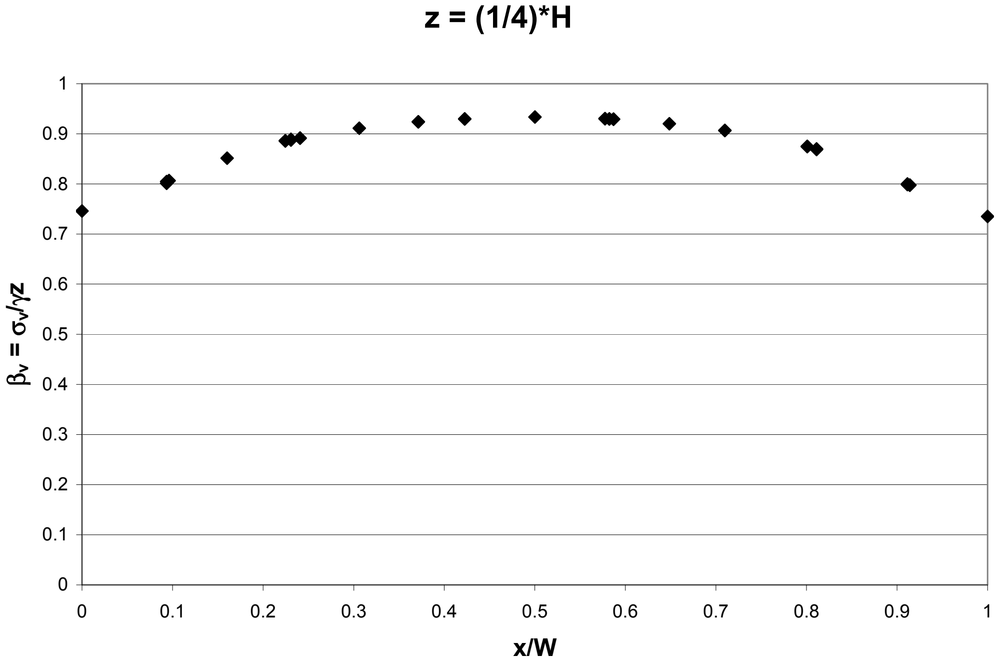

(a) Variation of vertical stress factor along a horizontal plane at one-fourth the wall height below the top of the wall

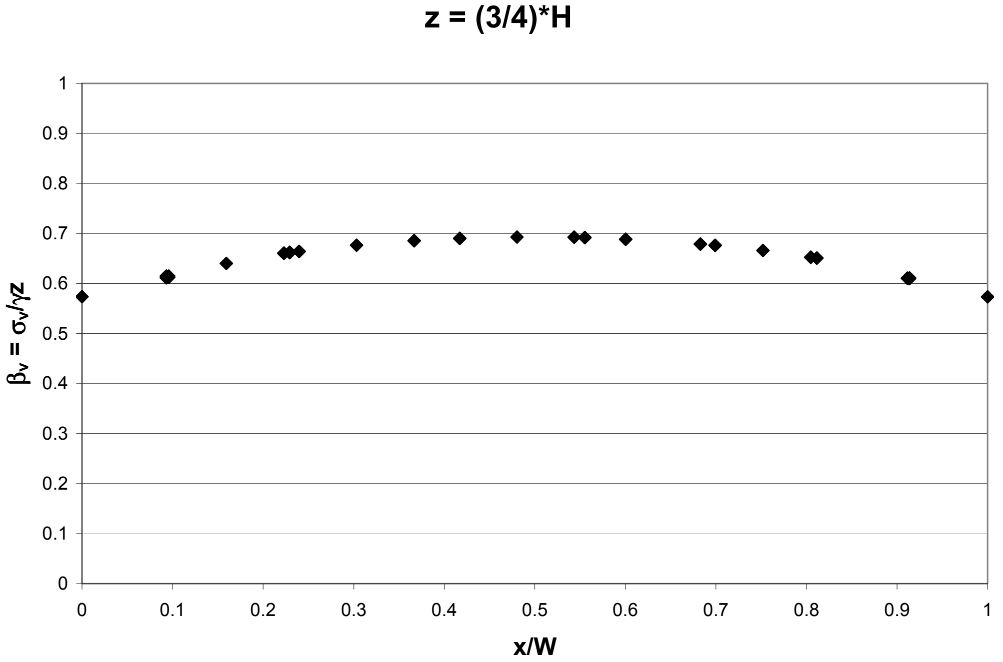

(b) Variation of vertical stress factor along a horizontal plane at three-fourths the wall height below the top of the wall

Figure 7.4: Plots of the vertical stress influence factor along a horizontal plane at two depths below the top of the wall for a wall aspect ratio equal to 0.30

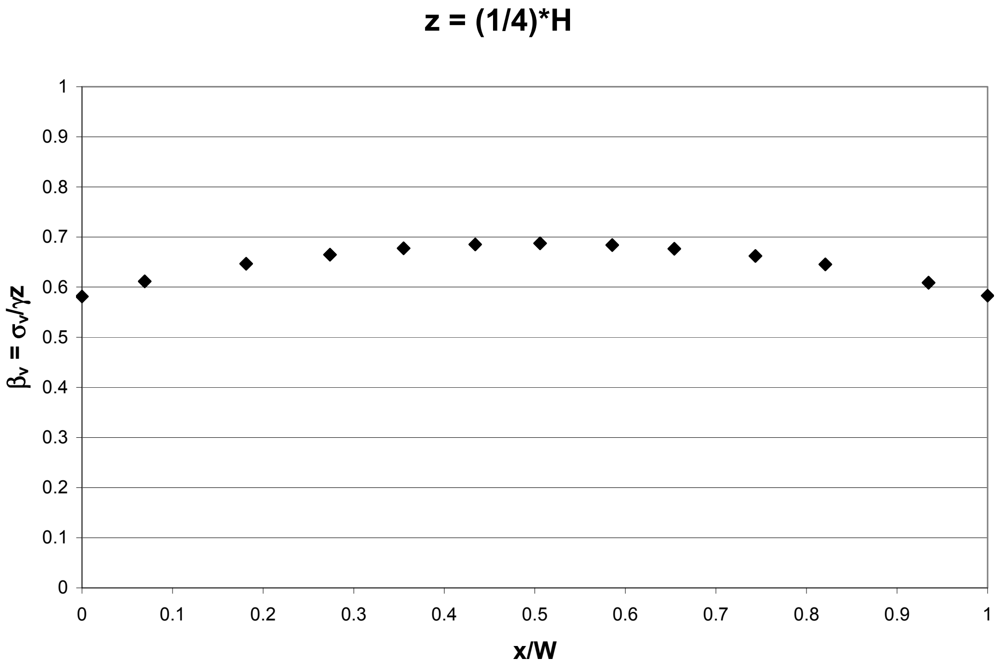

(a) Variation of vertical stress factor along a horizontal plane at one-fourth the wall height below the top of the wall

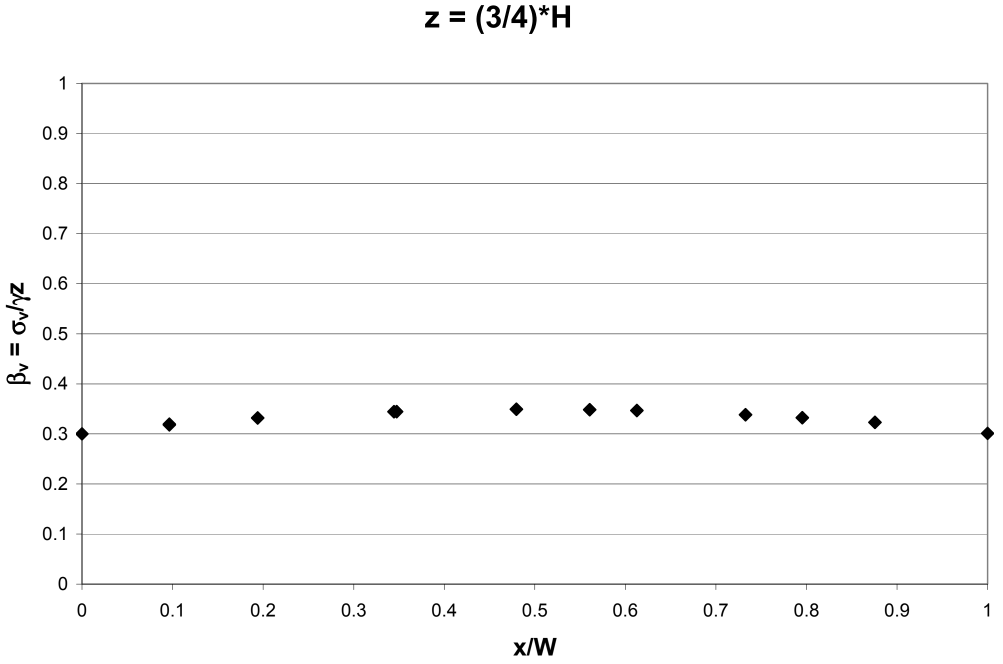

(b) Variation of vertical stress factor along a horizontal plane at three-fourths the wall height below the top of the wall

Figure 7.5: Plots of the vertical stress influence factor along a horizontal plane at two depths below the top of the wall for a wall aspect ratio equal to 0.10

7.1.2 Variation in vertical stress with depth

To understand better how the vertical stresses changed with depth, the vertical stress reduction influence factors (β_v) were plotted along a vertical plane at two locations: in the center of the backfill and adjacent to the wall face (Figure 7-6). The vertical stress influence factors at both locations are plotted in Figure 7-7 for a wall with an aspect ratio of 1.00. The vertical stress influence factors decrease with depth below the top of the wall and are less adjacent to the wall face than at the center of the backfill.

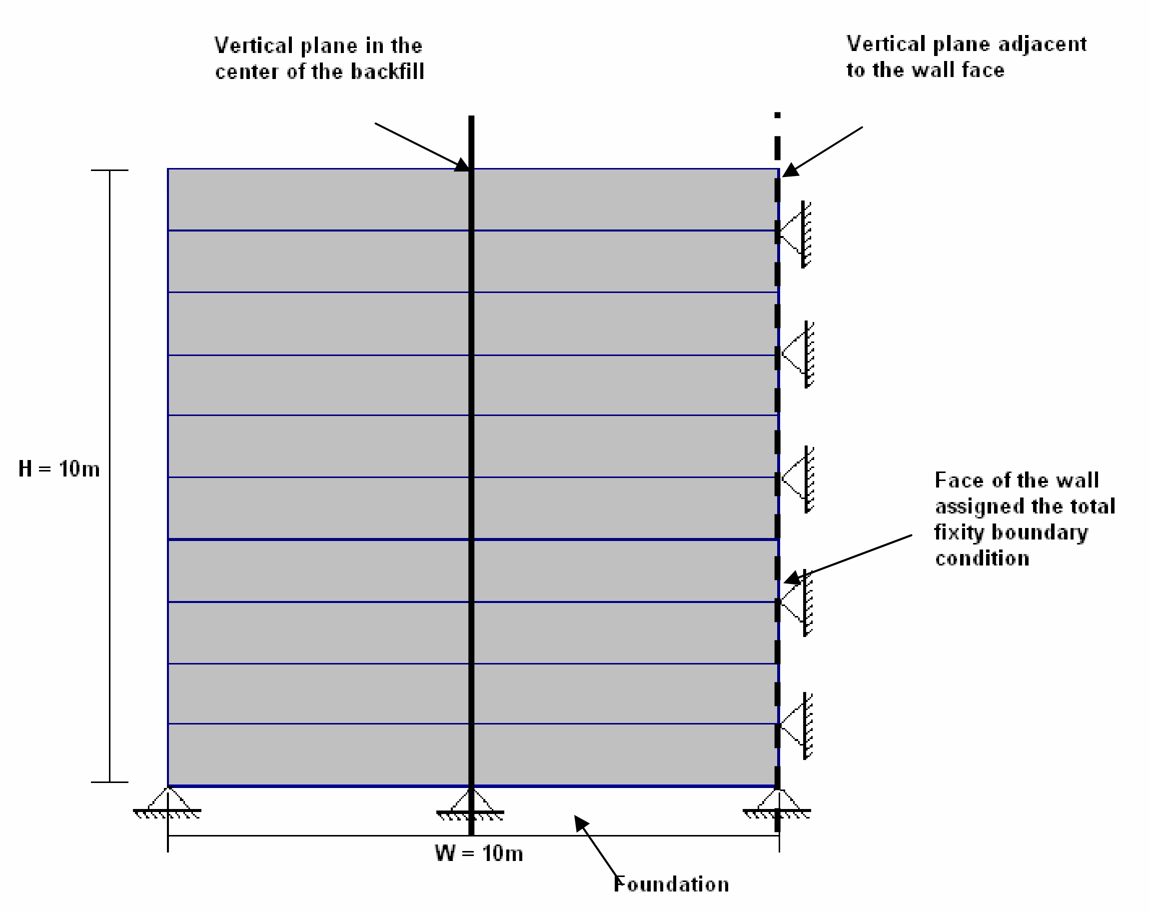

Figure 7.6: Locations of vertical planes in the center of the backfill and adjacent to the wall face for a wall aspect ratio equal to 1.00 (Plaxis, 2005)

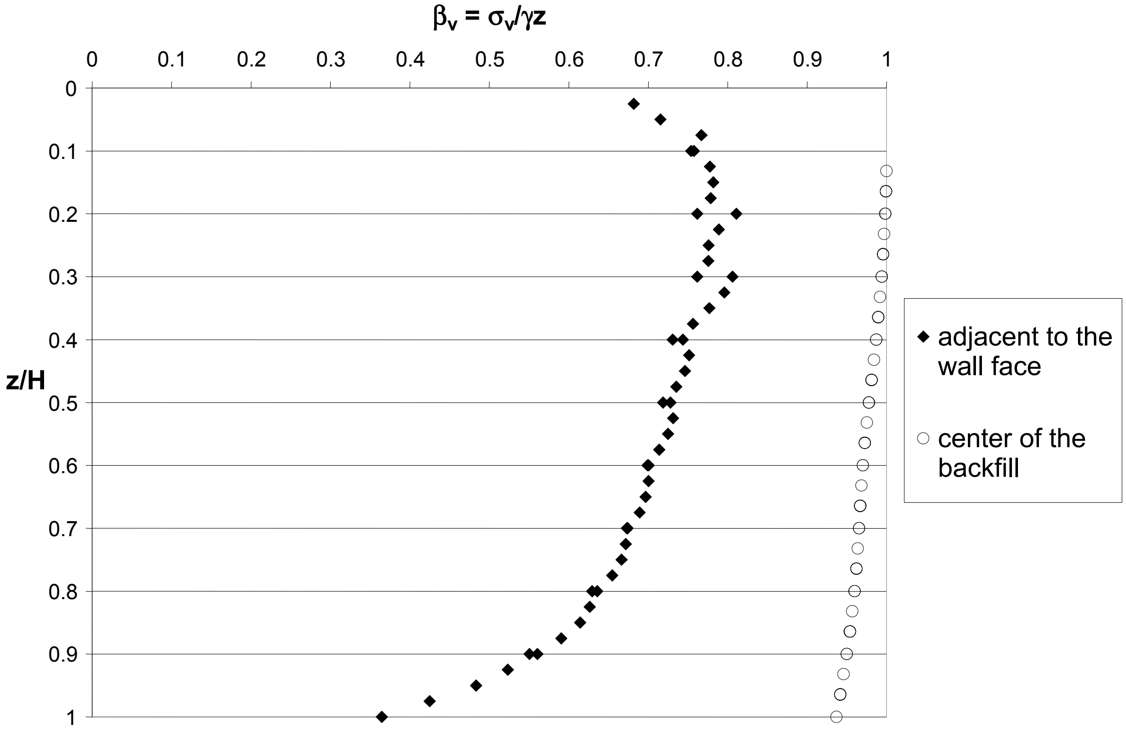

Figure 7.7: Normalized vertical stress influence factor in the center of the backfill and adjacent to the wall face for a wall aspect ratio equal to 1.00

The distribution of the vertical stress influence factor with depth for the stresses adjacent to the wall face is approximated by a straight line shown in Figure 7-8 based on the nearly linear portion of the distribution. An arithmetic average of the values adjacent to the wall face and in the center of the backfill is represented by triangles in the figure. The linear approximation tends to give values larger than those calculated by Plaxis near the top and bottom of the wall. However, it can be seen that the linear approximation does not give values that exceed the arithmetic average. The "best fit" straight line is always less than the arithmetic average and, thus, is believed to represent a conservative estimate of the vertical stress influence factors. Similar "best fit" straight lines are shown in Figures 7-9 through 7-12 for wall aspect ratios of 0.70, 0.50, 0.30, and 0.10, respectively.

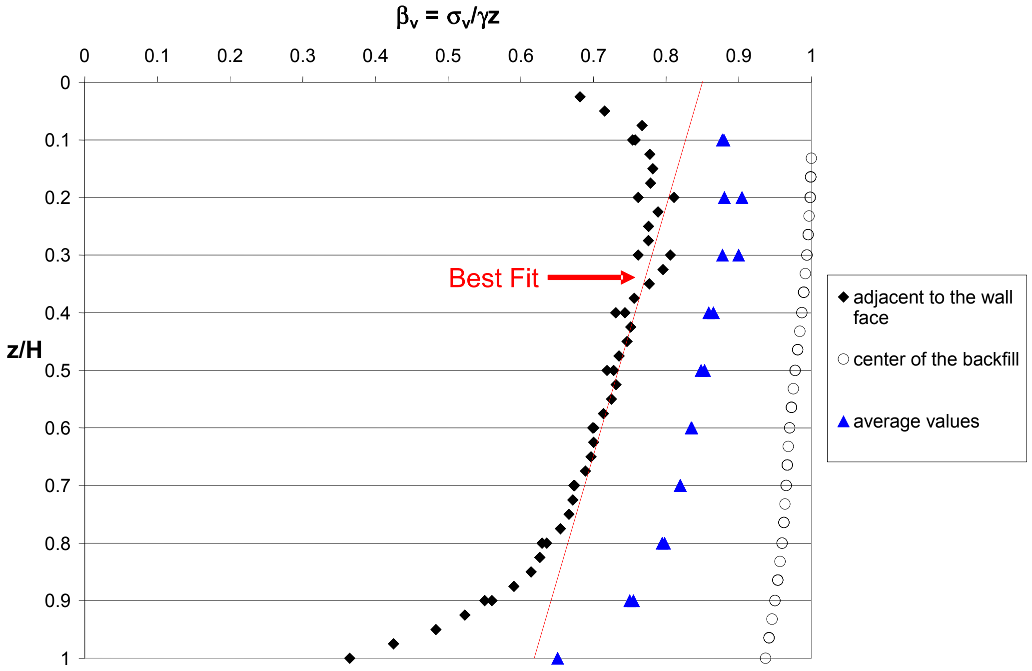

Figure 7.8: "Best fit" line for the vertical stress influence factors for a wall aspect ratio equal to 1.00

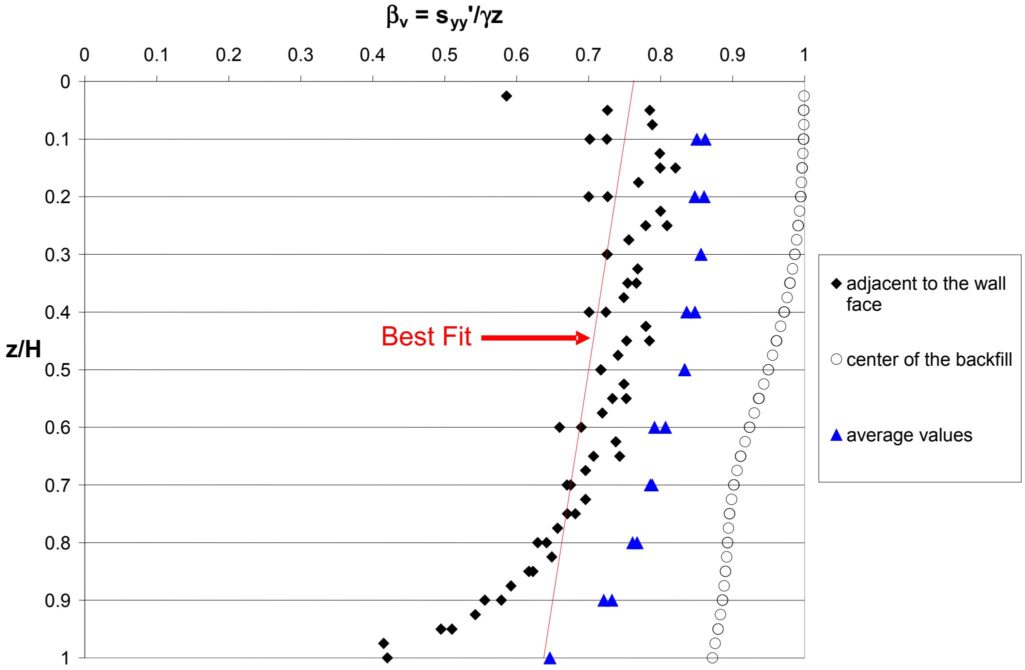

Figure 7.9: "Best fit" line for the vertical stress influence factors for a wall aspect ratio equal to 0.70

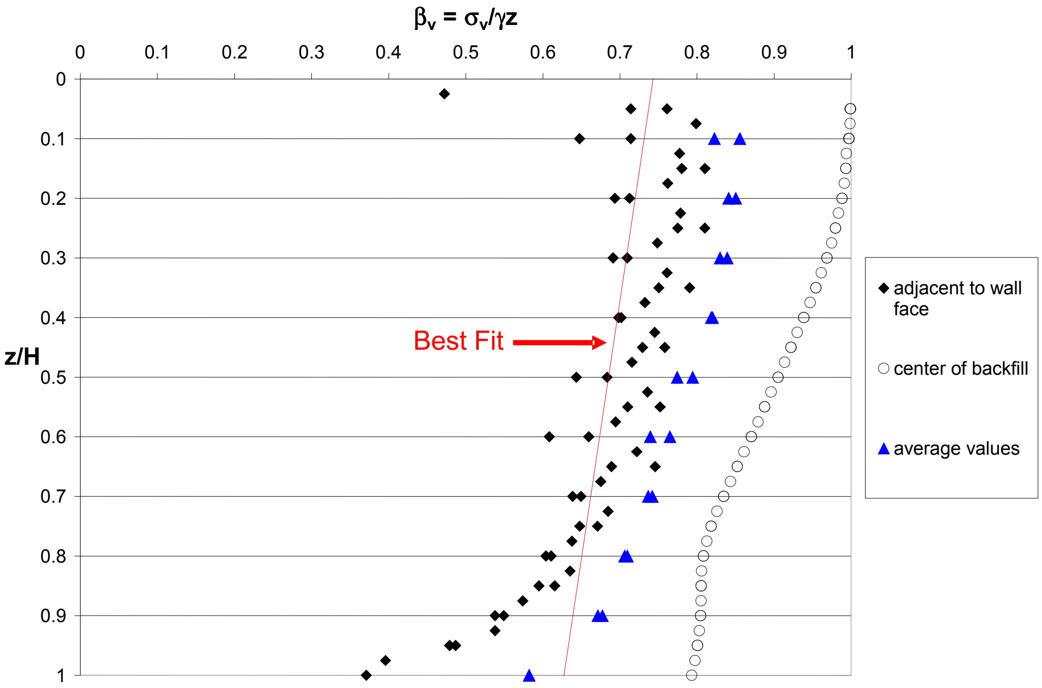

Figure 7.10: "Best fit" line for the vertical stress influence factors for a wall aspect ratio equal to 0.50

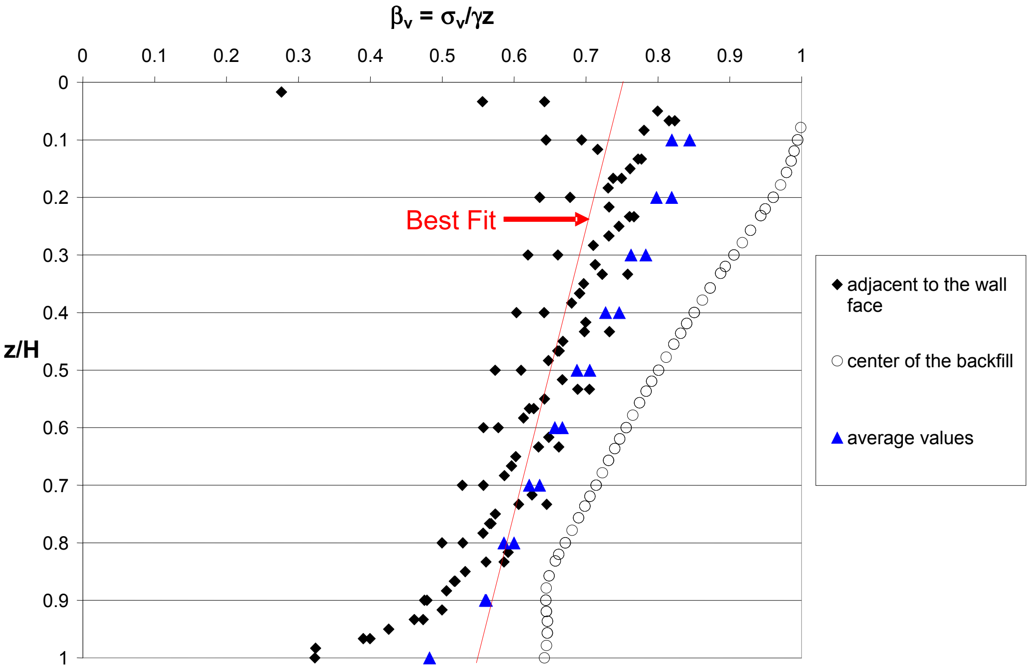

Figure 7.11: "Best fit" line for the vertical stress influence factors for a wall aspect ratio equal to 0.30

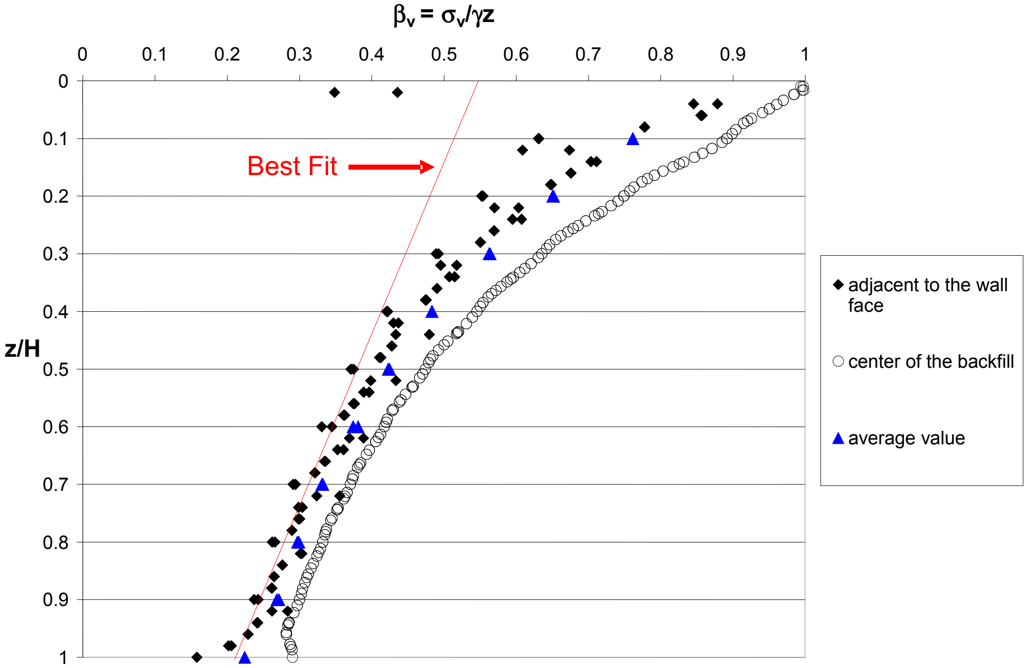

Figure 7.12: "Best fit" line for the vertical stress influence factors for a wall aspect ratio equal to 0.10

The linear "best fit" straight lines shown in Figures 7-8 through 7-12 can be defined by the values of β_v at the top (z/H = 0) and bottom (z/H = 1.0) of the wall. The values of β_v at the top and bottom for each wall aspect ratio are plotted in Figure 7-13 and summarized in Table 7-1. Smooth curves were drawn in Figure 7-13 to show the variations in vertical stress influence factors with wall aspect ratio. The values of the vertical stress influence factors corresponding to these curves are also tabulated in Table 7-2. It can be seen that the values from the smooth curves are very similar to the actual computed values shown in Table 7-1.

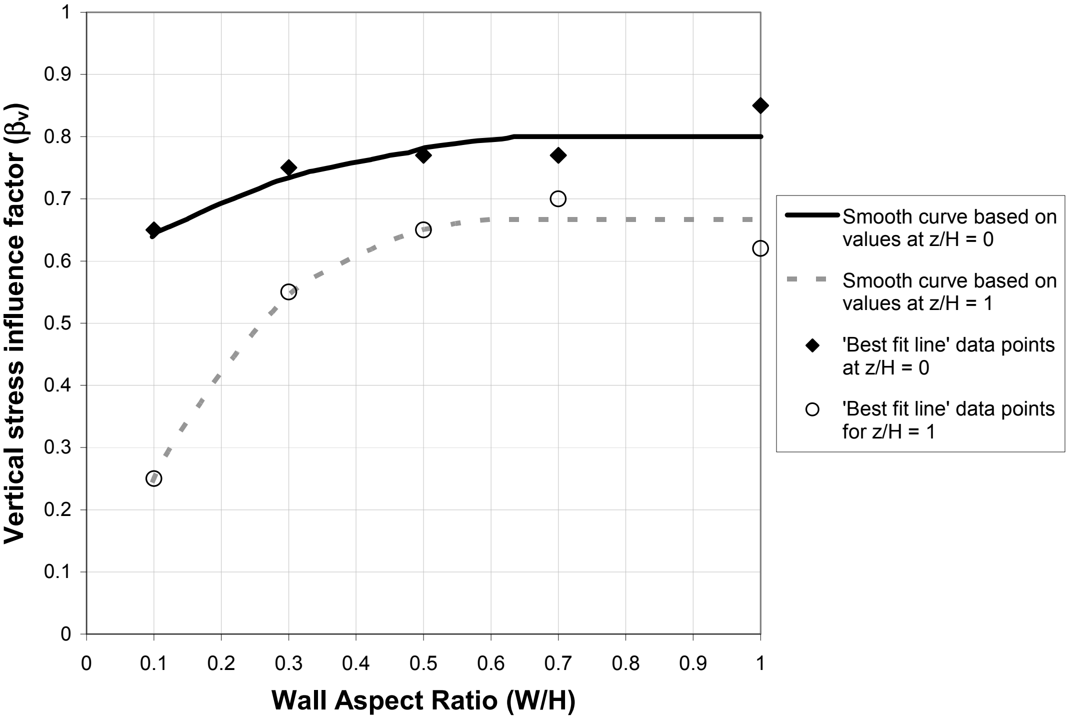

Figure 7.13: Values of the vertical stress influence factors at the top and bottom of the wall plotted as a function of the wall aspect ratio

Table 7.1: Values of β_v plotted in Figure 7-13

Aspect Ratio	β_v (z/H = 0)	β_v (z/H = 1)
1.0	0.85	0.62
0.7	0.77	0.70
0.5	0.77	0.65
0.3	0.75	0.55
0.1	0.65	0.25

Table 7.2: Values of β_v based on smooth curves in Figure 7-13

Aspect Ratio	β_v (z/H = 0)	β_v (z/H = 1)
1.00	0.80	0.67
0.70	0.80	0.67
0.50	0.78	0.65
0.30	0.73	0.54
0.10	0.64	0.25

The values presented in Figure 7-13 were developed for a friction angle of 37 degrees. To determine the applicability of Figure 7-13 for other friction angles, a sensitivity study was performed by repeating the calculations for friction angles of 30° and 44° and wall aspect ratios equal to 1.00, 0.70, 0.50, 0.30, and 0.10. Again, linear "best fit" straight lines were fit to the variation in vertical stress influence factors with depth. The resulting values of β_v are plotted in Figure 7-14. The smooth curves drawn previously to approximate β_v when $\phi' = 37°$ appear to provide a reasonable approximation for friction angles of 30° and 44° as well. The small differences in values of β_v for various friction angles may be a result of fitting straight lines to approximate the variation in vertical stress influence factors with depth. Based on the sensitivity study, the values of the vertical stress influence factors shown in Table 7-2 should be representative of values for any reasonable friction angle and an interface reduction factor equal to 0.667.

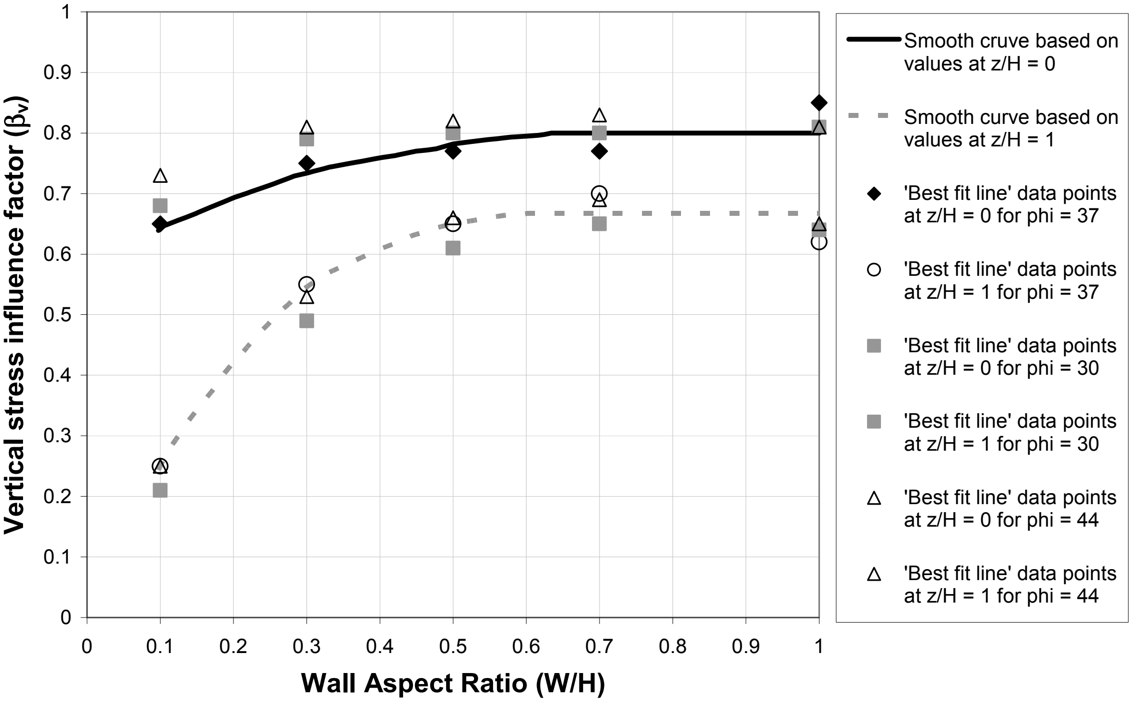

Figure 7.14: Values of β_v determined from sensitivity study

7.2 Definitions of horizontal earth pressure coefficients

The horizontal earth pressure coefficients discussed in Chapters 5 and 6 were defined as the ratio of the horizontal stress (σ_h) to overburden pressure (γz). However, the horizontal earth pressure coefficient may also be defined as the ratio of horizontal stress (σ_h) to vertical stress (σ_v). The potential differences in the two definitions of the earth pressure coefficients calculated from a finite element simulation of a nondeformable wall with an aspect ratio equal to 0.70 were examined.

For the purposes of this study, the ratio of horizontal stress to overburden pressure expressed as ($\sigma_h/\gamma z$) will be referred to as k_{ob} and the ratio of actual horizontal stress to actual vertical stress expressed as (σ_h/σ_v) will be referred to as k_{sr}. The vertical stresses used to compute k_{sr} are the ones calculated by Plaxis and discussed in detail in Section 7.1. The variation of the horizontal earth pressure coefficients with the nondimensional depth (z/H), expressed as k_{ob} and k_{sr}, at the center of the backfill are shown in Figure 7-15. As the nondimensional depth, z/H increases, the horizontal earth pressure coefficients based on the overburden pressure (k_{ob} =

$\sigma_h/\gamma z$) are lower than the values of the horizontal earth pressure coefficients based on the actual stress ratio ($k_{sr} = \sigma_h/\sigma_v$). Both distributions are nearly constant with depth.

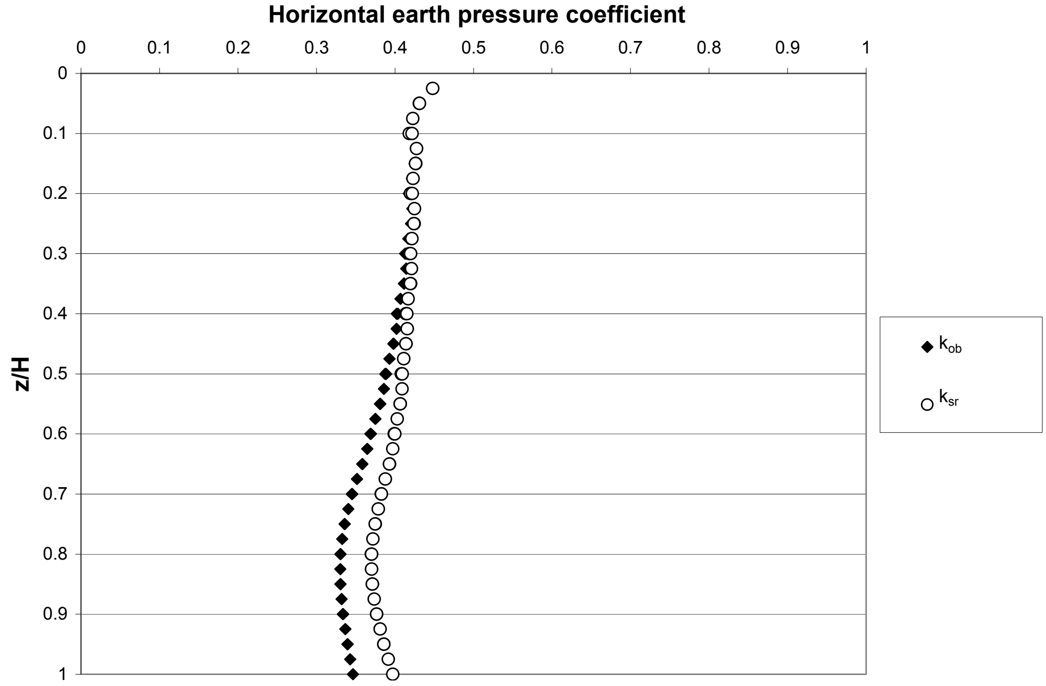

Figure 7.15: Variation in the horizontal earth pressure coefficients expressed by k_{ob} and k_{sr} at the center of the backfill with the nondimensional depth (z/H).

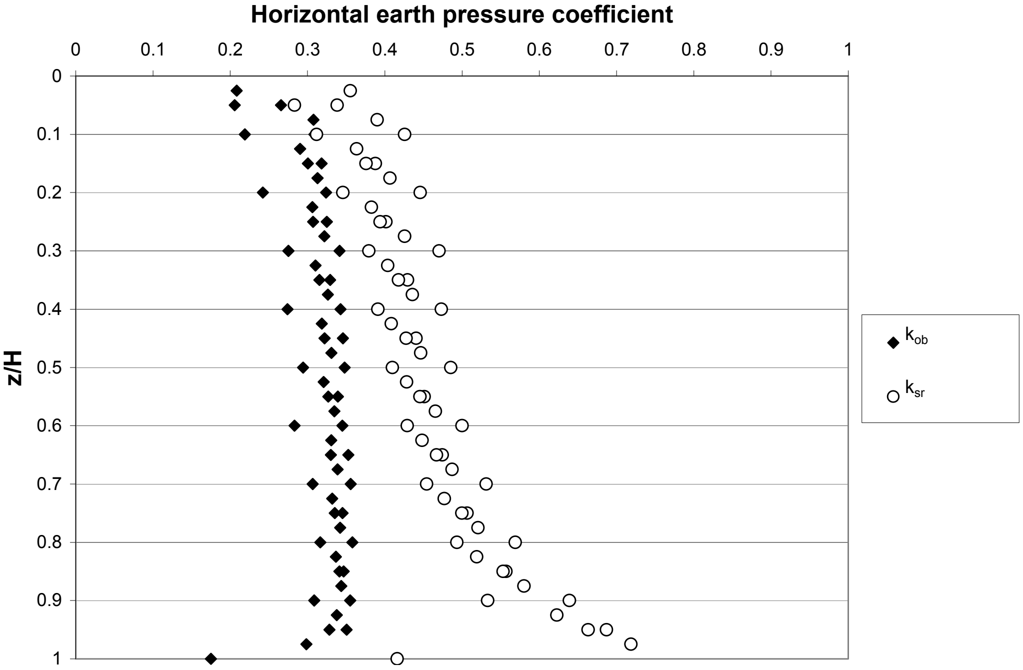

Figure 7.16: Variation in the horizontal earth pressure coefficients expressed by k_{ob} and k_{sr} adjacent to the wall face with the nondimensional depth (z/H).

Figure 7-16 shows the variation in the horizontal earth pressure coefficients similar to those shown in Figure 7-15, but for the earth pressures at the wall face. The horizontal earth pressure coefficients plotted in Figure 7-16 based on the overburden pressure are nearly constant for all values of z/H. On the other hand, the horizontal earth pressure coefficients based on the actual vertical stress increased as the values of z/H increased. This increase is due to the decrease in the vertical stress influence factors with depth rather than a reflection of proportionately higher horizontal stresses.

The earth pressure coefficients (k_{ob}) based on the ratio of horizontal stress to overburden pressure ($\sigma_h/\gamma z$) were judged to be more convenient because the earth pressure coefficient does not vary significantly with depth and overburden pressures can be calculated more easily than the vertical stresses. Therefore, the horizontal earth pressure coefficients presented hereafter will be expressed as a ratio of horizontal stress to overburden pressure.

7.3 Effect of wall aspect ratio on horizontal earth pressures for nondeformable walls

To determine how the values of the horizontal earth pressure coefficient varied with wall aspect ratio a series of finite element analyses was performed for wall aspect ratios of 0.70, 0.50, 0.30, and 0.10. The horizontal stresses were examined along vertical planes adjacent to the wall face and in the center of the backfill. The horizontal stresses (σ_h) were expressed by horizontal earth pressure coefficients. The symbol, k_w, was used to represent the horizontal earth pressure coefficients along a vertical plane adjacent to the wall face and k_c was used to represent the horizontal earth pressure coefficients along a vertical plane in the center of the backfill. The horizontal earth pressure coefficients are presented here as normalized values by dividing the horizontal earth pressure coefficients by the theoretical active earth pressure coefficient (K_a). In Figure 7-17, the variation of k_w/K_a and k_c/K_a are plotted versus the nondimensional depth (z/H) below the top of the wall for an aspect ratio of 0.70. The values of the horizontal earth pressure coefficients at the center of the backfill are greater than the values at the wall for depths less than about 60 percent of the wall height, i.e. z/H < 0.60. For depths greater than 60 percent of the wall height (z/H > 0.60), the horizontal earth pressure coefficients at the centerline of the backfill and face of the wall are generally similar.

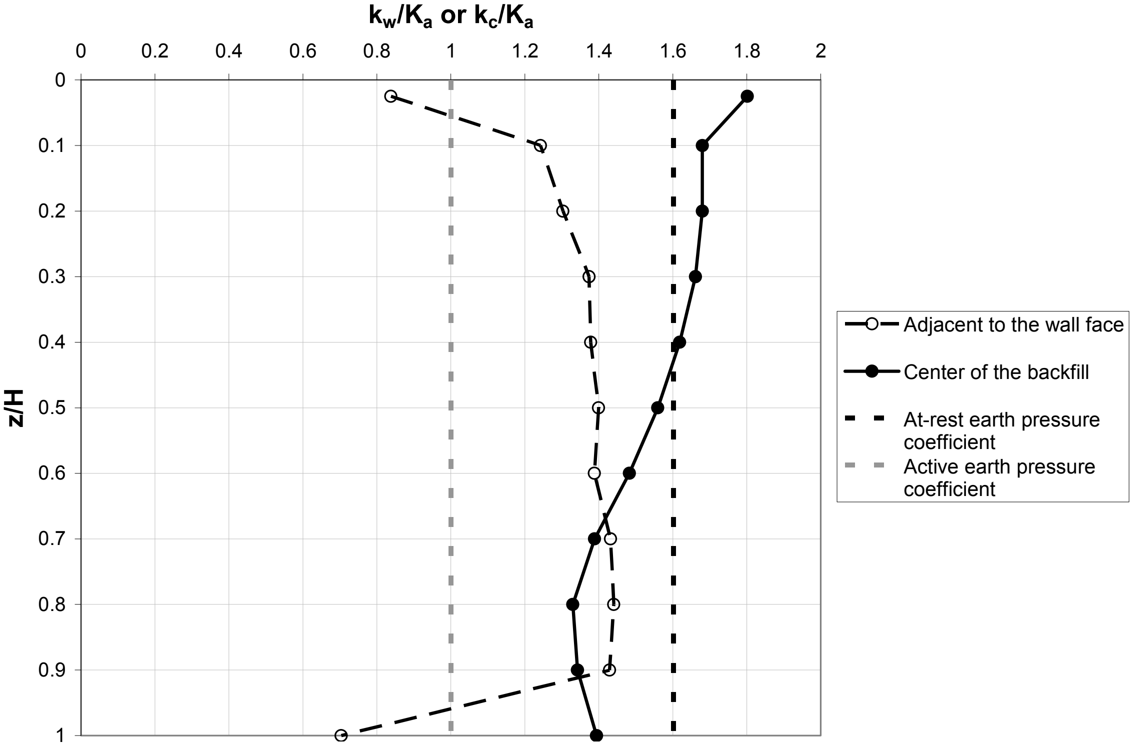

Figure 7.17: Distribution of horizontal earth pressure coefficients adjacent to the wall face and in the center of the backfill for a wall aspect ratio equal to 0.70

The variation of the normalized horizontal earth pressure coefficients with depth for wall aspect ratios of 0.70, 0.50, 0.30 and 0.10 adjacent to the wall face and at the center of the backfill are shown in Figures 7-18 and 7-19, respectively. The normalized earth pressure coefficients at the wall face decrease as the wall aspect ratio decreases (Figure 7-18). The horizontal earth pressure coefficients also tend to decrease with depth, particularly as the wall aspect ratio decreases. The normalized earth pressure coefficients at the center of the backfill decrease as the wall aspect ratio decreases. In addition, the normalized earth pressure coefficients decrease with depth and the rate of decrease becomes larger as the wall aspect ratio decreases.

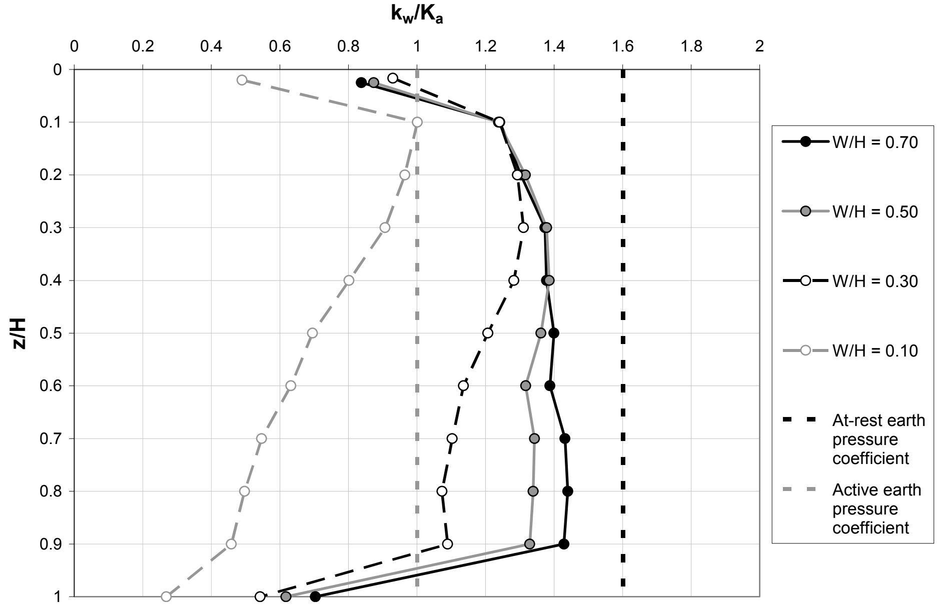

Figure 7.18: Variation in the normalized horizontal earth pressure coefficients at the wall face (k_w/K_a) with the nondimensional depth (z/H) for wall aspect ratios equal to 0.70, 0.50, 0.30, and 0.10

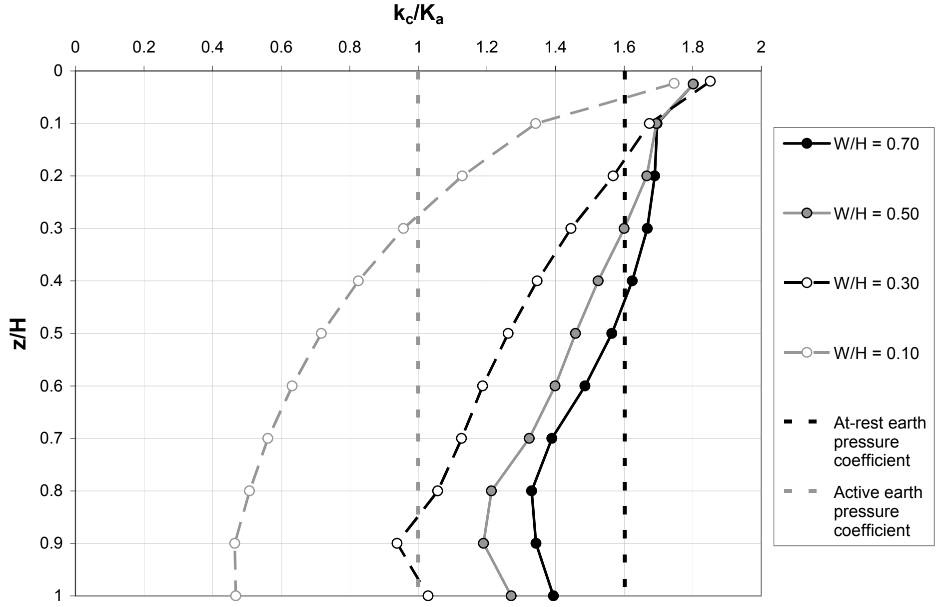

Figure 7.19: Variation in the normalized horizontal earth pressure coefficients at the center of the backfill (k_c/K_a) with the nondimensional depth (z/H) for wall aspect ratios equal to 0.70, 0.50, 0.30, and 0.10

The equivalent horizontal earth pressure coefficient (K_{eq}) corresponding to the total equivalent force, F_{eq}, on the vertical plane adjacent to the wall face and at the center of the backfill was calculated for the distributions of horizontal earth pressures represented in Figures 7-18 and 7-19. The equivalent total force, $F_{eq,}$ was obtained by integrating the horizontal stresses from the bottom of the wall (z = 0) to the top of the wall (z = H). The relationship between the equivalent total force and the equivalent horizontal earth pressure (K_{eq}) is expressed in Equation 7-1.

$$F_{eq} = \frac{1}{2}\gamma K_{eq} H^2 \qquad \text{Eq. 7-1}$$

Thus,

$$K_{eq} = \frac{F_{eq}}{\frac{1}{2}\gamma H^2} \qquad \text{Eq. 7-2}$$

The values of K_{eq} normalized by the theoretical active earth pressure coefficient (K_a) are plotted versus the wall aspect ratio in Figure 7-20. In addition to the values of K_{eq}/K_a calculated by Plaxis, the values of K_{eq}/K_a computed using Spangler and Handy's equation, and the theoretical at-rest and active earth pressure coefficients are shown in Figure 7-20. The values calculated by Plaxis at the center of the backfill are approximately 10 percent greater than the values computed using Spangler and Handy's equation, i.e. K_{eq} calculated by Plaxis at the center of the backfill equals K_{eq} computed by Spangler and Handy's equation multiplied by 1.1. Thus an improved estimate of the equivalent horizontal earth pressure coefficient may be calculated by increasing the value of K_{eq} computed using Spangler and Handy's equation by 10 percent.

As the wall aspect ratio decreases, the values of K_{eq}/K_a decrease. When the wall aspect ratio is 0.70, which the state-of-practice suggests as a minimum value, the value of K_{eq} for the center of the backfill is approximately 10 percent less than the value of K_0. For wall aspect ratios less than 0.25, the values of K_{eq} are less than the value of the theoretical active earth pressure coefficient; however, walls are not expected to be built with such low aspect ratios.

Although Figure 7-20 is based on a single friction angle of 37°, Leshchinsky, Hu, and Han (2003) suggest that normalizing the horizontal earth pressure coefficient in walls with narrow backfills by the Rankine active earth pressure coefficient significantly reduces the effect of the angle of internal friction on the equivalent horizontal earth pressure coefficient. Leshchinsky, Hu, and Han found the horizontal earth pressure coefficients normalized in this manner did not vary more than 3 percent for friction angles ranging from 25° to 45°.

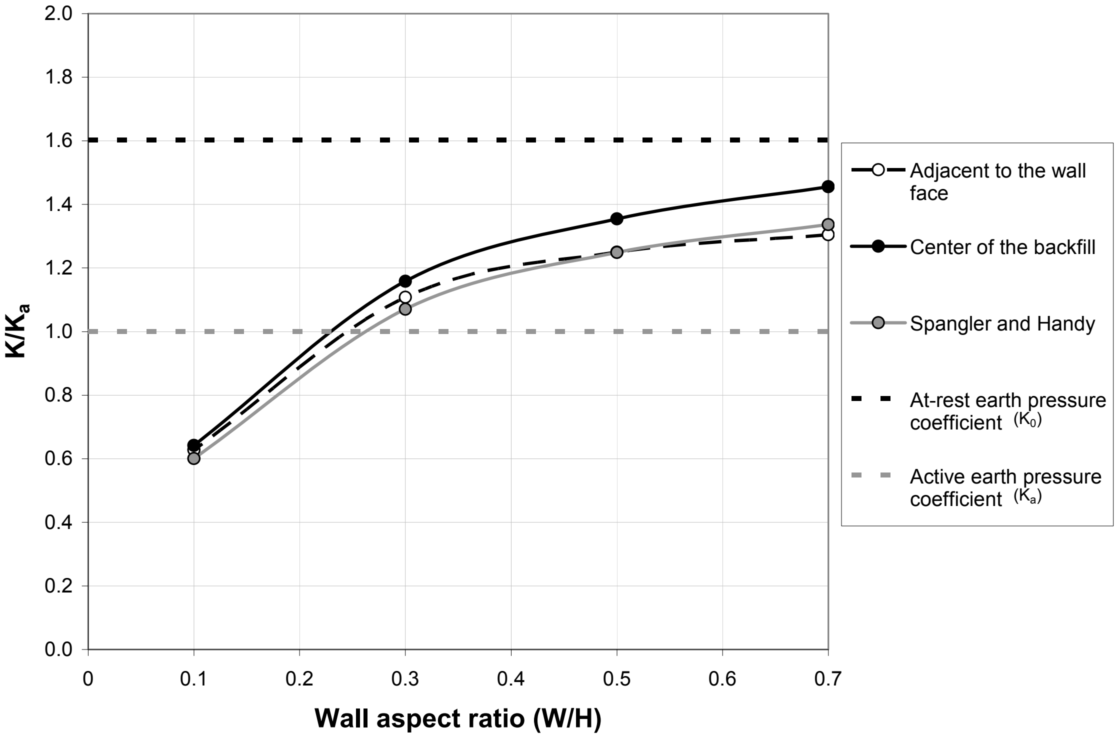

Figure 7.20: Normalized equivalent horizontal earth pressure coefficients along the wall and in the center of the backfill versus wall aspect ratios

7.4 Comparison of horizontal earth pressure coefficients calculated by Plaxis to values recommended by current FHWA design guidelines

The horizontal earth pressure coefficients calculated by Plaxis at the center of the backfill (k_c) for a wall aspect ratio equal to 0.70 are plotted versus the values recommended by the current Federal Highway Administration (FHWA) MSE wall design guidelines in Figure 7-21(Elias et al., 2001). The values of (k_c) were normalized by the active earth pressure coefficient (K_a). The values of the normalized horizontal earth pressure coefficients (k_c/K_a) calculated by Plaxis for a wall aspect ratio equal to 0.70 agree favorably with the values recommended by the FHWA design guidelines for metal bars, mats and welded wire grids, i.e. very stiff, inextensible reinforcement.

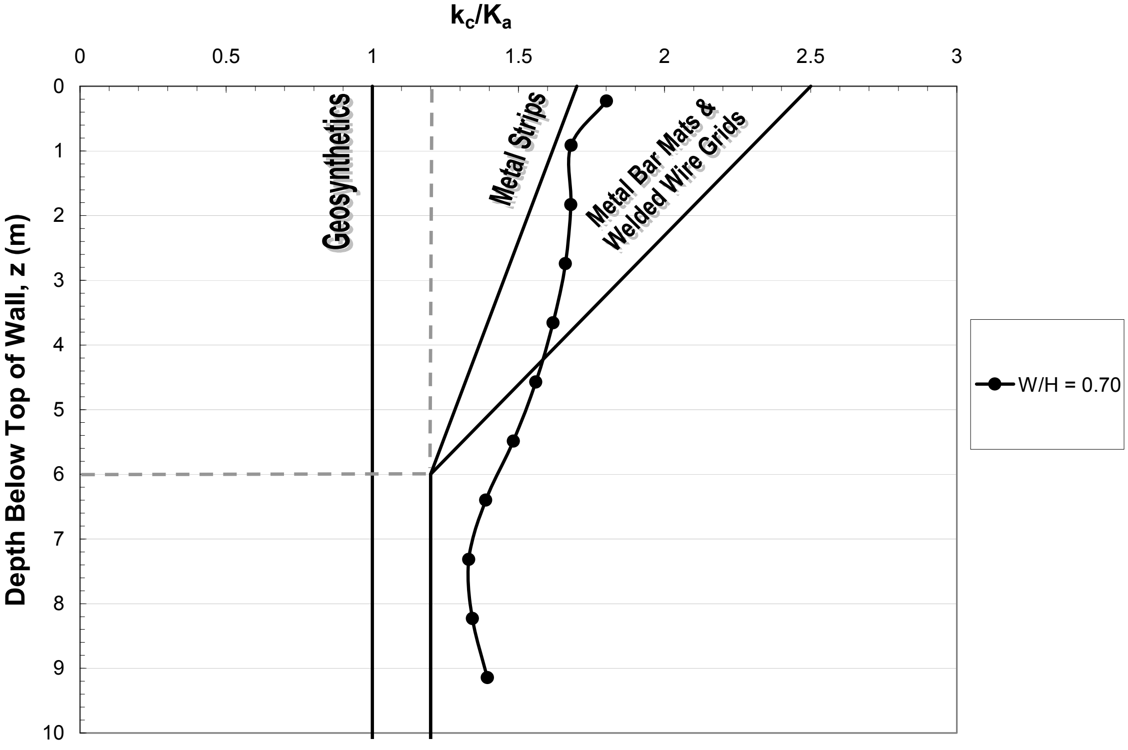

Figure 7.21: Variation of the normalized horizontal earth pressure coefficients with depth in the center of the wall versus the current FHWA MSE wall design guideline recommended values (Elias et al., 2001)

7.5 Application of reduced earth pressures for the internal stability design of nondeformable walls placed in front of an existing stable face

The current FHWA design guidelines do not account for the effects wall aspect ratio on the stresses behind MSE walls. The remainder of this chapter suggests ways in which the wall aspect ratio and results described in Sections 7.1 and 7.3 can be incorporated into current FHWA design guidelines for design of MSE walls using inextensible reinforcement, i.e. metal strips, metal bar mats, and welded wire grids, are explored.

Internal stability is based on two failure criteria: breakage and pullout of the reinforcement. Breakage occurs when the tension in the reinforcement is greater than the tensile strength of the reinforcing material and the reinforcement ruptures or breaks. Pullout occurs when the embedded end of the reinforcement pulls out from the soil because the interaction between reinforcement and the surrounding soil is not sufficient to prevent the reinforcing strip from pulling out.

7.5.1 Breakage

The factor of safety against breakage ($F_{breakage}$) is defined in the current design guidelines as

$$F_{breakage} = \frac{T_{allowable}}{T_{max.i}}$$ Eq. 7-3

where $T_{max,i}$ is the maximum tensile force per unit width of reinforcement at a given layer, i and $T_{allowable}$ is the allowable tensile force per unit width of reinforcement (Elias et al., 2001). The value of $T_{max,i}$ is equal to the maximum horizontal stress applied from the reinforced fill. In the current design guidelines $T_{max,i}$ is calculated using the following equation,

$$T_{max,i} = \left(\frac{k_r}{K_a}\right) K_a \sigma_{ov} S_v$$ Eq. 7-4

where k_r is the horizontal earth pressure coefficient based on empirical measurements of stresses in the reinforcement, K_a is the theoretical Rankine active earth pressure coefficient, S_v is the vertical spacing between layers of reinforcement and σ_{ov} is the vertical overburden pressure at the depth of the reinforcement. The value of k_r/K_a is found using Figure 7-22 for the type of reinforcement (geosynthetic, metal strip, or metal bar mats and welded wire grids) and the depth of the reinforcing layer (z). The vertical overburden pressure is found by multiplying the unit weight of the backfill (γ) by the depth of the i-th layer of reinforcement below the top of the MSE wall (z), i.e. $\sigma_{ov} = \gamma z$.

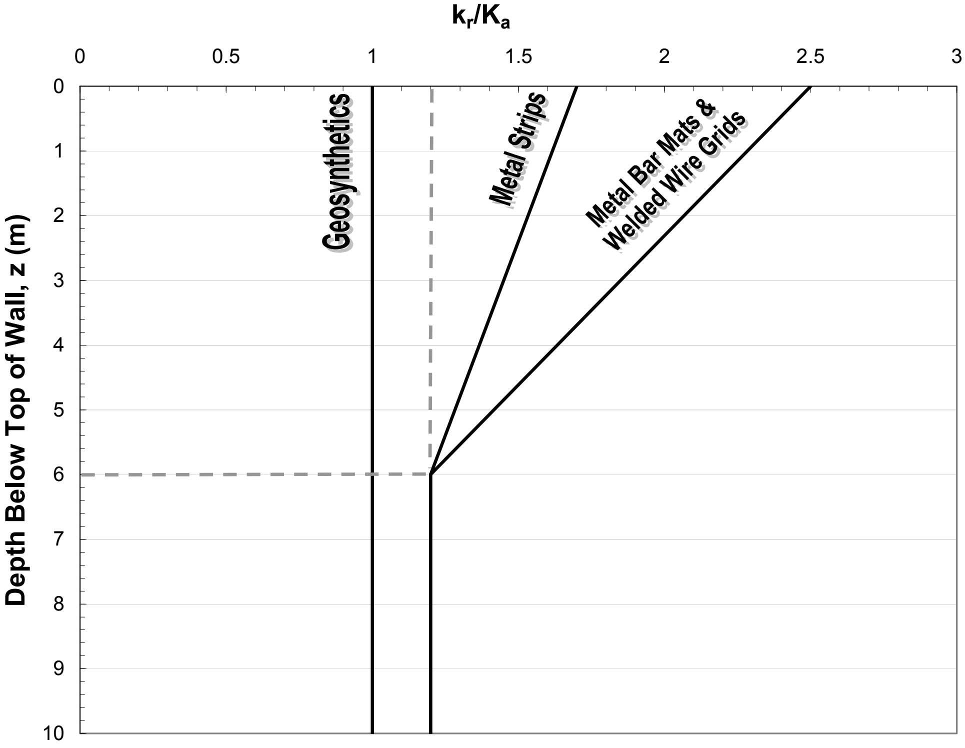

Figure 7.22: Design chart used to calculate the value of $T_{max,i}$ in the FHWA design guidelines (Elias et al., 2001)

The allowable tensile force per unit width of inextensible reinforcement is a material property of the reinforcement and for steel can be calculated using Equation 7-5.

$$T_{allowable} = \frac{0.55 * F_y * A_c}{b} \qquad \text{Eq. 7-5}$$

where A_c is the design cross-section area of the steel reinforcement (original cross-section minus losses due to corrosion during the design life of the wall), b is the width of the reinforcement strip, sheet or grid, and F_y is the yield stress of steel (typically 65 ksi).

In the case of walls with a reduced aspect ratio, the maximum force in the reinforcement, $T_{max,i}$ is calculated from Equation 7-4 written in the form,

$$T_{max,i} = \left(\frac{k_c}{K_a}\right) K_a \sigma_{ov} S_v \qquad \text{Eq. 7-6}$$

where k_c/K_a is determined from Figure 7-23. The values of k_c/K_a are based on the analyses and results presented and discussed in Section 7.3. Other than substituting the values of k_c/K_a for the values of k_r/K_a in Equation 7-6, the procedures for calculating a factor of safety against breakage ($F_{breakage}$) are the same as those for walls with conventional wall aspect ratios.

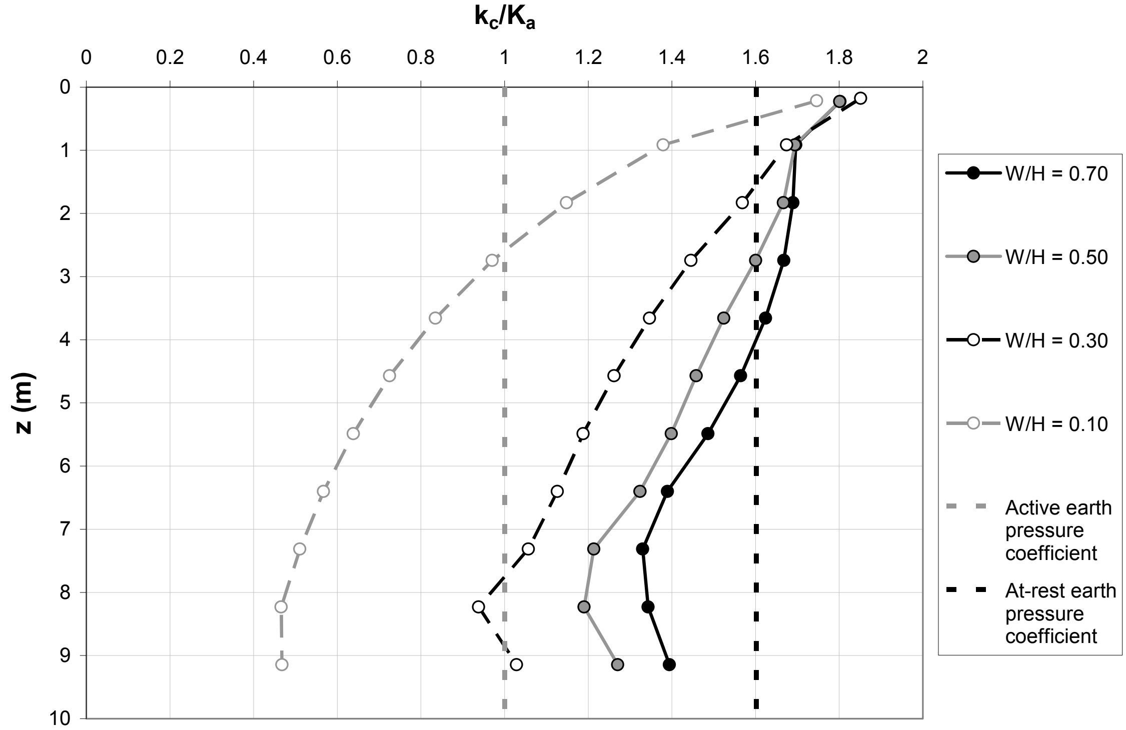

Figure 7.23: Proposed design chart produced from Plaxis simulations of nondeformable walls placed in front of an existing stable face for wall aspect ratios equal to 0.70, 0.50, 0.30, and 0.10.

7.5.2 Pullout

The factor of safety against pullout ($F_{pullout}$) is defined in the current design guidelines as

$$F_{pullout} = \frac{P_{r,i}}{T_{max,i}} \qquad \text{Eq. 7-7}$$

where $P_{r,i}$ is the pullout resistance of reinforcement in a given layer, i and $T_{max,i}$ is the maximum tensile force per unit width of reinforcement in a given layer, i (Elias et al., 2001). The value of $P_{r,i}$ is defined as follows:

$$P_{r,i} = F^{*}\sigma_{ov} L_e C R_c \alpha \qquad \text{Eq. 7-8}$$

where C is the reinforcement effective unit perimeter (assigned a value of 2 for strips), F^{*} is the pullout resistance (equal to 1.2 + log(C_u) for steel ribbed reinforcement), C_u is the uniformity coefficient of the backfill (equal to 4 when specific value is unknown at time of design), L_e is the embedment length of the reinforcement behind the failure surface, R_c is the coverage ratio (equal to b/S_h), where b is the width of the reinforcing strip or bar, S_h is the horizontal spacing between strips of reinforcement, S_v is the vertical spacing between strips of reinforcement, and α is the scale correction factor which accounts for non-linear stress reduction and is assigned a value of 1.0 for metallic reinforcement. The value of $T_{max,i}$ is the same as the value calculated using Equation 7-3.

In the case of wall with a reduced wall aspect ratio, the value of $T_{max,i}$ is calculated from Equation 7-6 rather than Equation 7-4. Also, the factor of safety against pullout is now calculated from the expression,

$$F_{pullout} = \left(\frac{1}{T_{max,i}}\right) F^{*}\sigma_{vr} L_e C R_c \alpha \qquad \text{Eq. 7-9}$$

where σ_{vr} is the reduced overburden pressure computed from,

$$\sigma_{vr} = \gamma\ z\beta_v \qquad \text{Eq. 7-10}$$

and β_v is the vertical stress influence factor shown in Figure 7-24. The vertical stress influence factors are based on the analyses presented previously in Section 7.1.

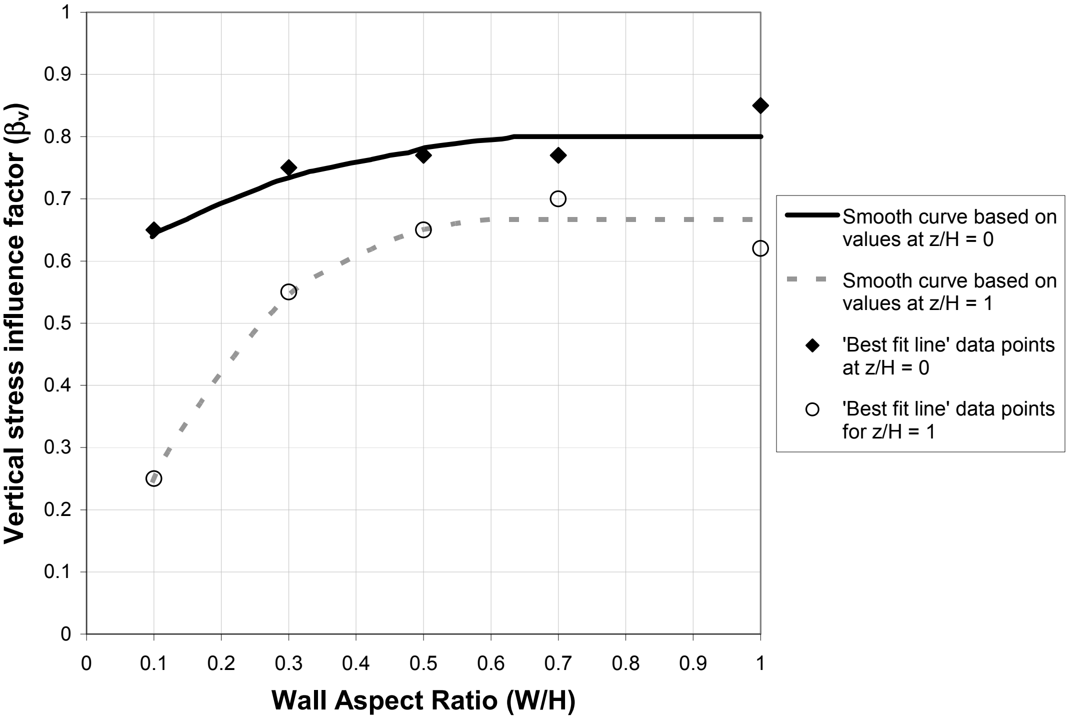

Figure 7.24: Values of the vertical stress influence factor, β_v at the top and bottom of the wall plotted as a function of the wall aspect ratio

7.6 Summary and Conclusions

In this chapter the effect of wall aspect ratio on both the vertical and horizontal earth pressures was examined for the case of a nondeformable wall placed in front of a stable face. A vertical stress influence factor (β_v) was introduced to describe how soil-wall interaction decreased the vertical stresses behind a wall. The vertical stress influence factor was shown to decrease horizontally from the center of the backfill to the wall face, with depth below the top of the wall and with decreasing wall aspect ratio.

Horizontal earth pressures were also examined. Two definitions of horizontal earth pressure coefficient were explored and it was decided that a horizontal earth pressure coefficient defined as the ratio of horizontal stress to vertical overburden pressure ($\sigma_h/\gamma z$) was the most useful. Values of this horizontal earth pressure coefficient were calculated along vertical planes at two locations: in the center of the backfill (k_c) and adjacent to the wall face (k_w). The values of k_c and k_w were then normalized by dividing them by the theoretical Rankine active earth pressure coefficient. The horizontal earth pressure coefficients were slightly higher along a vertical plane in the center of the backfill than along a vertical plane adjacent to the wall face. Thus, the horizontal earth pressure coefficients calculated at the center of the wall are conservative. It was found that the normalized horizontal earth pressure coefficients also decreased as the wall aspect ratio decreased. It was shown that values of the equivalent horizontal earth pressure coefficient (K_{eq}) calculated using Spangler and Handy's equation agreed favorably with the values of K_{eq} calculated by Plaxis. In fact, values of K_{eq} may be estimated quite well by increasing the values of K_{eq} computed from Spangler and Handy's equation by 10 percent.

The reduced vertical and horizontal stresses can be introduced into current design equations to calculate factors of safety against pullout ($F_{pullout}$) and breakage ($F_{breakage}$). The effect of wall aspect ratio on the horizontal earth pressures can be applied to current design equations by substituting the values of k_c/K_a for the values of k_r/K_a when calculating the driving force ($T_{max,i}$). The values of k_c/K_a can be determined using Figure 7-23. The effect of wall aspect ratio on the vertical stresses can be applied to current design equations by reducing the vertical overburden stress (σ_{ov}) by the vertical stress influence factor (β_v) when calculating the pullout resistance, $P_{r,i}$, in a given layer of reinforcement. The values of β_v can be determined using Figure 7-24. The factors of safety against pullout and breakage are applied to the internal stability of MSE walls. Both modes of instability have been considered in this chapter. In the next chapter the effect of wall aspect ratio on the more general global stability will be examined.

Chapter 8. Limit Equilibrium Analyses of Nondeformable MSE Walls in Front of a Stable Face

Limit equilibrium analyses were performed using the UTEXAS4 software program to evaluate the stability of MSE walls placed in front of a stable face. Limit equilibrium analyses were used in addition to the finite element analyses because they are commonly used in geotechnical practice to evaluate the stability of MSE walls. Also the UTEXAS4 software was able to model the soil and reinforcement properties, and quickly locate both the critical circular and noncircular slip surfaces. The shape of the slip surface is of interest because current design guidelines do not address the shape of the critical slip surface for MSE walls placed in front of a stable face or for MSE walls with wall aspect ratios (L/H) less than 0.70.

The limit equilibrium analyses do not consider displacements or strains directly. Accordingly, with limit equilibrium analyses no distinction is made between deformable and nondeformable walls.

In this chapter, the manner in which MSE walls were modeled using UTEXAS4 is discussed first. Results of the limit equilibrium analyses are then presented and discussed including conclusions regarding the shape and location of critical slip surfaces. Finally, design implications of the limit equilibrium analyses are presented.

8.1 Modeling a nondeformable MSE wall placed in front of a stable face using UTEXAS4

An example of a nondeformable MSE wall placed in front of a stable face is shown in Figure 8-1. A fixed height (H) of 30 ft was assumed for all the limit equilibrium analyses. The width of the backfill (W) was varied to investigate the influence of wall aspect ratio. Analyses were performed for wall aspect ratios of 0.70, 0.50, and 0.30. All reinforcement was assumed to extend to the back of the backfill such that the length of the reinforcement (L) was equal to the width of the backfill, i.e. L = W. It was also assumed that the foundation in front of the wall and the ground surface above and behind the MSE wall were horizontal.

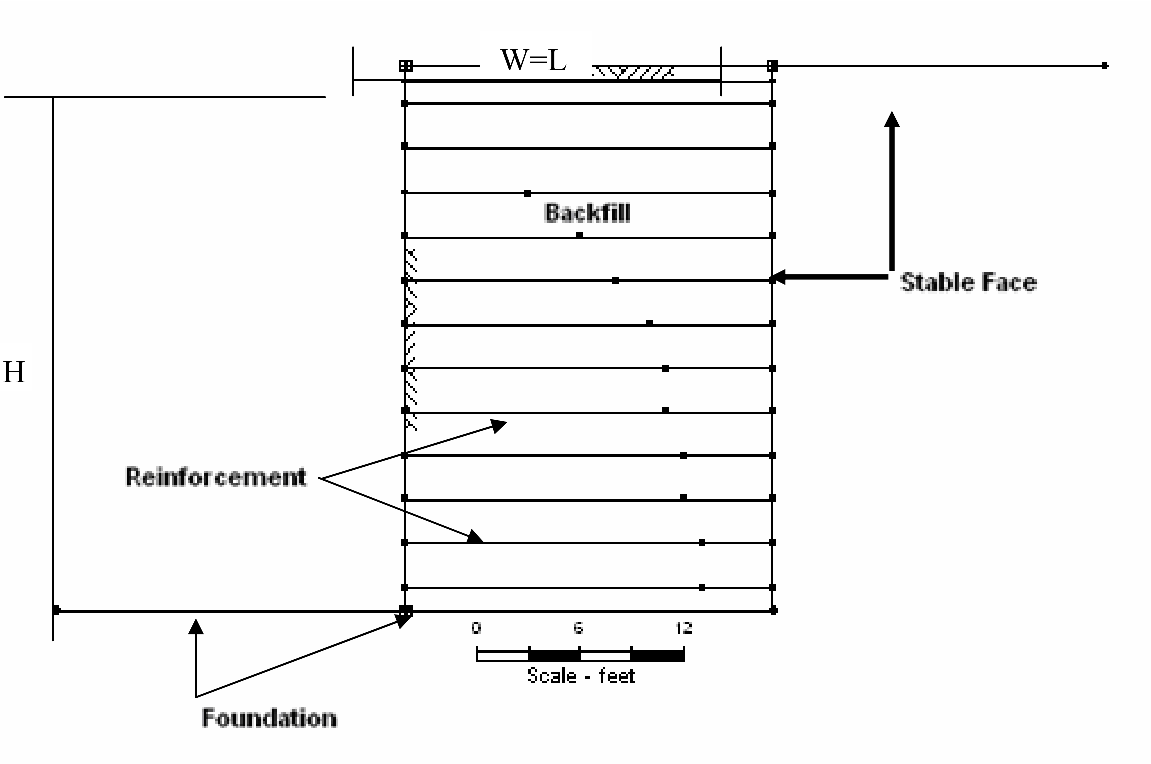

Figure 8.1: Geometry of a nondeformable MSE wall placed in front of a stable face in UTEXAS4 (Wright, 1999)

The input parameters for the limit equilibrium analyses included the soil properties, reinforcement properties, and tension crack location. Each are discussed separately in the following sections.

8.1.1 Soil properties

The backfill was assumed to be cohesionless with a unit weight (γ) of 116 pcf. An angle of internal friction (ϕ') of 37° and a cohesion (c') of zero were assumed. The values are the same as those used for the Hardening-Soil constitutive model in the Plaxis analyses described in Chapter 7.

To model the stable face shown in Figure 8-1, the material comprising the stable face was assumed to be infinitely strong such that the slip surfaces were restricted from passing through this zone. The purpose of ignoring slip surfaces passing through the "infinite strength" material is to preserve the assumption that the existing wall face is stable and constrain the search for the critical slip surface to include only the backfill, reinforcement, and foundation.

The foundation beneath the wall was assumed to be cohesionless with a unit weight of 116 pcf (17 kN/m^3. The angle of internal friction was assumed to be 30°; the cohesion was zero.

8.1.2 Reinforcement properties

The resistance provided by the reinforcement is characterized in UTEXAS4 by the longitudinal and transverse forces at selected points along each layer of reinforcement. The longitudinal force represents the resistance in the reinforcement parallel to the length of the reinforcement and the transverse force represents the resistance in the reinforcement perpendicular to the length of the reinforcement. However, it was assumed that the reinforcement only provided resistance in the longitudinal direction and the resistance in the transverse direction was assumed to be zero.

The reinforcement forces entered into UTEXAS4 are assumed to represent allowable forces for equilibrium. That is, the full forces specified as input data are applied in the equilibrium equations with no factoring or reduction. Thus, if a factor of safety is to be applied to the reinforcement, the factor of safety needs to be applied before the forces are entered as input to an analysis with UTEXAS4.

The forces in the reinforcement are limited by the ability of the reinforcement to resist failure by rupture and by pullout as discussed earlier in Chapter 7. For the limit equilibrium analyses the resistance of the reinforcement against failure by rupture was assumed to be the same for all layers of reinforcement, i.e. the same reinforcing material was assumed to be used in each layer. The available resistance was assigned based on stresses and forces in the lowest layer of reinforcement and the following assumptions: The vertical spacing (S_v) was assumed to be 2.42 ft. According to David Hutchinson, P.E., an employee of the Reinforced Earth Company, this vertical spacing corresponds to the typical vertical spacing used by his company to construct MSE walls with steel ribbed reinforcing strips attached to concrete cruciform shaped panels (personal phone conversation, April 30, 2007). In total, 13 layers of reinforcement were used in the model wall. The distance between the lowest layer of reinforcement and the bottom of the wall was assumed to be one-half the vertical spacing. Thus, the depth to the bottom layer of reinforcement below the top of the MSE wall (z) was 28.79 ft (8.84 m). A wall aspect ratio of 0.70 was assumed to calculate the horizontal stresses because the horizontal earth pressures are higher than for wall aspect ratios less than 0.70. The value of the normalized earth pressure coefficient (k_c/K_a) corresponding to a wall aspect ratio of 0.70 was selected from Figure 7-23. A value of k_c/K_a is equal to 1.31 was selected. The theoretical Rankine active earth pressure coefficient for an angle of internal friction of 37° was equal to 0.249. Thus the value of the horizontal earth pressure coefficient (k_c) used to compute the horizontal earth pressures was 0.326 (=1.31 x 0.249). The maximum horizontal (tensile) force, $T_{max,i}$, in the reinforcement was then calculated from Equation 7-6. The resulting force, $T_{max,i}$, for the bottom layer of reinforcement was 2,654 lb/ft. Finally, $T_{max,i}$ was multiplied by a factor of safety of 1.5 to obtain a reinforcement force of approximately 4,000 lb/ft. This force (4,000 lb/ft) was then assumed to be the allowable pullout resistance in the reinforcement for the limit equilibrium analyses.

The pullout resistance of the reinforcement was assumed to increase linearly from zero at the free end to a value equal to the allowable tensile strength of the reinforcement (4,000 lb/ft). Figure 8-2 illustrates the variation in longitudinal force in the reinforcement. The rate of change in force with horizontal distance, shown as S in Figure 8-2, is a function of the properties of the backfill, the type of reinforcement, the horizontal spacing (S_h) and the vertical overburden pressure (σ_{ov}). The slope of the line, labeled “S” in Figure 8-2 is given by Equation 8-1.

$$S = F^{*}\sigma_{\mathrm{ov}}\mathrm{CR}_{\mathrm{c}}\alpha_{v} \qquad \text{Eq. 8-1}$$

where C is the reinforcement effective unit perimeter (assigned a value of 2 for strips), F^* is the pullout resistance factor (equal to 1.2 + log(C_u) for steel ribbed reinforcement where C_u is the uniformity coefficient), R_c is the coverage ratio (equal to b/S_h) where b is the width of reinforcement strip and S_h is the horizontal spacing between the strips of reinforcement. Finally,

α is a scale correction factor which accounts for non-linear stress reduction (generally a value of 1.0 is assigned for metallic reinforcement), and σ_{ov} is the vertical overburden stress acting on the reinforcement. Given the slope of the line and the allowable tensile strength, the allowable embedment length (L_e) was calculated. Separate lengths of embedment were calculated for each layer of reinforcement.

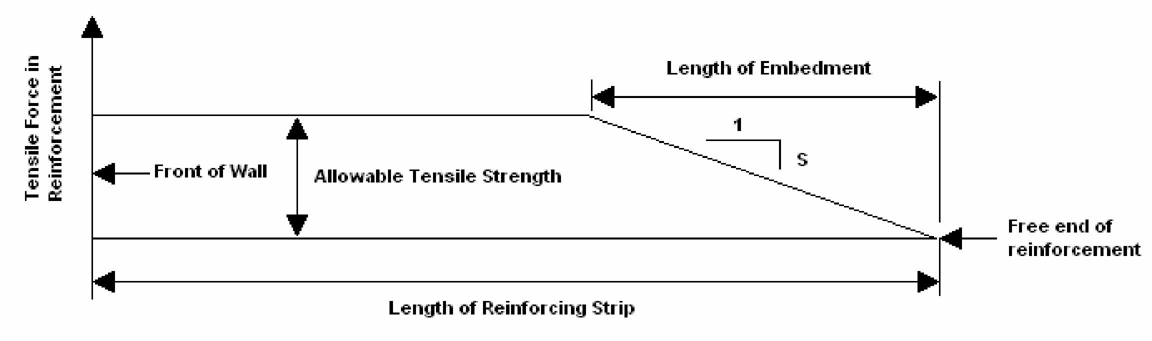

Figure 8.2: Schematic of assumed distribution of tensile stresses in the reinforcement

The slope, S, in Equation 8-1 depends on the vertical stress at the level of the reinforcement. The vertical stress is a function of the depth of the reinforcement below the top of the MSE wall (z), the soil-wall interaction, and the unit weight of the soil (γ). The soil-wall interaction can be characterized by the vertical stress influence factor (β_v) described in Chapter 7. The value of the vertical stress is calculated as follows:

$$\sigma_{ov} = \gamma \, z \beta_v \qquad \text{Eq. 8-2}$$

where z is the depth of the layer of reinforcement below the top of the backfill, β_v is the vertical stress influence factor, and γ is the unit weight of the reinforced backfill.

Substituting Equation 8-2 into Equation 8-1 yields

$$S = F^* \gamma \, z C R_c \alpha \beta_v \qquad \text{Eq. 8-3}$$

The embedment length is given by

$$L_e = \frac{T_{allowable}}{S} \qquad \text{Eq. 8-4}$$

Substituting Equation 8-3 into Equation 8-4 yields

$$L_e = \frac{T_{allowable}}{F^* \gamma \, z C R_c \alpha \beta_v} \qquad \text{Eq. 8-5}$$

where L_e is the embedment length of the reinforcement behind the critical slip surface required to develop the allowable tensile strength of the reinforcement.

The parameters used to compute S are described in the following text. The recommended equation for the pullout resistance factor (F^*) for steel ribbed reinforcement is given in the current FHWA design guidelines for MSE walls (Elias et al., 2001) as follows,

$$F^{*} = 1.2 + \log\left(C_u\right) \qquad \text{Eq. 8-6}$$

where C_u is the uniformity coefficient based on the gradation of the soil backfill. If no information is available on the soil grain size distribution, FHWA recommends using a value of 4 for the uniformity coefficient (C_u). Based on this value ($C_u = 4$), the value of F^* was 1.8. The coverage ratio, R_c, is the ratio of the width of the reinforcement (b) to the horizontal spacing (S_h) between strips of reinforcement. The width of the reinforcement, b, was assumed to be 2 inches (0.167 ft) and the horizontal spacing was assumed to be 16 inches (1.33 ft). Therefore, the coverage ratio was 0.125 (= 2/16). The distance from the bottom layer of reinforcement to the foundation was equal to one-half the vertical spacing or 1.21 ft. The distance from the top layer of reinforcement to the top of the MSE wall was also 1.21 ft. Using Figure 7-24, the values of the vertical stress influence factor (β_v) were selected for each layer of reinforcement.

An example of the distribution of tensile resistance in selected layers of the reinforcement for a wall having an aspect ratio equal to 0.70 is shown in Figure 8-3. The point at which the tensile strength of the reinforcement begins to decrease from $T_{allowable}$ to zero at the free end of the reinforcement is illustrated in Figure 8-4. In the top two layers of reinforcement the maximum tensile strength is not developed because the length of embedment required to develop the maximum tensile strength is greater than the length of the reinforcement. Thus, the resisting force begins to decrease immediately at the facing of the wall to zero at the free end.

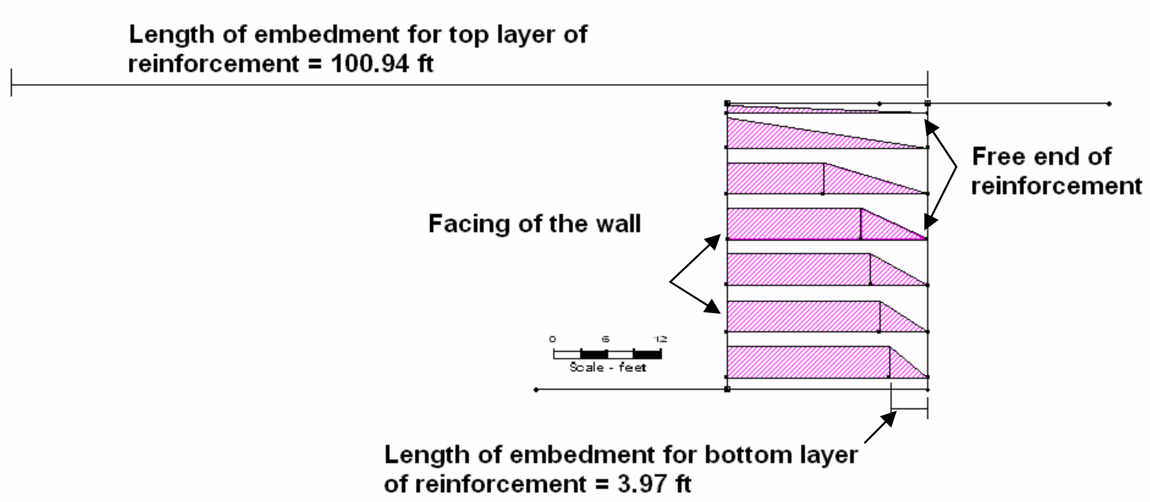

Figure 8.3: Distribution of tensile strength in the reinforcement for a wall with an aspect ratio equal to 0.70 (Wright, 1999)

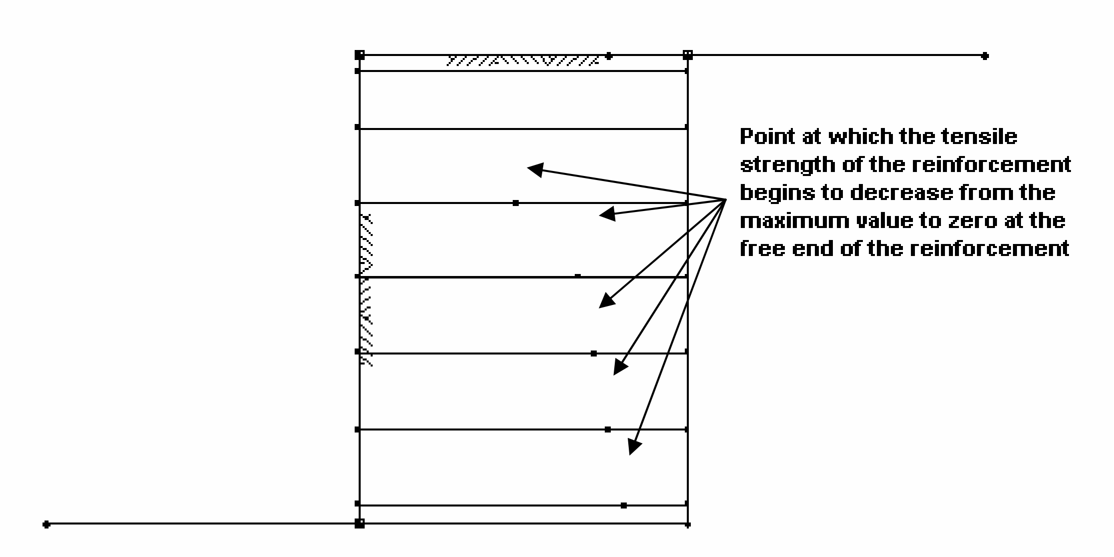

Figure 8.4: Location of points at which the tensile strength of the reinforcement begins to decrease from the maximum value to zero at the free end of the reinforcement (Wright, 1999)

8.2 Searching for the critical slip surface

The limit equilibrium analyses required searching to locate a critical slip surface having a minimum factor of safety. The factor of safety computed by the limit equilibrium analyses using UTEXAS4 is the conventional factor of safety for slope stability defined with respect to soil shear strength.

Analyses were performed with both circular and noncircular slip surfaces. For circular slip surfaces a "floating grid" search scheme employing a moveable grid was used to find the location of the critical center. A minimum spacing between grid points for the search of 0.3 ft was used. This spacing corresponds to 1 percent of the wall height and should have been more than adequate.

Searches for critical noncircular slip surfaces were done using the scheme implemented in UTEXAS4 for this purpose. To find the critical slip surfaces points were initially moved horizontally in increments of 2 ft and this distance was reduced to a minimum of 0.30 ft (one percent of the wall height) as the search progressed.

8.2.1 Circular slip surfaces

Searches with circular slip surfaces were conducted by finding the critical slip surfaces passing through the toe of the wall. During the search, circles whose centers were below the top of the wall such that the slip surface became inverted (Figure 8-5) were not analyzed. Table 8-1 shows the coordinates of the center of the initial circle for the three wall aspect ratios evaluated. The origin of the coordinates is to the toe of the wall (Figure 8-5). Bishop's Simplified procedure was used to calculate the factor of safety.

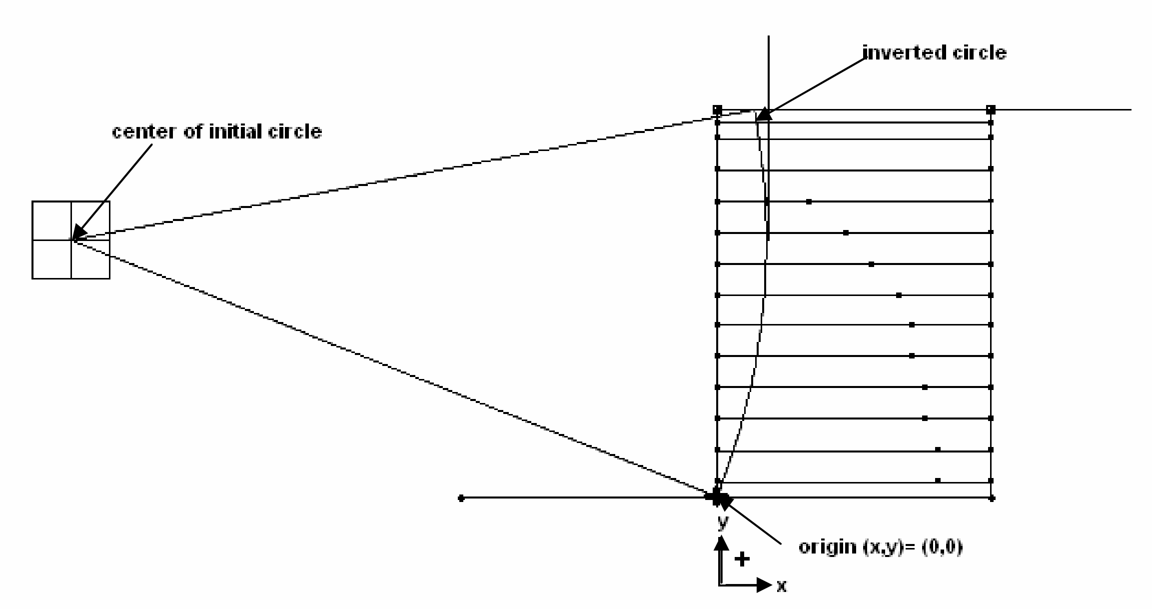

Figure 8.5: Example of an inverted circle (Wright, 1999)

Table 8.1: X-and y-coordinates of the center of the initial circle for the four wall aspect ratios analyzed in UTEXAS4

Aspect Ratio	x-coordinate (ft)	y-coordinate (ft)
0.30	-50	30
0.50	-30	30
0.70	-50	50

8.2.2 Noncircular slip surfaces

Searches for the critical noncircular slip surfaces were initiated by specifying the initial location of selected points along the slip surface. The number of points selected to define the initial slip surface was varied, however, in all analyses, the first point on the initial slip surface was at the toe of the wall. The last point was placed at the top of the MSE wall such that the initial location of the point was forward of the existing stable slope. The remaining, intermediate points were chosen such that the initial slip surface was nearly a straight line. As the number of points used to define the initial slip surface increases, the flexibility in the shape of the slip surface used in UTEXAS4 increases.

Spencer's procedure was used for all analyses with noncircular slip surfaces. Spencer's procedure is one of the more accurate limit equilibrium procedures because it completely satisfies both moment and force equilibrium. Also the procedure can be used to analyze any shape of slip surface.

An initial series of limit equilibrium analyses was conducted in which the number of points used to define the noncircular slip surface was systematically varied. The analyses were conducted for a single wall aspect ratio of 0.70 using 3, 5, 7, 9, and 11 points to define the noncircular slip surface. The vertical spacing between the points was uniform for each analysis. The vertical spacings and corresponding minimum factors of safety for these analyses are summarized in Table 8-2. In general, as the number of points on the slip surface increased, the factor of safety decreased. However, for the slip surface defined by 11 points, the highest number of points used, the factor of safety increased slightly. The higher factor of safety that resulted when 11 points were used can be explained as follows: When the number of points varied the location of the moveable points also varied. Thus, when 11 points were used the points were at different locations than when, for example, 7 points were used. This could allow the slip surface defined by 7 points to take on a more critical shape than the slip surface defined by 11 points. The slip surface composed of 7 points produced approximately the lowest factor of safety (2.6) and, thus, 7 points were judged to be sufficient to capture the shape of critical noncircular slip surfaces. An example of a noncircular slip surface defined by seven points is shown in Figure 8-6.

Table 8.2: Factors of safety and vertical spacings corresponding to the number of points used to define the general noncircular slip surface

Points on slip surface	Vertical Spacing (ft)	FS
3	15	2.8
5	7.5	2.6
7	5	2.6
9	3.75	2.6
11	3	2.7

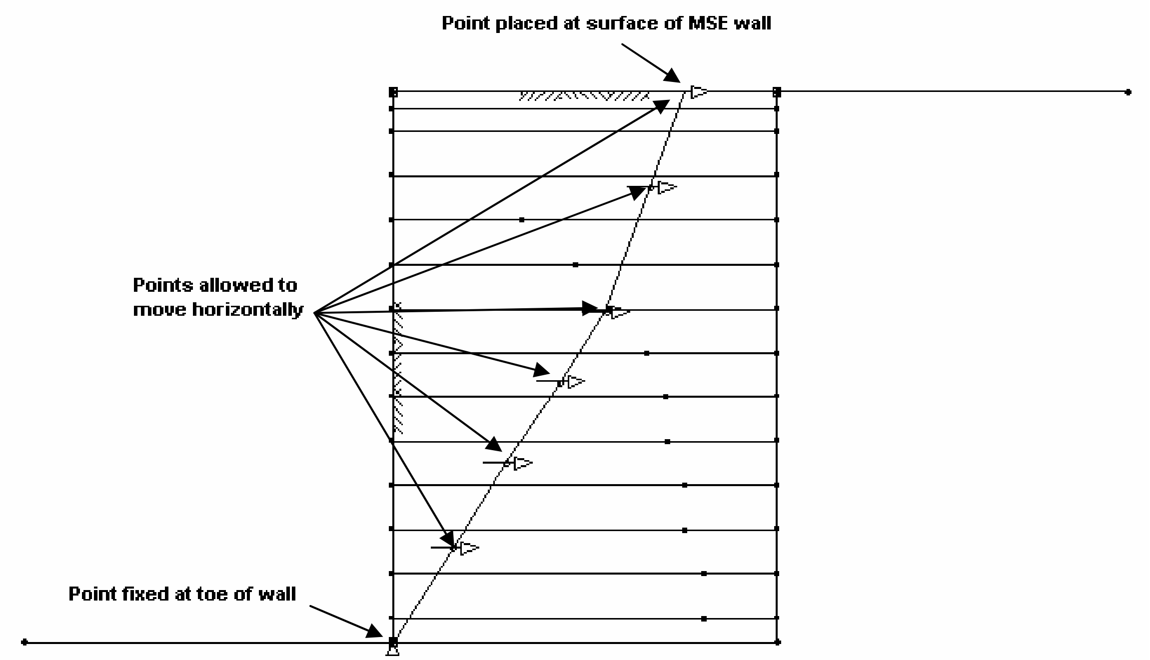

Figure 8.6: Initial noncircular slip surface defined by seven points for a wall with an aspect ratio equal to 0.70 (Wright, 1999)

Additional analyses were performed using a bilinear slip surface defined by only 3 points to compare the factors of safety found using a bilinear slip surface with the factors of safety found using a more general noncircular slip surface and circular slip surfaces. Searching for the critical bilinear surface with UTEXAS4 was done using two schemes. In the first scheme, the middle point on the initial slip surface was placed at the same elevation as a layer of reinforcement and allowed to move horizontally. Using this method, thirteen separate analyses were performed (one for each layer of reinforcement) for each wall being analyzed. For the case with a wall aspect ratio of 0.70, the critical bilinear slip surface was found by placing the middle point at the layer of reinforcement 15.73 ft above the bottom of the wall and allowing the point to move horizontally. The factor of safety was equal to 2.787.

In the second scheme, two analyses were performed for each wall being analyzed. First, the middle point used to define the initial slip surface was placed 0.01 ft (0.12 inches) in front of the existing stable face at the bottom layer of reinforcement and allowed to move vertically upward. Second, the middle point used to define the initial slip surface was placed 0.01 ft (0.12 inches) in front of the existing stable face at the top layer of reinforcement and allowed to move vertically downward. The purpose of searching for the critical slip surface in both directions was to reduce the possibility that the critical slip surface was influenced by local minima. For example, when the wall aspect ratio was equal to 0.70 and the search was performed by searching from near the bottom of the wall vertically upward, the calculated minimum factor of safety was 2.941 and the height of the midpoint on the noncircular slip surface was equal to 13.19 ft above the foundation. However, when the same wall aspect ratio was analyzed and the search was performed by searching vertically downward from near the top of the wall, the calculated minimum factor of safety was 2.906 and the height of the midpoint on the noncircular slip surface was equal to 15.68 ft above the foundation. An example of a noncircular slip surface defined by three points for the second method is shown in Figure 8-7 as a dashed line.

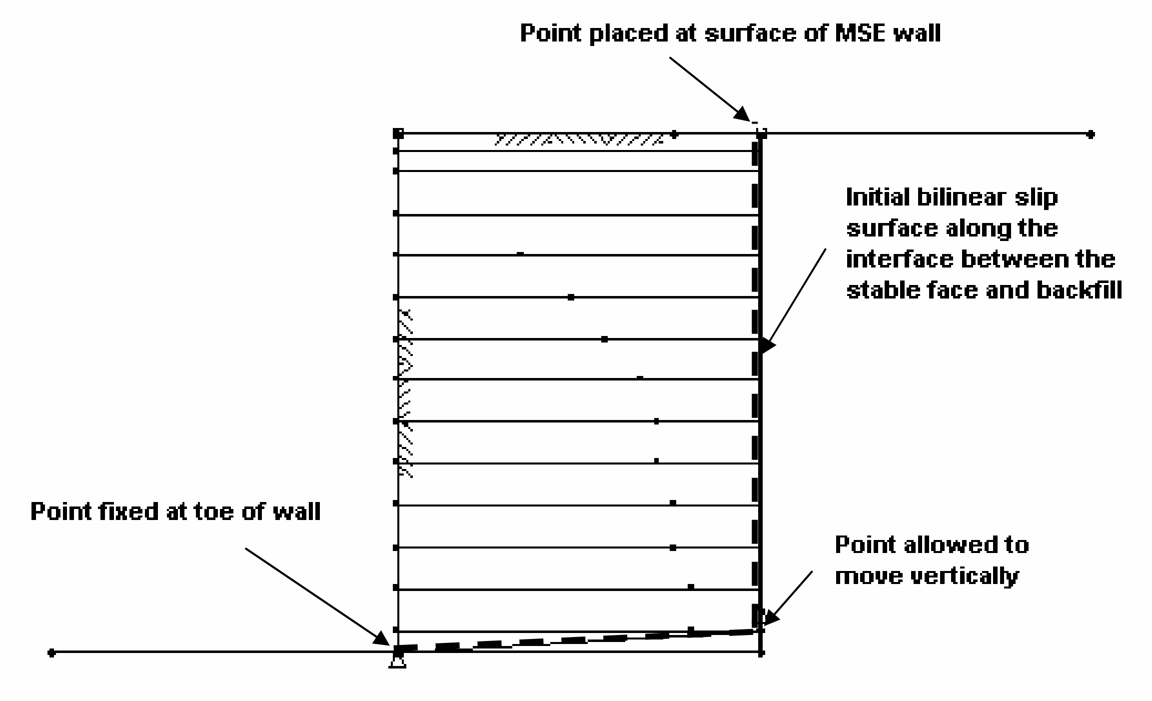

Figure 8.7: Initial noncircular slip surface defined by three points for a wall with an aspect ratio equal to 0.70 (Wright, 1999)

8.3 Results and discussion for critical slip surface

Analyses were first performed with circular slip surfaces for walls with aspect ratios equal to 0.70, 0.50, and 0.30. The respective locations of the critical slip surfaces and corresponding factors of safety are shown in Figures 8-8 through 8-10.

8.3.1 Critical circular slip surfaces

The location of the critical circular slip surfaces and corresponding factors of safety for walls with aspect ratios equal to 0.70, 0.50, and 0.30 are shown in Figures 8-8 through 8-10.

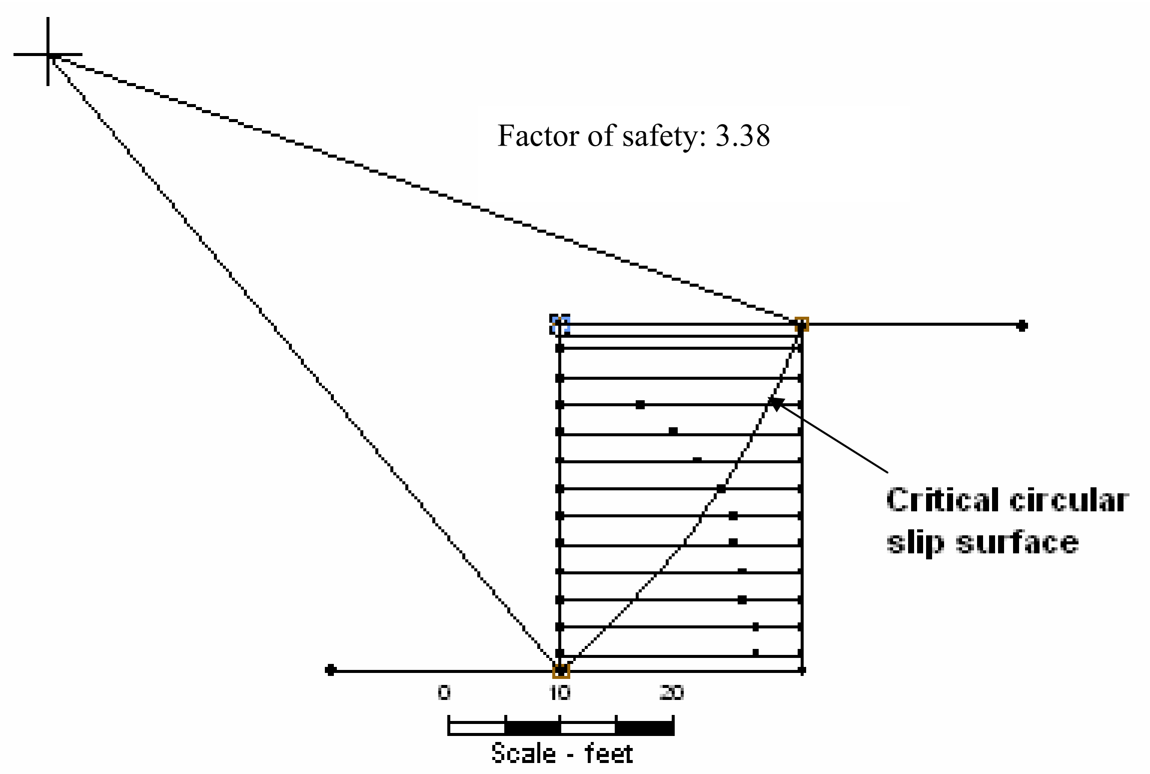

Figure 8.8: Critical circular slip surface for a wall aspect ratio equal to 0.70 (Wright, 1999)

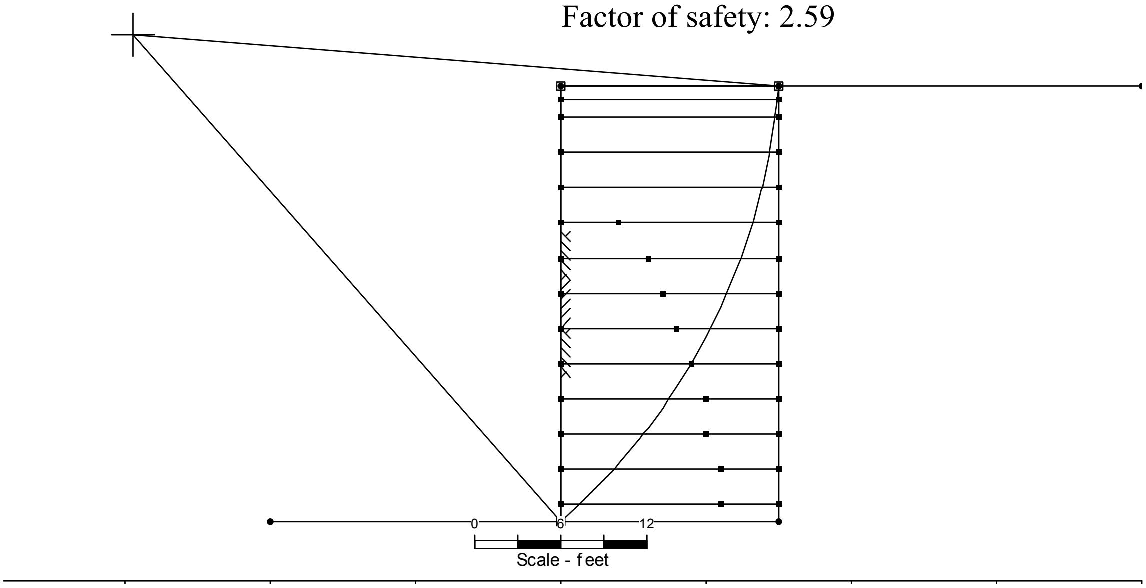

Figure 8.9: Critical circular slip surface for a wall aspect ratio equal to 0.50 (Wright, 1999)

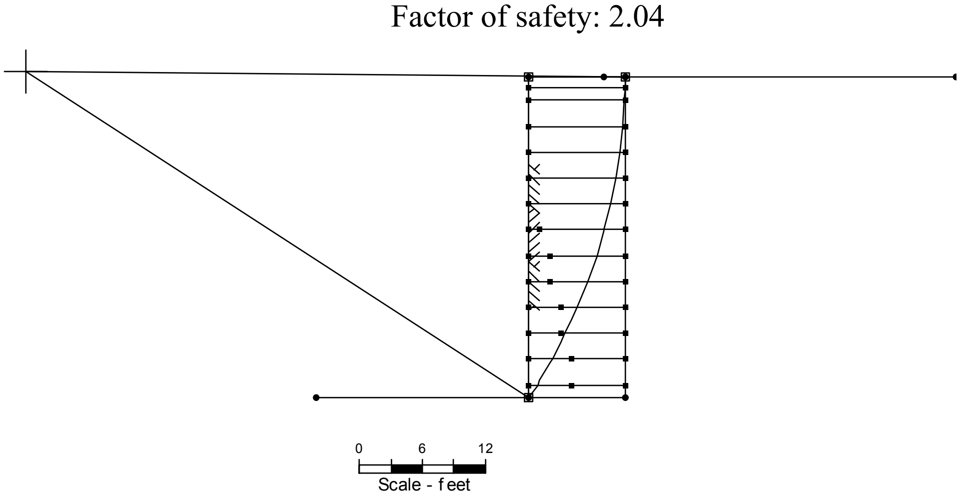

Figure 8.10: Critical circular slip surface for a wall aspect ratio equal to 0.30 (Wright, 1999)

8.3.2 Critical general noncircular slip surface defined by 7 points

The next series of analyses were performed with general noncircular slip surfaces for walls with aspect ratios of 0.70, 0.50, and 0.30. The locations of the critical general noncircular slip surfaces and corresponding factors of safety from UTEXAS4 are shown in Figures 8-11 through 8-13.

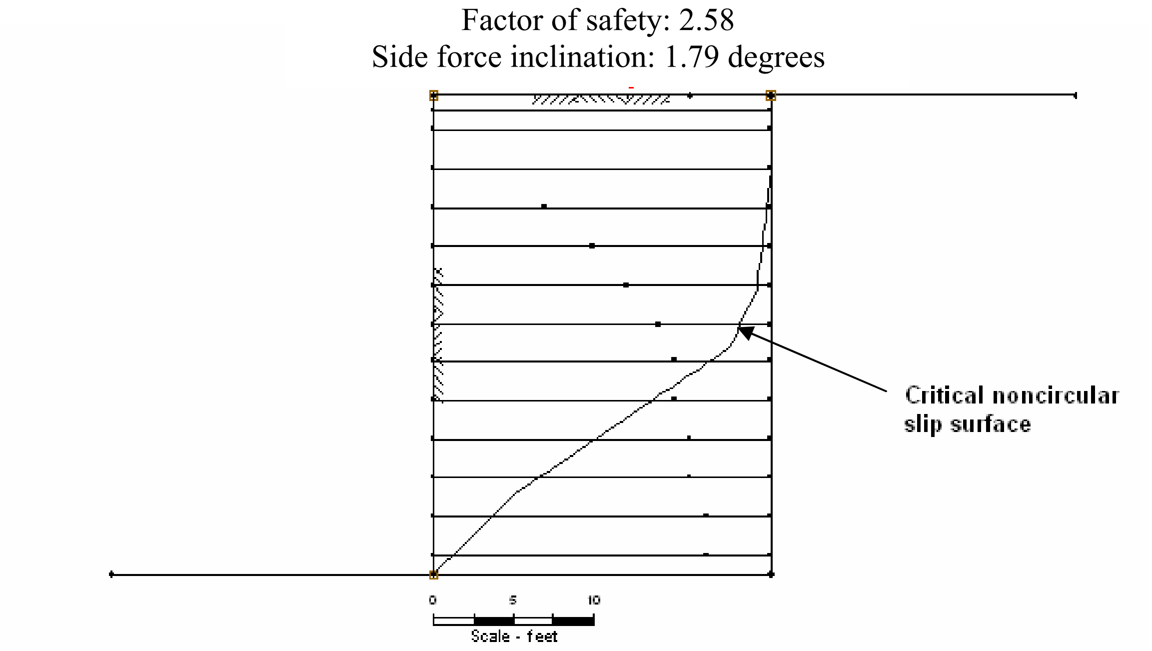
Factor of safety: 2.58
Side force inclination: 1.79 degrees

Figure 8.11: Critical noncircular slip surface for a wall aspect ratio equal to 0.70 (Wright, 1999)

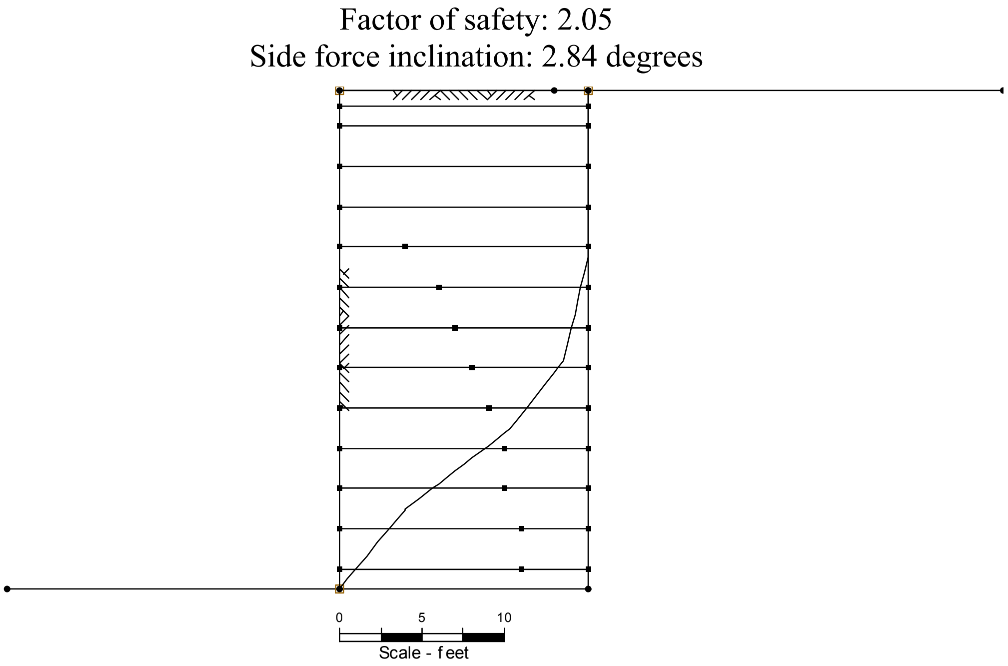
Factor of safety: 2.05
Side force inclination: 2.84 degrees

Figure 8.12: Critical noncircular slip surface for a wall aspect ratio equal to 0.50 (Wright, 1999)

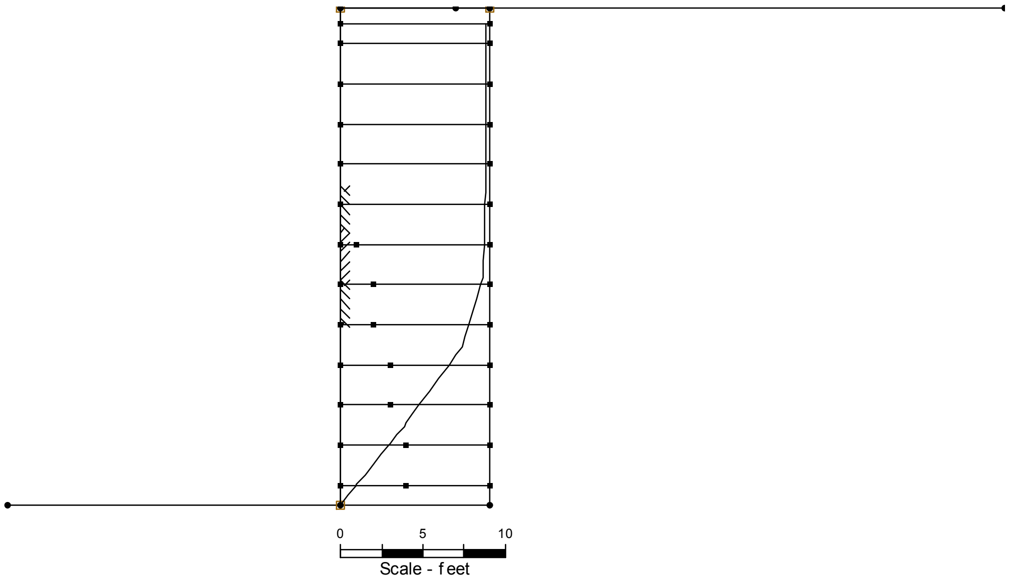

Factor of safety: 1.56
Side force inclination: 3.54 degrees

Figure 8.13: Critical noncircular slip surface for a wall aspect ratio equal to 0.30 (Wright, 1999)

8.3.3 Critical bilinear slip surface

The third series of analyses was performed with bilinear slip surfaces. The locations of the critical bilinear slip surfaces and corresponding factors of safety are shown in Figures 8-14 through 8-16.

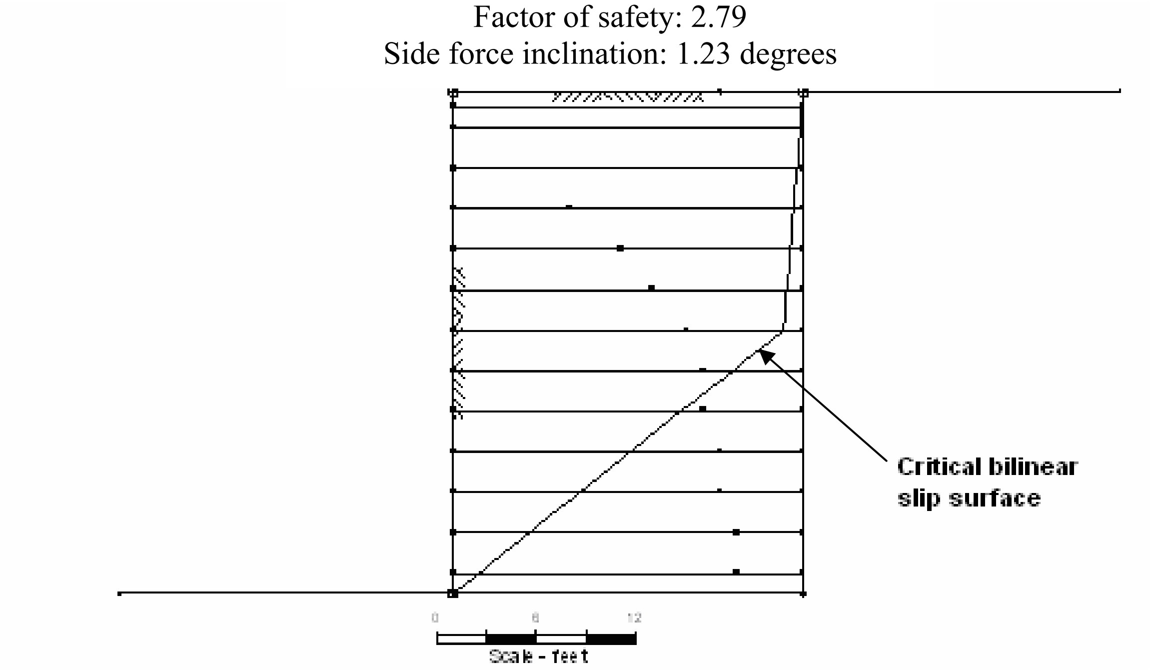

Figure 8.14: Critical bilinear slip surface for an aspect ratio equal to 0.70 (Wright, 1999)

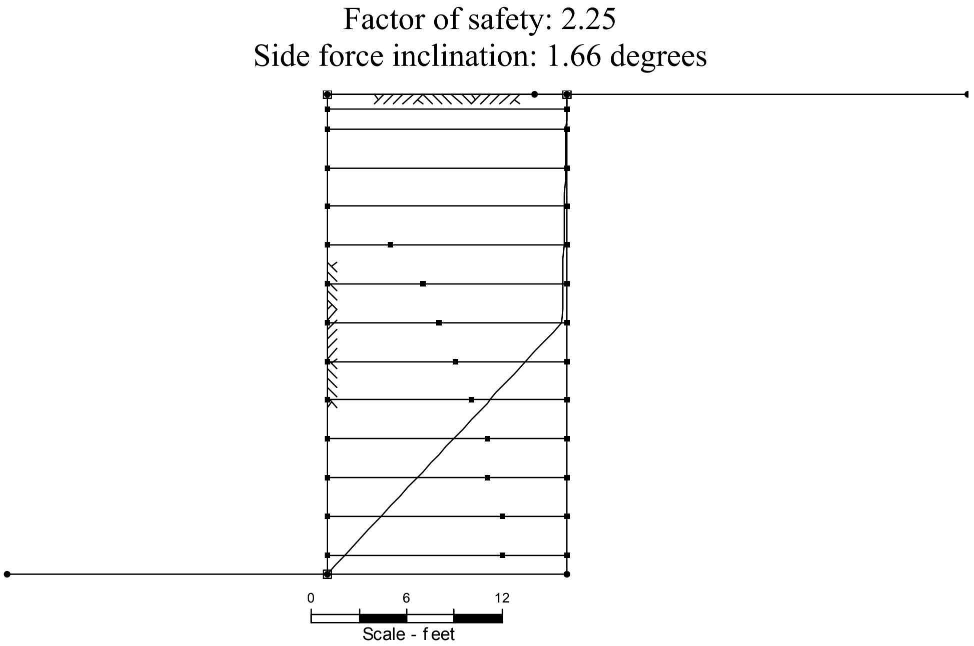

Figure 8.15: Critical bilinear slip surface for a wall aspect ratio equal to 0.50 (Wright, 1999)

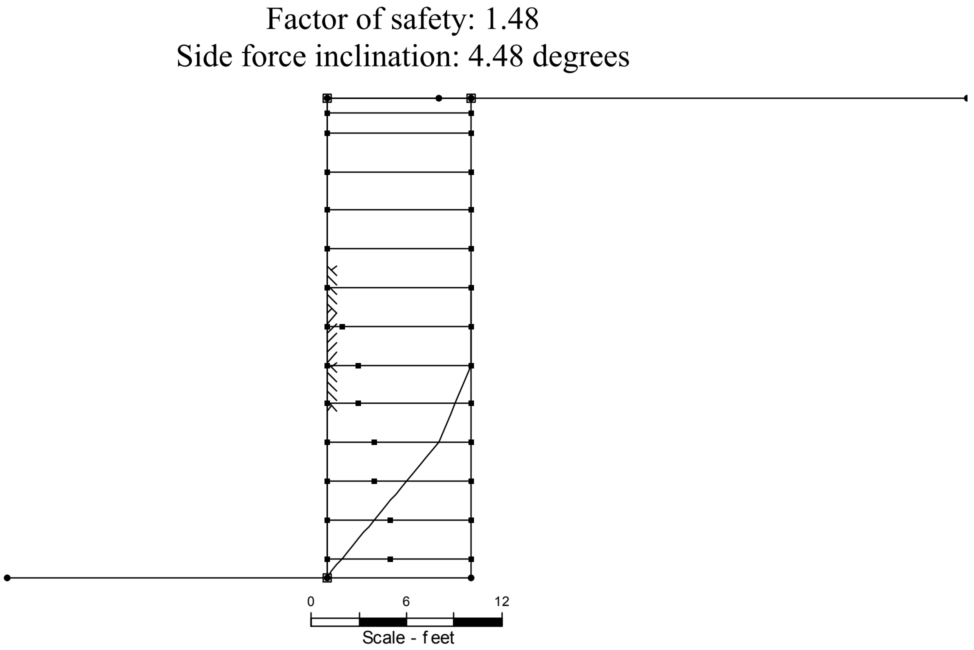

Figure 8.16: Critical bilinear slip surface for a wall aspect ratio equal to 0.30 (Wright, 1999)

8.3.4 Discussion of results

The computed factors of safety for the critical circular, noncircular, and bilinear slip surfaces are displayed in Table 8-3. For all the analyses, the critical slip surfaces (circular, general noncircular, and bilinear) intersected the toe of the wall and the point on the top of the wall where the backfill met the stable face. Also, regardless of the shape of the slip surface, the factor of safety decreased as the wall aspect ratio decreased as shown in Table 8-3. The search performed with the general noncircular slip surface defined by seven points yielded lower factors of safety than when circular or bilinear slip surfaces were used except in one case. The factor of safety found using the bilinear slip surface was slightly higher than the noncircular slip surface when the wall aspect ratio was 0.30. In this case, the location of the moveable point for the bilinear slip surface allowed the search to find a more critical slip surface than the noncircular search. The same circumstances were described in the discussion of how many points to use to define the noncircular slip surface in Section 8.2.2. The factors of safety found using the circular slip surface were the highest.

Table 8.3: Computed factors of safety for critical circular, noncircular, and bilinear slip surfaces

Aspect Ratio	FS - circular	FS - noncircular (7 points)	FS - noncircular (bilinear)
0.70	3.375	2.577	2.787
0.50	2.588	2.054	2.251
0.30	2.035	1.559	1.478

8.3.5 Comparisons between noncircular slip surfaces and the theoretical Rankine failure surface

The current design guidelines (Ref#) suggest the most critical slip surface is the theoretical Rankine failure surface which should be a plane starting at the toe of the wall and extending to the top of the wall at an angle (β) equal to 45 + ϕ'/2 measured from the horizontal. The value of the friction angle (ϕ') used to define the angle of inclination of the failure surface, β, assumes the shear strength of the soil is fully mobilized. However, in the limit equilibrium analyses, the shear strength was reduced until a slip surface was found that was in the just-stable condition. The shear strength of the soil in the just-stable condition is defined as

$$\phi'_{\text{developed}} = \arctan\left(\frac{\tan(\phi')}{\text{F}}\right) \qquad \text{Eq. 8-7}$$

where F is the factor of safety in the soil shear strength, and $\phi'_{\text{developed}}$ is the angle of internal friction required for the just-stable condition of the critical slip surface.

The limit equilibrium analyses indicate the general noncircular slip surface is the most critical slip surface. The shape of the noncircular slip surface was compared to the theoretical Rankine failure surface for wall aspect ratios of 0.70, 0.50, and 0.30. Two theoretical Rankine failure surfaces were calculated for the comparisons. One Rankine failure surface was calculated using the fully mobilized angle of internal friction (ϕ' = 37°) and the other Rankine failure surface was computed using the developed friction angle, $\phi'_{\text{developed}}$. The values of $\phi'_{\text{developed}}$ were calculated using Equation 8-7 and the factors of safety, F, corresponding to wall aspect ratios of 0.70, 0.50, and 0.30 for the critical noncircular slip surfaces in Table 8-3. The values of $\phi'_{\text{developed}}$ are tabulated in Table 8-4. The shapes of the critical noncircular slip surfaces and the theoretical Rankine failure surfaces for wall aspect ratios of 0.70, 0.50, and 0.30 are displayed in Figures 8-17 through 8-19. The depths of the critical noncircular slip surfaces are greater than the depths of either of the theoretical Rankine failure surfaces.

Table 8.4: Values of $\phi'_{\text{developed}}$ calculated for the critical noncircular slip surfaces

Wall Aspect Ratio	$\phi'_{\text{developed}}$ (°)
0.70	16
0.50	20.1
0.30	25.8

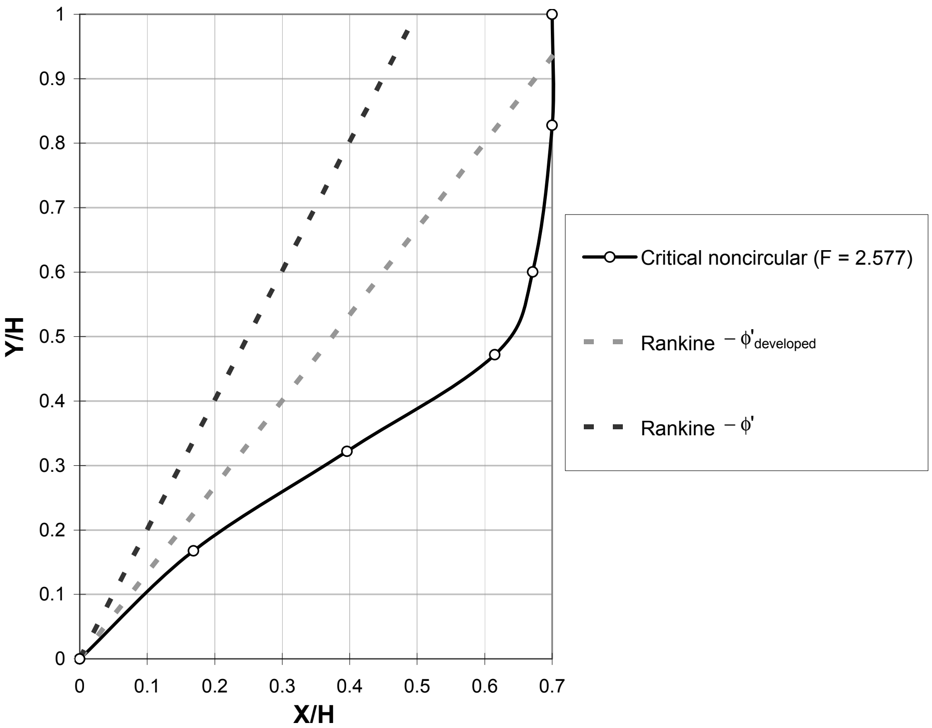

Figure 8.17: Shapes for the critical noncircular slip surface, theoretical Rankine failure surface for the fully mobilized shear strength (ϕ'), and theoretical Rankine failure surface for the developed shear strength ($\phi'_{developed}$) and a wall aspect ratio of 0.70

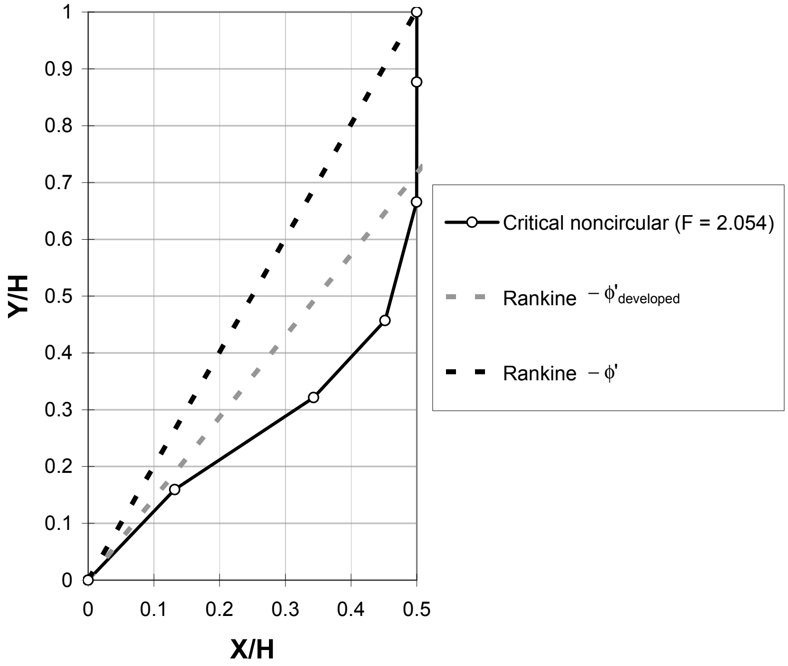

Figure 8.18: Shapes for the critical noncircular slip surface, theoretical Rankine failure surface for the fully mobilized shear strength (ϕ'), and theoretical Rankine failure surface for the developed shear strength ($\phi'_{developed}$*) and a wall aspect ratio of 0.50*

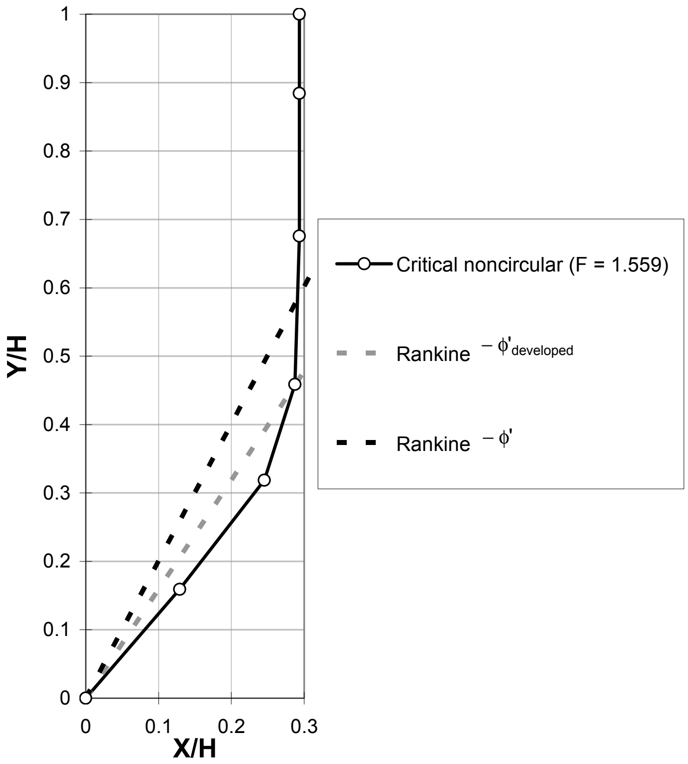

Figure 8.19: Shapes for the critical noncircular slip surface, theoretical Rankine failure surface for the fully mobilized shear strength (ϕ'), and theoretical Rankine failure surface for the developed shear strength ($\phi'_{developed}$) and a wall aspect ratio of 0.30

8.4 Weak interface

The preceding analyses assumed that the full soil shear strength was available between the back of the backfill and existing stable face. To determine how much the strength of the interface affected the factor of safety of the wall, a weaker interface was created between the existing stable face and backfill as illustrated in Figure 8-20.

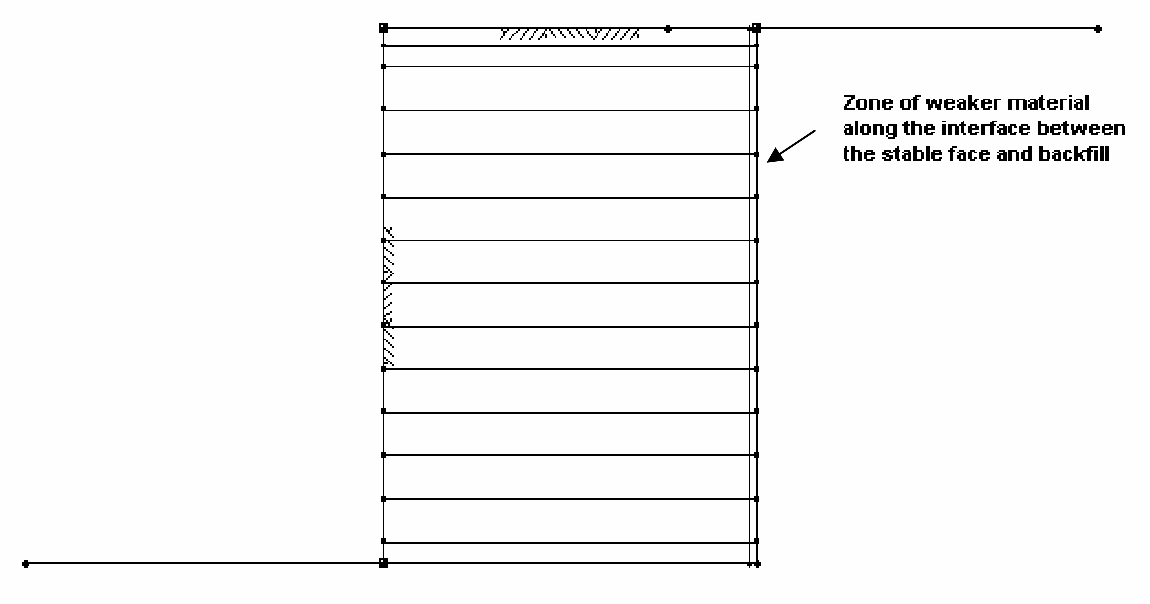

Figure 8.20: Example geometry for a MSE wall using a zone of material weaker than the backfill along the interface between the stable face and backfill (Wright, 1999)

The weak interface was modeled as a thin vertical column of weaker soil 6 inches (0.5 ft) wide. The interface was assumed cohesionless with the same unit weight (116 pcf) as the backfill. However, the angle of internal friction (ϕ') for the zone of weaker material was assumed to be less than the value for the backfill. Two different strengths were assumed for the weaker zone. In the first case, the strength was assumed to be represented by a friction angle (26.7°) equal to two-thirds the friction angle of the backfill. For the second case the zone of weaker material was assumed to have zero strength (c' = 0 and ϕ' = 0).

The computed factors of safety from analyses of walls having a weaker interface (ϕ' = 26.7°) are shown in Table 8-5. The critical slip surface from the general noncircular search with no interface for a wall with an aspect ratio of 0.70 is shown in Figure 8-21 and the critical slip surface from the general noncircular search with a weak interface for a wall with the same geometry is illustrated in Figure 8-22. The shape of the critical slip surfaces were not significantly changed by the weak interface. The critical slip surface for the case with a weak interface intersects less layers of reinforcement than the case with no interface and part of it passes through the zone of weaker material. As a result, the resisting forces are decreased and the corresponding factors of safety are decreased slightly.

Table 8.5: Computed factors of safety for the case of a weak interface between the existing stable face (interface friction angle = 26.7°) and the case of no interface

Aspect Ratio	FS - noncircular (ϕ' = 26.7)	FS - noncircular (no interface)
0.70	2.531	2.577
0.50	2.024	2.054
0.30	1.535	1.559

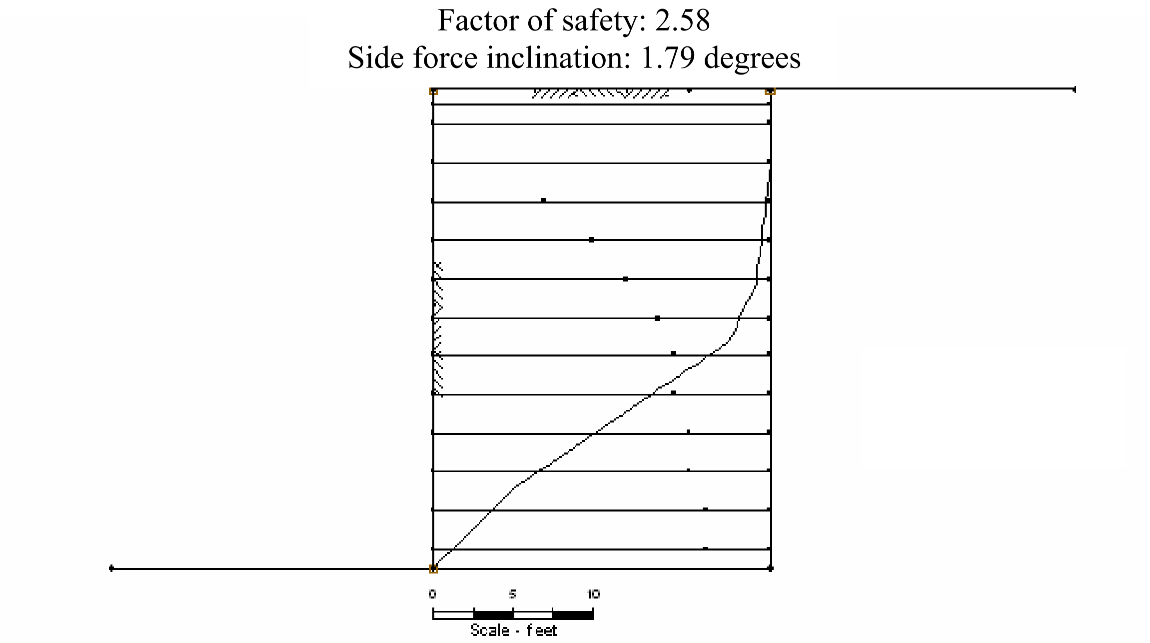

Figure 8.21: Critical slip surface from the general noncircular search for a wall aspect ratio equal to 0.70 with no interface (Wright, 1999)

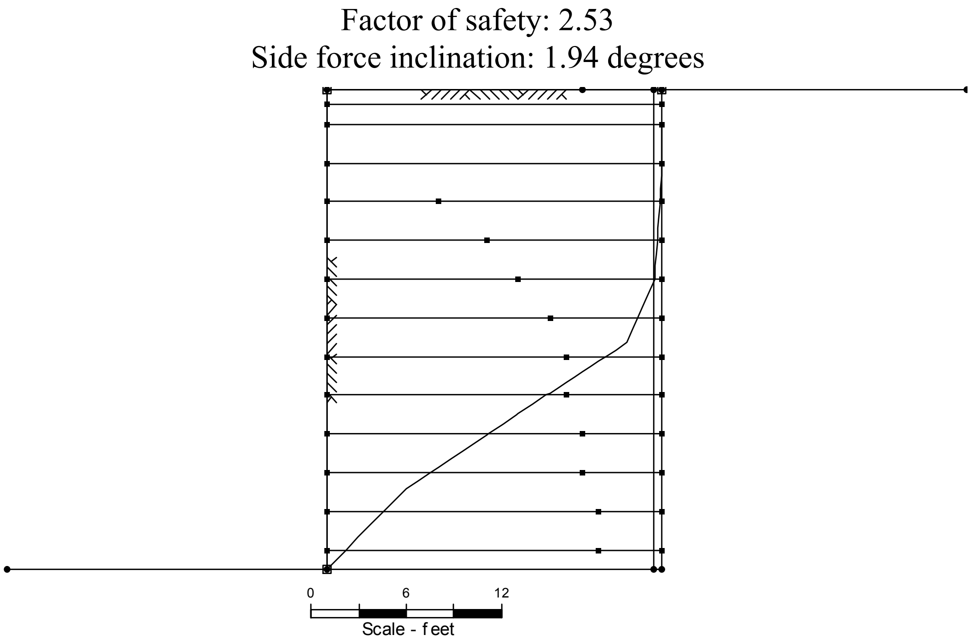

Figure 8.22: Critical slip surface from the general noncircular search for a wall aspect ratio equal to 0.70 with a weak interface (Wright, 1999)

The computed factors of safety for the case of an interface with zero strength (c = 0, ϕ' = 0) and the case of an interface with two-thirds (ϕ' = 26.7°) the strength of the backfill between the stable face and backfill, and no interface are shown in Table 8-6. The critical slip surface from the general noncircular search for a wall aspect ratio equal to 0.70 with no interface is exhibited in Figure 8-23 and the critical slip surface from the general noncircular search for a wall aspect ratio equal to 0.70 with an interface with zero strength is displayed in Figure 8-24. The shape of the critical slip surfaces were not significantly changed by the interface with no strength however, the critical slip surface intersects less layers of reinforcement than the case with no interface and partly passes through the zone of weaker material. As a result, the resisting forces are decreased and the corresponding factors of safety are decreased from 12 to 16 percent.

Table 8.6: Computed factors of safety for the case of an interface with zero strength and the case of an interface with two-thirds (ϕ' = 26.7°) the strength of the backfill between the stable face and backfill, and no interface

Aspect Ratio	FS - noncircular (c = 0, ϕ' = 0)	FS - noncircular (ϕ' = 26.7)	FS - noncircular (no interface)
0.70	2.240	2.531	2.577
0.50	1.738	2.024	2.054
0.30	1.370	1.535	1.559

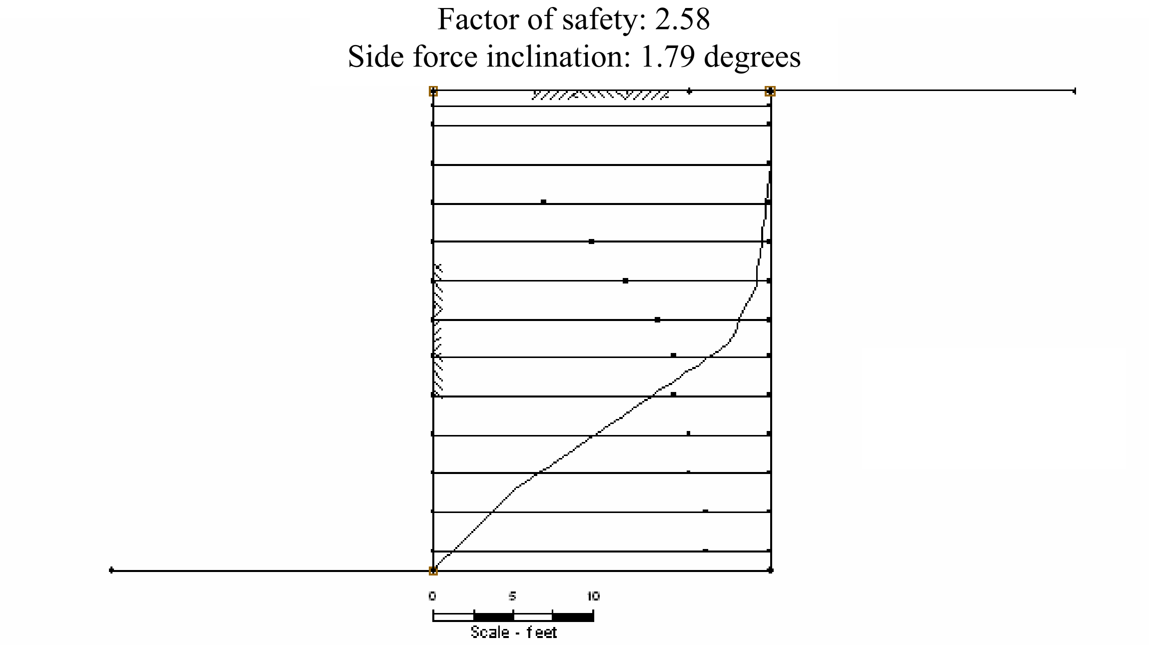

Figure 8.23: Critical slip surface from the general noncircular search for wall aspect ratio equal to 0.70 with no interface (Wright, 1999)

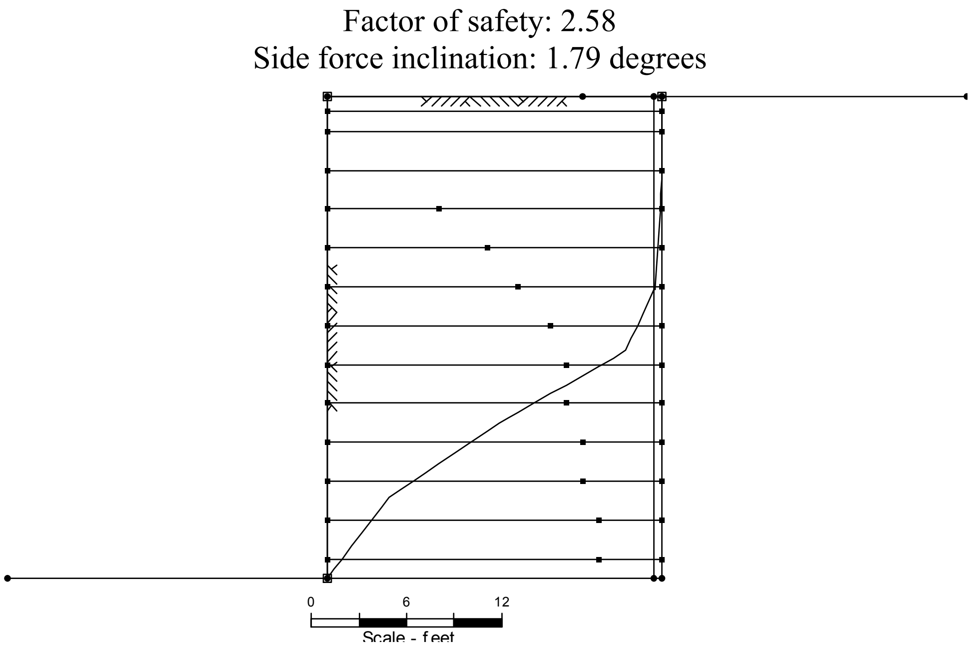

Figure 8.24: Critical slip surface from the general noncircular search for a wall aspect ratio equal to 0.70 with an interface with zero strength (Wright, 1999)

As the strength of the interface decreased, the corresponding factors of safety decreased. Also, as the wall aspect ratio decreased, the effect of the weak interface increased, i.e. the factors of safety decreased more for smaller aspect ratios when the interface strength was decreased. When the angle of internal friction of the interface was equal to 26.7° the effect of the interface was small. The interface friction angle was reduced by one-third from the case with no interface, but the factors of safety only decreased by approximately two percent relative to the case with no interface. Even assuming the extreme case of an interface with no strength, the factors of safety only decreased by approximately 12-16 percent relative to the case with no interface. Thus, a weaker interface does not significantly affect the factors of safety and probably does not need to be included in the limit equilibrium analyses.

8.5 Tension crack

To further simulate and investigate a weak interface between the existing stable face and backfill an alternative scheme was employed in additional analyses with UTEXAS4 in which a nearly vertical tension crack was assumed at the interface. The crack was assumed to extend from the top of the wall to the slip surface approximately 0.5 ft (6 inches) in front of the stable face. Figure 8-25 shows the location of the bottom of a tension crack (drawn as a dashed line) for an analysis with a wall aspect ratio (L/H) equal to 0.70. The computed factors of safety for a tension crack between the existing stable face and backfill are displayed in Table 8-7.

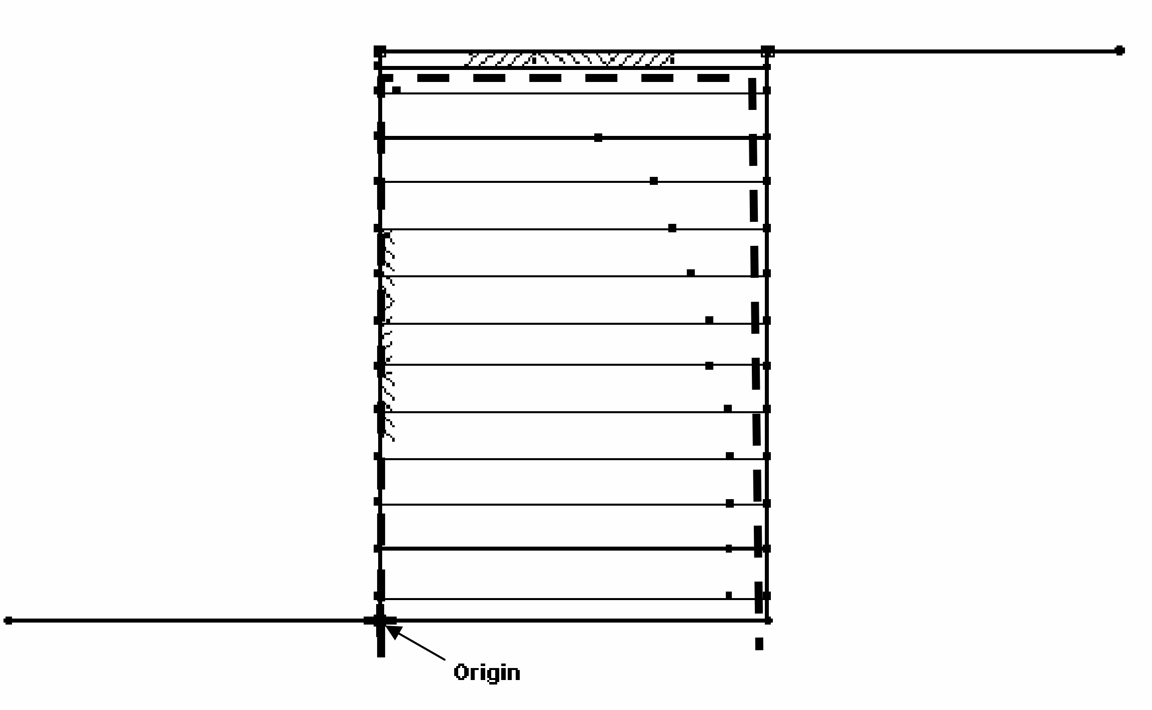

Figure 8.25: Location of the bottom of a tension crack for a UTEXAS simulation having wall aspect ratio equal to 0.70 (Wright, 1999)

Table 8.7: Computed factors of safety when a tension crack was introduced along the interface between the stable face and backfill

Aspect Ratio	FS - noncircular
0.70	2.735
0.50	2.269
0.30	1.752

The factors of safety found when the tension crack was included were higher than the factors of safety for the wall without the tension crack because a portion of the driving force on the critical slip surface is eliminated when the crack is introduced. In contrast, when a zone of material having zero strength was assumed to exist at the interface between the existing stable face and backfill (Section 8.4), the zone of zero strength still exerted a driving force on the critical slip surface while at the same time the weaker material did not have as much strength to resist the driving forces. As a result, the factors of safety for the case with an interface having zero strength were less than the case without an interface. The factors of safety for the three cases considered (no interface, interface with zero strength, and tension crack) are summarized for wall aspect ratios equal to 0.70, 0.50, and 0.30 in Table 8-8. In reality, a crack will probably not form in cohesionless material and thus the results are presented primarily for illustrative purposes.

Table 8.8: Computed factors of safety for analyses performed with general noncircular slip surfaces for walls having no interface, an interface with zero strength, and a tension crack

Aspect Ratio	FS - noncircular (no interface)	FS - noncircular (c = 0, ϕ' = 0)	FS - noncircular (tension crack)
0.70	2.577	2.240	2.735
0.50	2.054	1.738	2.269
0.30	1.559	1.370	1.752

8.6 Factor of safety in the reinforcement

In the previous limit equilibrium analyses the factors of safety were defined and computed with respect to the soil shear strength, i.e. as the ratio of available shear strength to shear strength required for just-stable equilibrium. An alternative approach to defining the factor of safety is to assume that the shear strength of the soil is fully mobilized and determine by what amount the reinforcement force has to be reduced to achieve just-stable equilibrium. Using this approach, a factor of safety applied to reinforcement forces can be found. This factor of safety is defined as follows:

$$F_{\text{reinforcement}} = \frac{T_{\text{allowable}}}{T_{R1}} \qquad \text{Eq. 8-8}$$

where $F_{\text{reinforcement}}$ is the factor of safety in the reinforcement, $T_{\text{allowable}}$ is the allowable tensile force in the reinforcement, and T_{R1} is the equilibrium force in the reinforcement when the soil shear strength is fully developed.

Searches for the critical circular and general noncircular slip surfaces yielding the minimum F defined by Equation 8-8 were performed for wall with aspect ratios equal to 0.70, 0.50, and 0.30. Both circular and noncircular slip surfaces were determined using the same methods described in Section 8.2. The initial resistance in the reinforcement was assumed to be 4,000 lb/ft based the procedure described in Section 8.1.2. The resistance in the reinforcement was reduced by the factor of safety against soil shear strength computed when the resistance was assumed to be 4000 lb/ft. For example, to find the critical circular slip surface for wall aspect ratio of 0.70, the following was done: The initial resistance (4,000 lb/ft) was divided by a factor of 3.375 (see Table 8-3) giving a new resistance of 1,185 lb/ft. This new resistance in the reinforcement was then substituted into Equation 8-5 to find new embedment lengths. Another limit equilibrium analysis was performed using UTEXAS4 with the new resistance and embedment lengths for the reinforcement to compute a factor of safety with respect to shear strength. This process was repeated until the factor of safety with respect to shear strength was approximately 1.00, i.e. the soil strength was fully developed.

8.6.1 Results and discussion for factor of safety in the reinforcement

The computed factors of safety in the reinforcement ($F_{\text{reinforcement}}$) for each wall aspect ratio are summarized in Table 8-9. As the wall aspect ratio decreased, the factors of safety in the reinforcement decreased. In addition, the computed factors of safety in the reinforcement ($F_{\text{reinforcement}}$) were higher for the critical circular slip surface than for the critical noncircular slip surface for wall aspect ratios less than 0.70.

Table 8.9: Factors of safety in the reinforcement from critical circular and general noncircular slip surfaces for wall aspect ratios equal to 0.70, 0.50, and 0.30.

Wall Aspect Ratio	$FS_{reinforcement}$ - circular	$FS_{reinforcement}$ - Noncircular
0.70	3.06	3.38
0.50	2.92	2.86
0.30	2.28	2.05

The locations of the critical slip surfaces for each wall aspect ratio are shown in Figures 8-26 through 8-27. The theoretical Rankine failure surface assumed by the current Federal Highway Administration (FHWA) design guidelines is also shown in these figures. The Rankine failure surface is a straight line extending from the toe of the wall to the top of the MSE wall at an inclination of 45 + ϕ'/2 degrees above the horizontal.

The critical noncircular slip surface shown in Figure 8-26 for a wall aspect ratio equal to 0.70 is nearly linear and matches the shape of the theoretical Rankine failure surface well. The critical circular slip surface has a more gradual slope than either the Rankine or critical noncircular slip surfaces near the bottom of the wall and a steeper slope near the top of the wall. For the wall with an aspect ratio equal to 0.50 (Figure 8-27) the critical noncircular slip surface is slightly deeper than the theoretical Rankine failure surface and becomes nearly vertical as it approaches the existing stable face at x/H = 0.5. Similar behavior was observed for a wall with an aspect ratio equal to 0.30 (Figure 8-28). In this case, the critical slip surface intersects the interface between the existing stable face and backfill at approximately the mid-height of the wall and then continues nearly vertically along the interface to the surface of the wall.

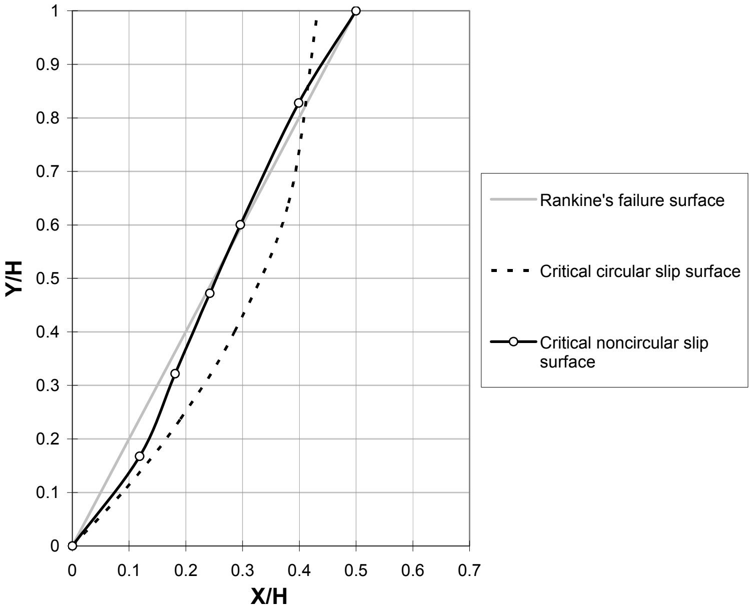

Figure 8.26: Critical slip surfaces when the soil shear strength is fully developed for a wall aspect ratio equal to 0.70

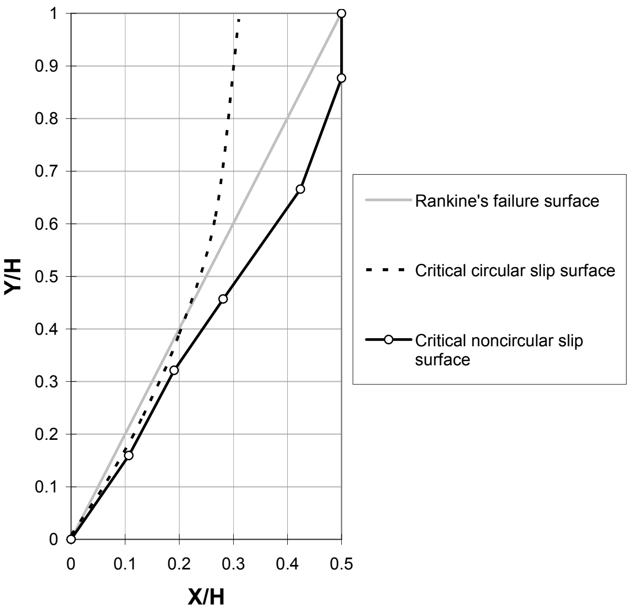

Figure 8.27: Critical slip surfaces when the soil shear strength is fully developed for a wall aspect ratio equal to 0.50

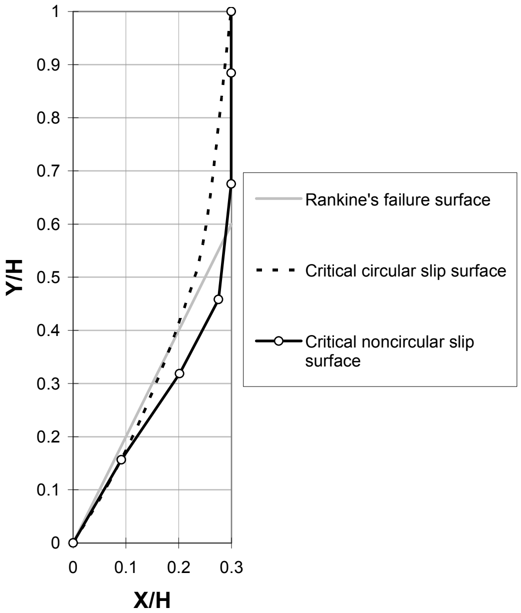

Figure 8.28: Critical slip surfaces when the soil shear strength is fully developed for a wall aspect ratio equal to 0.30

8.6.2 Comparisons between the shapes of the critical noncircular surfaces for the factor of safety in the soil shear strength and in the reinforcement

The critical noncircular slip surfaces found for the two definitions of the factor of safety are compared in Figures 8-29 through 8-32 for wall aspect ratios of 0.70, 0.50, and 0.30 respectively. The critical slip surfaces for the factor of safety applied to the soil shear strength are deeper than the critical slip surfaces for the factor of safety applied to the reinforcement. However, as the wall aspect ratio decreases, the shapes of the critical surfaces become similar.

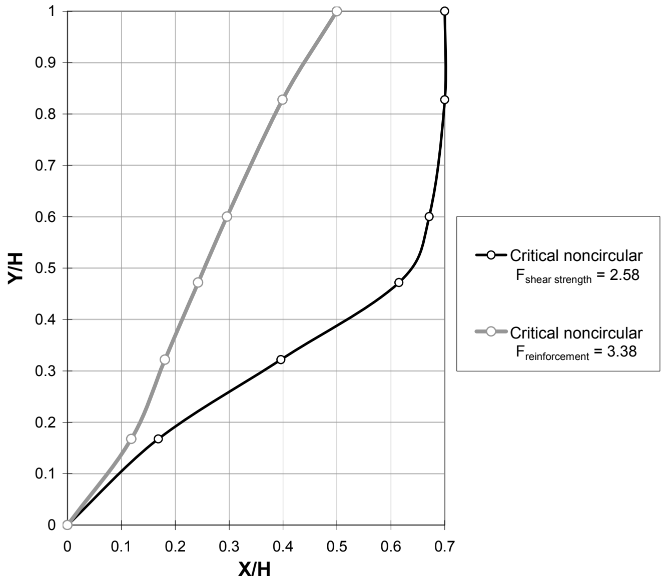

Figure 8.29: Critical noncircular slip surfaces found for the factor of safety in the soil shear strength and the factor of safety in the reinforcement for a wall aspect ratio of 0.70

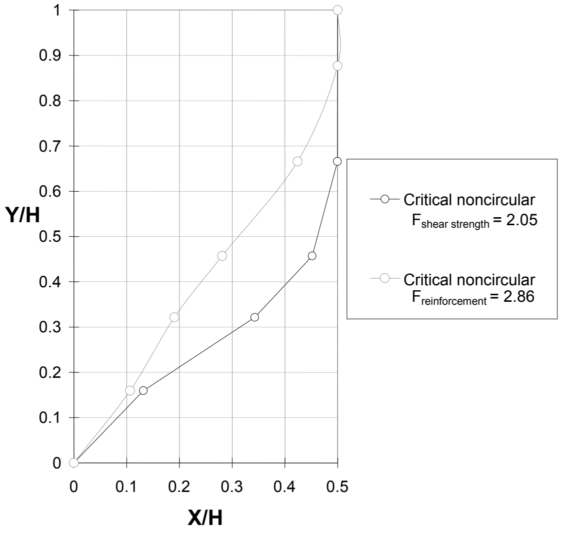

Figure 8.30: Critical noncircular slip surfaces found for the factor of safety in the soil shear strength and the factor of safety in the reinforcement for a wall aspect ratio of 0.50

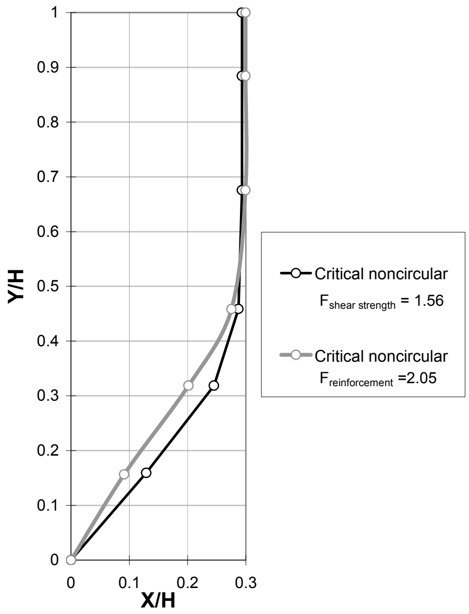

Figure 8.31: Critical noncircular slip surfaces found for the factor of safety in the soil shear strength and the factor of safety in the reinforcement for a wall aspect ratio of 0.30

8.7 Limit equilibrium analysis of a centrifuge model test

A limit equilibrium analysis was conducted of one of the centrifuge model tests performed by Woodruff (2003). Further details of Woodruff's tests are presented in Section 2.4.5. One test (Test 2b) was chosen for comparison with limit equilibrium analysis. The model in the chosen test wall was approximately 110 mm wide at the base and 95 mm wide at the crest. The model wall height was approximately 230 mm. Geosynthetic reinforcement with vertical spacing, S_v, of 20 mm was used to construct the wall. The backfill was placed at a relative density of 70 percent corresponding to a unit weight of 16.05 kN/m^3 (102 pcf). Woodruff used cohesionless backfill with a friction angle (ϕ') of approximately 42.2°. He increased the G-level in his test until failure occurred at approximately 40G, i.e. forty times the acceleration due to gravity.

To simulate the geometry of the centrifuge model wall in the limit equilibrium analysis, the wall was scaled based on the G-level at failure. The dimensions of the model were increased according to a one-to-one relationship with the G-level. Thus, the dimensions of the wall used in the limit equilibrium analyses were 40 times larger than the dimensions of the centrifuge model wall. Using this scaling relationship the scaled wall was 13.4 ft wide at the base, 11.6 ft wide at the crest and the wall height was 28 ft. The bottom layer of reinforcement was located 1.6 ft above the base of the wall, and a vertical spacing of 2.4 ft was used for the remainder of the wall. Eleven layers of reinforcement were used. The properties of the backfill were assigned based on data from Woodruff (2003). The angle of internal friction (ϕ') was 42.2°, the cohesion (c') was zero, and the unit weight (γ) was 102 pcf.

The depth to the bottom layer of reinforcement was used to compute an allowable tensile force ($T_{allowable}$) in the reinforcement. This depth was 26.4 ft (8.05 m). A wall aspect ratio of 0.48 (=13.4/28) was used to calculate the horizontal stresses. The value of the normalized earth pressure coefficient (k_c/K_a) corresponding to a wall aspect ratio of 0.48 was selected from Figure

7-23. A value of k_c/K_a equal to 1.2 was selected. The theoretical Rankine active earth pressure coefficient for an angle of internal friction of 42.2° was equal to 0.196. Thus the value of the horizontal earth pressure coefficient (k_c) used to compute the horizontal earth pressures was 0.235 (=1.2 x 0.196). The maximum horizontal (tensile) force, $T_{max,i}$, in the reinforcement was then calculated from Equation 7-6. The resulting force, $T_{max,i}$, for the bottom layer of reinforcement was 1,520 lb/ft. Finally, $T_{max,i}$ was multiplied by a factor of safety of 1.5 to obtain a reinforcement force of approximately 2,300 lb/ft. This force (2,300 lb/ft) was then assumed to be the allowable pullout resistance in the reinforcement for the limit equilibrium analysis. The development of the pullout resistance from the free end of the reinforcement to the allowable pullout resistance was calculated using Equation 8-5. Because geosynthetic reinforcement was used in the centrifuge model tests, some parameters used to compute the embedment length were different than for the steel ribbed reinforcement considered previously.

The recommended equation for the pullout resistance factor (F^*) for geosynthetic reinforcement is defined in the current FHWA design guidelines for MSE walls (Elias et al., 2001) by the following equation:

$$F^* = \left(\tfrac{2}{3}\right)\tan(\phi') \qquad \text{Eq. 8-6}$$

Based on this recommendation and a friction angle (ϕ') of 42.2°, the value of F^* was computed to be 0.60. The coverage ratio, R_c ($=b/S_h$), for geosynthetic reinforcement is 1.00 because the reinforcement is a uniform sheet of material, i.e. $b = S_h$. Using Figure 7-24 and assuming a wall aspect ratio of 0.48, the values of the vertical stress influence factor (β_v) were selected for each layer of reinforcement.

The distribution of force in each layer of reinforcement was entered into the limit equilibrium software and an analysis was performed. The factor of safety was 1.88. The allowable reinforcement force was then reduced by this factor to approximately 1223 lb/ft and the pullout resistance was recomputed. Based on the reduced reinforcement force the factor of safety was 1.08. The critical noncircular slip surface for this case is shown in Figure 8-32. The failure surface observed in Woodruff's centrifuge test is exhibited in Figure 8-33. The failure surface observed by Woodruff reaches the stable face at approximately 34 percent of the wall height below the top of the wall ($z = 0.34H$) and then follows the interface between the backfill and stable face to the top of the wall. Similarly, the critical slip surface from the limit equilibrium analysis turns abruptly upward at approximately 30 percent of the wall height below the top of the wall ($z/H = 0.30H$). The results of the limit equilibrium and centrifuge test agree very well.

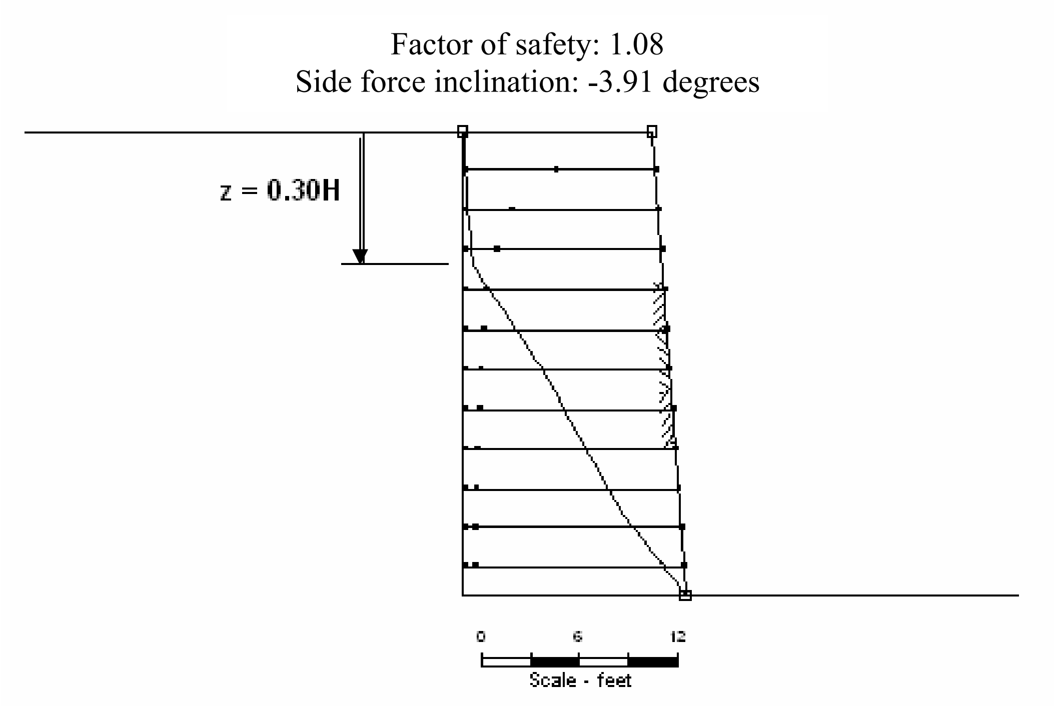

Figure 8.32: Critical noncircular slip surface for limit equilibrium analysis of centrifuge model test

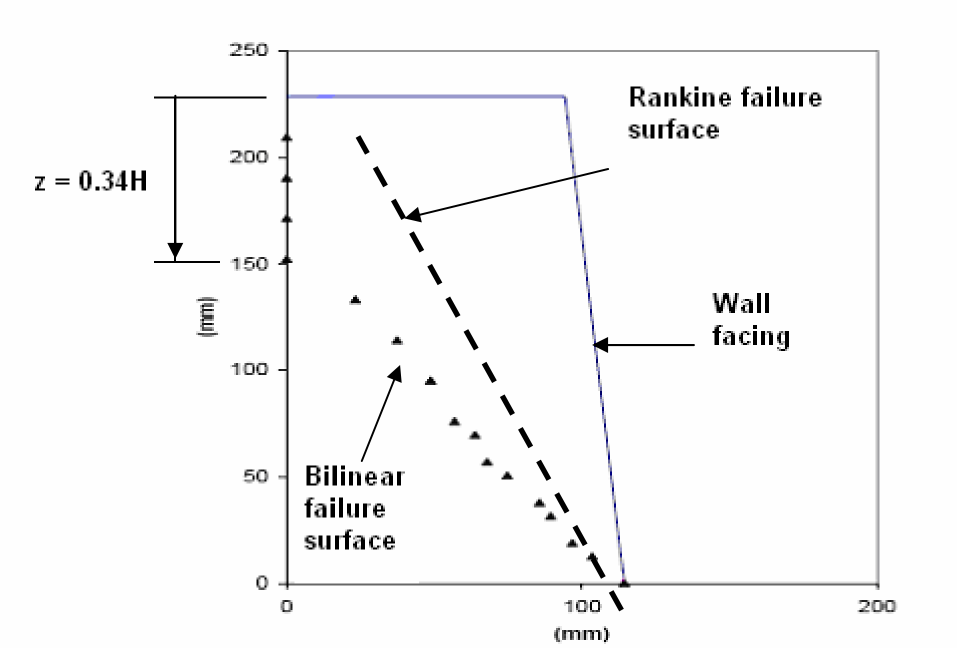

Figure 8.33: Cross-section of centrifuge model geometry showing a bilinear failure surface for L/H = W/H =0.40 (Woodruff, 2005)

8.8 Conclusions and design implications

The analyses presented in this chapter show that when the wall aspect ratio of a MSE wall is less than 0.70, the limit equilibrium analyses should be performed using noncircular slip surfaces. Regardless of how the factor of safety is defined, noncircular slip surfaces are more critical than circular slip surfaces for wall aspect ratios of 0.70 or less. The critical noncircular slip surfaces began at the toe of the wall and extended in nearly a straight line to the existing stable face and then continued to the top of the wall. The same trend was observed by Woodruff in the centrifuge tests described in Chapter 2.

Chapter 9. Summary, Conclusions, and Recommendations

The finite element software known as Plaxis and the limit equilibrium software known as UTEXAS4 were employed to study the stresses and stability of "narrow" MSE retaining walls placed in front of a stable face,. The finite element model was systematically developed through several parametric studies in which the characteristics of the wall, backfill-wall interface, and soil constitutive parameters were examined. Based on these studies, a finite element model was adopted and used to investigate the effects of wall aspect ratio on the horizontal and vertical stresses behind MSE walls. Methods were developed for incorporating the results of the studies into the current design procedures for MSE walls.

Limit equilibrium analyses were performed to examine the effects of wall aspect ratio on the stability of MSE walls placed in front of a stable face. The effects of wall aspect ratio were examined in terms of factors of safety, defined both with respect to soil shear strength and strength of the reinforcement. Analyses were performed employing both circular and noncircular slip surfaces. The following sections describe the finite element analyses with Plaxis and the studies of vertical and horizontal stresses. The limit equilibrium analyses are also described. Finally, recommendations on finite element modeling, design of MSE walls, and areas of future research are presented.

9.1 Modeling nondeformable walls using the finite element software known as Plaxis

The Plaxis finite element software was used to model the stresses in the backfill behind a nondeformable MSE wall constructed in a confined space. Consideration was given to the modeling of the backfill, soil-wall interaction, foundation, wall face, and existing stable face. A typical finite element model of the physical space is shown in Figure 9-1. The backfill was modeled using 15-node triangular elements. The backfill was assumed to be free-draining, cohesionless material. The interfaces between the wall, backfill and stable face, were modeled using 5-node interface elements. The outer nodes on the foundation, exposed wall face, and existing stable face were modeled by assigning total fixity boundary conditions. An example of the boundary conditions adopted for the finite element model with a wall aspect ratio of 0.20 are displayed in Figure 9-2.

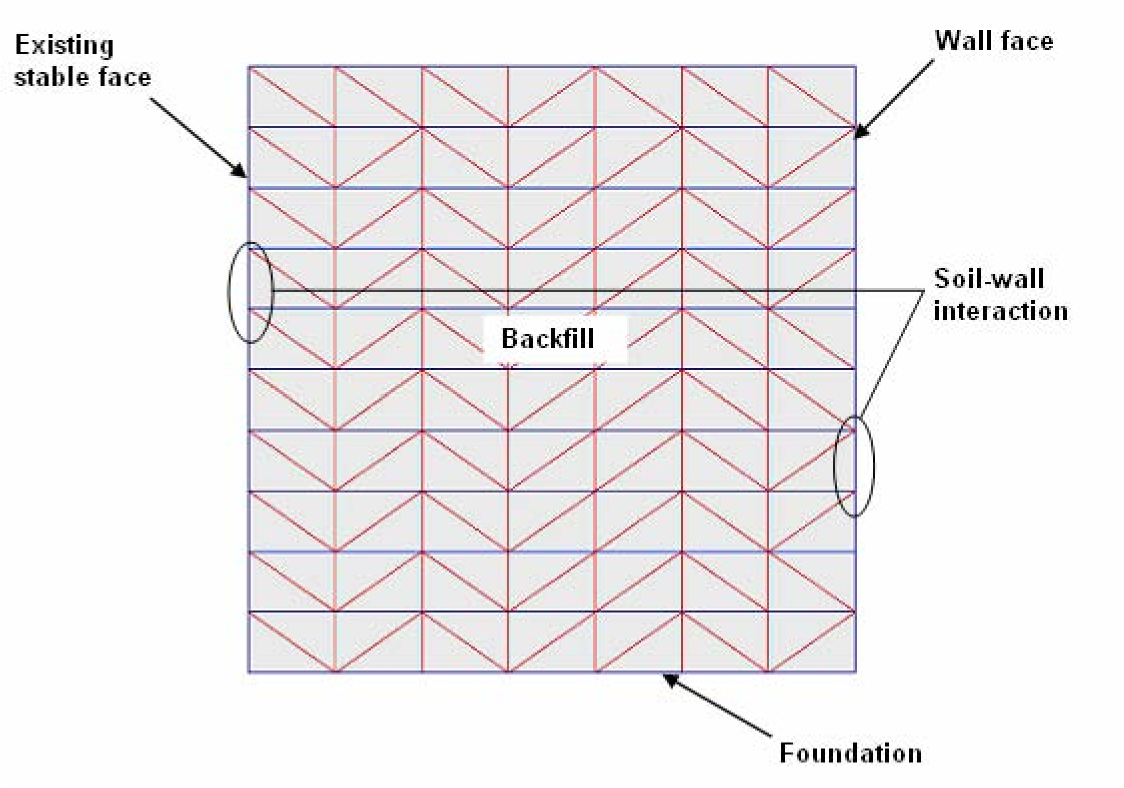

Figure 9.1: Example geometry showing finite element model of the physical space for an nondeformable retaining wall (Plaxis, 2005)

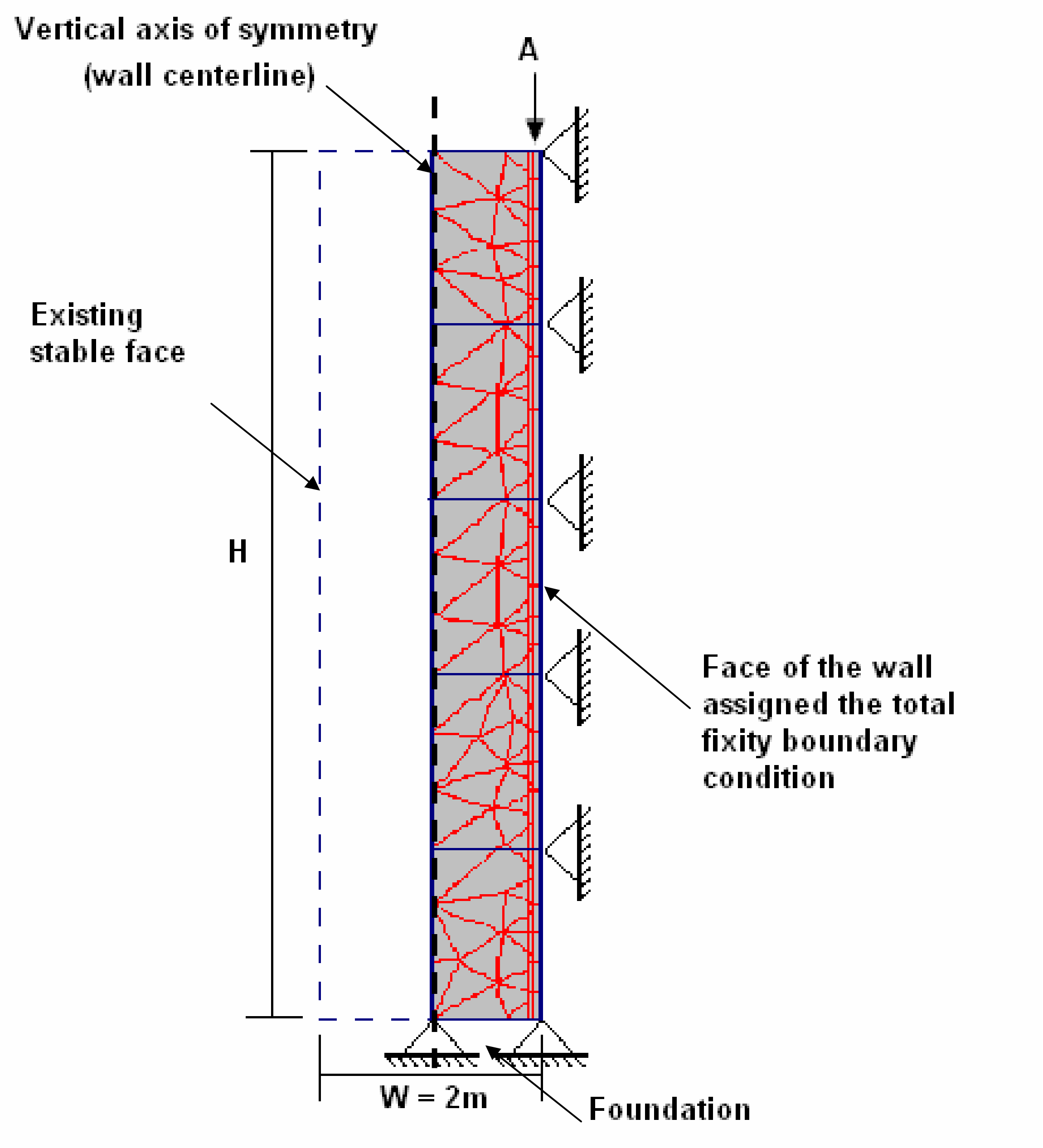

Figure 9.2: Adopted model for finite element simulations having interface elements and the total fixity boundary condition assigned to the face of the wall (Plaxis, 2005)

In Chapter 5, finite element analyses were performed to simulate centrifuge model tests performed by Frydman and Keissar (1987) and Take and Valsangkar (2001). The horizontal earth pressure coefficients (k_w) calculated from the measured earth pressures were compared with values calculated by Plaxis and found to agree favorably. Because the results of Plaxis simulations agreed well with the horizontal earth pressure coefficients based on measured data, Plaxis is believed to be capable of capturing effects of soil-wall interaction and wall aspect ratio on horizontal earth pressures.

In Chapter 6 a study was performed to determine the constitutive model best suited for the purpose of evaluating horizontal earth pressures behind a nondeformable wall. Two soil constitutive models, the Mohr-Coulomb and Hardening-Soil were examined in the study. Values of various soil parameters were changed one-by-one and the effect of changes was observed. Equivalent horizontal earth pressure coefficients (K_{eq}) were used to evaluate the effect of changes in the soil parameters for both the Mohr-Coulomb and Hardening-Soil models. Based on this study, the Hardening-Soil model was selected for further studies.

9.2 Studies of vertical and horizontal earth pressures

Finite element analyses were performed to study how vertical and horizontal stresses vary as the wall aspect ratio decreases. An equation proposed by Spangler and Handy (1982) to account for arching effects in the backfill was also used to compute the horizontal earth pressures. Finally, the manner in which the appropriate stresses can be incorporated into current design procedures was examined.

9.2.1 Vertical stress (σ_v)

The vertical stresses calculated by Plaxis were less than the computed overburden pressure (σ_{ov}). To describe how soil-wall interaction influenced the vertical stresses behind a wall, a vertical stress influence factor (β_v) was introduced. The vertical stress influence factor was shown to decrease horizontally from the center of the backfill to the wall face, with depth below the top of the wall and with decreasing wall aspect ratio.

9.2.2 Horizontal stress (σ_h)

Two definitions of a horizontal earth pressure coefficient were explored and it was decided that a horizontal earth pressure coefficient defined as the ratio of horizontal stress to vertical overburden pressure ($\sigma_h/\gamma z$) was the most useful. Values of this horizontal earth pressure coefficient were calculated along vertical planes at two locations: in the center of the backfill (k_c) and adjacent to the wall face (k_w). The values of k_c and k_w were then normalized by dividing them by the theoretical Rankine active earth pressure coefficient. It was found that the normalized horizontal earth pressure coefficients decreased as the wall aspect ratio decreased. Furthermore, the horizontal earth pressure coefficients were slightly higher along a vertical plane in the center of the backfill than along a vertical plane adjacent to the wall face. Thus, the horizontal earth pressure coefficients calculated at the center of the wall are conservative and recommended for design of “narrow” MSE walls placed in front of a stable face.

9.2.3 Stresses calculated by Plaxis and Spangler and Handy’s equation

Spangler and Handy, 1982, developed an “arching” theory and principle to compute horizontal earth pressure coefficients for granular material next to a nondeformable wall. Comparisons of the horizontal earth pressures were made between values computed using Spangler and Handy’s equation, values measured in the centrifuge model tests and values calculated by Plaxis in Chapters 5 and 6. The horizontal earth pressure coefficients computed using Spangler and Handy’s equation agreed favorably with the horizontal earth pressures both measured from the centrifuge model tests and calculated by Plaxis. It was also shown that values of the equivalent horizontal earth pressure coefficient (K_{eq}) computed using Spangler and Handy’s equation were slightly less conservative than the values calculated by Plaxis. Better agreement can be obtained by increasing the values computed from Spangler and Handy's equation by 10 percent.

9.2.4 Application of reduced horizontal and vertical stresses to current design guidelines

The reduced vertical and horizontal stresses calculated by Plaxis can be introduced into current design equations to calculate factors of safety against pullout ($F_{pullout}$) and breakage ($F_{breakage}$). The effect of wall aspect ratio on the horizontal earth pressures can be applied to current design equations by using the revised earth pressure coefficients presented in Chapter 7 (Figure 7-23) to calculate the required force to prevent breakage of the reinforcement ($T_{max,i}$). The effect of wall aspect ratio on the vertical stresses and pullout resistance can be applied to current design equations by reducing the vertical overburden stress (σ_{ov}) by the vertical stress influence factor (β_v) when calculating the pullout resistance, $P_{r,i}$, in a given layer of reinforcement. The values of β_v can be determined using Figure 7-24.

9.3 Limit equilibrium analyses

Limit equilibrium analyses were performed using the UTEXAS4 software and both circular and noncircular slip surfaces to evaluate the effect of wall aspect ratio on global stability of the walls. The shape of the slip surface was of interest because current design guidelines do not address the shape of the slip surface either for walls in front of a stable face or for MSE walls with an aspect ratio (L/H) less than 0.70.

In the limit equilibrium analyses with UTEXAS4 the distribution of allowable force along the reinforcement was assumed to be zero at the free end and then increase linearly from zero to a value equal to the allowable tensile strength of the reinforcement (Figure 8-2). The rate of change in the resisting force with horizontal distance (shown as S in Figure 8-2) is a function of the properties of the backfill, the type of reinforcement, the horizontal spacing (S_h) and the vertical overburden pressure (σ_{ov}). The rate of change was calculated for each layer of reinforcement.

The UTEXAS4 software was used to search for a critical slip surface having a minimum factor of safety. Bishop's Simplified procedure was used to calculate the factors of safety for circular slip surfaces and Spencer's procedure was used to compute the factors of safety for the noncircular slip surfaces. Circular, bilinear, and general shaped noncircular slip surfaces were analyzed.

Factors of safety, F, were defined and calculated in two ways. In the first way the conventional definition where the factor of safety is defined with respect to soil shear strength was used. In the second way the soil shear strength was assumed to be fully mobilized ($F = 1.00$) and a factor of safety was applied to the reinforcement forces. The reinforcement was reduced by this second factor of safety until equilibrium was achieved with the shear strength fully mobilized. Factors of safety were calculated by both definitions for both circular and noncircular slip surfaces. A comparison of the factors of safety using both definitions is shown in Table 8-9. Regardless of how the factor of safety is defined, noncircular slip surfaces were more critical than circular slip surfaces for wall aspect ratios less than normal ($L/H < 0.70$). The shapes of the critical noncircular slip surfaces began at the toe of the wall and extended in nearly a straight line to the existing stable face and then continued to the top of the wall for all walls and aspect ratios analyzed. The critical noncircular slip surface was also deeper than the theoretical Rankine failure surface. The same trend was observed by Woodruff (2003) in the centrifuge tests described in Chapter 2.

9.4 Recommendations

Recommendations can conveniently be made in three categories: (1) Use of Plaxis to analyze MSE walls, (2) guidance for design of MSE walls in a confined space in front of a stable face, and (3) suggestions for future research. These are each discussed in the following sections.

9.4.1 Finite element modeling of MSE walls using Plaxis

The recommended finite element model for the study of nondeformable MSE walls is described in Section 9.1 and illustrated in Figure 9-2. Using this model, the displacements, stresses and strains can be calculated for any wall geometry.

9.4.2 Design of MSE walls

The results from the study of vertical and horizontal stresses should be used to evaluate the required reinforcement strength and pullout resistance for internal stability. A conservative design approach to internal stability is to ignore the reduction in horizontal stresses and their effect on the required reinforcement strength, i.e. use the current design guidelines (Elias et al., 2001) to calculate the maximum tensile force, $T_{max,i}$ (Eq. 7-4). Once a tentative design has been established, limit equilibrium analyses should be performed as a check.

Although surcharge loads were not explicitly addressed in this study, it is recommended that normal traffic surcharge loads be addressed in the same manner that they are addressed in current FHWA guidelines for reinforced walls. Appropriate surcharge loads should also be included in all limit equilibrium analyses for internal, compound or external stability. Caution should be used if unusual (in excess of nominal traffic) surcharge loads are imposed. In such cases further finite element analyses may be necessary to judge the impact of the surcharge loads.

The external stability of the MSE wall is important as the wall aspect ratio decreases because the wall becomes more susceptible to failure caused by sliding, overturning and plunging, i.e. a bearing capacity failure. Until more is known regarding the external stability of MSE walls placed in front of a stable face, it is recommended that the wall width be greater than 30 percent of the wall height ($W/H > 0.30$). This recommendation is based largely on the judgment of the authors, and is supported also by the centrifuge model tests reported by Woodruff (2003).

Although no analyses were performed in which the reinforcement was considered to be anchored at the back of the rectangular wall section, considerable thought and discussion was given to this possibility. At the present time the researchers feel that anchoring of the reinforcement to the stable face could lead to unknown consequences and should only be done with great caution. As a minimum finite element analyses should be performed for the particular configuration being considered to examine the possible overstressing of the reinforcement at the connection points.

While anchorage of the reinforcement to the stable face in general is not recommended, extension of the uppermost levels of reinforcement beyond the nominal stable face seems feasible for new walls that are built to heights above the existing (or possible excavated to reduced height) stable wall and face. Appropriate pullout resistance for the reinforcement extensions should be estimated and used to determine the available resistance of the extended reinforcement. Once the resistance is determined it can be included in limit equilibrium analyses to determine how the additional resistance provided by the extended reinforcement contributes to stability. It should be noted however that since such extended reinforcement at the top of the wall will have only low overburden stresses, its resistance to pullout may be limited. Limit equilibrium analyses should always be performed when considering such alternatives as longer, extended reinforcement at the top of the wall.

9.4.3 Future Research

It was assumed that the walls being studied were nondeformable. However, if the walls are deformable the earth pressures are expected to be lower which could reduce the cost of designs. Therefore, it is recommended that further analyses be conducted to study the design of deformable walls. Another assumption was that the existing wall was stable, however further studies are recommended to explore how strong the ground would need to be to reasonably prevent the possibility of failure through this zone. Finally, the geometries analyzed herein were for simple MSE wall geometries. The effects of surcharges, sloping backfill and sloping or weak foundations should also be analyzed using finite element and limit equilibrium analyses.

There are little field data available from which to base design recommendations. Thus, it is recommended that a MSE wall placed in front of a stable face be instrumented similarly to the walls discussed in Section 2.3 of the literature review. In order of importance, the MSE walls should be instrumented with strain gauges to find the locations of maximum tensile stress in the reinforcement, inclinometers at the wall face and existing stable face to determine displacements, survey points to measure the deformations of the wall facing, and pressure cells to study the vertical and horizontal earth pressures.

References

Apostol, T.M. Calculus. Vol. 2. New York: Blaisdell Publishing Company, 1962

Duncan, J.M. et al. “Strength, Stress-Strain and Bulk Modulus Parameters for Finite Element Analyses of Stresses and Movements in Soil Masses,” Report No. UCB/GT/80-01, Office of Research Services, University of California, Berkeley, California, 1980.

Elias, V., Christopher, B.R., and Berg, R.R. "Mechanically Stabilized Earth Walls and Reinforced Soil Slopes Design and Construction Guidelines," *Report No. FHWA-NHI-00-043*, National Highway Institute, Federal Highway Administration, Washington, D.C., March, 2001.

Filz, G.M. and Duncan, J.M. “Vertical Shear Loads on Nonmoving Walls,” Journal of Geotechnical and Geoenvironmental Engineering, ASCE, Vol. 123, No. 9, Sept., pp. 856-852, 1997.

Frydman, S. and Keissar, I. "Earth pressure on retaining walls near rock faces," *Journal of Geotechnical Engineering, ASCE,* Vol. 113, No. 6, June, pp. 586-599, 1987.

Holtz, R.D. and Kovacs, W.D. An Introduction to Geotechnical Engineering. New Jersey: Prentice-Hall, 1981.

Lawson, C.R., and Yee, T.W. "Reinforced soil retaining walls with constrained reinforced fill zones," *Proceedings*, Geo-Frontiers 2005, ASCE Geo-Institute Conference, 2005.

Leshchinsky, D., Hu, Y., and Han, J. "Design implications of limited reinforced zone space in SRW's," *Proceedings of the 17th GRI Conference on Hot Topics in Geosynthetics IV*, Las Vegas, Nevada, 2003

Morrison, K.F. et al. “Shored Mechanically Stabilized Earth (SMSE) Wall Systems Design Guidelines,” *Report No. FHWA-CFL/TD-06-001*, Federal Highway Administration, Central Federal Lands Highway Division, 2006.

Plaxis. *Plaxis Finite Element Code for Soil and Rock Analyses*, Version 8.2, P.O. Box 572, 2600 AN Delft, The Netherlands (Distributed in the United States by GeoComp Corporation, Boxborough, MA), 2005.

Simac, M.R. et al. “Design Manual for Segmental Retaining Walls,” 2nd ed. Ed. J.G. Collin. *NCMA Pub. No. TR127A*, National Concrete Masonry Association, Herndon, VA, 1997.

Spangler, M.G. and Handy, R.L. Soil Engineering. 4th ed. New York: Harper and Row, 1982.

Sperl, M. “Experiments on corn pressure in silo cells – translation and comment of Janssen’s paper from 1895,” *Granular Matter*, Vol. 8, pp.59-65, December 2006.

Take, W.A. and Valsangkar, A.J. “Earth pressures on unyielding retaining walls of narrow backfill width,” *Can. Geotech. Journal,* 38: 1220-1230

Turner, John P. and Jensen, Wayne G. "Landslide stabilization using soil nail and mechanically stabilized earth walls: case study," *Journal of Geotechnical and Geoenvironmental Engineering*, ASCE, Vol. 131, No. 2, Feb., pp. 141-150, 2005.

Woodruff, Ryan "Centrifuge modeling of MSE-shoring composite walls," Thesis submitted to the faculty of the Graduate School of the University of Colorado in partial fulfillment of the requirements for the Master of Science degree, Department of Civil Engineering, Boulder, 2003.

Wright, S.G. "UTEXAS4 A Computer Program for Slope Stability Calculations." Shinoak Software, Austin, Texas, September, 221p, 1999.